Mitigating The Corrosion Reaction In Alkaline Silicon-Air Batteries Through Nonuniform Doping

by

Rutger Coerkamp

to obtain the degree of Master of Science
at the Delft University of Technology,
to be defended publicly on Monday July 18, 2022 at 14:00.

Student number:	4480724	
Project duration:	December, 2021 - July, 2022	
Thesis committee:	Dr. R.A.C.M.M. van Swaaij	TU Delft (ESE - PVMD), supervisor
	Prof. dr. ir. A. H. M. Smets	TU Delft (ESE - PVMD)
	Dr. ir. L. Bannenberg	TU Delft (RST - SEE)

Abstract

The mass production of lithium-ion batteries used in, for instance, electric vehicles led to significant cost reductions. However, concerns are emerging about the availability of resources and the environmental impact of the production. Metal-air batteries use more resource-efficient materials and potentially have higher energy densities than lithium-ion batteries. A little over a decade ago, a promising new type of metal-air battery was discovered, the silicon-air (Si-air) battery.

The Si-air battery uses a c-Si anode and a porous air cathode, combined with a liquid electrolyte. Si-air batteries have a theoretical cell potential up to 2.2 V and a very high theoretical energy density of 8,470 Wh/kg. However, Si-air batteries that use alkaline electrolytes, such as potassium hydroxide (KOH), are not rechargeable and the Si anode suffers from passivation and corrosion. Currently, corrosion is considered as the dominant factor that limits the conversion efficiency of alkaline Si-air batteries. In this work, the role of the electrons participating in the corrosion reaction is further investigated. This is based on a model where electron transfer is considered as a rate-limiting step. The research objective of this work is the mitigation of the corrosion reaction in alkaline Si-air batteries through nonuniform doping of the Si anode.

The corrosion in the Si-air battery setup was first quantified for uniformly doped c-Si. These results function as reference to nonuniformly doped Si. The corrosion rates for uniformly doped n-type and p-type Si using 6.6M KOH were found to be constant at 1.25 μm/h and lower than the 2.2 μm/h measured in previous research. This lower corrosion rate increased the conversion efficiency from 2.0% to 3.4%, corresponding to a specific capacity of 130 mAh/g_{Si}. Based on these results, corrosion in Si-air batteries is still significant.

Nonuniformly doped wafers were made by depositing thin impurity layers on c-Si through PECVD or epitaxial growth. Subsequently, drive-in of the impurity atoms into the c-Si was performed at a temperature of 1250°C for 36 hours. The shape and junction depth of the dopant profiles were verified by the four-point probe and spreading resistance profiling. These results show the presence of doping profiles with junction depths up to 36 μm.

In the samples made with PECVD, corrosion slightly increased in nonuniformly doped p-type and n-type Si with respect to uniformly doped Si. However, the corrosion is not clearly affected by the implemented doping profiles. For nonuniformly doped p-type Si samples made with epitaxial growth, corrosion clearly decreased to 0.82 μm/h compared to 1.25 μm/h with uniformly doped Si. Corrosion decreases by having a high boron concentration above 2×10^{19} atoms/cm^3 in the Si and not through the implementation of a dopant profile.

It is concluded that nonuniform doping does not affect the corrosion in alkaline Si-air batteries and, therefore, does not mitigate the corrosion reaction.

Acknowledgements

Many people have played an instrumental role in the process that has led me to this moment. Therefore, I would like to thank the following people, who have all in their own way played an important part in my journey.

First, I would like to express my deepest gratitude to my supervisor, Dr. René van Swaaij. He first piqued my interest in this subject matter and his support and guidance have been indispensable for the course of my research. I thoroughly enjoyed our collaboration and fruitful discussions. René was a very approachable supervisor and he was always willing to take time to exchange ideas and views with me and to sharpen my thoughts about hurdles I encountered during the past seven months. Without René, my results would not have been where they are today, so I am very grateful for his contribution.

Furthermore, I would like to thank the thesis committee, consisting of Prof. Arno Smets and Dr. Lars Bannenberg, for taking time out of their busy schedules to take a seat in this committee and to delve into the subject matter of this thesis.

I would also like to extend my sincerest thanks to the technicians of the PVMD-group; Martijn Tijssen and Stefaan Heirman. They both have been very helpful and have played a vital part in the experimental part of this research project. Martijn has taught me how to use all the machinery and equipment in the CR10000 and has assisted me with the process steps for making the samples. Stefaan has helped me optimize the setup by, amongst other things, together redesigning the electrical contacts, which has improved the setup significantly.

My gratitude also goes out to the EKL technician Tom Scholtes, who has been willing to help think of solutions for the challenges encountered during this unconventional project and who has put time and effort to make the epitaxial samples, which have provided useful results. Moreover, special thanks go out to Johan de Haas of the Reactor Instituut Delft (RID) for allowing me to use the facilities of the RID for this research project. At the RID, I was able to carry out the diffusion steps at high temperatures, something that was not possible within the facilities of EKL.

I would also like to acknowledge my fellow students at PVMD group, in particular my roommate Mathijs van Kouwen and neighbour Mohua Fardousi. I very much enjoyed our coffee tastings and breaks at our coffee bar, where we discussed a wide variety of topics. It was a very nice distraction from the long, and sometimes frustrating, experimental work.

A special thanks goes to my girlfriend Charlotte. She managed to support me throughout the entire thesis process, while also giving feedback on my writing. She understood the topic of Si-air batteries quite well in the end.

Lastly, I would like to thank the people surrounding me outside the TU Delft for their support during not only this research project, but during the whole course of my academic career at the TU Delft. They have made my time here in Delft a very special and memorable experience.

R.G. Coerkamp
Delft, July 2022

List of Figures

List of Tables

Contents

Chapter 1

Introduction

The average temperature on Earth has been rising steadily over the last couple of decades [1][2]. This increase in temperature, also referred to as global warming, causes events such as droughts, floods, severe rainfall and storms to occur more often [3]. In addition to that, snow and ice sheets on land will melt faster than usual and cause the sea level to rise.

In fact, the decade 2011-2020 was the warmest ever recorded. The average global temperature has risen 1.2 °C above pre-industrial levels as can be seen in figure 1.1 [4]. The year 2020 was in the top three of warmest years recorded.

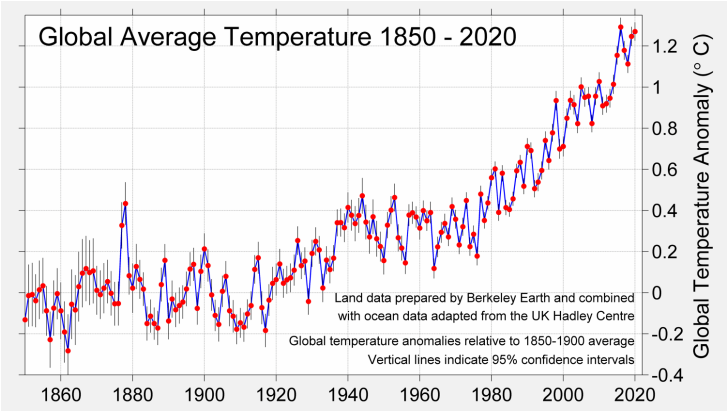

Figure 1.1: The global average temperature is increasing rapidly as indicated by the blue line. The figure shows the globbal average temperature from 1850, at the height of the industrial revolution, up to the year 2020. The global average temperature has increased 1.2 C in the years between 1850 and 2020. Figure taken from [5].

99.9% of 88,125 climate-related studies agree on the fact that human actions are the main cause for the climate to change [6]. The increased emission of greenhouse gases (GHG) following from burning fossil fuels, such as coal and oil, has a warming effect on the Earth's climate.

The combustion of these fuels started late in the 18th century with the industrial revolution. From that moment up until now, human society has become dependent on using fossil fuels in, for instance, the production of goods or transport of people. These fossil fuels originate from the energy of the sun that is stored underground as chemical energy. It took millions of years to produce these fuels through photosynthesis, but the rate at which these fuels are depleted is much higher than the rate at which they are generated. This means that the availability of these energy sources is finite and it will become increasingly difficult to extract the final reserves.

Due to the growing world population and improving living standard in developing countries, the demand for energy is increasing. The Energy Information Administration (EIA) from the United States estimated that the energy consumption will grow by 50% in the period 2018-2050, mainly caused by Asian markets [7]. A big part of this growing demand for energy is still fulfilled by fossil fuels.

If demand for energy continues to increase but the supply cannot match it, the prices of fossil

fuels will rise and products will become more expensive. This can lead to geopolitical tension regarding the extraction of fossil fuels and the availability on markets. As fossil fuels are stored underground in certain places, there are strategic advantages for certain countries or companies. The sky-high gas prices in Europe at the moment are a very recent example of geopolitical tension caused by the availability of energy on the markets. Gas prices have increased drastically as a result of the Russian-Ukrainian war, low strategic reserves due to a cold winter in the beginning of 2021 and an increase in demand for energy from recovering industries after COVID 19-lockdowns. This had led gas prices to reach record values of 180 euro per MWh. In comparison, at the beginning of COVID 19, the prices were 4-8 euro per MWh [8].

To fulfill the commitments that have been laid down in the Paris Agreement and that recently have been reaffirmed during the climate summit in Glasgow, CO_2 emissions have to be lowered. Over 84% of the worldwide primary energy supply, i.e. 135,000 TWh, came from fossil fuels in 2019 and the use of these fossil fuels is responsible for two thirds of the global emissions [9][10]. An energy transition has to take place to lower the CO_2 emission intensity, while still supplying sufficient energy to match economic growth.

A way to lower the emissions is by switching to more renewable energy sources that do not emit CO_2 on producing energy and do not necessarily require the input of fuel as a feedstock. Solar and wind energy are considered as the most promising large-scale renewable energy sources to reach the climate goals [11], mainly because of their maturity level and cost competitiveness. Their levelized cost of electricity (LCOE) has dropped significantly over the past decade, making it cheaper to install and operate a wind or solar farm than building a fossil fueled power plant. The LCOE of solar photovoltaics dropped by 89% to 40 euro per MWh in the period 2010-2019. Onshore wind power LCOE's decreased by 70% in the same period to a price of 41 euro per MWh [12].

Unlike fossil fuel power plants, solar and wind energy have a variable production as they depend on solar irradiance level and wind speeds. This is called intermittency and currently, conventional fossil fuel power plants often have to compensate for this effect to stabilize the grid [13].

Supply and demand of energy on the electricity grid has to be matched at all times [14]. With an increasing share of solar and wind energy it is possible that supply is larger than demand or vice versa, resulting in a mismatch of supply and demand of energy. As electricity cannot be stored on the grid, an option is to shift the demand for energy to times with an oversupply of electricity. But shifting the demand for energy is often limited to shorter timescales as, for instance, a household cannot postpone its laundry or cooking for a whole month or season. For these moments, the storage of energy proves to be a viable option. The role that energy storage can play in solving the challenges surrounding climate change, will be discussed in the next section.

1.1 The role of energy storage

Storage can play a role in mitigating the mismatch of energy [15]. There are many forms of energy storage, ranging from mechanical and electrical to chemical storage, and with timescales ranging from seconds up to whole seasons. There is no single solution that can provide energy storage at all scales. For example, maintaining the grid frequency requires a fast response time, but not necessarily a large storage capacity as the timescale is short, whereas shifting the energy demand of consumers away from peak hours will require MWh's of energy to enable discharge capacities of several hours. To overcome the seasonal effect of solar and wind energy, TWh's of energy storage is needed to prevent using fossil fuels. This requires a high cycle efficiency, high energy density and a low cost per stored unit of energy [13]. An overview of the different storage technologies and their corresponding timescale is summarized in figure 1.2.

An energy storage technology that received much attention recently is the battery. Batteries convert electrical energy to chemical energy on charging and vice versa on discharging. They can

respond fast and rechargeable batteries have high cycle efficiencies close to 100% [16]. Prices of batteries have dropped significantly, making batteries an attractive option [17][18]. For example, battery systems used in residential or utility scale stationary applications are expected to reach price levels of 280-400 $/kWh and batteries used in transportation vehicles 150-200 $/kWh. Smaller, portable batteries are expected to reach higher energy densities and lower price levels in the order of 135 $/kWh at 1 TWh of installed capacity [18].

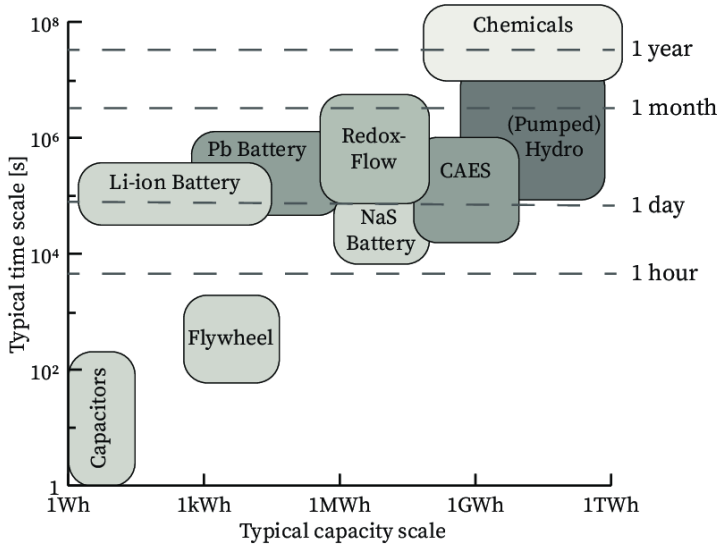

Figure 1.2: The time and capacity scales of different storage technologies. Chemical storage (fuels) is suitable for seasonal storage whereas batteries are suitable for daily energy storage. Figure taken from [19] and based on [20].

These price levels indicate a bright and cost-competitive future for batteries as a storage technology. As can be seen in figure 1.2, the energy density of batteries is more than one order of magnitude smaller than the energy density of chemical fuels, such as hydrogen and ammonia, and is therefore fit for day-to-day timescales. Monthly or season energy storage requires storing TWh's of energy and it is, therefore, more logical to store large quantities of energy in physical fuels than in batteries [14]. According to the IEA Sustainable Development Scenario (SDS), cheap energy storage, including storage in batteries, is indispensable to reach the world's climate goals. A total energy storage capacity of 10 TWh, supplied by batteries, is needed by 2040. This is equal to 50 times the current market size [21].

A brief introduction into the working principle and the types of batteries that have been described in literature, is discussed in the next section. Special attention is given to metal-air and silicon-air batteries in separate subsections.

1.2 Batteries

A battery converts stored chemical energy into electrical energy by using electrochemical cells that undergo electrochemical reactions [22][23]. An electrochemical reaction is a reaction where at least one of the species undergoes a change in its valence. The electrochemical cell consists of two half cells that include different conducting (metal) electrode materials. The half cells are separated by an electrolyte to prevent electronic conduction, i.e. short-circuit, but allow ionic conduction. Electricity is generated by electrons that move between the electrodes through an external circuit in a oxidation-reduction reaction, or redox-reaction. The electron flow in the external circuit produces a current that is used to deliver work to the demanded load [23]. On discharging, the electrochemical cell is also referred to as a galvanic or voltaic cell.

A battery is recharged by reversing the redox reaction through the application of a current to the cell. This type of cell is then called an electrolytic cell. The current is supplied by a charger. The voltage of the charger has to be higher than the cell's voltage to overcome the

internal resistance and enable current to flow into the cell [24]. When the redox reactions cannot be reversed easily, the batteries can only be discharged once. This is called a primary battery. While this type of battery can only be discharged once, an advantage of primary batteries is that they can be tiny, light and cheap. A secondary battery can be recharged by reversing the redox reactions. Electrical energy is then converted back to chemical energy.

There are multiple types of rechargeable batteries available such as redox-flow, sodium-sulfur, lead-acid and lithium-ion (Li-ion). Batteries are a mature type of technology, but suffer from a relatively low energy density compared to fuels and are therefore available on a kWh to MWh scale and thus more suitable for day-to-day storage [25]. An example of a scenario where batteries can be used on a daily timescale, is given in figure 1.3.

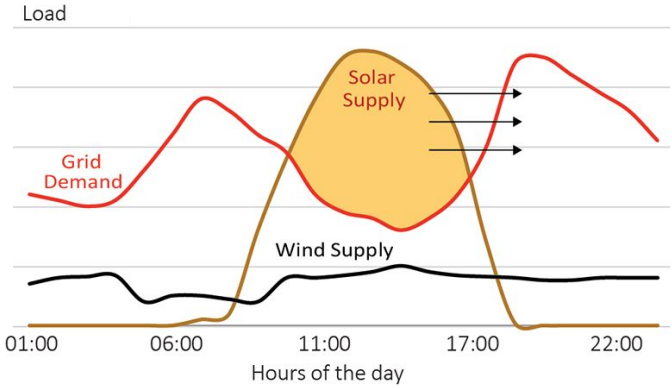

Figure 1.3: Intra-day storage of energy by using batteries. At daytime excess generated energy is stored and used at a later time when demand is higher than supply, as indicated by the black arrows. Figure taken from [26].

As said before, the intermittent nature of solar and wind energy results in mismatches between supply and demand. During daytime hours, especially around noon, solar panels generate their peak power while demand for energy is often lower than in the morning or evening. Storing the excess generated energy at daytime into batteries, and using it when demand for electricity is higher appears to be a logical solution.

A very popular type of battery that gained much attention recently is the Li-ion battery. Li-ion batteries use the principle of intercalation of Li^+-ions. This means that Li^+-ions travel through the electrolyte between so-called host-structures while oxidation and reduction takes place at the electrodes [13]. The anode is made of graphite while the cathode is made of a lithiated metal-oxides that can include cobalt (Co) or manganese (Mn). Li-ion cells have a high operating voltage of 3.7 V and are featured with high energy densities of roughly 200 Wh/kg and 500 Wh/L [27]. The relatively high volumetric energy density allows Li-ion batteries to be used in small and portable electronic devices.

However, the extraction of the cathode material Co from the earth is a controversial topic as the mining activities are concentrated in the Democratic Republic of Congo and rely on child labor [28]. Besides, lithium has an availability in the earth's crust of only 20-70 parts-per-million (ppm), is concentrated in only a number of geographical locations in Chile and Australia and consumes 65% of the already scarce local water supply [29][30]. Moreover, prices of lithium have increased by more than 500% in 2021 due to increased demand for Li-ion batteries in electric vehicles [31]. Therefore, the search for more abundant materials on earth that can be used in batteries has accelerated. When batteries are exploited on a very large scale as a storage technology, the use of abundant and environmentally benign materials will become more important. In the next two subsections, two types of promising, resource-efficient batteries will be discussed.

1.2.1 Metal-air batteries

Metal-air batteries rely on more widely available materials with a higher theoretical energy density than Li-ion. The first primary metal-air battery, a Zinc-air battery, was designed in

1878, well before Li-ion batteries were invented [32].

A metal-air battery uses a metal, such as zinc (Zn), aluminum (Al), iron (Fe), magnesium (Mg), silicon (Si), potassium (K) or Li as an anode. It has an air cathode that includes a porous carbon structure covered by catalysts. The electrolyte can be aqueous, non-aqueous or a solid polymer membrane. Aqueous electrolytes have a high ionic conductivity, are cheap and non-flammable and are therefore used most often for anode materials made of Zn, Al, Fe, Mg [33]. Other metals, such as Li, Na and K, are, however, very reactive in aqueous electrolyte solutions and thus non-aqueous electrolytes have to be used [34]. This can be a solid-state electrolyte or an ionic liquid. In a solid-state electrolyte, leakage and evaporation is minimized and the energy density is higher than for liquid electrolytes. Ionic liquid electrolytes are not flammable and have a high ionic conductivity. A popular example of ionic liquid is the room temperature ionic liquid (RTIL), a salt that is a liquid below 100 °C [33].

The fact that a metal-air battery uses oxygen from the ambient air instead of a metal electrode as a cathode, means that the cost and weight of the cathode can be significantly reduced. The amount of oxygen available is also practically inexhaustible [35]. Ambient air consists for 21% out of oxygen. The remaining 79% mainly consists of the inert gas nitrogen (78%) and some other gases (0.93%). In some cases, the anode material can still react with nitrogen to form a sort of metalnitride which enhances the cycling efficiency [36]. The metal material used for the anode is directly involved in the redox reactions and therefore no other materials are required [33]. This further increases the energy density of the battery.

Recharging a metal-air battery means that the reactions have to be reversed and the reverse reaction at the cathode should be catalyzed as well. But using the optimal catalysts in both reactions still creates a large polarization and thus a limited cycle efficiency that is significantly lower than those of Li-ion batteries. It is difficult to find a bifunctional catalyst for the air cathode for both charging and discharging [34].

The theoretical energy densities of metal-air batteries is in the order of thousands of Wh/kg and, therefore, considerably higher than those of the previously discussed batteries. Li-air batteries have an energy density of 11,430 Wh/kg, which is much higher than the several hundred Wh/kg of Li-ion batteries and is close to that of gasoline, i.e. 13,000 Wh/kg, making it a suitable candidate for long-range electric vehicle batteries [37].

Figure 1.4 shows a selection of popular metal-air battery anode materials. This includes the gravimetric (Wh/kg) and volumetric (Wh/L) energy density by including only the active materials. If multiple types of electrolyte are possible, the one with the highest theoretical energy density is showed. The next subsection will zoom in on the silicon-air couple.

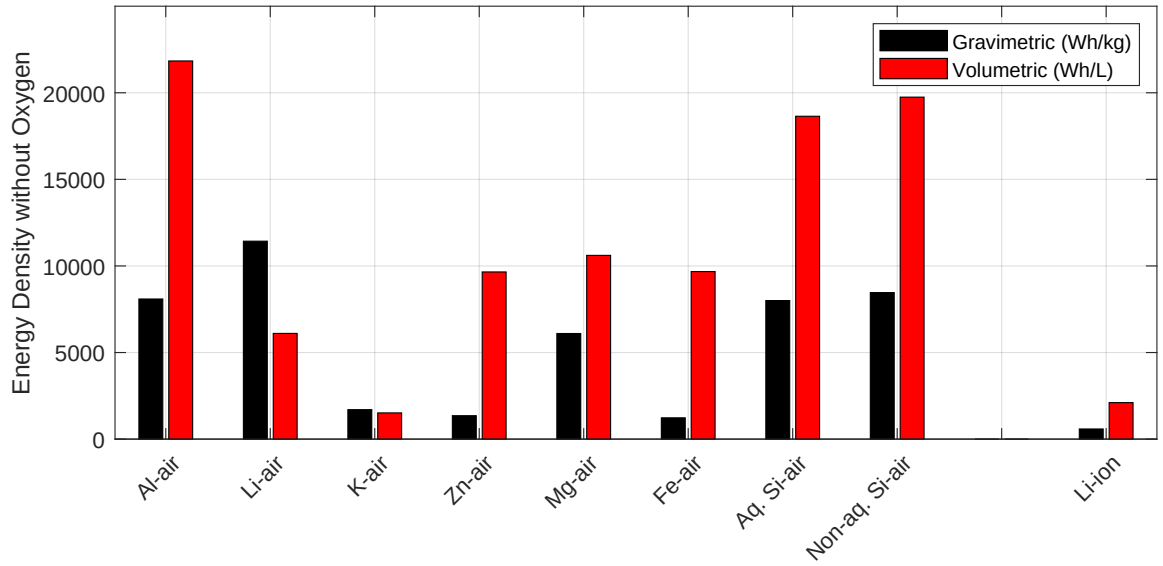

Figure 1.4: Comparison of the theoretical energy densities of different metal-air battery anode materials and Li-ion. Energy densities are given in both Wh/kg (blue) and Wh/L (red) and the metal-air batteries do not include the mass of oxygen. Data taken from [38] and [39].

1.2.2 Silicon-air batteries

A promising new type of anode material for metal-air batteries is silicon (Si). The first publication dates back to 2009 and was written by the group of Cohn et al. at the Technion-Israel Institute of Technology [40]. A patent filed by the same group followed in 2011. Since then, Si-air batteries have come under the attention of different research groups including Zhong et al. [41], Durmus et al. [42][43][44][45], Park et al. [46] and Garamoun et al. [47].

Strictly speaking, Si is a semiconductor material and not a metal, but in literature it is referred to as a metal-air type of battery as it is based on the same working principle, i.e. a Si anode combined with a porous air cathode connected through a liquid or solid electrolyte. Besides, the Si used is heavily doped which gives it more metal-like properties.

In the semiconductor industry, Si has been the most used material for compact electronic devices for the past decades [48]. The knowledge of this material to improve and tweak its properties is therefore large, but although the material Si has been researched for decades in integrated circuits or as a photovoltaic material, using it as a storage device in a metal-air battery was only introduced just over a decade ago.

As can be seen in figure 1.5, the element Si is the second most abundant element in the earth's crust and therefore much more abundant than Li used in Li-ion and Li-air batteries. The availability of Si is above 10^5 parts-per-million (ppm), while Li is in the order of 10^1 ppm [49]. Besides, the availability of Si is not limited to certain geographical locations, reducing the risk of geopolitical tensions. Its high availability makes Si a more low-cost type of battery.

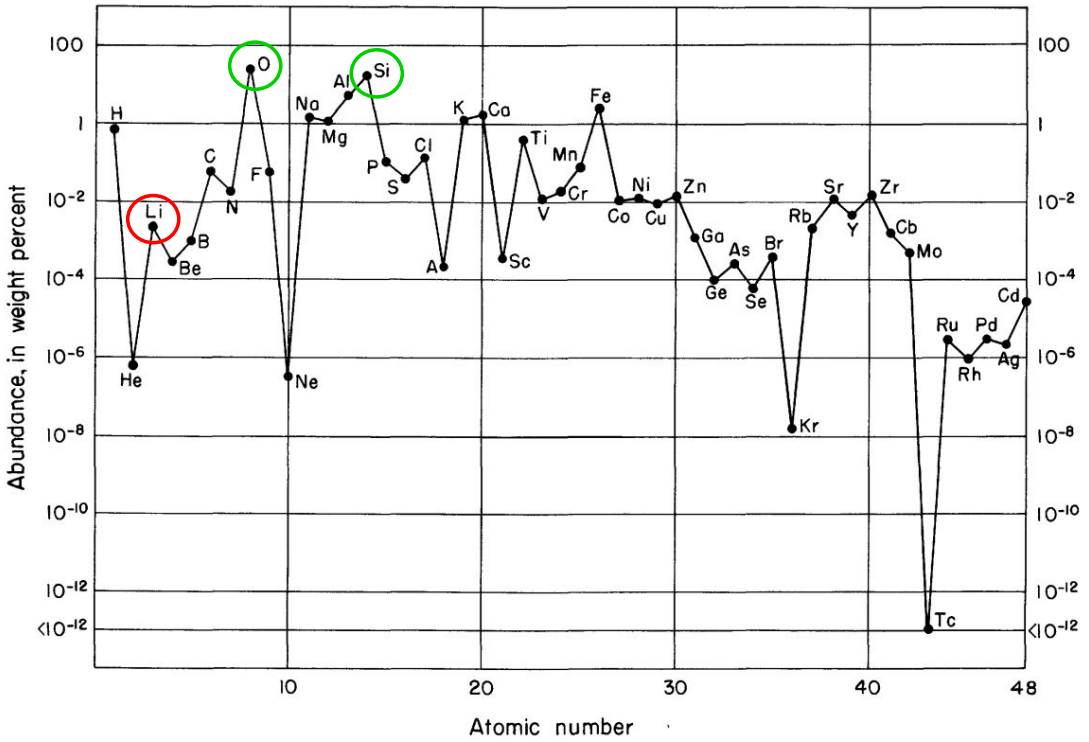

Figure 1.5: The abundance of materials in the earth's crust. Oxygen and silicon, indicated by the green circles, are the most and second most abundant materials available, respectively. lithium, marked red, is far less abundant. Figure taken from [50].

However, Si as a pure element is not available in nature. It is mainly found as silicon-dioxide (SiO_2) and requires further processing reactions to end up with pure Si. In addition to that, in the production of the materials currently used in Si-air batteries, only quartzite can be used to produce the needed crystalline Si (c-Si). There are no accurate estimations for quartzite reserves and resources available, but it is assumed they are sufficient to supply the world demands for many decades [51]. The annual production rate of Si is greater than 10^{10} kg/year, while Li production is below 10^8 kg/year [49]. Another advantage of the material Si is that it is also non-toxic and safe.

Another advantage of a Si-air battery is that it has as a high gravimetric and volumetric energy density of up to 8,470 Wh/kg and 19,748 Wh/L excluding oxygen, respectively. This is due to the high specific capacity of the Si anode through the release of four electrons in the redox-reactions, resulting in a specific capacity of 3822 mAh/g. The energy density in Wh/kg is calculated by multiplying the specific capacity with the theoretical cell potential, which ranges between 2.09-2.22 V and depends on the used electrolyte. The fact that the battery uses a cathode that operates on the oxygen available from the ambient air, means that it does not require a metal electrode. This significantly reduces the mass of the cathode. The high volumetric energy density, combined with the ability to operate in humid environments, makes Si-air batteries attractive to use in small applications such as hearing aids. Based on the high volumetric energy densities, Si-air batteries could be capable of powering laptops or phones for longer periods using the same form factors and battery volume than with Li-ion batteries.

The first experiments by Cohn et al. showed that the Si-air battery cell had a constant discharge potential of 1.0-1.2 V, a very low self-discharge rate and could endure high current densities up to 0.3 mA/cm^2 [40]. These results were obtained by using non-aqueous electrolytes that are based on a room temperature ionic liquid (RTIL). The electrolytes were tested using different Si dopant materials and orientations as anode material [52]. The used RTIL electrolyte, i.e. $EMIm(HF)_{2.3}F$, is featured with very low corrosion rates, but includes the use of the dangerous chemical HF that requires careful handling and disposal. Other research groups chose to use the safer, inflammable aqueous or solid state electrolytes. The used aqueous electrolytes are often potassium hydroxide (KOH), also called alkaline electrolytes due to their high pH value. KOH is cheap, widely available, has a very high ionic conductivity up to 0.6 S/cm and its concentration can be changed through dilution. The solid state electrolytes are based on gel polymers and were already used in the more popular Li-ion batteries [53]. The use of solid-state electrolytes in Si-air batteries is still limited [54][55]. The gel polymers are safe, enable flexibility in the shape design of the battery, but show lower ionic conductivities compared to liquid electrolytes. This decreases their discharge voltages and makes them suitable for low-power devices only.

Despite the promising theoretical energy density and material abundancy of Si-air batteries, there are a number of challenges that currently withold the battery from becoming a commercial success like Li-ion batteries. These challenges include the lack of rechargeability at room temperature, passivation of the anode or cathode surface and severe corrosion in using alkaline electrolytes. These challenges will be elaborated below.

Rechargeability

As of now, Si-Air batteries with an aqueous, non-aqueous RTIL or gel-polymer electrolyte are not rechargeable under normal atmospheric conditions [38]. The reaction products $Si(OH)_4$ and SiO_2 are extremely stable, implying high voltages to decompose the reaction products. Besides, this reduction reaction is a very sluggish reaction which increases the overpotential quickly. Since the electrode potentials in alkaline electrolytes lie outside of the stability window of water, the water is decomposed and hydrogen is produced on recharging instead of reducing Si. In theory, a rechargeable Si-air battery is possible. A concept introduced by Inoishi et al. uses a solid oxide-ion conducting electrolyte and performed over 20 stable cycles, but had to operate at elevated temperatures of 1073 K to directly reduce Si [56]. This makes this specific type of Si-air battery not practical in daily use, at least for the time being.

Passivation

As was already observed in the first successful discharge of Si-air batteries using alkaline aqueous electrolytes, the reaction product $Si(OH)_4$ is formed and dissolves in the electrolyte [41]. If the dissolution rate of $Si(OH)_4$ is slower than the rate at which it is produced, a layer of $Si(OH)_4$ can build up on the surface at the Si anode which further reacts into solid SiO_2 and water. This solid layer stops the anodic oxidation of Si and the discharge of the battery quickly stops after the formation of this layer. Passivation is postponed by increasing the dissolution rate of $Si(OH)_4$

through increasing the surface area of the Si anode [41]. As a result, the discharge time was increased significantly from seconds to hours. Another way to postpone passivation is to reduce the concentration of the reaction product $Si(OH)_4$ by continuously refreshing the electrolyte. This prevents the formation of a solid, passivating layer on the Si surface [43]. In general, highly doped materials are passivated quicker because the oxide film forms easier [57].

Si-air batteries using non-aqueous electrolytes also suffer from passivation by solid SiO_2, but then at the air cathode side [52][58]. At some point discharging stops as the SiO_2 layer prevents further diffusion of oxygen through clogging the micro-pores in the active carbon. The passivation was mitigated by increasing the applied current density. It turned out that this increased the SiO_2 particle size. The enlarged particles deposit on the macro-pores instead of micro-pores and allow the oxygen to continue to diffuse. Adding water to the non-aqueous electrolyte relocates the passivation to occur in the bulk of the electrolyte instead of at the air cathode [59]. Adding 10-15 vol% to the electrolyte led to an increased discharge capacity as well as an increased ionic conductivity and thus limited the formation of a blocking passivation layer.

Corrosion

Si-air batteries using alkaline electrolytes experience severe corrosion at the Si anode during discharge [41][43][44][60][61]. In a corrosion reaction, Si is consumed without contributing electrical energy to the external circuit from the produced electrons. This process happens simultaneously with the oxidation reaction, but the formed electrons react with water to form hydroxide (OH^-) ions and hydrogen (H_2) gas.

Si is not stable in water and aqueous solutions, such as KOH, since its potential is larger than the potential of the stability region of water. This means that Si is prone to instant oxidation at open circuit potential (OCP) and continues during discharge. The parasitic consumption of Si is significant when it is compared to the actual mass conversion of the battery. Mass conversions of alkaline Si-air batteries are in the order of only 3-5% [43][44]. Corrosion is, therefore, seen as the biggest challenge in the development of more efficient Si-air batteries [43].

For non-aqueous electrolytes, such as the RTIL $EMIm(HF)_{2.3}F$, the effect of corrosion is much smaller when compared to alkaline electrolytes [40][42][52]. Batteries with these electrolytes are capable of achieving efficiencies in the range of 40-50% [42], a tenfold increase compared to alkaline electrolytes. A logical step would be to switch to these RTIL electrolytes instead, but they have a high safety risk caused by the fluoride atom content [62]. Moreover, RTIL's are much more expensive than alkaline electrolytes such as KOH, costing over 300 euros for 25 grams of EMImCl, excluding the use of HF to produce the used electrolyte $EMIm(HF)_{2.3}F$ that was used in Si-air batteries [40][63].

Despite the fact that alkaline Si-air batteries are not rechargeable and suffer from passivation of the anode, the corrosion is considered as the biggest challenge [41][43][44]. To this day, the only solution to reduce the corrosion has been to decrease the concentration of the electrolyte [44]. The effect of this was that corrosion rates decreased from 2.2 to 1.5 μm/h for low current densities. For high current densities no clear reduction in the corrosion rates was observed and the efficiencies remained low and in the order of only 3%. A downside of decreasing the electrolyte concentration was that the discharge curves were less stable and discharge potentials decreased by more than 0.1 V [44].

Another possible solution to limiting the corrosion is the implementation of a nonuniform doping profile that lets electrons diffuse into the bulk of the Si instead of reacting at the anode surface. This thesis will focus on this possible solution which will be further introduced in the objective, in subsection 1.3.1.

1.3 Thesis

In this section the contents of this thesis will be introduced. This starts by the formulation of the objective of this thesis, after which the outline for the steps taken throughout the research process is explained. Finally, the structure of the report is described.

1.3.1 Objective

While corrosion in alkaline Si-air batteries is considered to be important limiting factor in the battery's current low efficiency level, the possible role of the surface electrons in the corrosion reaction has not yet been studied thoroughly. Experimental results indicate that the activation energy of Si is high enough to be a surface limiting process [44]. Besides, corroded masses increased through discharging at higher current densities than with respect to open circuit potential (OCP) [43]. This indicates that an increased electron injection through the higher discharge current densities also increased the corrosion.

Based on the corrosion model presented by Durmus et al. [44], a steep dopant profile might prevent the parasitic consumption of electrons at the Si anode surface. The dopant profile will cause the electrons to diffuse from the region of high to the region of low concentration, leaving behind donor ions with a positive charge. An internal electric field with a direction opposite to the diffusion current, directed into the bulk Si, is induced by this separation of charge. More electrons will then contribute to the external circuit current, reducing the corrosion and thus increasing the efficiency of the battery. Therefore, the research objective of this thesis is:

"Mitigating the corrosion in alkaline silicon-air batteries by applying a nonuniform dopant profile in the silicon anode."

1.3.2 Outline

The first experimental work done in the field of Si-air batteries with alkaline electrolytes at Delft University of Technology was studied by Prins [64]. He has shown remarkable results regarding discharge times of up to 70 hours with an applied current density of 150 μA/cm^2 by optimizing the pre-wetting time of the air cathode. Following student projects that studied different subtopics of Si-air batteries showed difficulties with reproducing the results made by Prins. Especially achieving a stable discharge curve over longer time periods proved to be a challenge. The initial experimental efforts of this thesis are, therefore, aimed at achieving stable discharges and to reproduce the results Prins has produced.

Following this, the corrosion in the used battery setup will be quantified using uniformly doped Si samples. This is used to set reference results. After setting the reference results, simulations are performed to design new samples that include a nonuniform dopant profile. In addition to this, the nonuniformly doped samples will be analyzed to inspect if the simulated dopant profiles are actually experimentally achieved. Finally, the corrosion will be quantified for these nonuniformly doped samples and compared to the results of the uniformly doped samples to see if the corrosion has been mitigated.

1.3.3 Structure

This thesis report will have the following structure. Chapter 2 elaborates more on the theory of Si-air batteries based on a literature review. This includes the working principle and components, but also the current challenges and the efforts to mitigate those challenges will be discussed. An approach in mitigating corrosion is also outlined here. Chapter 3 gives the experimental setup and approach in measuring the performance of the batteries. In chapter 4, adaptations to the experimental setup to stabilize the discharge results will be discussed. In chapter 5, dopant profiles are first simulated. Based on the simulations and the experimental method, nonuniformly doped Si samples are fabricated. These experimental dopant profiles are compared to the simulated profiles in this chapter as well. Chapter 6 gives the corrosion results for the uniformly and nonuniformly doped Si anodes. The discussion of the experimental method and results follow in chapter 7. In chapter 8 conclusions are drawn and recommendations for further research are given.

Chapter 2

Theory of silicon-air batteries

In this chapter, a literature study is conducted to gain insight in the theory behind silicon-air (Si-air) batteries. First, the working principle of batteries is explained after which the included parts of the battery are discussed. The current challenges that have to be overcome, which include reversibility, passivation and corrosion are discussed hereafter in separate sections. Modifications applied to the battery design to improve its performance from available literature are studied and analyzed in the next section. These modifications range from changing the dopant concentration or crystal orientation to increasing the anode surface area or electrolyte concentration. A new modification is proposed and worked out in the final section. This modification entails the implementation of a nonuniform doping profile in the Si wafers.

2.1 Battery physics

On discharging, batteries convert chemical energy into electrical energy by using two electrochemical half-cells, or electrodes, that undergo electrochemical reactions in which the valence of the reacting species is changed. The half cells are separated by an electrolyte to prevent electronic conduction, i.e. short-circuit, but allow ionic conduction. Electricity is generated by electrons that move between the electrodes through an external circuit in a oxidation-reduction reaction, or redox-reaction [23]. The next subsection will discuss the redox reactions in more detail.

2.1.1 Redox reactions

In a redox-reaction one of the half cells undergoes an oxidation reaction and the other half cell a reduction reaction [65]. The reactions are solely based on the transfer of electrons as the chemical ions remain in the solution. Upon discharging, electrons are produced in the oxidation reaction while the electrode reacts with the electrolyte. The electrons are accumulated at the electrode, called the anode, causing an excess of electrons making the electrode charge more negative. The electrons flow through the external circuit from the anode to the other electrode, called the cathode, which has an electron deficit and is therefore more positive. At the cathode, the electrode reacts with the electrolyte which enables the acceptance of electrons and electrons are then gained. This process is summarized in equation 2.1.1, where Red is the reduced specie and Ox the oxidized specie. Ionic transfer between the cathode and anode takes place in the electrolyte to compensate for the electrons moving from anode to cathode in the external circuit.

$$\mathrm{Red} \Leftrightarrow \mathrm{Ox} + \mathrm{e}^{-} \tag{2.1.1}$$

A battery eventually produces electricity through a difference in electric potential between the anode, cathode and electrolyte. It is not possible to determine the electric potential of a single electrode accurately. Therefore, the magnitude of this potential is based on a reference electrode, the standard hydrogen electrode (SHE). This has, by definition, a potential of zero, according to the reaction in equation 2.1.2.

$$H_2 \rightarrow 2H^+ + 2e^- \quad (E = 0.00V) \tag{2.1.2}$$

The anode is oxidized and donates electrons. This means that it has a negative potential. A negative potential means a larger tendency of an electrode material to donate electrons, and thus oxidize, than the standard hydrogen electrode. The cathode accepts electrons and has a more positive potential which means that it has the tendency to get reduced more than hydrogen [23].

The actual voltage a galvanic battery cell produces is also referred to as the cell potential E_0 and follows by $E^0 = E^c$ - E^a, where E^c is the potential of the cathode with respect to the SHE and E^a the potential of the anode with respect to the SHE.

The redox-reactions in a battery occur spontaneously due to a thermodynamic driving force, that will be explained in the next subsection.

2.1.2 Driving force

The driving force for the electrochemical redox reactions is the Gibbs free energy, or G [22][66]. The Gibbs free energy can be seen as the chemically stored energy and is the maximum amount of work that can be derived from a system at constant temperature T and pressure p [67]. Instead of the absolute value of G, the change ΔG is determined for a system that goes from one state to another, such as a (electro)chemical reaction. A negative ΔG means that the reaction releases energy and thus takes place spontaneously, while a positive ΔG indicates that the reaction requires input of external energy to occur and, therefore, does not take place spontaneously. A ΔG of zero means the reaction is in thermodynamic equilibrium [22][67].

A charged battery is not in a thermodynamic equilibrium, i.e. the ΔG is non-zero. The excess available energy is due to a difference in electrochemical potential of the electrode materials, called the electromotive force (emf). The emf is not actually a force, but the difference in potential between the two electrode materials when there is no current flowing. A more common term for emf is the open-circuit potential (OCP).

As explained in the previous subsection, electrons move from the lowest potential reservoir, the anodic site, to the highest potential reservoir, the cathodic site, through an external circuit [22]. This drives the redox-reaction and product concentrations to an equilibrium and causes the electrons to transfer from the anode to the cathode. The tabulated values of ΔG induces the electrical cell potential E^0 according to equation 2.1.3.

$$\Delta G = -nFE^0 \tag{2.1.3}$$

The charge number of the mobile charges n indicates the number of elementary charges transported in the reaction. F is the Faraday constant and is equal to 96485 Coulombs per mole of material (C/mol).

A negative ΔG thus yields a positive potential. The tabulated values of ΔG can be used to calculate the potential under standard conditions of $T = 298$ K, $p = 1$ bar with concentrations of all reaction products equal to 1 mol/l. Changing these concentrations affects the actual cell voltage E according to the Nernst-equation in equation 2.1.4 [22].

$$E = E^0 - \frac{RT}{nF} \ln (K_C) \tag{2.1.4}$$

R is the molar gas constant and is equal to 8.3145 J $mol^{-1}K^{-1}$. K_C is the equilibrium constant and is defined according to:

$$K_C = \frac{[a_C]^\gamma [a_D]^\delta}{[a_A]^\alpha [a_B]^\beta} \quad ; \quad \alpha A + \beta B \rightarrow \gamma C + \delta D \tag{2.1.5}$$

The coefficients α, β, γ and δ are related to the overall electrochemical reaction. For a solid substance or water, the factor $[a_i]$ is 1. Because of overpotentials in the battery, the practical cell voltage is lower than the ideal reversible potential upon discharging [24]. The effect of this loss mechanism in batteries will be discussed in more detail in subsection 2.1.3.

2.1.3 Overpotentials

Less energy than thermodynamically possible can be extracted from a battery in real life, this is called polarization [24][68]. This also has an effect on the voltages of the battery, where the difference between the achieved E and theoretical reversible potential E_r is called the overpotential $\eta = E - E_r$ [24]. An overpotential can either be positive or negative, depending on the process. A galvanic cell produces energy spontaneously as it discharges and has a positive overpotential, while an electrolytic cell consumes energy and thus has a negative overpotential. The size of the overpotential determines the voltaic efficiency, i.e. the ratio of actual voltage to theoretical voltage. A large overpotential thus decreases the voltaic efficiency.

Overpotentials are not limited to a single origin, but can be subdivided into different components, such as activation losses, concentration losses and ohmic losses. The activation and concentration losses are considered to be the most significant [24]. Each component has an effect on the cell's performance and can be subdivided in a cathode and anode component. In general, the reactions at both electrodes in a battery take place at the electrode-electrolyte interface in several steps, including mass transport from bulk electrolyte to interface, electron transfer at the interface, surface conversions and the mass transport from the interface to the bulk of the electrolyte. The slowest step is called the rate-limiting step and determines the overall reaction kinetics.

The activation overpotential considers the energy loss due to the limiting reaction rates at the anode and the cathode electrodes. This overpotential is affected by the current density, temperature, pressure, material and originates from the needed potential to overcome the activation energy of the redox reaction needed to produce a current. It was mentioned earlier that redox reactions occur spontaneously during discharge, but it requires an energy barrier to be overcome to transfer the charges at the interfaces. The activation potential can be the rate-limiting step if, for instance, electrons accumulate at the surface forming a barrier for the incoming electrons.

Concentration overpotentials are caused by a fast surface reaction but slow mass transport. This means that the reaction products can not get to or leave from the reaction sites, causing depletion or accumulation at the electrode-electrolyte interface respectively. Mass can be transported by diffusion, migration or convection. This overpotential becomes dominant at higher current densities, as reaction rates increase and the mass transport can become a limiting step.

The ohmic overpotential is a result of the internal resistance of the battery cell. This can originate from the resistance of the electrode, electrolyte or current collector. The overpotential follows by applying Ohm's law, i.e. $V = iR$, meaning that the overpotential increases linearly with the current. Especially in batteries consisting of semiconductor materials, i.e. the Si-air battery, the electronic resistance can dominate over the ionic resistance of the electrolyte [68].

2.2 Anode

The used anode material in Si-air batteries is Si. This means that on discharging of the battery, Si is oxidized while the battery cell produces a voltage in the range of 0.8-1.3 V [41][42][43][44][52].

Si is a semiconductor material, which means it has a conductivity between that of an insulator and a metal [69]. The used Si is often doped mono-crystalline Si (c-Si) produced as wafers [35][40][41]. Doping means that the concentrations of electrons and holes inside Si are changed with respect to intrinsic Si. Si atoms in the crystal structure are then replaced by impurity atoms with three or five valence electrons, such as boron (B) or phosphorus (P), respectively. There are two types of doped Si, n-type and p-type, with either excess electrons or excess holes respectively [70]. What the effect of doping is on the discharge behavior of the battery will be discussed in more detail in section 2.9.1.

Instead of c-Si, thin-film, or amorphous Si (a-Si), also has been used as an anode material [47]. a-Si has no ordered crystalline structure which results in dangling bonds, or unfilled valences of a Si-atom. The result is that the carrier lifetime is reduced and the Si cannot be doped. A solution to the doping problem was the introduction of hydrogen in the deposition process which significantly reduced the dangling bond density [71]. This led to hydrogenated a-Si, or a-Si:H. A

benefit of using a-Si:H with respect to c-Si as an anode material is that the produced layers can be thinner, lighter and flexible [47].

Another Si-based anode material proposed by Zhang et al. was the use of silicides, that combine Si with a more electropositive material [72]. Silicides were offered as an alternative because of the high electron capacity, conductivity and operating voltages. Moreover, silicides consist of more abundant materials than Zn (79 ppm) and Li (7 ppm), such as titanium (6600 ppm). The material $TiSi_2$ has expected volumetric energy densities up to 24,000 Wh/l. However, this principle has only been applied to a proof-of-concept using $MgSi_2$, which has a much lower volumetric density than both Si and Ti_2 [72].

Using nanostructured c-Si instead of flat wafers in the anode material was first used in Li-ion batteries to prevent pulverization due to volume changes on cycling of the battery and to increase conductivity [73][74]. This technique was first applied to Si-air batteries by Zhong et al. [41] and increased the discharge capacity. Surface area modifications are discussed in section 2.9.4.

As Si is not as conductive as a metal, a current collector made of, for instance gold-plated stainless steel [40] or thin film gold with a titanium adhesion layer [41], is applied at the backside of the Si. This back-contact collects the produced electrons in the anodic half reaction. These metal-semiconductor contacts will be discussed in more detail in section 2.5.

2.3 Cathode

The cathode in Si-air batteries consists of a - often commercial - porous air electrode that is reduced on discharging of the battery [40][43][52]. The electrode includes an activated carbon black structure and a hydrophobic polytetrafluoroethylene (PTFE) binding powder pressed on a nickel 200 mesh [40]. A MnO_2 transition-metal catalyst is used to increase the reaction efficiency.

In room-temperature ionic liquid (RTIL) electrolytes containing fluorides, it was found that the MnO_2 transition metal changes on discharging of the battery to the non-oxygen reduction reaction (ORR) catalyst MnF_2 [58]. MnF_2 causes a loss of catalytic sites and a reduction of ionic conductivity. This affects the overall battery performance in a negative way by reducing the discharge capacity. Other catalyst options for the air electrode are, for instance, noble metals [75], metal-free carbonaceous [76], inorganic-organic composites [77] and hetero-atom doped carbons [78]. As the Si-air battery aims to be a resource-efficient battery, the use of metal-free catalysts is preferred [79].

Using a thicker electrode results in a slower oxygen diffusion and thus a lower specific capacity [80]. Increasing the amount of carbon reduces the specific capacity [81], while increasing the oxygen pressure increases the specific capacity linearly [82]. In order to use the oxygen from the ambient air, an open-like battery structure is needed. This can cause leakage of the electrolyte but also cause CO_2 and moisture to enter the battery. This can result in carbonation or decomposition of the anode material and eventually failure [83].

2.4 Electrolyte

The used electrolytes in Si-air can have a number of compositions. The first Si-air battery used a non-aqueous RTIL electrolyte [40], while more recent research used a more conventional, cheaper, alkaline aqueous electrolyte consisting of potassium-hydroxide (KOH) [41]. Besides, a form of solid-state electrolyte using gel-based polymers was proposed and used by Cohn et al. [54]. The next subsection will discuss the used electrolytes in more detail after which they electrolytes are compared.

2.4.1 Non-aqueous

The most used type of electrolyte is a non-aqueous RTIL called $EMIm(HF)_{2.3}F$. This RTIL was discovered in 1999 and is made through a synthesis reaction between 1-ethyl-3-methylimidazolium chloride (EMICI) and anhydrous hydrogen fluoride [62][84]. It comes with a high tolerance for

humidity, low viscosity and the highest measured RTIL conductivity of 0.1 S/cm [84][85]. Besides it has a wide electrochemical window, low vapor pressure and is non-flammable [84]. However, the high fluoride contents are cause for environmental and user-safety concerns. The Si-air battery using RTIL is still considered as a primary battery as the reduction of SiO_2 is still unclear [38]. This type of RTIL consists of one cation and two anions in the EMI and $(HF)_2F^-$ part respectively. The promising properties of RTIL electrolytes are the reason it was used in the first constructed Si-air battery [40].

The aqueous and non-aqueous electrolytes rely on the same mechanisms for the oxidation of Si to SiF_4 and reduction of O_2 at the anode and cathode respectively. However, the chemical reactions differ per type of electrolyte. The two anions of RTIL contribute to both reactions. Upon discharging a Si-air battery with RTIL electrolyte, the produced SiF_4 reacts with water to SiO_2. The following reactions will take place at the anode and cathode.

$$\text{Anode:} \quad Si + 12(HF)_2F^- \rightarrow SiF_4 + 8(HF)_3F^- + 4e^- \tag{2.4.1}$$

$$\text{Cathode:} \quad O_2 + 8(HF)_3F^- + 4e^- \rightarrow 2H_2O + 16(HF)_2F^- \tag{2.4.2}$$

The product SiO_2 is formed at the electrolyte-air electrode interface following the reaction in equation 2.4.3.

$$SiO_2 \text{ formation:} \quad SiF_4 + 2H_2O + 4(HF)_2F^- \rightarrow SiO_2 + 4(HF)_3F^- \tag{2.4.3}$$

Combining equations 2.4.1, 2.4.2 and 2.4.3 yields the overall reaction in equation 2.4.4.

$$\text{Overall reaction:} \quad Si + O_2 \rightarrow SiO_2 \tag{2.4.4}$$

As the standard potential of the half reactions is unknown, the Gibbs free energy can be used to calculate the theoretical standard potential, according to equation 2.1.3. This was found to be 2.16 V [62]. The processes that occur in the non-aqueous RTIL electrolyte are displayed in figure 2.1.

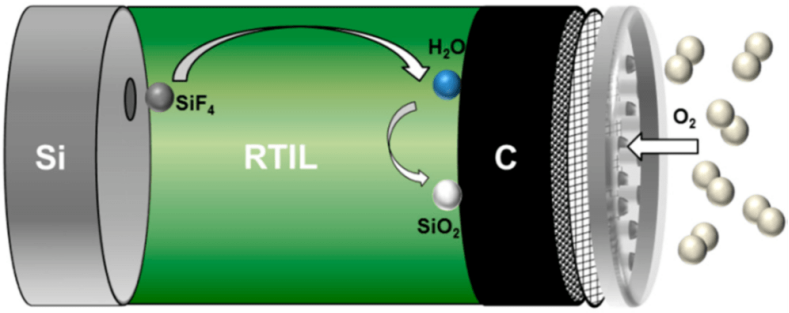

Figure 2.1: The included mechanisms inside a Si-air battery with a non-aqueous RTIL electrolyte. The SiO_2 forms a passivating layer at the cathode. Figure taken from [38].

The reaction mechanism in non-aqueous electrolytes is different from alkaline electrolytes as the discharge product will build up at the cathode instead of the anode. For RTIL, this means that the air electrode is important in the reduction reaction and the SiO_2 formation. The reaction product SiO_2 will build up in the porous carbon at the air cathode during discharging and will at some point prevent the diffusion of oxygen [52]. This lowers the theoretical discharge capacity. If the formation of SiO_2 is shifted from the electrolyte-cathode interface to the bulk of the electrolyte, the suffocation of the cathode can be postponed and the discharge capacity can be increased [59]. The effect that changing the nature of the electrolyte has on the discharge behavior will be discussed in subsection 2.9.5.

2.4.2 Aqueous

A Si-air battery using the alkaline electrolyte KOH also consists of a Si anode and air cathode and was first used by Zhong et al. [41]. Alkaline electrolytes are cheap, environmentally friendly and enable a high ionic conductivity up to 0.6 S/cm [86]. The Si is oxidized and produces four electrons and silicid acid ($Si(OH)_4$) at the anode. Diffused oxygen is reduced at the air cathode. Upon discharging a Si-air battery with a pH>12.5, the reactions in equations 2.4.5 and 2.4.6 take place at the anode and cathode, respectively.

$$\text{Anode:} \quad Si + 4OH^- \rightarrow Si(OH)_4 + 4e^- \quad (E^a = -1.69V) \tag{2.4.5}$$

$$\text{Cathode:} \quad O_2 + 2H_2O + 4e^- \rightarrow 4OH^- \quad (E^c = +0.40V) \tag{2.4.6}$$

This can be rewritten into a net reaction, as described in equation 2.4.7. The standard potential E^0 follows from $E^0 = E^c$ - E^a and equals 2.09 V.

$$\text{Net reaction:} \quad Si + O_2 + 2H_2O \rightarrow Si(OH)_4 \quad (E^0 = +2.09V) \tag{2.4.7}$$

In practice, according to the paper of Zhong et al. the potential will be closer to 1.5 V in open-circuit conditions and 1.2 V while discharging at low current densities of 50 $\mu A/cm^2$ [41]. In the bulk of the electrolyte the formed $Si(OH)_4$ reacts with OH^- to form silicates ($SiO_2(OH)_2^{2-}$) and water, according to the reaction in equation 2.4.8.

$$\text{Silicate formation:} \quad Si(OH)_4 + 2OH^- \rightarrow SiO_2(OH)_2^{2-} + 2H_2O \tag{2.4.8}$$

The included mechanisms that take place in the battery upon discharging are displayed in figure 2.2. The build up of the reaction product $Si(OH)_4$ on the Si can result in a passivating SiO_2 layer. To allow the discharging process to continue, $Si(OH)_4$ has to be removed from the Si surface. This is a benefit of alkaline electrolytes as it enables the dissolution of $Si(OH)_4$ into the electrolyte. However, the dissolution rate has to be larger than the formation rate of SiO_2 to prevent passivation. More background on the passivation process is given in subsection 2.7.

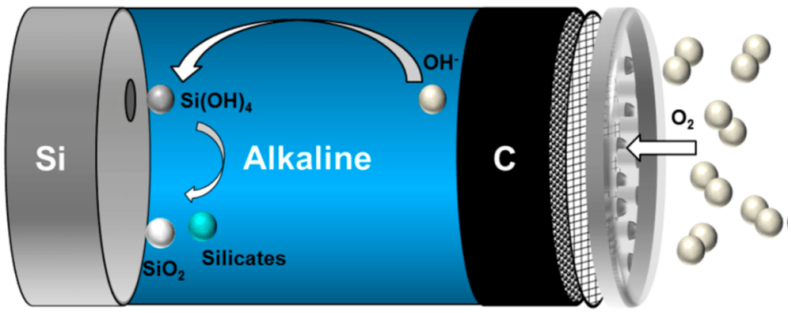

Figure 2.2: The included mechanisms inside a Si-air battery with an alkaline electrolyte. The SiO_2 forms a passivating layer at the anode. Figure taken from [38].

A downside of alkaline electrolytes is that it corrodes Si. This happens simultaneously with the oxidation reaction of Si. The corrosion process is a form of self-discharge where the active material is consumed and electrons do not contribute to the external circuit [41]. This lowers the efficiency of the battery. The corrosion reactions will be discussed in more detail in 2.8.

2.4.3 Solid-state

Another form of electrolytes is the incorporation of a liquid electrolyte in a polymeric matrix and these are called gel polymer electrolytes (GPE). GPE's are a solid type of electrolyte that conduct in the same way as a liquid electrolyte. The gel forms a sort of moisture barrier and removes the need for a liquid electrolyte. This means that it is safer, has flexibility in its shape and is mechanically stable. The ionic conductivity is, however, lower compared to liquid electrolytes

[55]. Currently, GPE's are used in Li-ion batteries, sensors and solar cells. Combining the gel with a RTIL, such as $EMIm(HF)_{2.3}F$, resulted in a wider electrochemical window than without the gel. The conductivity dropped from 0.1 S/cm to 0.023 S/cm [55]. This specific type of electrolyte was applied to a Si-air battery as well [54]. It was found that the GPE was compatible with the Si anode and air cathode while showing long discharge times of 850 hours at 0.1 mA/cm^2, albeit at a 0.5 V lower voltage caused by the reduced ionic conductivity. Increasing the concentration of the RTIL increased the operating voltage, but only up to a concentration of 70%. In general, GPE's are considered as an option for low-power devices [54].

2.4.4 Comparison and chosen type

The three discussed electrolytes are briefly compared in the table below based on the information from the previous subsections.

Table 2.1: A comparison of the types of electrolytes that have been used for Si-air batteries, derived from literature.

Type	Electrolyte	Advantages	Disadvantages
Aqueous	KOH (alkaline)	- Cheap - Environmentally friendly - High ionic conductivity	- High corrosion rates - Lower efficiency - Not rechargeable
Non-aqueous	$EMIm(HF)_{2.3}F$	- High tolerance for humidity - Wide electrochemical window - Low corrosion rates	- Pore clogging at cathode - HF dangerous in handling - Not rechargeable
Solid-state	GPE $EMIm(HF)_{2.3}F$	- Safe - Mechanically strong - Long discharge times	- Lower ionic conductivity - Lower discharge voltage - Not rechargeable

The use of the aqueous alkaline electrolyte KOH is preferred because of several reasons. The first and foremost reason is that the handling of the chemical KOH inside a lab is easier and safer than the RTIL $EMIm(HF)_{2.3}F$. The latter chemical contains HF and therefore requires careful handling when assembling and disassembling the battery. As this will happen frequently, the risk of an injury should be minimized. The cost of the RTIL electrolyte lies over 300 euros for 25 grams and excludes the synthesis reaction [63]. KOH is considerably cheaper, easier to acquire and has a higher ionic conductivity of 0.6 S/cm. A downside of KOH is, however, that it etches, or corrodes, Si quite fast and strongly. This will be explained in more detail in section 2.8.

2.5 Metal-semiconductor contacts

For semiconductors to make a good conducting contact with the external circuit of the battery, a metal has to be applied at the backside. Ideally, this contact should be an Ohmic and thus a nonrectifying contact. In an Ohmic contact the resistance is very low and the current can flow in both directions. However, when metals and semiconductor are in direct contact with each other, a potential barrier can emerge depending on the properties of the material that block charge carriers to move from the semiconductor to the metal or the other way around, i.e. a rectifying contact.

When a metal makes contact with a semiconductor in thermal equilibrium, the Fermi level of both materials aligns [69]. An important property in metals is the work function ϕ_m that indicates the energy needed to excite an electron from the metal to a point in vacuum near the metal surface, corresponding to the energy from the vacuum level to the Fermi level. Semiconductors also have a work function, i.e. ϕ_s and an electron affinity χ, both expressed in Volt (V). χ is defined as the difference in energy between the vacuum level and the bottom of the conduction band. This means that the work function of a semiconductor can also be defined as described in equation 2.5.1. Multiplying by q gives the unit of E_C and E_F, i.e. electron volt (eV).

$$q\phi_s = q\chi + (E_C - E_F) \tag{2.5.1}$$

The first semiconductor devices were made in the 1900's by attaching a metal contact to a semiconductor in a so-called point contact diode. These contacts were quite unstable and in the 1950's they were replaced by PN-junctions. These first metal-semiconductor contacts were rectifying contacts, also called Schottky barrier diodes. For a contact to be rectifying, the work function of the metal has to be larger than that of the semiconductor, i.e. $\phi_m > \phi_{s,n}$, in a n-type semiconductor or smaller, $\phi_m < \phi_{s,p}$ in a p-type semiconductor. For the Fermi level to be constant when the metal and semiconductor are connected, the electrons will have to flow from the semiconductor to the lowest energy states in the metal. This will create an energy barrier ϕ_{B0} seen by electrons in the metal. The barrier height, called the Schottky barrier, for a n-type semiconductor-metal contact is defined in equation 2.5.2.

$$\phi_{B0} = \phi_m - \chi \tag{2.5.2}$$

The electrons in the conduction band of the semiconductor also encounter a barrier to move into the metal, the built-in potential barrier V_{bi}, given in equation 2.5.3.

$$V_{bi} = \phi_{B0} - \phi_{s,n} \tag{2.5.3}$$

When the metal and semiconductor make contact, a space-charge region emerges inside the semiconductor. This spans from the interface up to a width W, also called the depletion region. The electric field inside the space charge region varies linearly and is zero at W while its maximum lies at the interface. The width W is defined in equation 2.5.4.

$$W = \sqrt{\frac{2\epsilon_0\epsilon_s\left(V_{\text{bi}} - V\right)}{qN_D}} \tag{2.5.4}$$

Taking into account the barrier height and width, the energy diagram of a Schottky contact for a n-type semiconductor is given in the figures 2.3 and 2.4, before and after making contact respectively.

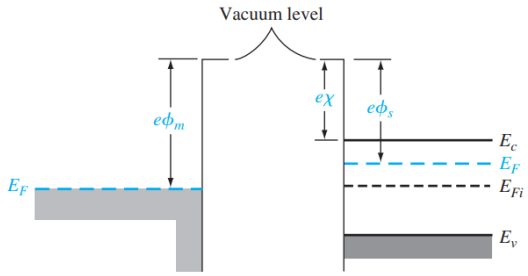

Figure 2.3: Band diagram before the metal and a n-type semiconductor make contact. The vacuum levels are aligned. In this case $\phi_m > \phi_{s,n}$. Figure taken from [69].

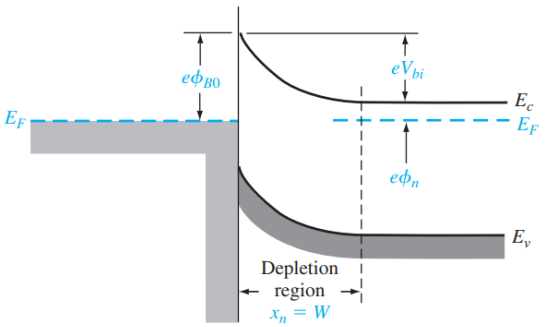

Figure 2.4: Band diagram after the metal and n-type semiconductor make contact. The Fermi level is aligned and an energy barrier ϕ_{B0} with width W emerges. Figure taken from [69].

Applying a bias voltage to the contact will have an effect on the semiconductor barrier side only. It does not affect the metal side barrier ϕ_{B0}. This means that the contact will only conduct for one bias polarity, making it a rectifying contact. Such a Schottky contact is ideal for diodes, but an Ohmic contact is wanted for signals to go in and out of the semiconductor material because it conducts for both bias directions.

To make the contact more Ohmic, the barrier height has to be lowered by choosing a different metal material with a smaller or larger work function for n-type or p-type semiconductor material respectively. This changes the case for n-type semiconductor to $\phi_m < \phi_{s,n}$ as can be seen in figure 2.5. In figure 2.6 the lower energy barrier can be observed.

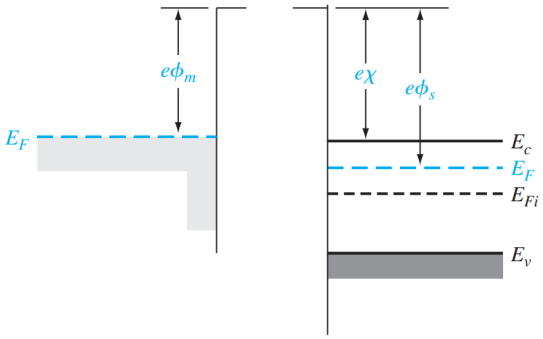

Figure 2.5: Band diagram before the metal and a n-type semiconductor make contact. The vacuum levels are aligned. In this case $\phi_m < \phi_{s,n}$. Figure taken from [69].

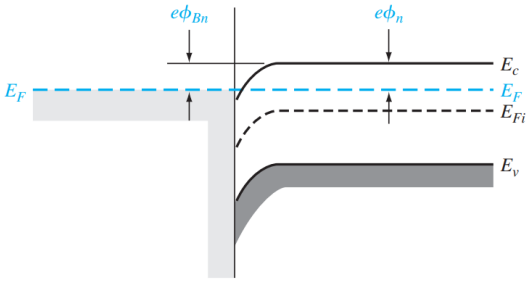

Figure 2.6: Band diagram after the metal and n-type semiconductor make contact. The Fermi level is aligned and a low energy barrier ϕ_{Bn} emerges. Figure taken from [69].

Electrons flow into the low energy states of the semiconductor to reach thermal equilibrium. This causes excess electrons at the interface. Applying a positive voltage to the metal removes the barrier for electrons to move from the semiconductor to the metal, while a positive voltage applied to the semiconductor enables electrons to transfer easily to the semiconductor. This means that the junction acts as an ohmic contact.

Another option to achieve a more ohmic contact is to make the barrier narrower such that electrons or holes can tunnel through a barrier instead of passing over it, i.e. field emission. The depletion region width in figure 2.4 can be decreased by increasing the dopant concentration, as can be seen in equation 2.5.4. A narrow barrier will increase the probability of tunneling. Figure 2.7 shows the implementation of such a highly doped layer and the resulting effect of field emission.

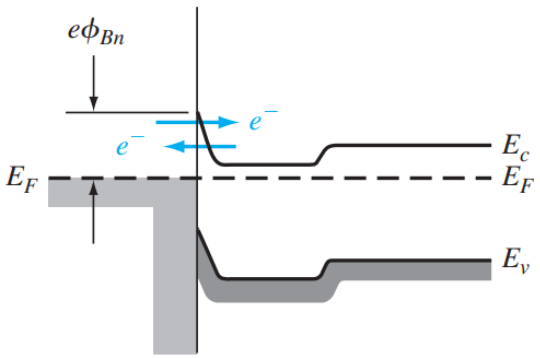

Figure 2.7: Implementing a highly doped region between the metal and semiconductor narrows the barrier width and increases the probability of electrons tunnelling through the barrier. Figure taken from [69].

2.6 Rechargeability

Currently, Si-Air batteries using (alkaline) aqueous, non-aqueos RTIL or gel-polymer electrolytes are not rechargeable because of two thermodynamic reasons [38]. First, the reaction products $Si(OH)_4$ (KOH) or SiO_2 (RTIL) are extremely stable, having high Gibbs-free energy values of -1,276 kJ/mol and -856.6 kJ/mol, respectively. This means that high voltages are needed to decompose the reaction products. Secondly, the reduction reaction is a very sluggish reaction, which increases the overpotential quickly. The sluggish behavior can be observed by the flat polarization curve of the cathode in figure 2.8.

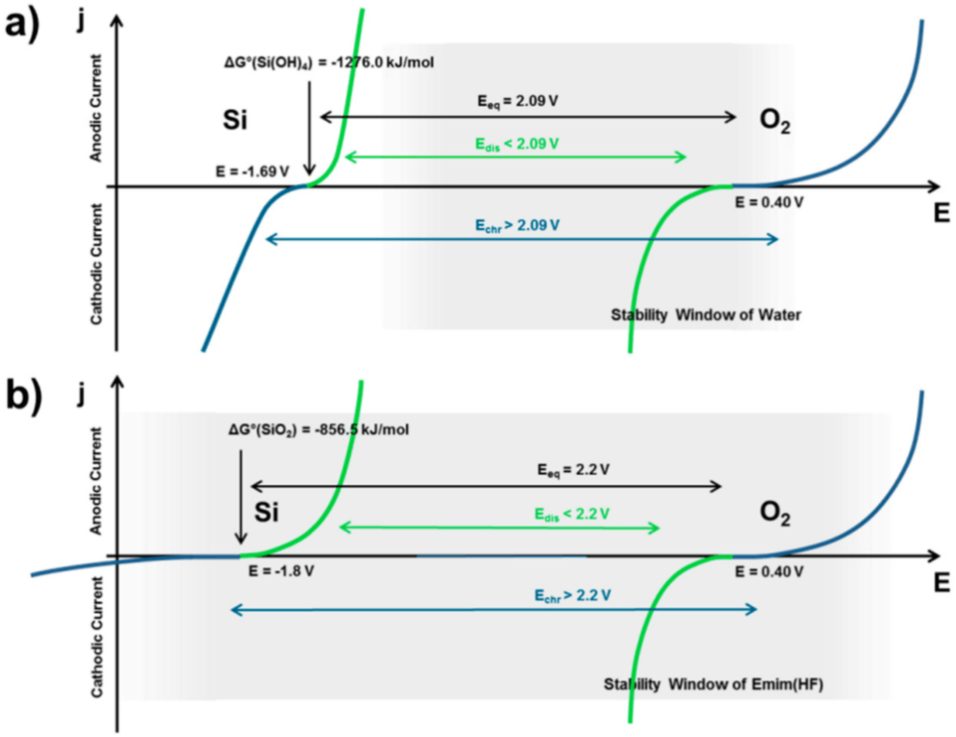

Figure 2.8: This polarization curve plots the applied current density as function of the electrode potential of Si-air batteries for a) aqueous and b) non-aqueous batteries. The flat curves at the O_2-cathode indicate a sluggish reaction that increase the overpotential on charging (blue lines). Figure taken from [38].

For too low reduction voltages using RTIL, the electrolyte might decompose on recharging as it lies within the stability window. Since the electrode potential in alkaline electrolytes lies outside of the stability window of water, the water is decomposed and hydrogen is produced on recharging instead of reducing SiO_2. A rechargeable Si-air battery is, in theory, possible [56]. The paper of Inoishi et al. describes a Si-air battery that showed over 20 stable cycles. The concept uses a solid oxide-ion conducting electrolyte. The conductor ZrO_2 is used where the oxygen is electrochemically pumped through the electrolyte. The solid oxide-ion is stable, does not suffer from evaporation of the electrolyte and has a wide temperature operational range of 373 - 1273 K. If Si operates at these higher temperatures, it is directly reduced or oxidized. This means that the battery can be recharged. With an increasing number of cycles, both the charge and discharge energy density of the battery increased, as can be observed in the red and blue lines in figure 2.9. The increase in discharge energy density is due to the formation of a porous structure, as observed by Scanning Electron Microscopy (SEM).

The specific capacity of the battery increased upon cycling from 368 mAh/g to 701 mAh/g. In order to achieve the reported 20 cycles with a discharge capacity of 600 mAh/g, the battery has to operate at a high temperature of 1073 K. Overall the battery suffers from a low round-trip efficiency of, on average, 45%, while Li-ion batteries are featured with efficiencies above 95% [16]. The electrodes consist of the noble metal Pt as this increases the stability needed for cycling the battery, but Pt has a low activity which decreases the cycle efficiency [56].

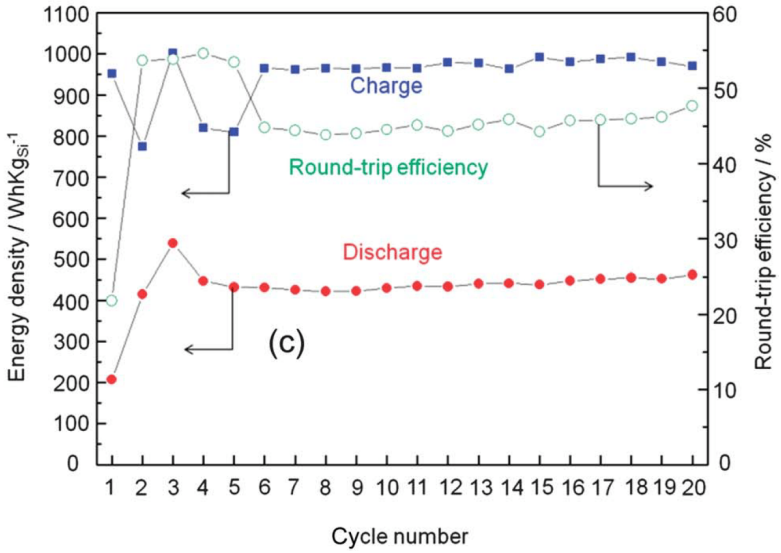

Figure 2.9: The charge and discharge performance of the solid-oxide Si-air battery are displayed. The energy density in Wh/kg_{Si} is plotted as a function of cycles. The green line indicates the cycle efficiency, which is in the order of 45%. Figure taken from [56].

2.7 Passivation

As observed in discharging Si-air batteries using alkaline aqueous electrolytes, the reaction product $Si(OH)_4$ is formed [41]. For alkaline electrolytes, this reaction product can be dissolved into the electrolyte. However, if the dissolution rate of $Si(OH)_4$ is lower than the rate at which it is produced, which happens during discharge, a layer of $Si(OH)_4$ can build up on the surface at the Si anode. The $Si(OH)_4$ can then react into solid SiO_2 and water. Solid SiO_2 passivates the surface of the anode. This causes the potential to drop and the anodic oxidation to stop. The consequence of the passivation is that the discharge time is severely limited to several minutes instead of hours [41]. The involved processes are shown in figure 2.10.

The passivation of the Si surface was experimentally shown by Durmus et al. in cyclic voltammograms (CV) for 5M KOH As-doped <100> flat Si [43]. In a CV the potential is ramped linearly while measuring the current. The current density (mA/cm^2) is then plotted against the potential versus a reference Hg/HgO electrode. Two regions were distinguished in the CV, i.e. an active and a passive region. In the active region, the Si can dissolve in the electrolyte as the production rate is lower than the dissolution rate. This happens for potentials lower than the passivation peak of -1.05 V. If the potential was increased to higher potentials, the production of Si increased at a faster rate than it is dissolved. A passivating layer is formed and as a result, the current decreases. This is called the passive region. As long as the potential is kept below this -1.05 V the Si surface is not passivated and remains active [43]. The maximum applied current density for flat c-Si wafers in aqueous solutions is only in the order of several $\mu A/cm^2$.

This was experimentally shown in the CV after scanning the battery for three times at the peak potential [43]. After the first cycle, a peak was shown, indicating an oxidation current. This current had disappeared when a second and third scan were performed, indicating that the Si surface was passivated. This behavior can be observed in figure 2.11 where the experimental CV's for the three scans are given.

The passivation of Si in alkaline electrolytes can be postponed in two ways. The dissolution rate of $Si(OH)_4$ can be increased by the forming of a porous structure on the Si surface through surface modification [41]. This leads to an increased surface area which increases the dissolution rate into the electrolyte. As a consequence, the discharge time can be increased significantly.

Another way to postpone passivation is to reduce the concentration of the reaction product $Si(OH)_4$ by continuously refreshing the electrolyte. This prevents the formation of a solid, passivating layer on the Si surface [43].

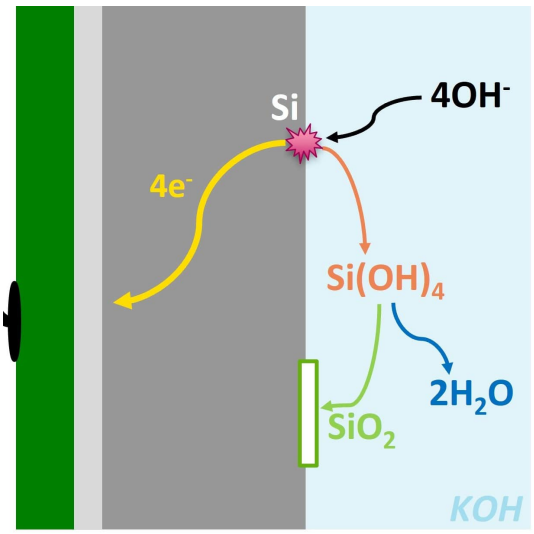

Figure 2.10: Passivation mechanism at the anode of the Si-air battery in aqueous alkaline electrolytes. A passivating layer of SiO_2 is formed on the anode surface.

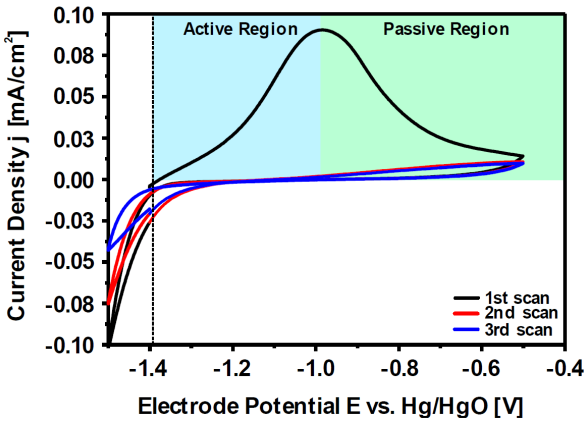

Figure 2.11: Cyclic Voltammetry (CV) diagram in 5M KOH electrolyte with the active and passive region for three scans. The Si is passivated for voltages above -1.05 V. Figure taken from [38].

For non-aqueous electrolytes, such as $EMIm(HF)_{2.3}F$, surface passivation also takes place, albeit at the air cathode instead of the Si anode. The reaction product in the oxidation reaction, i.e. SiF_4, further reacts with water and forms SiO_2 [52]. During discharge, the voltage decreases due to the formation of the reaction product SiO_2 at the porous carbon [52]. At some point, the SiO_2 layer prevents further diffusion of oxygen as it clogges the micro-pores in the active carbon and thereby reduces the number of sites for reduction. This terminates the battery operation. A Si rich deposit was assumed to be formed through the reaction in equation 2.7.1 [40].

$$Si^{4+} + 2O^{2-} \rightarrow SiO_2 \tag{2.7.1}$$

The deposition of SiO_2 on the air cathode surface is illustrated in figure 2.12 before and after discharging the battery, respectively. Energy-dispersive X-ray spectroscopy (EDX) indicated that Si is present on the air cathode after discharging the battery. The assumption that the reaction product was actually SiO_2, was showed by X-ray photoelectron spectroscopy (XPS) and confirms findings of earlier research [52][87]. Residues of the RTIL, especially F^--ions, were found, as drying the electrode after pre-wetting is difficult for low vapor pressures.

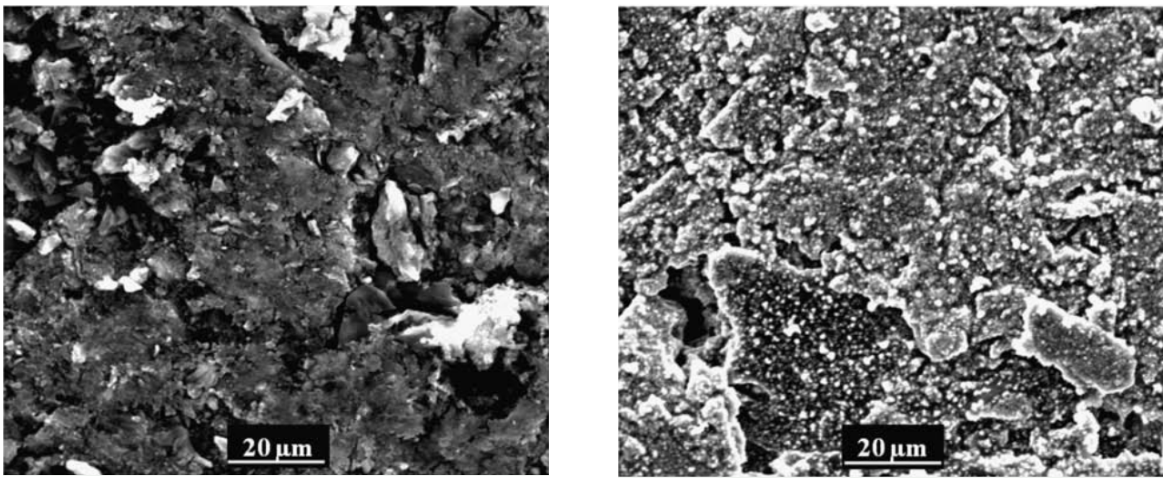

(a) (b)

Figure 2.12: A passivating layer of SiO_2 is formed on the active carbon surface in non-aqueous RTIL electrolytes. The surface is shown using SEM (a) before discharge, (b) after discharge. Figure taken from [40].

A solution proposed in the same paper of Cohn and Ein-El was to increase the applied current density on discharging [52]. Passivation in non-aqueous electrolytes occurs at higher anodic currents due to a lack of water in the solution and the fact that HF etches SiO_2 very fast [88]. This means that current densities of 1 A/cm^2 can be achieved without passivation [57]. These higher current densities increase the particle size of the formed SiO_2 that are deposited on the macro-pores of the active carbon. This means that the micro-pores remain free and that the oxygen can continues to diffuse. The battery can stay operational until the active carbon is blocked by the larger SiO_2 particles. This behavior can be observed in figure 2.13.

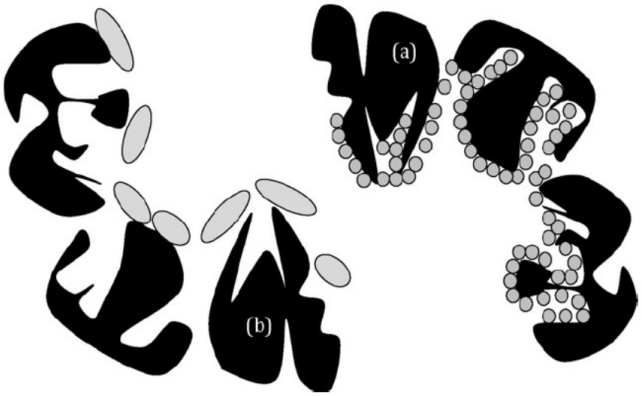

Figure 2.13: The deposition of solid SiO_2 on the air cathode in non-aqueous electrolytes for different current densities. a) indicates the clogging of the micro pores in the activated carbon for low current densities and b) the deposition on the macro-pores. Figure taken from [52].

Another approach that was studied to decrease the formation of SiO_2 at the air cathode is the addition of water to the RTIL electrolyte [59]. As can be seen in equation 2.4.3, water is needed in the formation of SiO_2. RTIL has the ability to take up 46 wt% of water at a humidity level of 94%. By adding water to the electrolyte, the reaction location moves to the bulk electrolyte and anode instead of the cathode. This prevents the clogging of the air cathode and increases the discharge capacity and ionic conductivity for a 10-15 vol% increase in water in the electrolyte at an applied discharge current density of 300 μA/cm^2.

A follow-up study concluded that the increase in discharge capacity is not only due to less clogging of pores but also due to a reduction in the catalyst through the formation of MnF_2 from MnO_2, a surface layer that severely impacted the discharge performance by filling the air electrode pores and losing sites where O_2 could be reduced [58]. The increase in water concentration causes, however, a decrease in potential of 0.1 V due to the formation of a SiO_2 layer at the anode. Increasing the amount of water by more than 15 % resulted in a resistive oxide at the anode and prevents the dissolution of Si. The battery completely stops discharging when 80% or more water content is reached.

2.8 Corrosion

Si-air batteries using alkaline electrolytes, such as KOH, experience severe corrosion at the Si anode during discharge [41][43][44][60][61]. In a corrosion reaction, the active Si material is consumed without contributing electrical energy. This process happens simultaneously with the oxidation. Due to the active nature of Si in alkaline electrolytes, the corrosion reaction already emerges spontaneously at OCP and continues during discharge.

The corrosive effect of KOH on Si has been a research topic in the semiconductor industry for many decades. In these experiments KOH was used to obtain desired structures, crystal orientations and surface characteristics through anisotropic etching, such as pyramids [60][89][90]. The size of the features could be altered by changing the KOH concentrations as this influenced the corrosion rates [44]. The corrosion mechanism involving electrons that was suggested to take place in Si-air batteries will be explained in more detail in the next subsection.

2.8.1 General process

Based on the model of Durmus et al. [44], the corrosion of Si in alkaline electrolytes takes place through a number of coupled electrochemical reactions at the Si surface: the oxidation of Si at anodic sites, water reduction at cathodic sites and the dissolution of the reaction product $Si(OH)_4$ from the oxidation reaction into $Si(OH)_2^{2-}$. The electrons generated at the anodic sites react with water to OH^- and hydrogen gas (H_2) and are consumed at the cathodic sites. Therefore, the electrons are not contributing to the external circuit. The reactions that take place are displayed in figure 2.14.

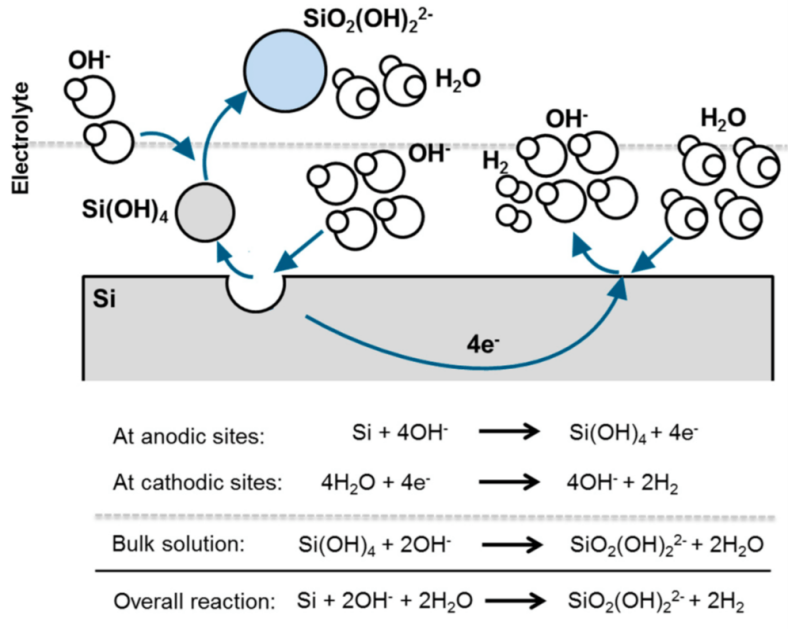

Figure 2.14: The corrosion reactions taking place at the Si surface at open-circuit potential (OCP) in an alkaline electrolyte. This process increases on discharging due to an increased flow of OH^- ions onto the Si surface. Figure taken from [38].

In the overall corrosion reaction, Si reacts with OH^- and H_2O to form $Si(OH)_2^{2-}$ and H_2 gas. This reaction causes viscous solutions for high concentrations of silicates, increased cell pressure leading to electrolyte leakage due to H_2 gas formation and consumption of the active Si material. The consumption of Si is significant when compared to the actual mass conversion. Anode mass conversions are in the order of only 3% for alkaline electrolytes [44]. Corrosion is, therefore, seen as the biggest challenge for further development of Si-air batteries [43]. To better understand why the corrosion reaction occurs in alkaline electrolytes, more background information will be given in the following subsections.

2.8.2 Stability window

The transfer of charges, including electrons, in a battery takes place at the electrode-electrolyte interface [91][92]. Whether an electron travels from the electrode to the electrolyte or vice versa, depends on the energy levels of the electron with respect to the molecular orbital of the electrolyte. The electrolyte is reduced if the electron energy level is higher than the lowest unoccupied molecular orbital (LUMO) of the electrolyte. The electron then travels from electrode to electrolyte, as their energy is high enough to move into vacant energy states in the electrolyte. This is called the cathodic current. The electrolyte is oxidized if the electron energy is lower than the highest occupied molecular orbital (HOMO) of the electrolyte and the electron travels from electrolyte to electrode, as it will be energetically more favourable for the electron to be in the electrode. This is called the anodic current. The charge transfer between the electrode and electrolyte is shown in figure 2.15 [64][92].

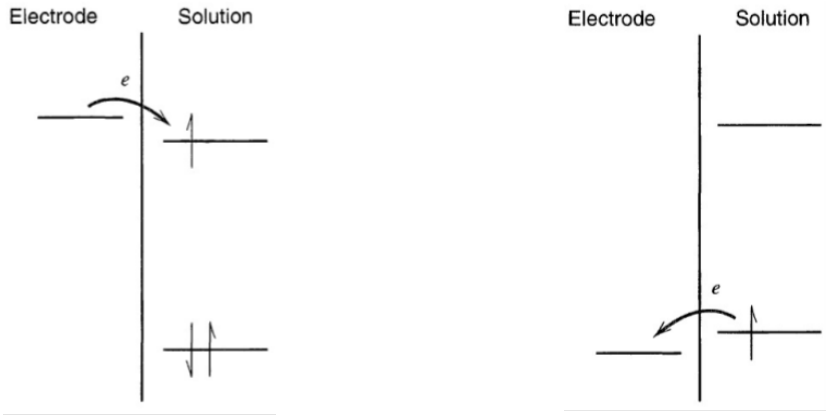

Figure 2.15: Processes that take place at the electrode-electrolyte interface. In (a) the electrolyte is reduced as the energy level of the electron is higher than the LUMO, while in (b) the electrolyte is oxidized when the electron energy level is lower than the HOMO. Note that in this figure the electrolyte is referred to as *solution*. Figure taken from [92].

The energy difference between the LUMO and HOMO is called the stability window. If the energy levels of the electron are outside of the stability window of the electrolyte, the electrolyte is either reduced or oxidized and thus decomposed.

For an aqueous electrolyte, the stability window is limited to the stability window of water. This can be explained by a Pourbaix diagram, named after its founder Marcel Pourbaix [93]. A Pourbaix diagram illustrates the thermodynamic and not experimentally determined equilibrium phases of elements in aqueous systems. Besides, reaction kinetics cannot be deduced from the diagram. The equilibrium phases are shown as a function of pH on the horizontal axis and the potential of Si versus the SHE on the vertical axis, while depending on temperature, pressure and concentration. By default, Pourbaix diagrams are shown at room temperature (298K), atmospheric pressure (1 bar) and concentrations of 10^{-6} mol/l. The stability window of water is often indicated by lines of which the more negative potential represents the LUMO and the more positive line the HOMO.

If a stable specie is a dissolved ion, the region is corrosive. If the specie is a solid oxide of solid hydroxide, the region is passivating. A specie that does not react with the alkaline solution is called immune. The Pourbaix diagram for Si in an alkaline aqueous solution is shown in figure 2.16 [38]. The dotted green lines indicate the stability window of water. The green area indicates the passivation region, the red area the corrosion region and the grey area the immune region.

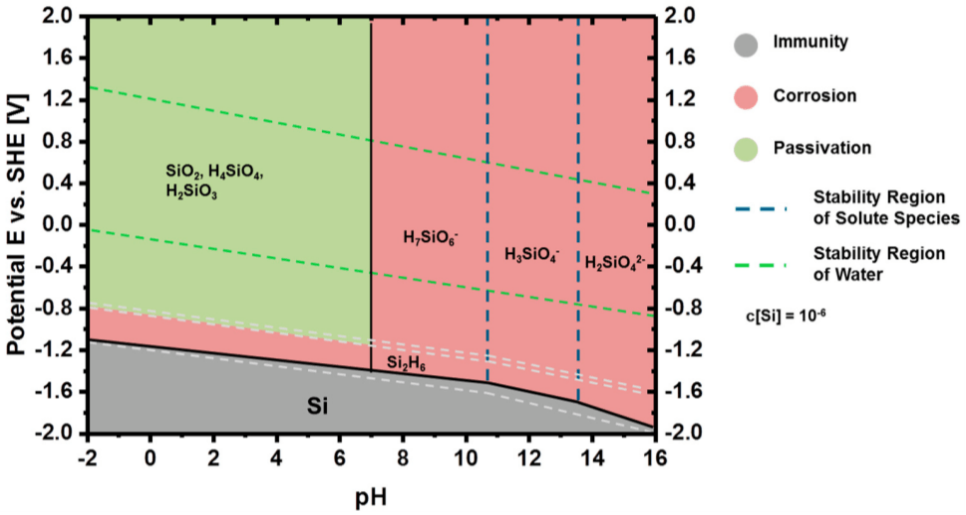

Figure 2.16: The Pourbaix diagram for Si in aqueous electrolytes at standard conditions. The coloured regions indicate whether corrosion or passivation takes place. The horizontal green lines indicate the stability window of water. Figure taken from [38] and based on [93].

Solid Si is not stable in water or aqueous solutions as it falls outside the stability window of water. This means Si will be oxidized and forms silicates or other products, depending on the pH. SiO_2 falls within the stability window of water and creates a passivating layer on the crystalline Si. For alkaline electrolytes, with a pH larger than 13, a Si anode suffers from corrosion and is thermodynamically unstable. It will form silicates and hydrogen gas as described by the overall reaction in figure 2.14.

2.8.3 Measuring the corrosion

The corrosion rates can be measured through several methods, being the polarization method or the mass-loss method. The polarization method is based on the Butler-Volmer equation that gives the relation between the electrode potential, versus a reference electrode, and the current density [94][95]. In the polarization method a scan is performed from cathodic to anodic potentials. The corrosion rate can be determined from the so-called Tafel slopes in the linear regime of the plot. The point where the slopes intersect represents the actual corrosion current [38]. Based on the slope, the corrosion rate can be calculated. This method is shown graphically in figure 2.17. For potentials higher than -1.0 V, the anodic current density decreases as the Si surface is passivated.

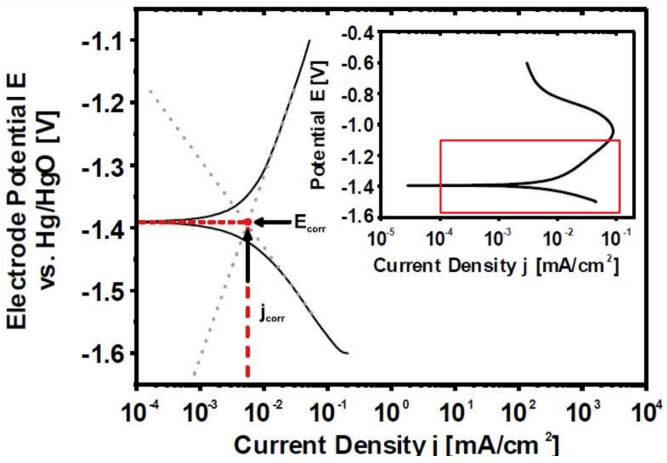

Figure 2.17: Polarization curve for Si in alkaline electrolyte. The red square box is enlarged in the left graph. The straight lines are the Tafel slopes. The E_{corr} is the point where the anodic reaction rate equals the cathodic reaction rate. Figure taken from [38].

The polarization method only takes into account the electrochemical reactions, while there may also be chemical reactions involved in the corrosion. This is due to the short scanning time during which the mass loss is negligible. The chemical corrosion is therefore not measurable.

Other methods such as weight-loss or etch-depth measurement include both the chemical as well as the electrochemical mechanisms. Typical results of the polarization method are in the order of several nm/h of corrosion [44], while a study that used the etch-depth method found several μm/h [96], a factor thousand larger. This indicates that multiple mechanisms may be present.

In the weight-loss method, the loss in weight of the Si anodes is measured by weighing the anode before and after the experiment. This total mass loss includes the corrosion mass loss as well as the electrochemically discharged anode mass loss. When the results of the weight-loss method were compared to the polarization method, it was found that the electrochemical corrosion rate was in the order of only 0.5%. Besides, only the 3% of the total mass loss was utilized in the anodic reaction during discharge. The rest of the mass was lost in the corrosion reaction, enabling a specific capacity of 120 mAh/g [44].

2.8.4 Nature of mechanism

Besides the electrochemical mechanism that involves transfer of charges described in figure 2.14, a chemical mechanism was also suggested in literature [97]. The underlying reaction mechanisms for chemical and electrochemical are different while the total reaction is similar. The chemical mechanism describes an attack of H_2O whereas the electrochemical mechanism describes an attack of OH^--ions on the hydrogen bond and injection of electrons into the conduction band [98].

At OCP, only 0.5% of the measured corrosion rate was electrochemical of nature. The remaning 99.5% was chemical and, therefore, the corrosion is of chemical nature at OCP and is dominated by free H_2O molecules [44]. When galvanostatically discharging the battery cells, the overpotential at the anode increased as electrons have to be provided. This, in turn, increased the flow of OH^- ions onto the anode surface. Eventually, this increased the corrosion rate to higher values up to 2.2 μm/h with respect to OCP conditions. The corrosion rate at OCP is smaller at 1.5 μm/h.

This was also observed in the mass consumptions of Si. After 24 hours of OCP the consumed mass was 4 mg, while discharging the battery over the same time period increased the consumed mass to 6 mg [43]. This indicates an influence on the number of electrons on the overall corrosion, as there is an active electrical current applied in the battery cell, requiring the transport of electrons through the external circuit. As the corroded mass increased with applying a current, more electrons were parasitically consumed at the cathodic sites in the Si anode.

The corrosion rate increases for high current densities, because the Si-Si bonds are weakened by the large electronegativity of Si and OH^- [44][98]. What is interesting to note from the experiments, is that the cell potential is not affected throughout the discharge of the battery even though high corrosion rates are present. The above information indicates that the electrochemical component can be of measurable influence in the total corrosion.

2.8.5 Corrosion in non-aqueous electrolytes

For non-aqueous electrolytes, such as $EMIm(HF)_{2.3}F$, the effect of corrosion is smaller when compared to the effect measured when using alkaline electrolytes [40][42][52]. Using the polarization method, the electrochemical corrosion rates were calculated. The associated corrosion rates were in the order of 0.01-0.08 nm/min, or 0.6-4.8 nm/h at a discharge current of 0.05 mA/cm^2 [52]. Besides the electrochemical rates through polarization, the anode weight-loss method was included as well [42]. In the weight-loss method, the mass of the anode is determined before and after discharging. Based on the material density and the active area, the corrosion rate can be determined. By measuring the total mass consumption, it was found that corrosion rates were over two orders of magnitudes higher, compared to measuring the corrosion with the polarization method., i.e. 1.1-2.9 nm/min or 66-174 nm/h at a discharge current of 0.05 mA/cm^2. Overall, anode mass conversion efficiencies of 40-50% were reached where the main loss mechanism was due to the mass loss in side reactions [42]. Compared to aqueous electrolytes, the corrosion rates in non-aqueous electrolytes are still an order of magnitude smaller, enabling a considerably higher anode mass conversion efficiency in the order of 40-50%.

2.9 Modifications

To overcome the challenges and improve the efficiency of both aqueous and non-aqueous Si-air batteries, proposed solutions in literature are discussed. These include changing the dopant concentrations, crystal orientation, the discharge current, anode surface area, electrolyte concentration, operating temperature and pre-wetting times of the air cathode.

2.9.1 Doping

As mentioned in section 2.2, the concentrations of electrons and holes inside Si can be changed. This is called doping. Atoms that increase the number of free electrons are called donors, while atoms that decrease the number of free electrons are called acceptors. There are two types of doped Si, n-type and p-type, either doped with donors or acceptors respectively. The majority carriers in n-type Si are electrons while in p-type Si these are holes. Therefore, it may be assumed that the acceptor concentration is much smaller than the donor concentration in n-type Si ($N_a \ll N_d$) and vice versa for p-type Si ($N_a \gg N_d$) [69].

Heavily doped Si has a lower internal resistivity, i.e. higher conductivity, which improves the cell performance. Using undoped Si is therefore not very appealing due to the relatively low electronic conductivity of an intrinsic semiconductor. The relation between the resistivity and dopant concentration for a n-type Si wafer is given in equation 2.9.1 [69]. This equation assumes complete ionization and the fact that the resistivity ρ is function of the majority carrier concentration N_a or N_d, depending on the type of Si. e is the electron charge and μ_n the electron mobility.

$$\rho \approx \frac{1}{e\mu_n N_d} \approx \frac{1}{\sigma} \tag{2.9.1}$$

The first paper about Si-air batteries, written by Cohn et al., already included heavily doped Si wafers for non-aqueous RTIL electrolytes [40]. Both n and p-type doped wafers with <100> orientations were included. This was extended in their next paper with As or Sb-doped (n-type) and B-doped (p-type) doped wafers with moderate or heavy doping and <100> or <111> orientation [52]. The effect of doping and crystal orientation was illustrated using polarization diagrams and is shown in figure 2.18. It was found that using heavily doped n-type Si had a higher OCP than p-type Si, while the corrosion rate in p-type Si was lower at less than 0.1 nm/min. The orientation of the crystal had almost no influence on the cell performance This means that the self-discharge rate is lower for p-type Si and it enables a longer shelf-life. But the battery potential in operation was considered more important and therefore n-type Si was found to be most potent [52].

In a more recent paper by Durmus et al. the effect of doping in non-aqueous electrolyte was again studied [42]. The As-doped Si anodes with the <100> orientation had the highest discharge potential, as can be seen in figure 2.19.

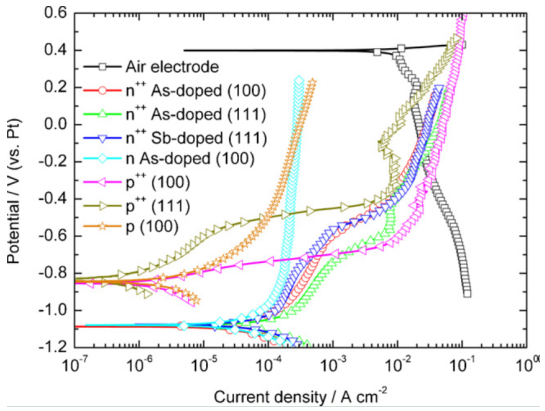

Figure 2.18: Polarization voltammogram for non-aqueous RTIL electrolyte for different doped Si anodes. The air cathode is also included. Figure taken from [52].

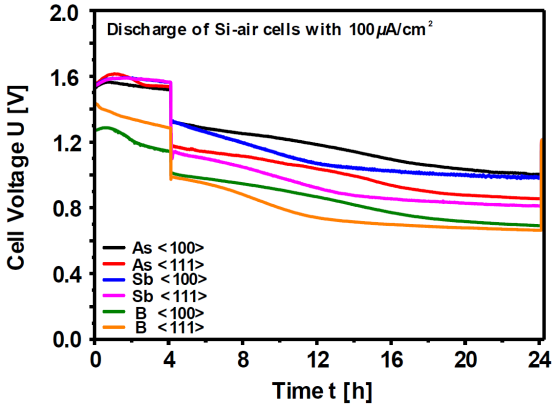

Figure 2.19: A 24h discharge profile for Si-air battery using non-aqueous RTIL electrolyte with different types of dopants. Figure taken from [38] and based on data from [42].

The corrosion rates, which were determined using weight loss and polarization experiments of the Si anode, were the lowest for B-doped <100> Si wafers. This resulted in the highest mass conversion efficiency of 45-50% compared to 30-40% for n-type dopants. What is interesting to note is that the corrosion mass is significantly lower for As <111> than for As <100> doped Si wafers.

The As <111> (n-type) Si wafer (0.001-0.01 Ωcm) was eventually considered to be the best option as anode material for Si-air batteries with non-aqueous RTIL electrolyte as it also provided a high energy density of 1600 Wh/kg at 0.5 mA/cm^2 discharge currents [42].

The effect of doping Si was also studied for alkaline electrolytes. The first paper that studied alkaline Si-air batteries used a heavily doped n-type Si wafer with a resistivity of 0.001-0.002 Ωcm [41]. Besides, the doping concentrations were adjusted and the results, which are shown in figure 2.20, were observed. A more recent paper used heavily As-doped <100> Si wafers with a resistivity of 0.001-0.007 Ωcm [44].

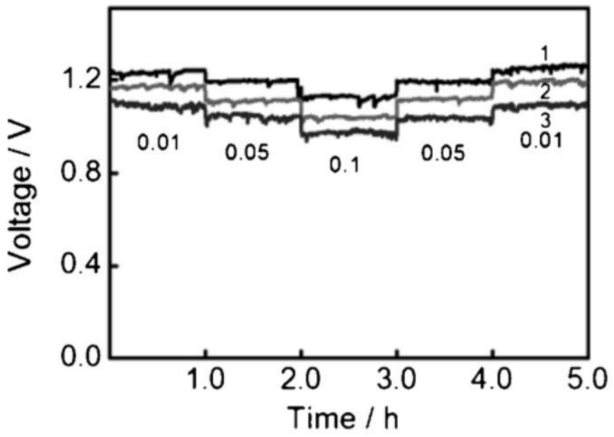

Figure 2.20: The effect of dopant concentrations on the discharge curve of Si is indicated in this graph. Three lines indicate a different resistivity of 1) 0.001-0.002 Ωcm, 2) 0.008-0.01 Ωcm and 3) 0.3-0.8 Ωcm caused by different dopant concentrations. Figure taken from [41].

Corrosion rates for n-type wafers were in the order of 0.24-2.2 μm/h [41][44]. Another paper by Park et al. used alkaline electrolytes in combination with B-doped, p-type <100> Si with a resistivity smaller than 0.005 Ωcm [46]. It is not explicitly mentioned why p-type wafers were used, but based on the corrosion rate data for non-aqueous electrolytes by Ein-Eli et al [52] the effect of corrosion was smaller in p-type Si. However, the effect of corrosion is not mentioned in this paper. Therefore, directly comparing the corrosion in n-type and p-type wafers with alkaline electrolytes is not possible as of now.

Several reasons have been suggested in literature for the decrease in corrosion (etching) rate caused by doping Si wafers. For B concentration up to 10^{19} cm^{-3}, the etch rate of Si in alkaline solutions hardly changes, while for concentrations above 2 x 10^{19} cm^{-3} the etch rate starts to decrease quickly with up to three orders of magnitude [57]. The etching in B-doped wafers practically stops above a concentration of 10^{20} cm^{-3}, while for n-type doped wafers using germanium (Ge) and P this happens for higher concentrations than for B. This behavior can be observed in figure 2.21.

Possible causes for the reduced etching rates are lattice distortion and defect density, electron deficiency or surface passivation [57]. It was found that neither lattice distortion nor crystal defects caused by the p-type doping had a significant role in the etch rate reduction. In one study, the etch rate actually increased with increasing lattice defect density [99].

In the electron deficiency model, the etch rate decreased when the B doping level reached a value of 2.2 x 10^{19} cm^{-3}. At this concentration the Fermi level moves into the valence band making the Si behave as a metal [60]. This model then implies that the etch rate should not decrease for n-type Si as it has excess electrons. However, it was also found for n-type Si that the etch rate decreased, albeit it to a smaller extent [100]. Besides, this model assumes the electrochemical mechanism to be dominant while experimental results indicate that etching is also of chemical nature [57].

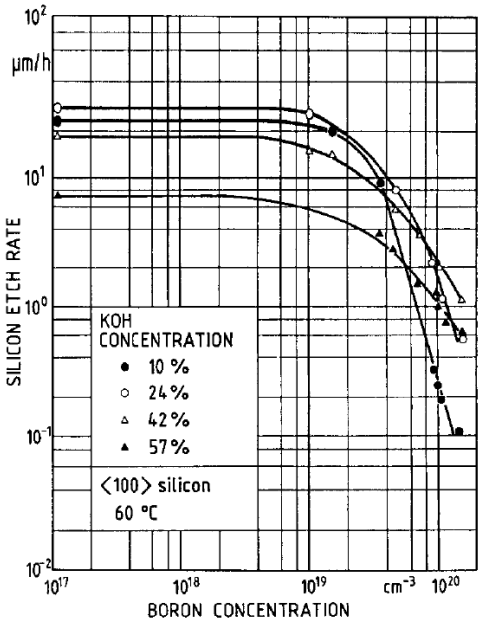

Figure 2.21: The effect of B (p-type) concentrations on the etch rate of Si wafers in alkaline electrolytes with varying concentrations. Figure taken from [57] and based on [60].

In the passivation model, the reduction in corrosion rate is due to the easier formation of an passivating oxide film on highly doped Si [97]. Experiments showed that p-type Si electrodes show more "passive" behavior than n-type Si electrodes and therefore show lower corrosion rates [101]. However, passivation of the Si anode prevents the further discharge of Si-air batteries and should therefore be prevented.

2.9.2 Crystal orientation

Aside from the effect of changing the dopant atoms, also the effect of changing the crystal orientations was studied for Si-air batteries. The corrosion rates in non-aqueous (RTIL) electrolytes, which were determined using weight losses and polarization experiments of the Si anode, were the lowest for B-doped <100> Si wafers [42]. This resulted in the highest mass conversion efficiency of 45-50% compared to 30-40% for n-type dopants. What is interesting to note is that the corrosion mass is significantly lower for As <111> than for As <100> doped Si wafers. The As <111> (n-type) Si wafer (0.001-0.01 Ωcm) was eventually considered to be the best option to use as anode material in non-aqueous electrolytes.

Alkaline substances, such as KOH, are often used for anisotropic wet etching of Si [89][88]. Corrosion in Si-air batteries is considered to be the same as the wet etching. Anisotropic means that the etch rate and direction of etching depend on the crystal orientation of the Si wafer [89]. The etched structures will align with the crystal planes. KOH has become the standard for etching <100> planes at fast rates of up to 1 μm/min at 80°C, while the <111> oriented crystals etch considerably lower at 0.4 μm/h at 80°C. The <100> plane is etched with concave corners along the slow-etching <111> plane, while the bottom is etched along the fast etching <100> plane. The angle between the corners and bottom is 54.7° [102]. The etching profile of <100> is visualized in figure 2.22. The thick SiO layer on top of the Si substrate is etched considerably slower than Si and functions as a mask to obtain the etched structure only in designated areas. The etching will practically stop when the planes of <111> orientation meet as is indicated in the left trench in figure 2.22.

The reason that <111> planes etch much slower in KOH is because the surface Si atom is backbonded by three bonds instead of two, as is the case for <100> and <110> planes. This means that <111> Si has only one dangling bond available per unit cell. Dissolving Si into the electrolyte to keep discharging the battery, requires breaking of the back bonds. It thus requires more energy to break the bonds and dissolve a $Si(OH)_4$ atom, effectively lowering the etching rate [44][100].

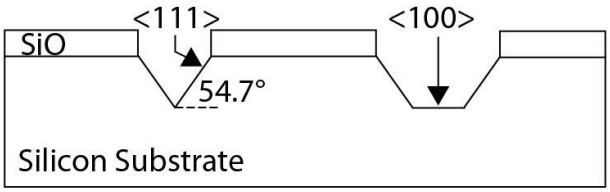

Figure 2.22: The etching profile for <100> Si. The sidewalls are etched along <111> orientation. The etching stops when the <111> planes meet. This happens in the left trench. Figure taken from [102].

2.9.3 Discharge current

Throughout literature, Si-air batteries are discharged at different current densities, ranging from 0.001 mA/cm^2 up to 0.5 mA/cm^2.The cells are often discharged using a galvanostat with current densities set at 0.05-0.1 mA/cm^2. The effect of changing the discharge current density will be discussed for the most often used electrolytes, i.e. alkaline and non-aqueous RTIL electrolytes. First, non-aqueous electrolytes will be discussed.

As mentioned in subsection 2.7 about passivation, the current density in non-aqeous electrolyte Si-air batteries was changed on discharging to prevent the formation of a passivating layer of SiO_2 on the cathode [52]. With this increased discharge current density, a higher discharge capacity in mAh was reached. This means that the battery operates more efficiently for higher discharge currents. This can be observed in figure 2.23.

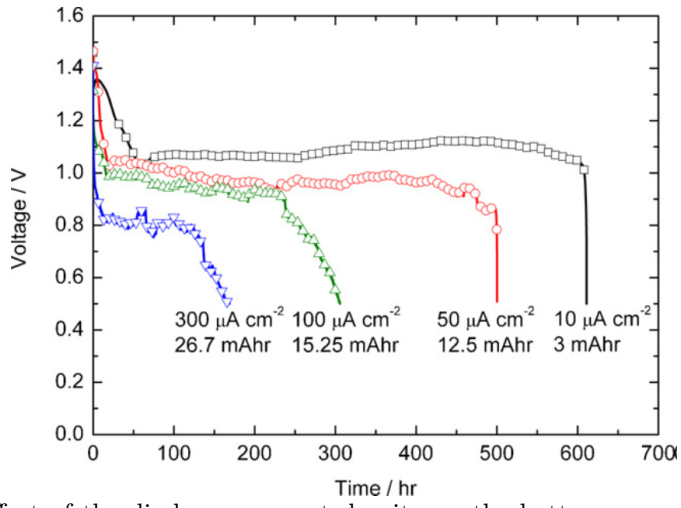

Figure 2.23: The effect of the discharge current density on the battery capacity. A higher discharge current density leads to a larger discharge capacity. Figure taken from [52].

At low current densities, the micro-pores of the active carbon inside the air cathode are clogged by small SiO_2 particles. Higher current densities increase the particle size of the formed SiO_2 deposited on the macro-pores of the active carbon. This means that the micro-pores remain free and that the oxygen can continue to diffuse. The battery can stay operational for longer until the active carbon is blocked by the larger SiO_2 particles.

In a different paper that used non-aqueous RTIL electrolytes, the discharge behavior under different current densities for multiple dopant types and crystal orientations was studied [42]. The current densities varied between 0.05 mA/cm^2 and 0.5 mA/cm^2. The effect of changing the current densities was measured for the cell voltage, corrosion mass, conversion efficiency and specific energy density.

When observing the cell voltage, the cell operated 4 hours at OCP, followed by 20 hours of discharge. At OCP the current flowing through the cell is zero. The results of the experiments are shown in figure 2.24.

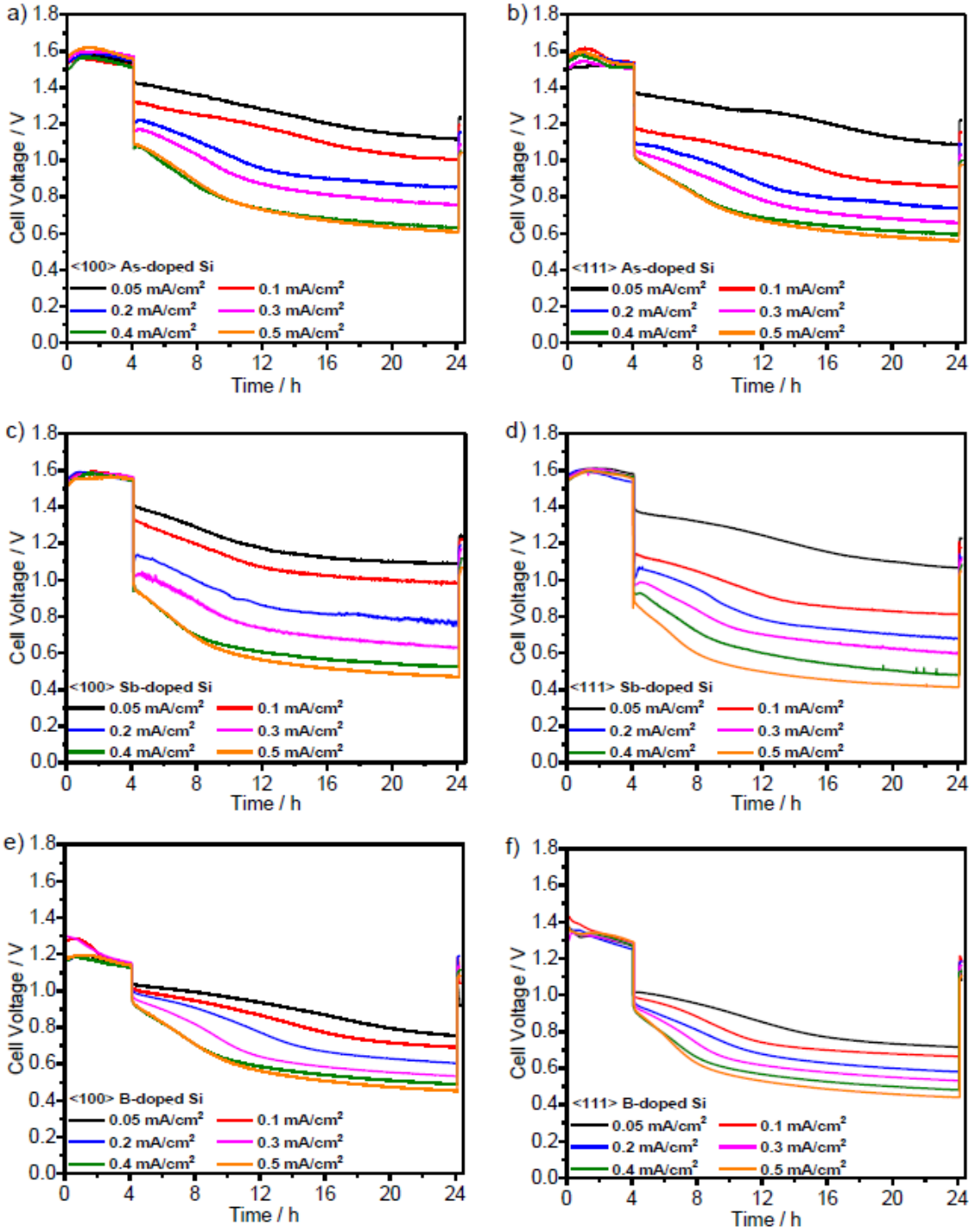

Figure 2.24: The effect of varying the discharge current density on the potentials at OCP and on discharging the battery. Several dopant materials are used with different crystal orientations. Figure taken from [42].

The potentials for current densities using n-type dopants, i.e. As and Sb, were stable between 1.5 and 1.6 V during OCP conditions. At the start of discharging, the potential decreased by only 0.1 V for low current densities (0.05 mA/cm^2), while for high current densities (0.5 mA/cm^2) the potential decreased by 0.45 V. This increased to 0.3 and 0.5 V, respectively, at the end of discharging. The discharge currents affected the rate of change in the potential curve. For high current densities there is a clearer and less smooth transition between the beginning and end of discharge. Overall, doping with As and Sb leads to similar results. However, applying high current densities to Sb leads to more reduced potentials compared to As. The voltage profile is independent of crystal orientation.

P-type dopants, i.e. B, show lower OCP potentials of 1.15 V. Just as with n-type dopants, the potentials decrease further and faster with higher current densities. At the highest current density, the potential of B-doped and Sb-doped is comparable at 0.45 V and 0.47 V respectively. Again, the effect of crystal orientation is small.

After discharging for 20 hours at different current densities, the corroded masses of the Si-anodes show significant differences. For n-type and p-type Si, the corroded mass increased when the current density increased, albeit at a significantly lower rate for p-type Si than for n-type Si. Up to 0.3 mA/cm^2 the increase is linear, but for higher current densities the increase flattens.

The specific energy density is the largest for low current densities up to 0.1 mA/cm^2 for n-type Si and up to 0.05 mA/cm^2 for p-type. Overall, the n-type Si wafers showed a higher specific energy density than p-type.

The effect of changing the current density was also studied for alkaline electrolytes. The first paper describing a n-type Si-air battery with an alkaline electrolyte by Zhong et al. found that the potential - like RTIL electrolytes - decreased for higher current densities [41][42]. The drop in potential could be caused by the internal resistance between the Si-electrolyte interface. Increasing the discharge current density from 0.05 mA/cm^2 to 0.1 mA/cm^2 increased the corroded mass of Si by roughly 20%, while also increasing the specific capacity by almost 70% [41]. It should be noted that this was only valid for diluted electrolyte concentrations and 7 hour discharge times.

Another paper focused on nanoporous p-type Si in alkaline electrolytes [46]. The Si anode was able to discharge for 24,000 seconds at a higher potential when a lower current density of 0.001 mA/cm^2 was used instead of 0.01 mA/cm^2. At high current densities the Si surface was passivated faster, deteriorating the performance. This can be observed in figure 2.25. The effect of changing the current density on corrosion was not explained. Another paper by Durmus et al. using n-type wafers, recorded no passivating behavior for current densities below 0.05 mA/cm^2 [43].

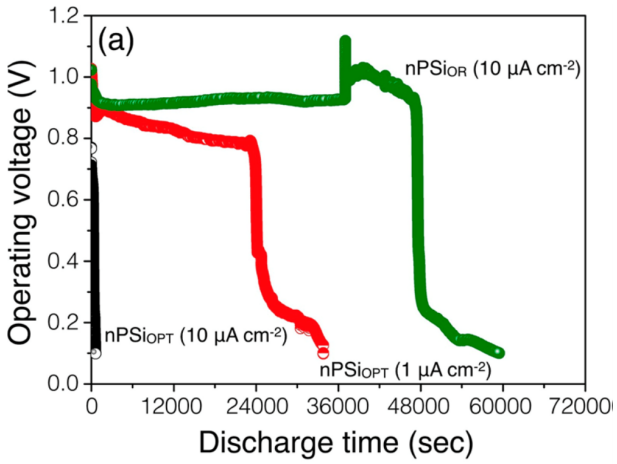

Figure 2.25: This diagram shows the measured potentialof the battery as function of time. The effect of the discharge current density on the total discharge time is studied. A lower current density (red) enables a much longer discharge time than the higher current density (black). The green line indicates the discharge potential over time when an oxide layer was removed. This allowed the battery to be discharged for longer periods at higher current densities. Figure taken from [46].

In a more recent paper of Durmus et al., the corrosion behavior of As-doped (n-type) Si wafers in alkaline electrolytes was researched [44]. Polarization effects cause the cell voltage to drop by 200 mV at high discharge current densities compared to low current densities. This effect can be observed in figure 2.26.

The corrosion rates increase with increasing current densities, up to 2 μm/h at 0.05 mA/cm^2. When the current density is further increased to 0.07 mA/cm^2, the corrosion rate still increased but only by 5% to 2.1 μm/h. These high discharge current densities increase the anode mass

conversion efficiencies as more Si is used in the reaction. Therefore, the highest mass conversion efficiency of 3% was reached for the highest current density of 70 mA/cm^2. This led to a specific capacity of 120 mAh/g. The corrosion rate for different current densities are shown in figure 2.27.

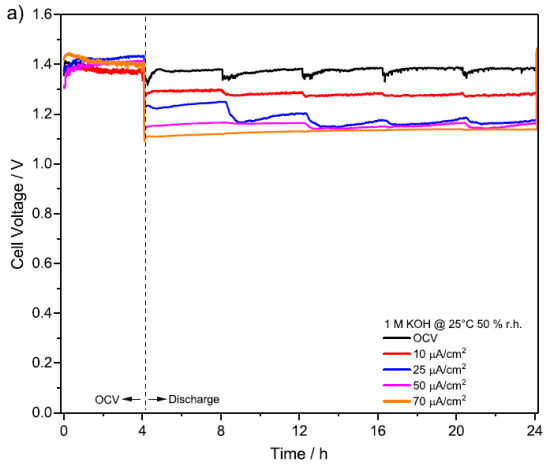

Figure 2.26: The cell voltage as function of time with 4h OCP and 20h discharge. The current density is increased from 10 μA/cm^2 to 70 μA/cm^2. Figure taken from [44].

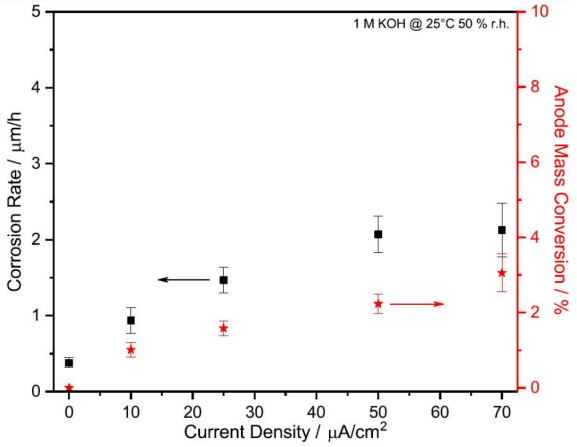

Figure 2.27: The corrosion rates are plotted as a function of current density. The anode mass conversion is given on the right vertical axis. Figure taken from [44].

2.9.4 Anode surface area

The first Si wafers that were used, were flat, single crystal and doped wafers with varying orientations [40]. As the passivation of Si takes place at the air cathode in non-aqueous electrolytes, the anode remains free from a passivating layer and long discharge times are possible. According to Cohn et al., Si dissolves well in the RTIL while discharging, due to the formation of Si-F bonds [52].

This is different for Si-air batteries using alkaline electrolytes. The reaction product $Si(OH)_4$ has to be removed continuously to prevent the formation of the passivating SiO_2 layer, implying that the dissolution rate of $Si(OH)_4$ has to be higher than the rate at which it is generated. According to Zhong et al. for an unmodified flat n-type Si wafer, the surface passivates quickly. This caused the discharging of the battery to stop after only 400 seconds [41]. The solution of Zhong et al. was to increase the surface area of the Si anode by forming a rough, porous surface structure that increased the dissolving rate of $Si(OH)_4$. Using metal-assisted chemical etching, the surface was chemically modified by Si nanowires of 1.5 μm thick deposited on top of the Si. The use of nanowires originates from an earlier paper of Zhong et al. [103]. With this modified and enlarged surface area, the discharge time was increased to over 30 hours as it removed the $Si(OH)_4$ effectively. This specific surface modification is visualized using SEM in figure 2.28.

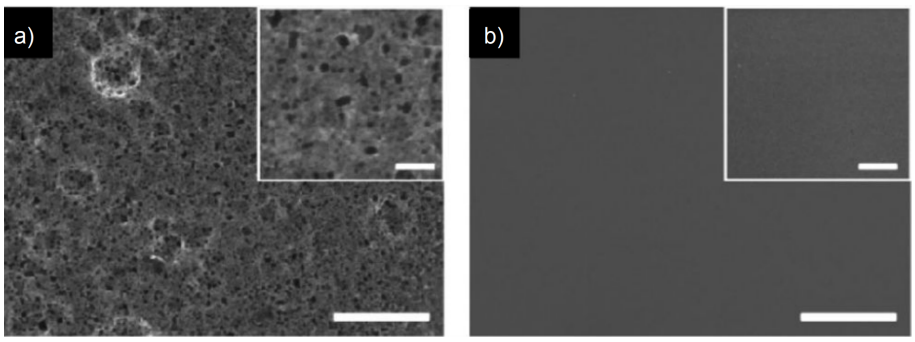

Figure 2.28: The effect of surface modifications through chemical etching is visualized using SEM. a) includes a modified rough, porous surface while b) includes the unmodified, flat surface. The modified surface enables discharge times up to 30 h. Figure taken from [41].

A follow-up paper by Park et al. used a p-type Si wafer of which the surface was modified [46]. The surface modification was done through electrochemical etching in a HF-based solution. With electrochemical etching, the diameter and thickness of the pores can be controlled. The optimal structure featured deep pores (20 μm) with a small diameter (10 nm), as this enabled the longest discharge times.

Applying a constant discharge current density of 1.0 mA/cm^2 resulted in a constant porous layer, where the etch time affected the thickness. Increasing the thickness reduces the voltage drop and increases the energy capacity. A constant potential was used in the etching process to affect the pore diameter. A small pore diameter resulted in a flat discharge curve without abrupt voltage changes. Overall, the pore diameter is of larger influence on the discharge capacity than the depth. The effect of increasing the pore depth and pore diameter is given in figures 2.29 and 2.30.

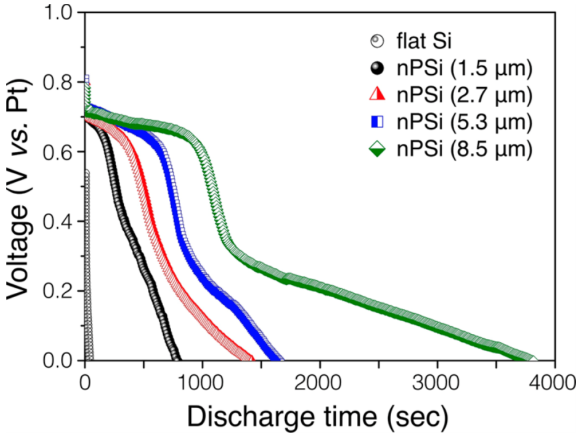

Figure 2.29: Discharge profile with varying pore depth with 0.1M KOH. A deeper pore increases discharge times. Figure taken from [46].

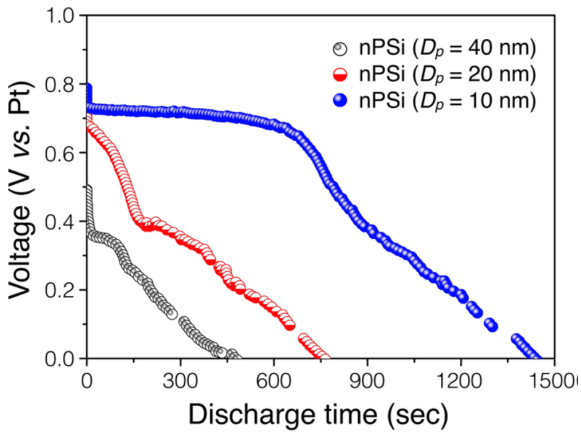

Figure 2.30: Discharge profile with varying pore diameter with 0.1M KOH. A smaller diameter increases discharge times. Figure taken from [46].

On discharging with the optimal pore depth and diameter, the Si surface is mildly anodized creating a passivating SiO_2 layer. When this oxide-layer is removed by, again, etching with a HF solution, the battery can be discharged for more than 48,000 seconds at the elevated current density. In figure 2.25 this is indicated by the green line. The oxide removal step is indicated in figure 2.31, where the pore depth and diameter are also shown.

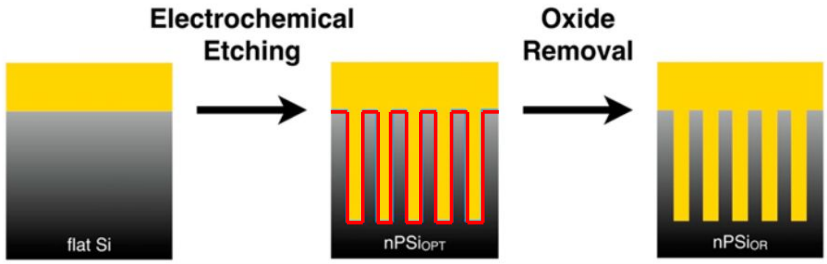

Figure 2.31: The steps that are taken to create the optimal nanoporous Si wafer. First electrochemical etching is performed after which the extra oxide removal step is added to increase the discharge capacity. Figure adapted from [46].

A more porous Si surface increases the surface area per volume. A larger surface area increases the electrode-electrolyte contact interface, which in turn increases the dissolution rate. However, a high surface area also increases the corrosion at the anode [38]. The corrosion eventually has a much larger impact than the passivation on lowering the mass utilization efficiency to a maximum of 3% [43][44].

2.9.5 Electrolyte concentration

The electrolyte used in Si-air batteries is often a non-aqueous RTIL or aqueous alkaline electrolyte. Throughout literature, the composition of aqueous electrolyte was often varied in concentration to study the effect on the discharge performance of a battery cell. The effect of changing the electrolyte composition will be discussed for both non-aqueous and aqueous electrolytes.

For non-aqeous RTIL electrolyte, which are in fact molten salts, only the water content that is added to the electrolyte can be changed [59]. This was mentioned earlier at the end of section 2.7. The addition of water caused the formation of the passivating SiO_2 layer to transfer from the air cathode to the bulk of the electrolyte. This prevented the pores in the activated carbon to be clogged and enabled the oxygen reduction to continue. The capacity could be increased by 40% to 70 mAh/cm^2 by adding 10-15 vol% water. With the addition of water, the potential was lowered by roughly 0.1 V due to the formation of a passivating SiO_2 layer at the anode surface. However, when too much water is added, i.e. above 40 vol%, the oxide layer at the anode becomes too thick and resisitive and a continuous discharge is prevented.

For alkaline electrolytes the effect of the electrolyte concentration can be measured and adjusted as it is a water-based solution. The first paper that mentioned an alkaline (KOH) electrolyte by Zhong et al. also studied the effect of changing the concentration on the OCP [41]. Based on the Nernst equation as provided in equation 2.1.4, it is expected that the anodic potential increases in absolute value with increasing KOH concentration. This means that anodic potential will be more negative, and thus releasing electrons more easily. This leads to a higher OCP. It was experimentally found by Zhong et al. for a 24h measurement of OCP at 0.6M KOH that the OCP reaches 1.10 V, while for a 6M KOH solution the OCP reached 1.32 V [41]. The potential decreased slightly over time for all concentrations. This can be observed in figure 2.32 and is due to the reduced concentration of the electrolyte. On discharging at 0.05 mA/cm^2, the potentials decreased to 1.01 V and 1.18 V for 0.6M and 6M KOH respectively.

The effect on the OCP is not directly visible in the findings of another paper, by Durmus et al. [43]. Here it was found that the OCP was constant around 1.4 V over 4 h, without large influence of the KOH concentration. This can be observed in figure 2.33.

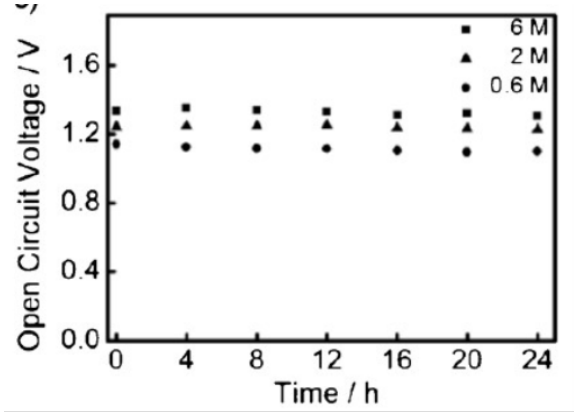

Figure 2.32: The OCP for different KOH concentrations measured for 24h. Figure taken from [41].

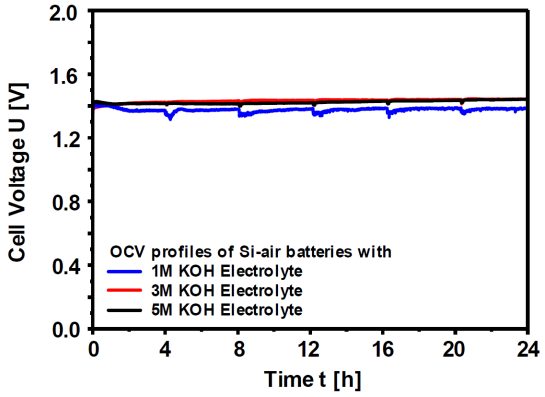

Figure 2.33: The OCP for different KOH concentrations measured for 24h. Figure taken from [38].

On discharging, two regions were observed. One for concentrations below 2M and one for concentration above 2M, where the highest concentrations show the highest potentials [43]. Figure 2.34 shows this. The increase in discharge potential for higher electrolyte concentrations is due to lower overpotentials that are caused by faster reaction kinetics.

The concentration of the electrolyte affects the ionic conductivity. The ionic conductivity increases when increasing the concentration up to 6M, after which the ionic conductivity starts to decrease [86]. Too high concentrations cause viscous solutions that are also more resistive. The relation between the concentration and conductivity is displayed in figure 2.35.

However, there is a trade-off for using a high KOH concentration to increase the operating potential, as it also increases the corrosion rate of Si [41][43][44]. It was found that the corrosion rate for Si using alkaline electrolyte at discharging was in the order of 1-1.5 μm/h for high 6M KOH concentrations, while it dropped to 0.25 μm/h for 0.6M. This enables, in theory, a lifetime up to 2000 hours [41]. However, the electrolyte has to be refreshed continuously as reaction products build up during discharge that can saturate the electrolyte and reduce its conductivity.

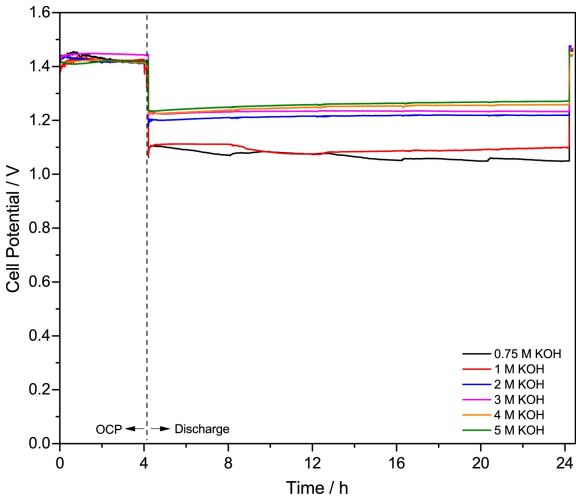

Figure 2.34: The discharge profile for different KOH concentrations measured for 24h. Figure taken from [41].

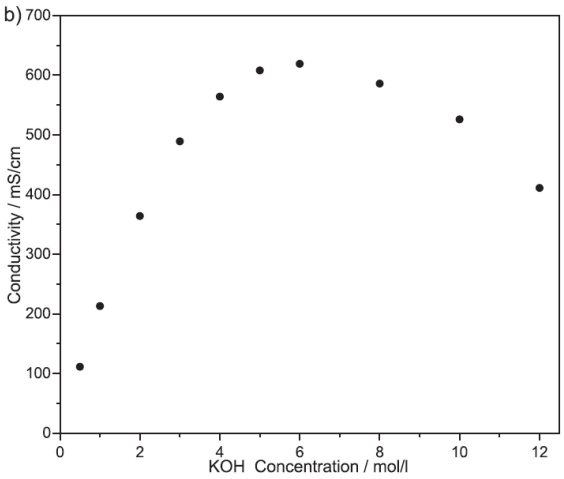

Figure 2.35: The conductivity of the electrolyte as function of KOH concentrations. Figure taken from [44].

The corrosion rates obtained by Durmus et al. show very similar sizes for low concentrations up to 2M, even when the concentration is increased [44]. The corrosion at these low concentrations is suggested to be controlled by excess H_2O, as their concentration does not change much for low concentrations and their activity is high [61]. Besides, the ionic conductivity is low for low concentrations. For concentrations between 2M and 6M, the corrosion rate is significantly increased and controlled by both H_2O and OH^- as the increased conductivity cause OH^- ions to move faster, acting as a reaction catalyst. For concentrations above 6M, the corrosion rates decrease as the electrolytes becomes more viscous, has a lower conductivity and H_2O molecules are scarcer. The overall behavior at all concentration intervals is shown in figure 2.36.

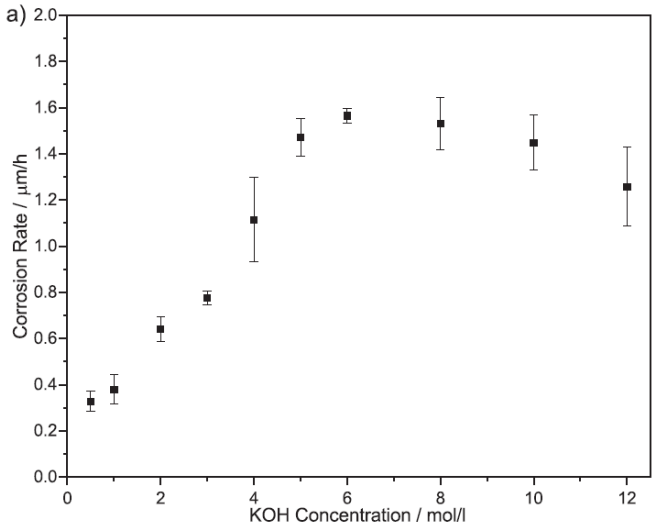

Figure 2.36: The corrosion rate of Si in an alkaline (KOH) electrolyte as function of the electrolyte concentration. For high (>6M) concentrations, the corrosion rate decreases. Figure taken from [44].

In addition to being used as an electrolyte in a battery, KOH is used as an anisotropic etchant for Si [89][90]. The concentration of KOH has an effect on the etching. Low concentrations cause

rough surfaces with pyramidal hillocks that become larger and rougher for concentrations up to 4M. For higher concentrations the surfaces become smoother again. The corrosion rates for 4M and 12M are comparable, while their surfaces are very different. It was concluded that Si etching changes from anisotropic to isotropic-like for high (>4M) concentrations [44].

With low concentration KOH electrolytes, the shelf-life of Si-air batteries at OCP can be increased. However, with higher concentrations of KOH, the discharge voltage is increased and more stable, while the corrosion rate does not increase significantly at high current densities [44].

2.9.6 Operating temperature

The operating temperature of the Si-air batteries in literature was almost all at room temperature (298 K). Durmus et al. studied the effect of changing the temperature for a n-type As-doped <100> Si wafer in an alkaline electrolyte (KOH) [44]. It was found that the corrosion rate increased from 0.66 μm/h at 15 °C to 13.62 μm/h at 60 °C as can be seen in figure 2.37. When the obtained values were plotted, clear Arrhenius behavior was observed as the etch rates increased exponentially with the temperature [104]. The Arrhenius equation includes an exponential term and is provided in equation 2.9.2.

$$k = A \exp\left(\frac{-E_a}{k_b T}\right) \tag{2.9.2}$$

k is the reaction rate coefficient, A the pre-exponential factor, E_a the activation energy, k_b the Boltzmann constant and T the temperature in Kelvin. With the obtained datapoints, an Arrhenius plot was constructed which plots the corrosion rates as function of the inverse temperature ($1/T$). The exponential curve becomes a straight line when a logarithmic y-scale is used, showing that the relationship is indeed exponential within the studied temperature range. Equation 2.9.2 can be rewritten to equation 2.9.3. With the Arrhenius plot the E_a and A can be obtained.

$$\ln(k) = \ln(A) - \frac{E_a}{k_b}\left(\frac{1}{T}\right) \tag{2.9.3}$$

Based on the slope in figure 2.38, the activation energy equals 0.57 eV and is in accordance with comparable Si wafers in KOH [60]. As the activation energy is within 0.44-0.87 eV, it is a surface-limited process originating from either the transfer of electrons, adsorption or desorption or by chemical reactions [44].

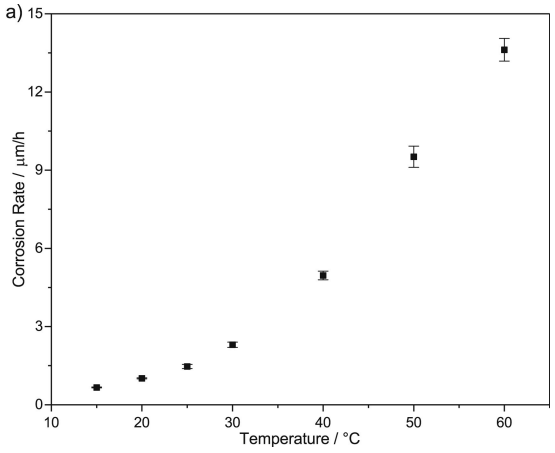

Figure 2.37: The effect of increasing temperature on the corrosion rate of Si in alkaline electrolyte. Figure taken from [44].

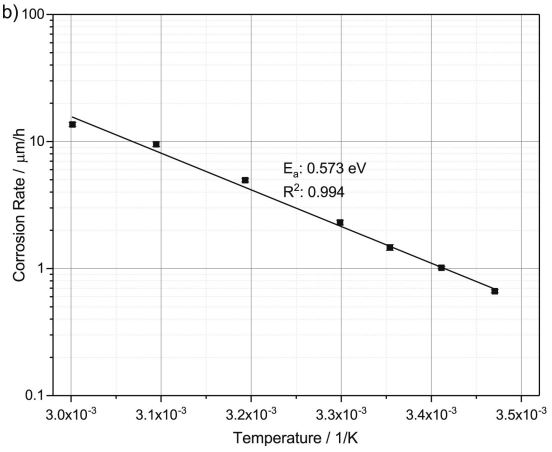

Figure 2.38: The corrosion rates are plotted in an Arrhenius plot as a function of 1/T. Figure taken from [44].

Based on the diagrams, operating a Si-air battery at temperatures higher than room temperature significantly increases the corrosion rates. Using a battery with KOH in a hot environment will therefore decrease the discharge lifetime of the battery.

2.9.7 Pre-wetting air cathode

A suggested solution to improve the discharge potential and discharge capacity is the pre-treatment of the air cathode with an alkaline solution before being used in a Si-air battery with an alkaline electrolyte [64][105]. The pre-treatment increases the surface-to-volume ratio of the micro-pores in the air cathode and decreases the charge transfer resistance. As the reduction of oxygen takes place at the cathode, the reduction rate can be increased by the increased area but also through the absorption of OH^--ions. Besides, the ohmic resistance is reduced.

The pre-treatment with KOH was compared to using only H_2O [64]. It was found that a pre-treatment time of 8 hours with 30 vol% KOH was needed to increase the discharge time from practically zero to over 70 hours. Shorter or longer pre-treatment times reduced the discharge time and potential of the battery. Pre-treating with H_2O instead of KOH resulted in a discharge time of only tens of seconds, albeit at a higher potential. The pre-treatment proved to be a useful and straightforward way to increase the discharge time and potential.

2.10 Nonuniform doping

In the electrochemical corrosion reaction that emerges in alkaline electrolytes, the generated electrons in the oxidation reaction and the available free electrons in the material are involved at the so-called cathodic site reaction. This means that electrons generated at anodic sites are consumed at the cathodic sites instead of contributing to the external circuit. The reactions are provided in equation 2.10.2. In a paper of Durmus et al. it was stated that corrosion is the main cause for the low conversion efficiency when alkaline electrolytes are used [44].

$$\text{Anodic site:} \quad Si + 4OH^- \longrightarrow Si(OH)_4 + 4e^- \tag{2.10.1}$$

$$\text{Cathodic site:} \quad 4H_2O + 4e^- \longrightarrow 4OH^- + 2H_2 \tag{2.10.2}$$

N-type Si has excess electrons and, therefore, it can be expected that electron transfer from the electrode to the electrolyte (cathodic current) is more pronounced than with p-type Si. Therefore, it can be expected that n-type Si suffers from increased corrosion compared to p-type Si. This is also experimentally found for non-aqueous electrolytes by Cohn et al. [42]. A solution to this electrochemical corrosion mechanism could be to direct the generated electrons in the anodic reaction to the current collector instead of the electrolyte by means of nonuniform dopant distribution [69].

As discussed earlier in sections 2.2 and 2.9.1, doping Si is very common in Si-air batteries. In fact, it is needed in Si-air batteries to reduce overpotentials and achieve higher discharge voltages [106]. The doping concentration in Si wafers used in Si-air batteries is uniform throughout the wafer, while nonuniform doping could potentially reduce the corrosion [69]. The effect of nonuniform doping on Si will be explained in the next section.

2.10.1 General principle

Nonuniform means that there is a concentration gradient of dopant atoms. Electrons in the conduction band, in response to this concentration gradient, diffuse - through random motion - from the region with high to the region with lower dopant concentrations. Electrons are negatively charged and therefore leave positively charged donor ions behind that are, unlike electrons, not mobile. This causes a separation of positive and negative charges that induces an internal electric field. This prevents the further diffusion of electrons, as there is no net current flow in a semiconductor under thermal equilibrium. An equilibrium is eventually reached when the diffusion current of electrons is opposite and equal to the internal electric field. Figure 2.39 gives an overview of the processes for a one dimensional situation in n-type Si. Here, the diffusion gradient and thus the electron diffusion are in the positive direction to the right. The electric points in opposite direction to the electron diffusion current, i.e. also in the positive direction to the right.

This electric field E_x can be quantified as the derivative of the electric potential ϕ with respect to the distance in the x-direction, as given equation 2.10.3. This follows through Poisson's equation.

$$E_x = -\frac{d\phi}{dx} = \frac{1}{e}\frac{dE_{Fi}}{dx} \quad , \quad \phi = +\frac{1}{e}\left(E_F - E_{Fi}\right) \tag{2.10.3}$$

E_{Fi} is the intrinsic Fermi level and E_F the Fermi level. In a nonuniformly doped semiconductor in thermal equilibrium, E_F remains constant throughout the crystal, implying that the work function ϕ_s varies as a function of position. E_{Fi} has a fixed position between the top of the valence band E_v and the bottom of the conduction band E_c. With nonuniform doping, $E_{Fi}(x)$ varies as a function of distance. As a consequence, an electric field emerges. For a n-type semiconductor that is quasi-neutral, the electron concentration n_0 may be assumed to be equal to the donor concentration $N_d(x)$. This leads to the expression in equation 2.10.4.

$$n_0 = n_i \exp\left(\frac{E_F - E_{Fi}(x)}{k_B T}\right) \approx N_d(x) \tag{2.10.4}$$

n_i is the intrinsic carrier concentration and k_B is the Boltzmann constant. This can be rewritten to equation 2.10.5.

$$-E_{Fi}(x) = k_B T \ln\left(\frac{N_d(x)}{n_i}\right) - E_F \tag{2.10.5}$$

As the Fermi level is constant in thermal equilibrium, the expression of the electric field can be formed to equation 2.10.6 by taking the derivative of E_{Fi} with respect to x.

$$E_x = -\left(\frac{k_B T}{e}\right)\frac{1}{N_d(x)}\frac{dN_d(x)}{dx} \tag{2.10.6}$$

An exponentially varying dopant profile over position x yields a linear profile in the energy bands, as can be seen in figure 2.39.

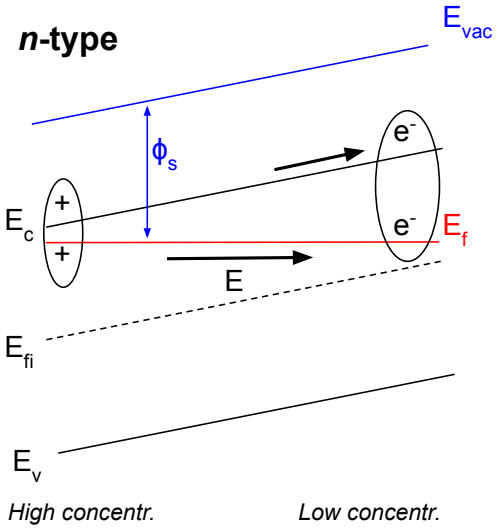

Figure 2.39: The energy-band diagram of a n-type semiconductor with a nonuniform doping concentration profile. Due to the dopant profile, the work function ϕ_s also varies as a function of position. It is therefore easier to excite an electron to the vacuum level in the area of high concentration. Excited electrons diffuse to an area with a lower concentration and leave behind positive donor ions. This separation of positive and negative charges induces an internal electric field, as no net current flows in thermal equilibrium. This principle can be used to move excited electrons in the conduction band away from the electrode-electrolyte interface in the Si-air battery [69].

This will induce a constant electric field over the depth x, causing an electrostatic potential difference U across the semiconductor material. The size of this potential depends on the slope of the profile. For a profile that exponentially varies, the electric field is uniform. This means that

the potential difference between two points only depends on the carrier densities. The electric field for an exponential decreasing profile $N_d(x) = c \cdot \exp(-bx)$ is given in equation 2.10.7 by using equation 2.10.6.

$$E(x) = \frac{k_b T}{e} b \tag{2.10.7}$$

Equation 2.10.3 can be used to calculate the change in electric potential $d\phi$.

$$d\phi = -E(x)dx = \frac{k_b T}{e} \frac{dN_d}{N_d} \tag{2.10.8}$$

The electrostatic potential difference U_{12} between points with decreasing carrier concentration N_1 and N_2 follows through integration of $d\phi$:

$$U_{12} = \phi_1 - \phi_2 = \int_{N_2}^{N_1} d\phi = \frac{k_b T}{e} \int_{N_2}^{N_1} \frac{dN_d}{N_d} = \frac{k_b T}{e} \ln \frac{N_1}{N_2} \tag{2.10.9}$$

When the profile varies exponentially from 10^{16} atoms/cm^3 to 10^{12} atoms/cm^3, the potential difference, based on the above equation, is equal to 0.24 V. Increasing the slope of the profile thus increases the electric field strength for an exponential varying dopant profile.

While profiling a varying dopant concentration on Si wafers is more common in solar cells and integrated circuits, such as bases, emitters, drains and sources [107][108], using this principle in Si-air batteries has not yet been demonstrated in literature.

Available techniques that are used to create a dopant profile are introducing the dopants during the crystal growth, by neutron transmutation doping (NTD), epitaxial growth, ion implantation or by diffusion. For brevity, the next section will only discuss the steps used in the diffusion process as this type of process can be conducted within the facilities available during the experiments of this work.

2.10.2 Diffusion process

In a diffusion process chemical species move from a region with a high specie concentration to a region with a lower concentration. With the implementation of a concentration gradient $\partial N/\partial x$ in a finite volume, the specie wants to redistribute and spread itself more evenly. This reduces the concentration gradient.

There are three common diffusion mechanisms, vacancy, direct interstitial and indirect interstitial diffusion [109]. At elevated temperatures, atoms in a lattice vibrate around their equilibrium point in the lattice. Through the high temperature, there is a finite probability that these atoms leave their lattice position and create a vacancy. These atoms then become interstitial atoms. A neighbouring impurity atom can then migrate into the vacancy. The vacancy takes the role of a diffusion vehicle and this mechanism is therefore called vacancy diffusion. Small atoms can fit into interstitial sites more easily. This allows these small atoms to move between these interstitial sites without moving the lattice atoms. This mechanism is called direct interstitial diffusion. The third mechanism, also called interstitialcy, uses self-interstitials, or defects in the lattice, as the diffusion vehicle. This means that an impurity atom is replaced by a self-interstitial. The impurity atom then in turn replaces a lattice atom. This third mechanism is the dominant diffusion mechanism of impurity atoms, such as B, in semiconductors [110].

Fick's first law describes the flux of diffusion J and is given in equation 2.10.10.

$$J = -D \frac{\partial N}{\partial x} \tag{2.10.10}$$

D is the diffusion coefficient in cm^2/s and N the concentration in atoms/cm^3, resulting in a flux J in atoms/cm^{2}s. The diffusion coefficient can be calculated by using equation 2.10.11.

$$D = D_0 e^{-E_a/k_b T} \tag{2.10.11}$$

The D_0 is the maximum diffusion coefficient in cm^2/s and depends on the material, E_a is the activation energy in eV (1 eV = 1.602 $\times 10^{-19}$ J) for the atoms to overcome, k_B the Boltzmann's constant of 1.38$\times$ 10^{23} J/K and T is the temperature in K. For both dopant atoms B and P, the constants D_0 and E_a are given in table 2.2.

Table 2.2: Maximum diffusion coefficient and activation energy for B and P. Data taken from [88].

Parameter [unit]	Boron	Phosphorus
D_0 [cm^2/s]	0.76	3.85
E_a [eV]	3.46	3.66

However, equation 2.10.10 does not take into account that the concentration gradient within a finite volume decreases over time. This means that, according to the law of mass conservation, the change in concentration over time $\partial N/\partial t$ is the same as the change in the flux $\partial J/\partial x$. This leads to the expression in equation 2.10.12.

$$\frac{\partial N(x,t)}{\partial t} = -\frac{\partial J(x,t)}{\partial x} \tag{2.10.12}$$

This relation can be simplified to equation 2.10.13 by using equation 2.10.10 and in case the coefficient D is independent of position this can be further rewritten to the final expression.

$$\frac{\partial N(x,t)}{\partial t} = \frac{\partial \left(D \frac{\partial N(x,t)}{\partial x} \right)}{\partial x} = D \frac{\partial^2 N(x,t)}{\partial x^2} \tag{2.10.13}$$

In the case of Si, there are two methods to diffuse dopant atoms into the substrate. Both methods use an additional deposited layer on top of the substrate. The first method is called predeposition and has a constant flux of atoms, often referred to as impurities, that are supplied to the substrate surface. The concentration of impurities at the surface remains constant over time.

The other method, called drive-in, uses a thin deposited layer of which the concentration gradient decreases over time as it is not constantly being refreshed at the surface. The effect on the impurity concentration as a function of the distance inside the substrate is shown in figure 2.40 for both predeposition and drive-in.

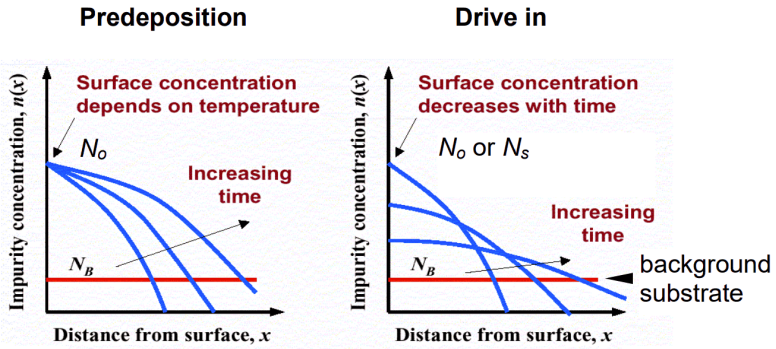

Figure 2.40: The concentration of impurities as a function of the depth inside the substrate for the predeposition process on the left and the drive-in process on the right. The surface concentration remains constant over time for the predeposition process, while it decreases with time for the drive-in process. N_b is the base substrate concentration. Figure taken from [111].

The further distribution of the impurities inside the substrate, called the dopant profile, depends on the diffusion temperature and the duration of the diffusion. The diffusion temperature affects the diffusion coefficient D. Typically, diffusion processes take place at temperatures ranging from 1000 to 1250 °C inside a furnace [88]. The impurity atoms enter the furnace as a gas, liquid or solid. For each impurity type a different chemistry is needed. If gasses are used, p-type impurities are made with diborane (B_2H_6), while n-type is made with either arsine (AsH_3) or phosphine (PH_3). The eventual dopant profile $N(x,t)$ can be analytically determined through

equations and boundary conditions. In case of a predeposition process, the profile is based on an errorfunction erf and has boundary conditions $N(0,t) = N_0$, $N(x,0) = 0$ and $N(\infty,t) = 0$. This errorfunction is expressed in equation 2.10.14 [88]. The function erfc stands for complementary erf, i.e. 1 - erf.

$$\begin{aligned} N(x,t) &= N_0 \text{erfc}\left(\frac{x}{2\sqrt{Dt}}\right) = N_s\left(1 - \text{erf}\left(\frac{x}{2\sqrt{Dt}}\right)\right) \\ &= N_s(1 - \text{erf}(u)) = N_s\left(1 - \frac{2}{\sqrt{\pi}}\int_0^u \text{e}^{-v^2} dv\right) \\ \text{Using:} \quad u &= \frac{x}{2\sqrt{Dt}} \end{aligned} \tag{2.10.14}$$

How far the impurities diffuse inside the substrate before their concentration is equal to the base concentration N_b is called the junction depth x_j [111]. Filling this in in the first part of equation 2.10.14 yields equation 2.10.15.

$$N(x_j,t) = N_0 \text{erfc}\left(\frac{x_j}{2\sqrt{Dt}}\right) = N_b \tag{2.10.15}$$

Rewriting this to x_j gives the expression in equation 2.10.16. The graph will then look similar to the left graph in figure 2.40.

$$x_j = 2\sqrt{Dt} \cdot \text{erfc}^{-1}\frac{N_b}{N_0} \tag{2.10.16}$$

For the drive-in process, in contrast to the predeposition process, the initial impurity layer has a certain fixed dose S expressed in atoms/cm^2. As the dose is not constant over time, the dopant profile follows a Gaussian distribution according to equation 2.10.17 [88].

$$N(x,t) = \frac{S}{\sqrt{\pi Dt}}\text{e}^{-\frac{x^2}{4Dt}} \tag{2.10.17}$$

The first boundary condition is similar to the predeposition case, i.e. $N(\infty,t) = 0$. Another boundary condition is that the concentration at the surface is constant. From this it follows that the surface concentration $N(0,t)$ is equal to 2.10.18.

$$N(0,t) = \frac{S}{\sqrt{\pi Dt}} \tag{2.10.18}$$

Using this boundary condition, the junction depth x_j is defined in equation 2.10.19.

$$x_j = 2\sqrt{Dt} \times \left(\ln\frac{S}{\sqrt{\pi Dt}N_b}\right)^{1/2} = 2\sqrt{Dt} \times \left(\ln\frac{N(0,t)}{N_b}\right)^{1/2} \tag{2.10.19}$$

The maximum gradient, and thus largest internal electric field, can be obtained by differentiating equation 2.10.17. This yields equation 2.10.20

$$\frac{dN(x,t)}{dt} = -\frac{x}{2Dt}N(x,t) \tag{2.10.20}$$

Using this equation yields the maximum gradient at position $x = \sqrt{2Dt}$.

Chapter 3

Experimental method

This chapter discusses the experimental methods used to prepare the battery setup, discharge the battery, measure and quantify the corrosion, and analyze the silicon samples afterwards. First, the experimental enivironment will be discussed in section 3.1. The preparation of the silicon anode before being oxidized is explained in section 3.2. As in this work nonuniform doping is introduced in the silicon anode, section 3.3 will explain the methods used to achieve the dopant profile. The air cathode will be discussed in section 3.4 and the electrolyte in section 3.5. These parts are combined in the cell design described in section 3.6. With the finished setup, measuring and characterizing the performance of the battery is explained in section 3.7. This includes the galvanostatic discharge, mass consumption, step height, surface inspection and dopant profile analysis methods.

3.1 Experimental environment

Experiments in this work are executed in a cleanroom environment inside the Else Kooi Laboratory at Delft University of Technology. This means that the temperature, humidity and number of particles are controlled to reduce the contamination and allow for processing semiconductor materials with very high precision. The quality of the cleanroom is indicated by the number of particles with a size of 0.5 μm or larger per cubic foot of air. The available classes at EKL are Class 100 (CR100) and Class 10000, meaning only 100 and 10000 particles per cubic foot of air respectively. These cleanroom classes fulfill ISO standard 5 (CR100) and 7 (CR10000) [112].

The cleanroom environment allows for the experiments to be conducted under very consistent circumstances with as little external influences as possible. The temperature inside the cleanroom is regulated at 21$\pm$2 °C and the humidity level at 48$\pm$5%. Besides, working with the needed chemicals inside the cleanrooms can be done in dedicated wet benches that reduce the risk of spillage or other unsafe situations.

3.2 Uniformly doped silicon anode

As explained in section 2.2, the anode material of the battery is silicon (Si). More specific, in this work four inch (100 mm) mono-crystalline silicon wafers, also referred to as c-Si, are used. Mono-crystalline wafers have a continuous crystal structure without any grain boundaries. This can be observed in the very uniformly colored surface [70].

Dopant atoms are introduced in the material to increase the conductivity, as was explained in section 2.9.1. There are two types of doped Si, n-type and p-type, with either more donors or acceptors respectively. Available dopant atoms in EKL are phosphorus (P) for n-type and boron (B) for p-type. Using undoped Si is not very attractive due to the low electronic conductivity. The resistivity of a wafer is given in Ωcm and can be used to determine the dopant level using equation 2.9.1. The resistivities of the used wafers are 1-5 Ωcm for both n and p-type Si and >1000 Ωcm for p-type Si. Based on findings in literature by Ein-Eli et al. and Durmus et al. [42][52], n-type Si showed higher discharge potentials than p-type, but is affected more severely

by corrosion in RTIL electrolytes. A direct comparison of corrosion rates of p-type and n-type in alkaline electrolytes has not yet been made. Both types of Si wafers will therefore be used to compare the effects of corrosion. For p-type Si also a higher resistivity wafer is used, which means that there are more free electrons available in the material compared to a low resistivity p-type wafer. In addition to that, using wafers with a lower dopant concentration means that the formation speed of a passivating layer is decreased [57].

The thickness of the Si anode has an effect on how long the battery can be discharged, as the silicon is actively being consumed. The thicknesses of the processing wafers at EKL are 500-525 $\pm$10-15 μm. Wafers used in solar cells are often thinner as the thickness of the absorber layer should not exceed the diffusion length of minority carriers by much [70]. This limits the thickness to 220-300 μm. In this work, the discharge time of the battery should ideally be as long as possible. Therefore, the thicker processing wafers are used instead of the thinner solar cell wafers.

Different crystal orientations are available within EKL, which include the <100> and <111> for both n and p-type Si. These wafers can be recognized by specific cuts at the bottom or side under certain angles. The different orientations are visualized in figure 3.1. As indicated by the paper of Durmus et al. [44], discharging Si-air batteries using <111> wafers proved difficulties as the current densities that could be achieved were significantly lower even though the active surface area was increased. Therefore, using <100> wafers are preferred.

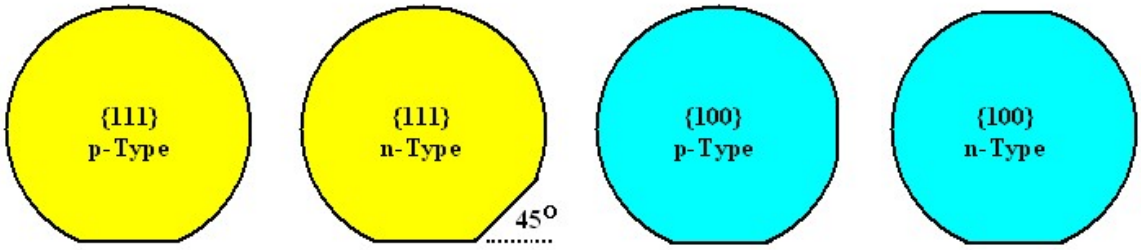

Figure 3.1: Different oriented c-Si wafers available for use as an anode material. The wafer orientation can be recognized by the wafer flats. Figure taken from [113].

With a chosen Si wafer as starting material, the next step is to process the wafer into samples that fit into the battery setup. The exact parameters of the used Si wafers are listed in appendix A.1.

3.2.1 Wafer preparation

Before any processing step can be performed on a new silicon wafer, it has to be cleaned from any dust or other unwanted particles using HNO_3 in several steps. This process happens in the cleaning line in the CR100. Besides, silicon is a material of which the surface oxidizes when exposed to air for ambient conditions, i.e. at room temperature and normal pressure [114]. This means that a layer of SiO_x, with $x \leq 2$, is formed at the surfaces of a wafer, also known as the native oxide formation. The formation of SiO_x is a self-limiting process, since the layer growth converges to a thickness up to 2.1 nm in several hours, but this process happens immediately upon exposure to air [115]. The layer of SiO_x affects the performance of silicon used as electrodes in a negative way, as it increases the impedance and acts as a sort of insulator [116]. Therefore, it is key to remove this native oxide layer when silicon wafers are further processed with layers that require a low contact resistance. A common way to do this is by performing an hydrofluoric-acid (HF) dip with the Marangoni setup in the CR100 [117]. The cleaning process is described in detail in Appendix A.2 and is the same for both n and p-type Si.

3.2.2 Back-contact deposition

With the silicon surface cleaned and free from SiO_2, the next step is to apply a metal back-contact that functions as a current collector. This further improves the performance of the battery cell. An Al back contact is often used as it enables a low contact-resistivity [118]. In fact, an Al:Si alloy containing 1% Si is used. This prevents the formation of spikes into the silicon, as this would happen for pure Al. It is key to handle fast as the native oxide starts to grow once the wafer is exposed to air again. A 675 nm thick Al:Si layer is deposited at elevated temperatures of 350 ° C on the clean silicon wafer using the principle of sputtering. This happens in the Trikon Sigma 204 dealer inside the CR100. Sputtering is a form of Physical Vapor Deposition (PVD) where material is ejected from a target material and transported to the desired surface, in a vacuum. The released target atoms then travel to the wafer and eventually hit the wafer surface and form a thin film on top of the silicon wafer [88].

The Trikon Sigma has several target materials available in different chambers to deposit on wafers and is placed in the plasma etch corridor of the CR100. The 99% Al/1% Si is a standard target in the EKL CR100 and is therefore always available while other targets might fluctuate in availability. The Trikon Sigma can handle up to two wafer boxes simultaneously containing 25 wafers each and is therefore suitable for large scale back-contact processing. The steps and recipes used for the deposition using Trikon Sigma are listed in Appendix A.3.

As explained in section 2.5, when a semiconductor and a metal make contact, the charge carriers can be blocked by a barrier to move from the semiconductor to the metal. Ideally, the contact should be an Ohmic contact which has a low contact resistance and allows current to flow in both directions, unlike a Schottky barrier that is rectifying. As the doping level is not considered high, tunnelling of charge carriers is not possible.

For both n-type and p-type Si, the barrier height can be calculated with the Al:Si alloy back contact, based on equation 2.5.2. For n-type Si the barrier height is calculated in equation 3.2.1. The electron affinity of Si is 4.01 eV, while the work function of Al is 4.28 eV [69]. For the scope of this work, it is assumed that the work function of Al is equal to the work function of Al:Si.

$$\begin{aligned} q\phi_{Bn} &= q(\phi_m - \chi) \\ &= 4.28 - 4.01 = 0.27\ eV \end{aligned} \tag{3.2.1}$$

The Al-Si contact results in a barrier ϕ_{Bn} of 0.27 eV, which is fairly low. A lower barrier can be achieved by choosing a material with a lower work function, such as indium or manganese [119]. These materials were, however, not available for deposition and are also less abundant than the metal Al [51].

For p-type Si it should hold that the work function of the metal has to be larger than that of the semiconductor, i.e. $\phi_m > \phi_{s,p}$, to have an Ohmic contact. The barrier height for Al can be calculated by using equation 3.2.2 [70]. A metal with a large work function provides a more Ohmic contact.

$$\begin{aligned} q\phi_{Bp} &= E_G - q(\phi_m - \chi) \\ &= 1.12 - (4.28 - 4.01) = 0.85\ eV \end{aligned} \tag{3.2.2}$$

The barrier height for the p-type wafers is fairly high at 0.85 eV and can be lowered by changing to a metal with a higher work function, such as Gold or Platinum, but these metals are expensive.

3.2.3 Laser cutter

After the wafer has been processed with a metal back-contact, the wafer can be cut into smaller square samples that fit inside the battery cell setup. As a <100> oriented wafer is used, the cut lines have to align with the crystal, i.e. an angle of 0° or 90° with the primary flat. If a different angle is used the wafer will break in small random pieces. Making square samples is therefore the most straightforward option. In previous studies using the same setup the samples were cut

in 20 mm by 20 mm squares [64]. This allows for sufficient room around the active surface area of 1 cm^2 in contact with the electrolyte. An O-ring makes sure that the setup does not leak. A total of eleven samples can be cut from a single 100 mm Si wafer, as indicated in the patterns in figure 3.2. How the cut samples eventually align with the opening is shown in figure 3.3.

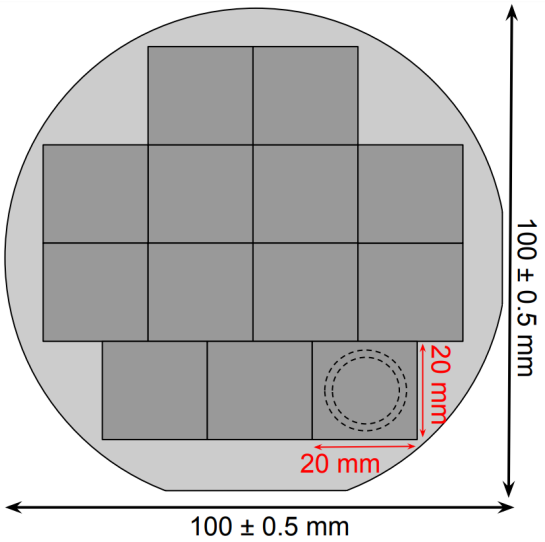

Figure 3.2: A single wafer can be cut into eleven equally sized samples of 20 by 20 mm. The dotted lines indicate the active surface area of 1 cm^2 including a sealing O-ring.

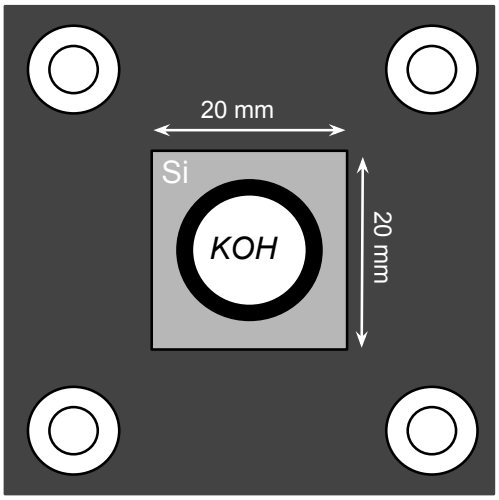

Figure 3.3: The cell setup on the anode site with the Si sample of 20 by 20 mm in place. The black O-ring ensures a proper seal with the active surface area and electrolyte.

A powerful 20 W laser is used to design and cut the pattern on the wafer's front or back side, after which the wafer can be broken manually in the samples. The laser will need to scribe multiple times over each line to be able to break the wafer. This will cause defects at the edges of the sample, but the edges can be disregarded in the battery setup as the active area lies in the middle of the sample. The full steps of the laser cutter are indicated in Appendix A.7. To make a distinction between different samples, a diamond pen is used to scribe sample numbers and batches on the back side of the sample.

3.3 Nonuniformly doped silicon anode

Based on the model of Durmus et al. [44], a suggested solution to the corrosion mechanism in alkaline Si-air batteries is to direct the generated electrons in the oxidation reaction to the current collector instead of reacting with the water molecules in the electrolyte. The electrons can be directed to the current collector by implementing a dopant profile in the Si anode.

The most often used techniques to create a dopant profile are mainly by ion implantation or by diffusion. Because the implanter at EKL is no longer available for ion-implantation, the diffusion process as explained in section 2.10.2 will be used to create a doping profile.

In the following subsections, the steps taken to create a nonuniformly doped Si wafer are discussed. In subsection 3.3.1, plasma enhanced chemical vapour deposition (PECVD) will be explained and also how it is used. A similar process is performed by using epitaxial growth, which is explained in section 3.3.2. Next, the drive-in process will be explained in subsection 3.3.3. After the drive-in process, the emerged oxide layer has to be removed. This process is explained in subsection 3.3.4. Finally, a different technique than sputtering will be used to deposit the back-contact on the Si samples. This is explained in subsection 3.3.5.

3.3.1 PECVD

A thin impurity layer is deposited on top of the c-Si wafer to function as a source layer for the drive-in process, as explained in subsection 2.10.2. Chemical Vapour Deposition (CVD) is used to produce a solid, high concentration, uniform, good adhesive impurity layer on top of the c-Si. A specific type of CVD is used, namely Plasma Enhanced CVD (PECVD), as it is a widely applied technique used for depositing very uniform thin layers on solar cells at low temperatures around 200 °C [88]. Deposited materials are, for instance, amorphous silicon or microcrystalline silicon.

In PECVD, controlled amounts, expressed in standard cubic centimeters per minute (sccm), of reacting gases, including dopant gases such as diborane (B_2H_6) or phoshpine (PH_3), are admitted to a high vacuum through a reaction chamber where the c-Si wafer is mounted on a heated grounded electrode. A RF electrode is mounted parallel to the c-Si wafer, forming a capacitive coupling between the two electrodes. An oscillating electric field is used to create a plasma of the reacting gases that are deposited as a solid layer on top of the c-Si [70]. The main benefit of PECVD with respect tot conventional CVD is that lower substrate temperatures can be used. The plasma provides the energy for the reaction, meaning that temperatures can be kept low. The reaction chamber of PECVD is depicted in figure 3.4. The composition of gases, reaction temperature, pressure and RF power determine the quality of the layer. The thickness of a layer can be increased by extending the time the plasma is active, as the growth rate of the layer will be fairly constant.

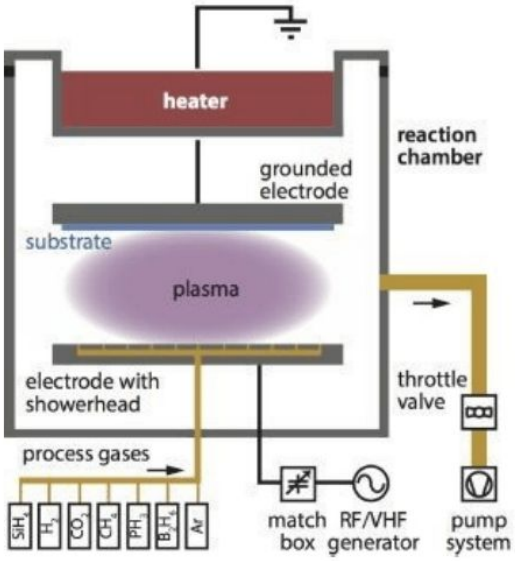

Figure 3.4: A PECVD reactor. The reacting gases are excited by an oscillating electric field to a plasma and deposit as a solid layer on top of the c-Si wafer (substrate). Figure taken from [70].

Doped hydrogenated amorphous silicon (a-Si:H) is used to deposit as an impurity layer on top of the c-Si wafer. The PECVD system used for this work, AMOR, was built by Elettrorava. This device is capable of depositing intrinsic, n-type and p-type a-Si:H in dedicated reactor chambers. In this work, both n-type and p-type a-Si:H layers will be deposited. a-Si:H crystallizes to poly-crystalline Si (poly-Si) when it is heated above 700 °C for at least four minutes [120]. This process is called rapid thermal annealing (RTA). Poly-Si is not as ordered as monocrystalline Si, but dopant atoms can move easier through the disorderded poly-Si than the defect-rich amorphous Si. Thus, a poly-si layer can still provide sufficient electron mobility.

The deposited layer needs a certain dose S in atoms/cm^2 for the impurities atoms to travel deep into the c-Si. The concentration at the surface decreases over time as the impurity atoms are not constantly being refreshed. The reacting gas compositions are based on earlier depositions done with the AMOR by other researchers. In these earlier experiments, 10 nm thick layers with B and P concentrations of 10^{21} atoms/cm^3 were achieved. These recipes were used as a basis in

the depositions performed on the wafers in this work. A 50 nm thick layer of p-type and n-type a-Si:H is deposited by extending the deposition time of the 10 nm layer with a factor five. A 50 nm layer with a concentration of 10^{21} atoms/cm^3 yields a dose $S = 5 \times 10^{15}$ atoms/cm^2, a common dose used in ion-implantations which should be sufficient to drive-in the impurity atoms [121]. The gas flow rates, recipes and further experimental settings of the AMOR are listed in Appendix A.5.

3.3.2 Epitaxy

Epitaxy, or epitaxial growth, is another CVD method used to grow thin layers on top of a substrate with a crystal structure that is perfectly aligned with the crystal of the substrate. Epitaxy is derived from the greek word *epi* meaning "above" and the word *taxis* meaning "in an ordered manner". The epitaxy process allows to continue to build the same crystallographic orientation of the substrate on top of it. The substrate will act as a seed for the further deposition.

Epitaxy is performed in a quartz reactor chamber that is heated through powerful lamps. This means that it is a cold-wall reactor. Only the wafer is directly heated, such that the deposition only takes place on the substrate. Reaction gases enter the chamber from one side only and are forced laminar along the substrate in the longitudinal direction, while diffusing transversal. The substrate holder rotates during deposition to create a uniform thickness. The ASM Epsilon 2000 is available at EKL to perform epitaxial growth.

Epitaxy will be used in this work to deposit a thin layer of pure B on top of c-Si by using the gas diborane (B_2H_6). The B_2H_6 decomposes into borane (BH_3) due to the high operating temperatures at the substrate. BH_3 is highly reactive and is used to grow an amorphous boron (a-B) layer [122]. First, a monolayer of a-B is deposited on Si according to reaction 3.3.1.

$$BH_3 + Si \rightarrow H_2B\text{-}Si + H \tag{3.3.1}$$

After this, the BH_3 keeps depositing on a-B, indicated in reaction 3.3.2.

$$BH_3 + B \rightarrow H_2B\text{-}B + H \tag{3.3.2}$$

Defects on the Si substrate, such as metal impurities and native oxides, can destroy the epitaxial growth as it is such a delicate process. Therefore, the Si surface should ideally be very clean and dipped in HF to remove any SiO_2 just before being placed inside the load lock. The HF H-terminates the Si surface atoms, which requires more energy to break these bonds than with unsaturated surface atoms. To break these bonds, temperatures between 400-700 °C are required. At lower temperatures the a-B will grow nonuniformly over the surface, as the H-Si bond is not desorpted. At higher temperatures, B will diffuse into the Si and the a-B layer is depleted.

The deposited pure B has a concentration of roughly 1.3×10^{23} atoms/cm^3. As the deposited layers can not be much thicker than at most 10 nanometers, the dose S of the layers is roughly 1.3×10^{17} atoms/cm^2, almost two order of magnitude larger than with PECVD. To protect the very thin B layer and to allow all B to diffuse inside the Si, a high B-doped Si layer is deposited on top of the a-B layer that functions as an encapsulation layer. On top of this B-doped Si layer, another, but thinner, layer of pure B is deposited. Operating the ASM Epsilon 2000 requires thorough training. For the scope of this work, the process steps on this tool are performed by a trained technician of EKL.

3.3.3 Drive-in process

When the thin layer with a high impurity concentration is deposited on the c-Si wafer, the next step is to drive-in the impurity atoms deep into the wafer. Based on equation 2.10.19, the variables are the temperature T inside the diffusion coefficient, the dose S, dopant concentration in the uniform part of the wafer, i.e. background concentration, N_b and the diffusion time t. Based on these variables, the desired dopant profile can be simulated. These simulations will be performed by using Excel and Matlab.

The dose for the PECVD grown a-Si:H layers was set at 5×10^{15} atoms/cm^2 and the dopant concentration of the used wafers varies between roughly 1×10^{13} atoms/cm^3 for p-type and 3×10^{15} atoms/cm^3 for n-type, based on the resistivity levels indicated on the wafer boxes, see A.1. For the epitaxially grown layers, as was explained in the previous subsection, the dose is significantly higher at 1.3×10^{17} B atoms/cm^2.

Based on the theory explained in section 2.10.2, increasing the temperature will have a large effect on the diffusion coefficient as it scales exponentially. Therefore, using a high temperature will result in a large junction depth.

A furnace is needed that is capable of maintaining a high temperature for long periods. Within the cleanroom facilities of EKL this is not possible. Therefore, a tube furnace at the Reactor Institute Delft (RID) was used. This specific furnace is capable of reaching a temperature of 1600 °C for several days continuously, while actively being cooled at the outside, as depicted in figure 3.5. The tube has a diameter of 105 mm and thus fits a four inch wafer (100±0.5mm). The wafers are placed with the deposited layer upwards on a ceramic holder that slides in the tube. An additional sub-prime wafer is placed between the ceramic holder and the wafer of interest to prevent any contamination diffusing through from the back side. This is shown in figure 3.6. The furnace is attached to a vacuum turbo-pump to remove any oxygen left in the tube before the furnace is switched on to reach the desired temperature. During operation, the furnace is flushed with the inert gas nitrogen (N_2) to prevent the growth of a thermal oxide.

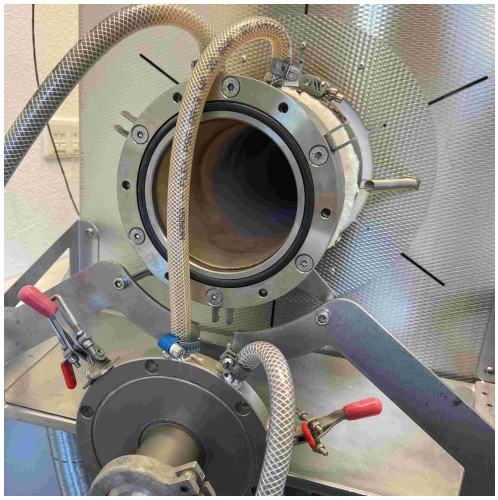

Figure 3.5: The load lock of the tube furnace used for the drive-in process. The furnace can be flushed with N_2 during operation and the load lock is liquid cooled.

Figure 3.6: A four inch wafer fits in the load-lock. A protective wafer is placed on the bottom to prevent any residue material from the white ceramic to diffuse through.

The furnace can ramp its temperature up and down at a rate of 3 °C/min. At this rate, the hydrogen present in the a-Si can diffuse out gradually [123].

3.3.4 Thermal oxide

During the drive-in process the furnace is flushed with the inert gas N_2 to prevent the formation of a thermal oxide. However, there is a possibility of oxygen to leak through. This leakage can occur if the flush rate drops over time and oxygen from the ambient air enters the furnace through the seals. If this happens at elevated temperatures as low as 150 °C, the Si on both sides of the wafer will react with the oxygen to form silicon-oxide (SiO_x, $x \leq 2$), called a dry thermal oxide layer [124]. The higher the temperature at which this happens, the faster the oxide layer grows and the thicker the oxide layer will become. SiO_2 creates a passivating layer on the Si surface that prevents the dissolution of the reaction product $Si(OH)_4$ and stops the discharge in the Si-air battery. Besides, SiO_2 is a very good insulator with a high resistivity. An insulating layer will prevent an Ohmic contact between the back-contact and the Si [125]. This layer thus

has to be removed before the nonuniformly doped wafer can be further processed.

During a possible thermal oxidation in the presence of oxygen, the impurity atoms, such as B and P, are redistributed within the Si [126]. A redistribution of impurity atoms occurs when two solids are directly contacted. The impurities redistribute until the chemical potential at the interface is equal. In other words, an interface is created when Si is oxidized, i.e. Si-SiO_x, and the growth of SiO_x is directed into the Si as the oxidation continues. The impurities inside the Si are then redistributed. The redistribution of impurity atoms can also occur after the diffusion of a two-layer structure with different impurity concentrations [127].

In general, when an oxidizing atmosphere is used that is free of impurities, the impurities have an inclination to escape the oxide. This escape affects the impurity concentration in the Si. There are two scenarios possible for the redistribution of the impurity atoms, which depends on the segregation coefficient. This coefficient expresses the ratio between the impurity concentration in the Si and the impurity concentration in the oxide. In scenario 1, the segregation coefficient is smaller than one, indicating that the oxide is taking up the impurity atoms and depleting it from the Si. In scenario 2, the segregation coefficient is larger than one. This indicates that the oxide repels the impurity atoms. However, if the impurity diffuses fast, it might be possible that the impurity atoms escape through the oxide layer. The impurity atom B depletes fast in the oxide during oxidation, while P atoms are repelled and pile up. The depletion effect is often more pronounced than the pile up and thus B-doped impurity layers are affected more [126].

The thickness of the oxide layer can be estimated using the Deal-Grove model [128]. In this model it is assumed that the oxidation takes place at the interface of the oxide and substrate. The oxidation layer moves into the Si instead of growing on the surface. The thickness X of the oxide layer grows in a process time t on a bare Si surface following the relation in equation 3.3.3.

$$t = \frac{X^2}{B_0} + \frac{X}{(\frac{B}{A})_0} \tag{3.3.3}$$

The linear rate constant $(B/A)_0$ and parabolic rate constant B_0 are determined through the conditions during the oxidation process, including temperature, crystal orientation and environment (wet or dry). The analytical determination of the thermal oxide thickness on the wafer lies outside the scope of this work. Instead, a visual inspection is performed when the wafers are removed from the furnace.

The color of the oxide layer SiO_2 depends on the thickness, incident angle of light and luminance of the light that shines on the surface. For each oxide thickness up to 1 μm, the color is indicated in figure 3.7. In this figure, the incident angle θ is 0°.

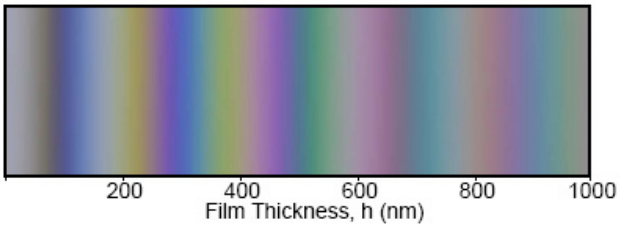

Figure 3.7: The apparent color of SiO_2 as a function of the thickness for a viewing angle of $\theta = 0°$. This scale can be used to determine how thick the oxide layer is. Figure taken from [129].

SiO_x layers can be removed by putting the wafer inside hydrofluoric acid (HF). HF has an infinite selectivity for etching Si and leaves the bare Si surface H-terminated [88]. This means Si becomes hydrophobic until the native oxide starts to grow again. The thin native oxide layer on Si can best be removed with a diluted 0.55% HF-solution at room temperature, while thicker thermal oxide layers should be removed by using a buffered HF solution (BHF) as this etches faster. The BHF allows the etch rate to remain constant throughout the etching [130].

The color shift on the wafer should be checked throughout the etching process to determine which thickness can be expected. After leaving the wafer long enough in the etching solution, the color returns to the greyish color of Si. This means that the entire oxide layer is removed.

BHF with a 1:7 composition, 1 part HF and 7 parts buffer fluid (NH_4F), etches SiO_x at a rate of 74-80 nm/min [130].

3.3.5 Back-contact deposition

After the oxide layer has been removed from both the front and back side of the wafer, the back-contact can be deposited. Due to contamination issues, the Trikon Sigma cannot be used to deposit Al:Si (99:1%) as was done for the uniformly doped wafers. The reaction chambers of the Trikon Sigma have to remain free from any unknown particles that may come from outside the cleanroom. As the tube furnace at RID does not fulfill any cleanroom standards, a different method of applying a back-contact is performed.

Depositing thin metal films can also be done with evaporation, a form of PVD. Materials that are heated in a vacuum will evaporate. The vapor travels in in the line-of-sight to a substrate. When the vapor hits the substrate, it deposits into a solid. The lower the vacuum pressure, the better the quality of the deposited film. Electron beam evaporation, often referred to as Electron Beam PVD (EBPVD), is such an evaporation technique [125].

In EBPVD electrons are thermally emitted from a filament. A magnetic field bends the electrons by 270° to prevent any contamination of the filament on the source material. The electrons bombard the surface and the deposition material's atom transform into the gas phase to evaporate on the substrate. The wafer is mounted on a carousel that rotates at a fixed rate to allow a uniform material deposition. The thickness of the deposited layer is measured with a quartz crystal. Deposition rates are chosen between 0.2-1 nm/s. The EBPVD process is illustrated in figure 3.8. The Provac Pro500S is used to deposit materials in the CR10000. In Appendix A.4 full steps and settings are indicated.

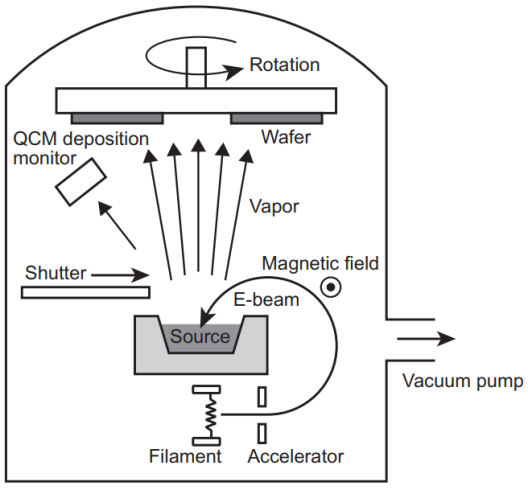

Figure 3.8: A schematic overview of the EBPVD process. Electrons are thermally excited and hit the source material which evaporates. The vapor hits the substrate (wafer). Figure taken from [125].

Available deposition materials in the EBPVD device are titanium (Ti), chromium (Cr), Al, magnesium fluoride (MgF_2) and silver (Ag). A downside of the used Al in the Trikon Sigma is that it etches very fast in highly concentrated KOH [131]. This issue can be resolved by first depositing a layer of Al and secondly a Cr layer that protects the Al from KOH. Cr is barely etched by KOH. A common issue in evaporation methods is that internal stresses can emerge as the thermal expansion coefficient of Si and the deposited material differ. In some cases this can lead to bending of the wafer or peeloff of the deposited layer [125]. This can be mitigated by depositing only relatively thin layers of several hundred nanometers. Especially Cr-layers are prone to peeling off and should therefore be thin. Besides, Cr-layers do not stick well to Si. Thus a layer of Al is deposited in between, as illustrated in figure 3.9. The Al layer has a thickness of 500 nm, while the Cr layer has a thickness of just 50 nm to prevent too much build up of stress in the layers.

Figure 3.9: A schematic plot showing the deposited layers using EBPVD as a back-contact. The top Cr layer protects the Al from being etched by KOH.

3.4 Air cathode

As explained in section 2.2, the cathode in Si-air batteries consists of a porous air electrode that is reduced on discharging of the battery by letting oxygen from the outside air diffuse through it. The air electrode consists of an activated carbon structure combined with a hydrophobic poly-tetrafluoroethylene (PTFE) binding powder. This is pressed on a nickel 200 mesh for structural integrity [40]. A MnO_2 transition-metal catalyst increases the reaction efficiency.

Cutting the air electrode into the required size does not require a laser cutter, but can be done with regular scissors. To create a proper seal with the battery cell setup the air cathode is cut slightly larger than the Si anode, roughly in squares of 25 mm.

The air electrode is provided by the company Electric Fuel and is shipped on a roll, as shown in figure 3.10 [132]. This specific air electrode has been used in other research papers that studied Si-air batteries as well [40][42][43][44][52]. The reference voltage for the air electrode in the alkaline electrolyte KOH is given in figure 3.11.

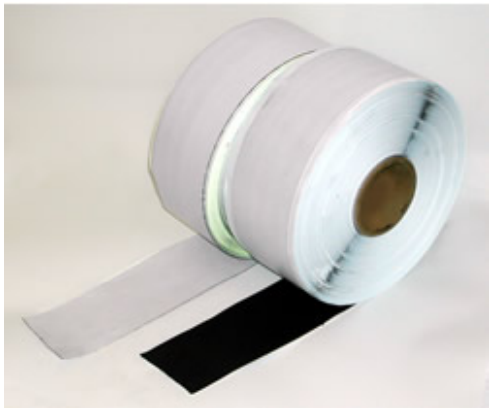

Figure 3.10: The air electrode is shipped on a roll. The material can be cut with scissors. Figure taken from [132].

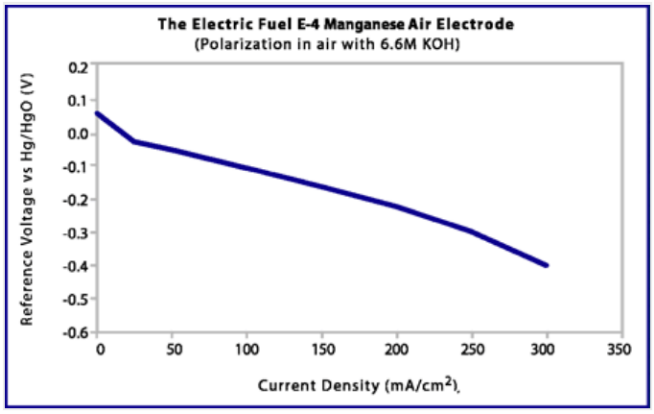

Figure 3.11: The reference voltage of the air electrode as a function of discharge current density in KOH. Figure taken from [132].

What is interesting to note from figure 3.11 is that the electrode potential mentioned in equation 2.4.6, i.e. 0.4 V, is only achieved for current densities of 300 mA/cm^2, while the current densities applied by Durmus et al. using alkaline electrolytes had a maximum of 70 μA/cm^2. This means that the open circuit potential (OCP) of the battery is lowered by roughly 0.4 V because of the air cathode.

In the work of Prins [64], the effect of wetting the air cathode before discharging was studied to optimize the discharge performance. This pre-wetting was also used in the first experiments of this work, but resulted in mixed outcomes. Therefore, in the rest of the experiments, a one hour OCP period was used to achieve a stable discharge. The measurement procedure will be discussed in more detail in section 3.7.1.

3.5 KOH electrolyte

The used electrolytes in Si-air batteries can have differnt compositions. In the experimens of this work the aqueous alkaline electrolyte KOH will be used, because its allows for safer and easier chemical handling, is considerably cheaper than the non-aqueous electrolytes and has the highest maximum ionic conductivity of 0.6 S/cm. A downside of KOH is, however, that it etches, or corrodes, silicon quite fast and strongly.

To have an electrolyte with the highest conductivity, as was shown in figure 2.35, the concentration has to be in the order of 5-7 mol/liter. This corresponds the closest to a KOH mass-percentage of 30%, as is used often in fast anisotropic etching Si [88]. At this concentration level Si etches the fastest, as was observed in figure 2.36 and can be observed in figure 3.13 as a function of temperature. The experiments are conducted at room temperature, corresponding to an etch rate of ca. 3 μm/hour. The high ionic conductivity comes at a trade-off of high corrosion. This allows for a good quantification of the corrosion reaction and to observe the clearest effect of any corrosion mitigation.

A sufficient volume of pre-made solution of 30% KOH, i.e. 6.6M [133], was available in the cleanrooms of EKL, allowing each experiment to be conducted with a new volume of electrolye that has the exact same composition of elements. This specific 5 liter container, UN1814 made by Fischer Chemicals, can be observed in figure 3.12. Another option is to dissolve an exact mass KOH pellets in Deionized (DI) water to achieve the desired concentration of 30%. The work of Prins has used the pre-made KOH electrolyte while other students used the pallets. Thus far, Prins was the only student that reached discharge times of several days using the pre-made electrolyte. Therefore, it is chosen to use this pre-made electrolyte in this work as well.

Figure 3.12: A pre-made container with 30% KOH providing the highest conductivity.

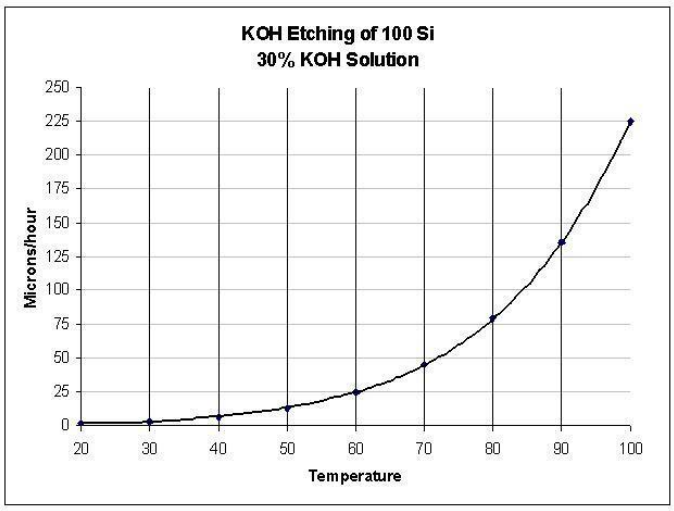

Figure 3.13: Etching speeds of 30% KOH as a function of temperature. The experiments are conducted at room temperature, corresponding to an etch rate of ca. 3 μm/hour. Data taken from [100].

3.6 Cell design

The anode, cathode and electrolyte are combined within one cell structure such that it can be assembled and disassembled fast and straightforwardly. There are multiple identical setups available, such that separate experiments can be conducted simultaneously. The cell was designed at Delft University of Technology and consists of three parts that are sealed together by O-rings. Both electrodes are connected with each other through the electrolyte and the external circuit. The parts of the cell setup will be discussed in more detail in subsection 3.6.1.

3.6.1 3D battery parts

The Si anode and air cathode are connected to an identical square Teflon holder of 50 by 50 mm and 16 mm thick, shown in figure 3.14. This holder holds a cable exiting at the top connected to the external circuit. Both electrodes connect through a spring current collector to the cable. The air cathode relies on diffusion of oxygen from the outside air. This means that the holder should have an opening to function as the oxygen inlet. Both electrodes connect to a different middle Teflon holder of 50 by 50 mm and 20 mm thick, shown in figure 3.15.

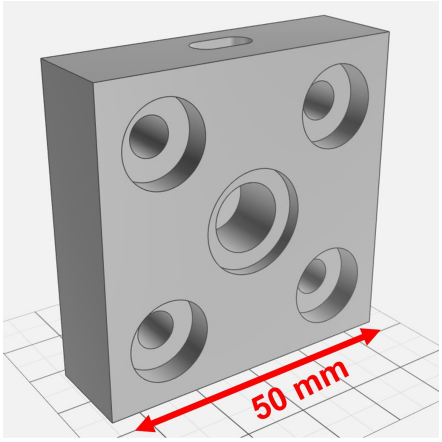

Figure 3.14: Teflon holder connecting to the electrodes in the center. A cable with current collector is fed through from the top to make contact with the electrode.

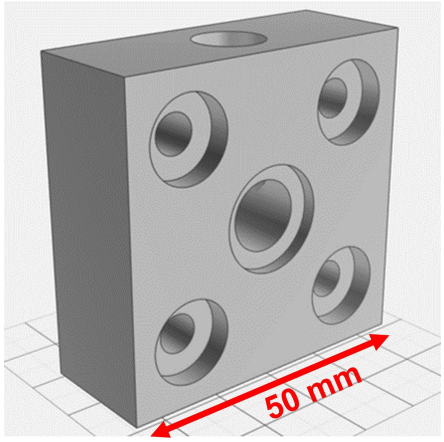

Figure 3.15: Middle Teflon holder that connects both electrodes with the electrolyte that is poured in from the top. The active surface area of the electrodes is 1 cm^2.

In the middle holder the electrolyte is poured in from the top. The opening in the middle has a surface area of 1 cm^2 and a length of 20 mm, giving an electrolyte volume of 2 ml in the horizontal part. There is also a cylinder part at the top with roughly the same volume. This gives the electrolyte a total volume of 4 ml. At both ends O-rings ensure a seal to prevent leakage.

In contrast to other experimental setups, the volume of the electrolyte is deliberately chosen to be larger. The volume in this setup is in total an estimated 4 ml, compared to 0.5 ml in the papers of Durmus et al. and Ein-Eli et al. [40][42][43][44][52]. This larger electrolyte volume allows the limiting effect on the discharge performance caused by the build up of reaction products to be delayed, as the solution will be saturated with reaction product at a much later stage. Besides, the reaction product $Si(OH)_4$ can continue dissolving into the electrolyte. The effect of the larger volume on the conductivity of the electrolyte can be determined by calculating the overpotential it creates. This can be calculated using equation 3.6.1, where j is the applied current density in A/cm^2, l the length of the volume in cm and σ the conductivity of the electrolyte in $1/\Omega cm$.

$$\eta = \frac{jl}{\sigma} \tag{3.6.1}$$

Using this equation yields an overpotenial of just 0.17 mV at an applied current density of 50 $\mu A/cm^2$. This means an expected decrease in discharge voltage, i.e. ca 1.2 V, of just 0.014%.

When the three separate holders are connected, nylon bolts and solid nylon wires can be screwed tightly at the four corners to ensure a proper seal. The connected cell is shown in figure 3.16.

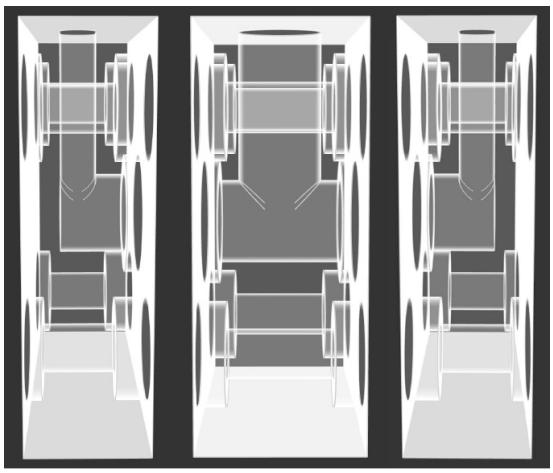

Figure 3.16: The layout of the battery cell when all the parts are connected. The electrolyte is poured in from the top. Figure taken from [64].

3.6.2 Initial setup

Unfortunately, the setup quickly appeared to be a large uncertainty in the measurements for several reasons. The material Si is a strong but brittle material. When placing the Si sample on the O-ring and attaching the back side resulted in breaking the Si sample if screwed together too tightly, as can be seen in figure 3.17. It turned out to be difficult to determine the correct torque such that the sample does not break but also prevent the setup from leaking. A quick solution turned out to be to remove the large O-ring at the electrolyte side. A smaller O-ring at this side provides a sufficient seal.

A more significant issue was the spring current collectors that connected to the air cathode and Si anode. These springs were not fixed, but laid loose inside the holder. This resulted in some misalignment of the electrical contact when put together. Moreover, some of these springs and cables were the original ones from the first discharges performed by Prins [64], which led to a build-up of solid KOH around the contact interfaces. When measuring the contact resistance between the front of the current collector and the end of the cable connected to it, values of 10 kΩ were measured. This would result in a significant voltage drop of $\eta = iR = 0.5$V at 50 μA/cm^2. Redesigning the electrical contact interfaces is needed to improve the battery's performance.

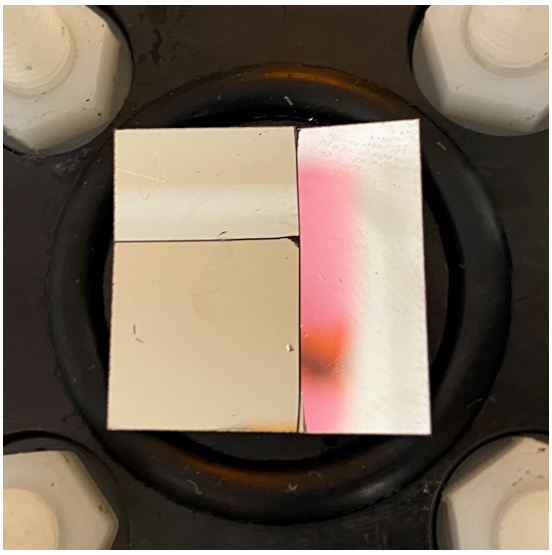

Figure 3.17: Si samples tend to break through an uneven pressure distribution. The large O-ring should be removed.

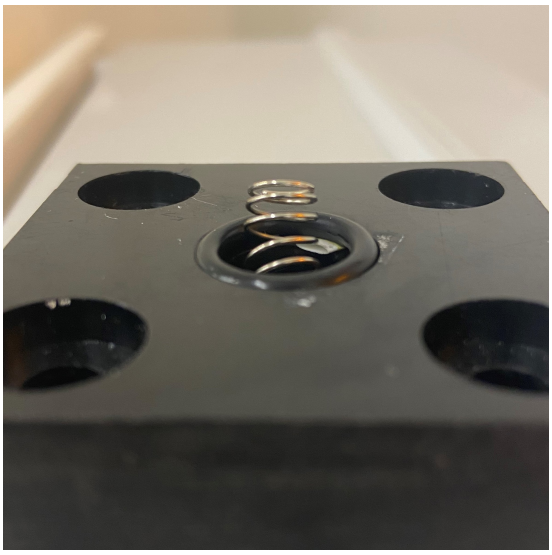

Figure 3.18: The spring moves in all directions when applied at the back side. Besides, resistances of 100 kΩ were measured here.

3.6.3 Improved setup

The issues regarding the original setup were studied and solved by the following steps. First, the big O-ring was removed to prevent the samples from breaking. This also allowed the samples to be cut into smaller sizes than the original 20 by 20 mm. After several attempts, a sample size of 16 by 16 mm was found large enough to fit over the O-ring without leaking. With the decreased sample size it is possible to extract a maximum of 22 samples from one wafer, an increase of 100% with respect to the previous dimensions. The design is shown in figure 3.19.

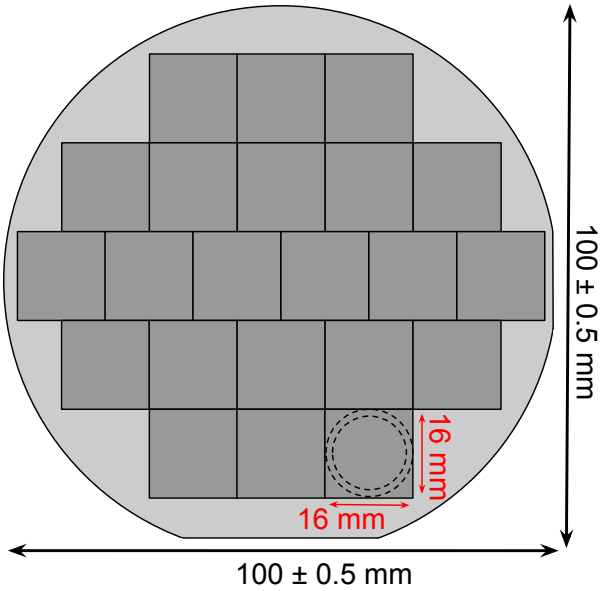

Figure 3.19: After decreasing the sample size, a single wafer can now be cut into 22 equally sized samples of 16 by 16 mm instead of 11.

Secondly, the unstable electrodes were replaced by a solid printed circuit board (PCB) that was gold plated at both sides. To allow the oxygen from the air to diffuse through the electrode, it is perforated with a large number of holes without sacrificing the structural integrity. The gold plating combined with copper wiring has a high electrical conductivity and is less susceptible to the chemical KOH. This allows the electrode to be used for longer periods before it has to be replaced. The PCB design is shown in figure 3.20 and figure 3.21 shows the PCB installed in the setup.

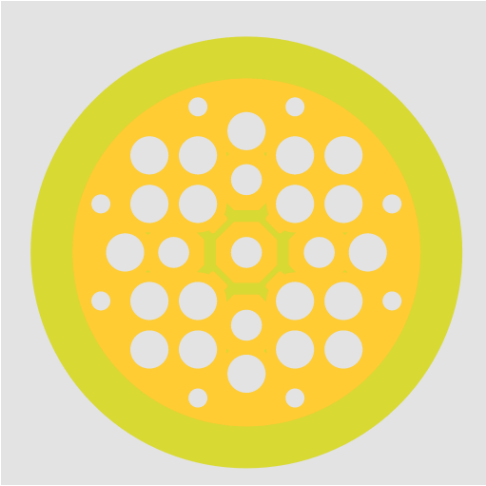

Figure 3.20: The adjusted electrical contacts built on PCB. The holes allow the oxygen to diffuse through. A cable can be connected at the back side.

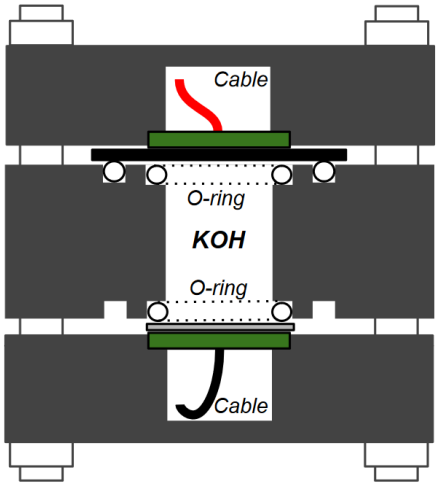

Figure 3.21: The cell setup viewed from the top. The PCB (green) submerges in the original hole, but is elevated by 0.5 mm above the surface to make an even contact.

The PCB is 1.55 mm thick. The original depth of the circular hole that would fit the PCB was 2.0 mm. This was reduced to 1.5 mm by scraping of 0.5 mm of the entire front side. The PCB then submerges into the circular hole with a 0.05 mm elevation above the surface. This will make an even contact with the electrode that is placed on top, as can be seen in figure 3.21.

3.7 Measurements and characterization

Once all parts are connected in the battery cell and the electrolyte is poured in, the battery can be discharged and its performance can be measured through several methods. This section discusses several measurement setups, which includes galvanostatic discharge and the anode mass consumption. Sample characterization includes the corrosion step height. To observe whether the simulated dopant profile is experimentally achieved, two methods are used. These include scanning resistance profiling (SRP) and measuring the sheet resistance (SR) with a four-point probe.

3.7.1 Galvanostatic discharge

The battery is discharged using a galvanostat. A galvanostat maintains a constant current that runs through a load. This is achieved by a nearly infinite internal resistance. The current can range from picoampères up to several ampères. The galvanostat obeys Ohm's law, meaning that it responds to any changes in the resistance of the load by varying the potential. As the current levels remains constant, the potential and resistance are directly proportional.

The Metrohm Autolab PGSTAT, equipped with Nova Software version 2.1, is used to discharge the battery cell in this work through a two-electrode setup. In the Nova software, the current can be set and the output voltage is measured and stored over time. As the active surface area in the battery is 1 cm^2, the applied current on the Autolab is in fact a current density in A/cm^2. The applied currents vary between 10 and 70 $\mu A/cm^2$ in this work.

The Nova software can be programmed to go through a sequence of steps, while indicating what the galvanostat has to do at each step. This procedure is illustrated in figure 3.22. In the *Autolab control*, the device is set into galvanostatic mode with a current range of 100 μA and the bandwith set to high stability. Based on the 0.2% accuracy level of the applied current, the accuracy is ± 0.2 μA with this current range. The next block *OCP* is used to measure the OCP of the battery for a duration of 3600 seconds. This data is stored in a separate plot. After the one hour OCP period, a current is applied to the battery. As a convention, negative current levels indicate a discharging battery, thus a negative current has to be set to discharge the battery. The galvanostatic discharge period and the number of measurement points can be set in the tab *Record signals*. Once the measured discharge potential reaches 0 V, the discharge is terminated.

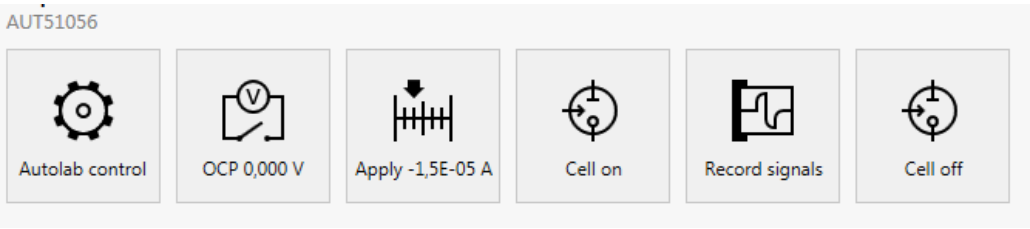

Figure 3.22: The used procedure on the Autolab programmed by the NOVA software. Under OCP-conditions, the plot is added manually. The discharge current is currently set at 15 $\mu A/cm^2$.

More background information on the measurement accuracy and connections of cables to the anode and cathode is explained in Appendix A.8.

3.7.2 Mass determination

To quantify the effect of corrosion in the used Si-air battery setup, the mass consumption of the Si anode is measured over time. The Si is actively being consumed by on the one hand the

electrochemical discharging m_d and on the other hand the parasitic consumption through the corrosion mechanism m_c. So in the total mass consumption m_t of Si only these two systems are considered, i.e. $m_t = m_d + m_c$. Other possible side reactions that consume Si are not taken into account. In the electrochemical discharge, Si is consumed and the reaction product $Si(OH)_4$ dissolves in to the electrolyte. The mass consumption in grams of Si through this process can be calculated by using equation 3.7.1.

$$m_d(t) = \frac{3.6 \cdot JAt}{\left(\frac{nF}{M_{Si}}\right)} \tag{3.7.1}$$

J is the applied current density in mA/cm^2, A the active area in cm^2 and t the discharge time in hours. n indicates the number of electrons involved in the reaction, i.e. four, and F is the Faraday constant of 96,485 C/mol. M_{Si} represents the molar mass of Si, i.e. 28.05 g/mol. The factor 3.6 is used to convert the mAh in the numerator to the used Coulombs in the denominator.

The total discharged mass m_t is determined using an accurate scale. The mass m_i is measured before discharging and m_f after discharging. As there will likely be some KOH left on the Si surface, it is key to remove any residue before measuring the mass. First, the samples are rinsed in DI-water. With a N_2 blow gun the samples are dried. After the drying step, the samples can be weighed on the scale. The total mass then follows through $m_t = m_f - m_i$. the scale has an accuracy σ_i of 10^{-4} g. The difference between two masses is determined, increasing the error in the measurement to $\sigma = 1.4 \times 10^{-4}$ g, according to equation 3.7.2 [134].

$$\begin{aligned} y &= a - b \\ \sigma_y &= \sqrt{(\sigma_a)^2 + (\sigma_b)^2} \\ &= \sqrt{(10^{-4})^2 + (10^{-4})^2} = 1.4 \times 10^{-4} \end{aligned} \tag{3.7.2}$$

Combining the above information, the corroded mass $m_c(t)$ as function of time follows through the calculation in equation 3.7.3

$$\begin{aligned} m_c(t) &= m_t - m_d(t) \\ &= (m_f - m_i) - \frac{3.6 \cdot JAt}{\left(\frac{nF}{M_{Si}}\right)} \end{aligned} \tag{3.7.3}$$

With the consumed masses, the anode conversion efficiency η can be calculated. The conversion efficiency indicates which part of the mass consumption is effectively used to electrochemically discharge the battery and thus which part is lost to corrosion. The conversion efficiency is calculated using equation 3.7.4.

$$\begin{aligned} \eta &= \frac{m_d}{m_t} \times 100\% \\ &= \frac{3.6 \cdot JAt}{m_t} \cdot \left(\frac{nF}{M_{Si}}\right)^{-1} \times 100\% \end{aligned} \tag{3.7.4}$$

3.7.3 Step height determination

In addition to studying the mass consumption and the conversion efficiencies, the effect of corrosion can also be studied by looking at the step height. This has been demonstrated by Zhong et al. [41]. The step height is determined through a profilometer, the Veeco Dektak 150. With a profilometer the topography of a surface is analyzed and the roughness determined. The Veeco Dektak 150 uses a stylus that scans the surface laterally over a pre-set scan distance. The vertical displacement is then given as a function of position. The scan speed is set by the time a measurement takes. The longer the measurement time, the slower the stylus will move over the surface and the higher the detail of the surface topology. The maximum range can be set

between 6.54 μm and 524 μm, depending on how large the expected step height is. The stylus can measure step heights smaller than 10 nm.

As Si is actively consumed during OCP and discharging of the battery, the initially flat wafer surface is anisotropically etched under an angle of 54.7°. The longer the Si is etched, the larger the step height will be between the area that is etch and the area that is not. This step height, and the corresponding corrosion rate in μm/h, can be determined using the profilometer.

To see whether the corrosion has decreased, increased or remained the same, the step height of the uniformly doped samples can be compared to the samples that have a doping profile. In order to have a fair comparison, the same time periods should be used to compare the step heights.

3.7.4 Dopant profile analysis

Simulations are performed to study the effect on the dopant profile by changing certain parameters, such as the temperature and the dose of the impurity layer. To verify if these simulations are in fact experimentally achieved in the used samples, several analysis tools that can be used to inspect the dopant profile will be discussed in this subsection. Based on the simulations in figures 5.4, 5.6 and 5.5, a large dynamic range in atomic concentration is needed to fully characterize the dopant profiles over the simulated depth as the concentrations range from 10^{12} up to 10^{20} atoms/cm^3. In addition to that, the detection limit should be very low, reaching less than parts-per-billion (ppb) accuracy, i.e. $< 10^{13}$ atom/cm^3.

Popular methods to analyze dopant profiles are secondary ion mass spectroscopy (SIMS) and neutron depth profiling (NDP). These methods are, however, not suitable for the deep dopant profiles that are used in this work. Therefore, two other - more suitable - options will be discussed that can be used to achieve the dopant profile. These are spreading resistance profiling (SRP) and measuring the sheet resistance (SR).

Spreading resistance profiling (SRP)

SRP was originally designed to determine the lateral resistance in samples. Today it is mainly used to determine the resistivity and consequently the electrically active dopant density inside semiconductors [135]. The concept uses two probes with a known length, width and distance between the two probes. A bias voltage of 5 mV is applied to the probes and the resulting resistance is measured. The probes are stepped along a surface that is beveled under a small angle of several degree and the resistance is determined at each step. The probes make visible imprints in the surface and is therefore a destructive method of analysis. A weight is applied to the probes such that they can break through the insulating native oxide layer on Si. The bevelled surface is illustrated in figure 3.23. The measured resistance between the probes consists of several parts, indicated in equation 3.7.5.

$$R = 2R_p + 2R_c + 2R_{sp} \tag{3.7.5}$$

The probe resistance R_p, contact resistance R_c and spreading resistance R_{sp} are added up and have the unit Ω. The R_{sp} emerges from the current I that is sent through the cylindrical probe as a result of the bias voltage. The current enters the semiconductor surface with resistivity ρ. The current I spreads radially into the semiconductor, illustrated in figure 3.24.

The R_{sp} between two highly conductive probes that touch a near-infinite surface is given in equation 3.7.6 [136]. This approximation holds if the probe spacing S is much larger than the contact radius r.

$$R_{sp} = \frac{\rho}{2r} \tag{3.7.6}$$

For a 1 μm wide probe, based on equation 3.7.6, the R_{sp} is 5000 times larger than the resistivity. Therefore, the R_{sp} is dominant in equation 3.7.5. A bevel angle of 1-5° combined with a step size of 5 μm means that the step height resolution is equal to 87 nm. SRP has a high dynamic range

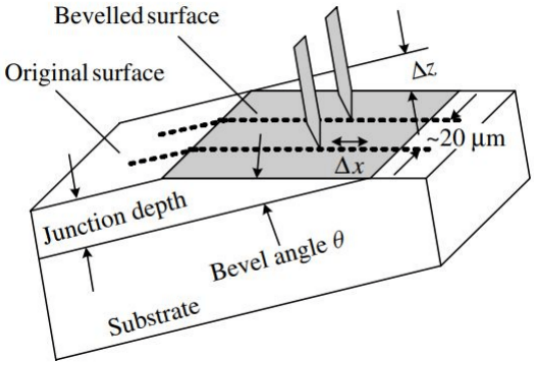

Figure 3.23: The bevelled surface and the travel direction of the probes. The probe spacing is here 20 μm. A typical measurement has 100-150 data points. Figure taken from [135].

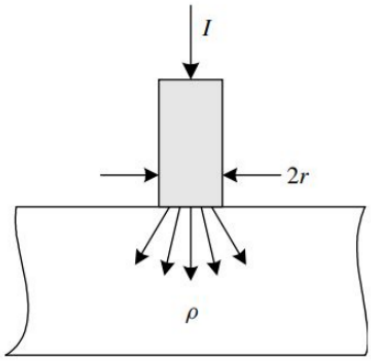

Figure 3.24: The arrows indicate the spreading direction of the current when the cylindrical probe makes contact with the semiconductor. Figure taken from [135].

of 10^{12} - 10^{21} atoms/cm^3. In SRP, it is assumed that the spreading resistance along a beveled surface yields the same carrier distribution as the vertical profile. Note that it is assumed that the carrier profile is the same as the doping profile. For a shallow junction of tens of nanometers this may not necessarily be true, but for the samples analyzed in this work the dopant profiles spread over tens of micrometers and therefore this may be assumed.
The R_{sp} is converted to a doping profile through complicated models that perform data smoothing, deconvolution and noise reduction. An important note is that SRP only determines electrically active dopant atoms, but it is assumed that this is indeed the case at the high temperatures of the diffusion process. The measured resistance is converted to a resistivity by using calibration charts where spreading resistance is plotted as a function of resistivity for n-type and p-type Si [137]. The raw resistance data as a function of depth can then be converted to resistivity data over the depth. When the type of wafer is known and a Poisson solver is used, the resistivity can be used to calculate the impurity concentration by using the graph data in figure 3.25 [135].

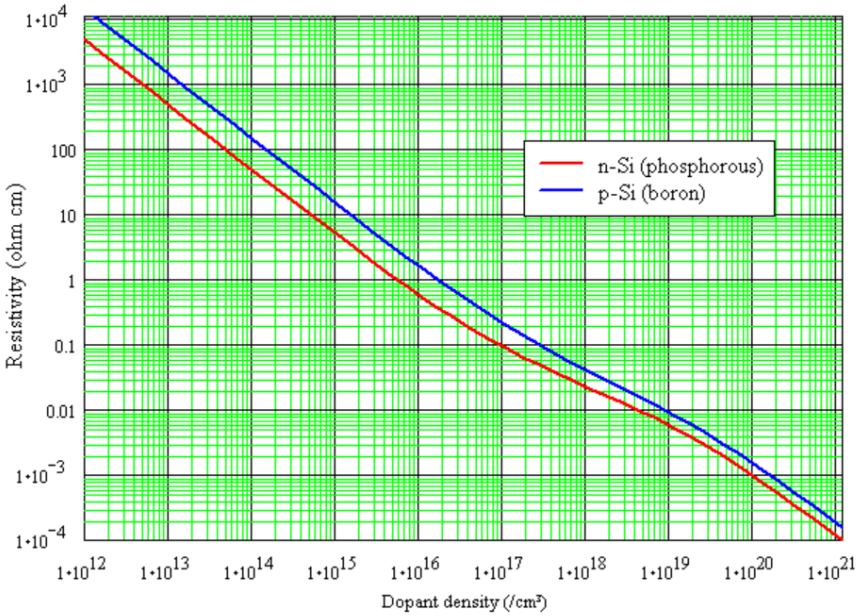

Figure 3.25: Resistivity values for n-type and p-type Si are plotted as a function of impurity concentration. With know resistivity values from SRP, the carrier concentrations can be determined. Figure taken from [138].

The facilities at EKL do not allow to execute a SRP analysis. Therefore, an external company is found that can perform such an analysis. The company SGS Fresenius GmbH has an office in Dresden, Germany, that has expertise in SRP analysis. They will perform a measurement where the probes will step in 100-200 steps over the surface. For a 50-60 μm depth, this creates a step size of around 0.25-0.60 μm.

Sheet resistance (SR)

Another method to determine the resistivity of a Si surface is by using a four-point probe. As the name indicates, it uses four probes that are equally spaced by a distance S in a straight line. A current is fed through the outer probes and the induced voltage is measured by the inner two probes. Using the voltage and current, the sheet resistance can be measured. Figure 3.26 shows a schematic overview of a four-point probe.

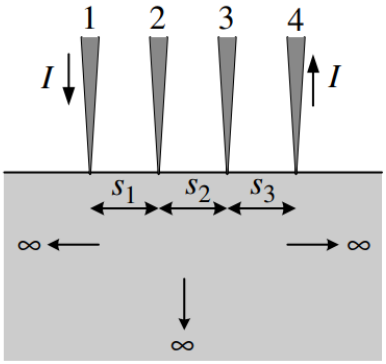

Figure 3.26: Working principle of a four-point probe. A current is sent through probe 1 and 4 while probes 2 and 3 measure the voltage. All probes are equally spaced by a distance S. In this example the sheet is infinitely thick and wide, while thin sheet with finite dimension can also be used. Figure taken from [135].

For a sheet with finite dimensions L and W and thickness t, the resistance in the sheet is given by equation 3.7.7.

$$R = \frac{\rho L}{Wt} \tag{3.7.7}$$

For a square sheet, i.e. $L = W$, the sheet resistance is defined as $R_s \equiv \rho/t$ with unit $\Omega/\square$. The sheet resistance is independent of the size of the square. Possible paths for the current to travel within the sample become limited through the proximity of a boundary, i.e. the edges of the sample. This led to the introduction of correction factors that depend on the geometry of the sample. This geometric factor g depends on the shape and the ratio t/S. A distinction between thick ($t \gg S$) and thin ($t \ll S$) is made in equation 3.7.8 [139].

$$\begin{aligned} t \gg S: &\quad g = 2\pi S \\ t \ll S: &\quad g = \frac{\pi}{\ln(2)} = 4.532 \end{aligned} \tag{3.7.8}$$

As the Si wafers are between 500-525 μm thick, the samples are squared and the probe distance S is 1.0 mm, the scenario where $t \gg S$ is not applicable. The other scenario, $t \ll S$, may be used for a thin square sample up to $\frac{t}{S} \leq 0.5$ [140]. This means that a correction factor of 4.532 has to be applied. With the four-point that is available at EKL, the calculated sheet resistance already takes into account this geometric factor. The resistivity ρ follows by multiplying R_s with the thickness of the sample. With the resistivity, the dopant concentration can be determined by using figure 3.25. Only activated carriers will be measured though. The four-point probe can be used as a nondestructive form of analyzing the sheet resistance.

It is more complicated to determine the sheet resistance for nonuniformly doped samples. The doping concentration varies over the depth x, which means that the resistivity, and consequently the dopant concentration, also depends on the depth. Moreover, the electron and hole mobility, μ_n and μ_p, respectively, depend on the dopant concentration and are also a function of the depth x. This is illustrated in equation 3.7.9.

$$N(x), \mu(x) \rightarrow \rho(x) = \frac{1}{q\mu(x)N(x)} \tag{3.7.9}$$

When a current is sent through a nonuniform layer, charge carriers will distribute according to a local resistivity, which is an averaged effect over the layer thickness. In general, as the resistivity is lower for high dopant concentrations, current flows more easily in highly doped areas than in lowly doped areas. This creates parallel sheet resistances over the depth x with each layer having a uniform dopant concentration N_i and thickness t_i. Figure 3.27 illustrates such a two layer parallel resistance with equal length L and width W.

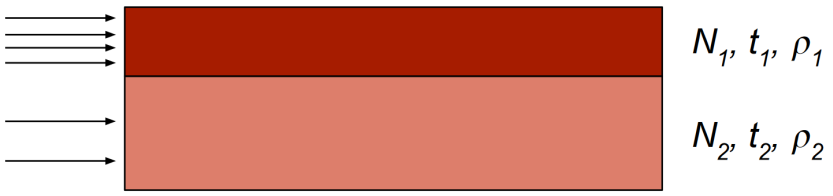

Figure 3.27: In nonuniform doped layers, the resistivity varies as function of depth. This effectively creates many parallel sheet resistances with each layer contributing to the overall parallel sheet resistance.

The resistance of each layer is expressed in equation 3.7.10.

$$\begin{aligned} R_1 &= \frac{\rho_1}{t_1}\frac{L}{W} \\ R_2 &= \frac{\rho_2}{t_2}\frac{L}{W} \end{aligned} \tag{3.7.10}$$

The total resistance R_{tot} can be expressed using the parallel resistance. This is expressed in equation 3.7.11.

$$\begin{aligned} \frac{1}{R_{tot}} &= \frac{1}{R_1} + \frac{1}{R_2} = \frac{t_1}{\rho_1}\frac{W}{L} + \frac{t_2}{\rho_2}\frac{W}{L} \\ &= \left[\frac{t_1}{\rho_1} + \frac{t_2}{\rho_2}\right]\frac{W}{L} = \frac{1}{R_S}\frac{W}{L} \end{aligned} \tag{3.7.11}$$

This leads to an expression for the sheet resistance R_S of the parallel resistance structure in equation 3.7.12.

$$\frac{1}{R_S} = q\mu_1 N_1 t_1 + q\mu_2 N_2 t_2 \tag{3.7.12}$$

This two layer structure can be expanded to many uniformly doped layers with thickness Δx up to the junction depth x_j, where the dopant concentration is equal to the background concentration N_b. This is illustrated in figure 3.28.

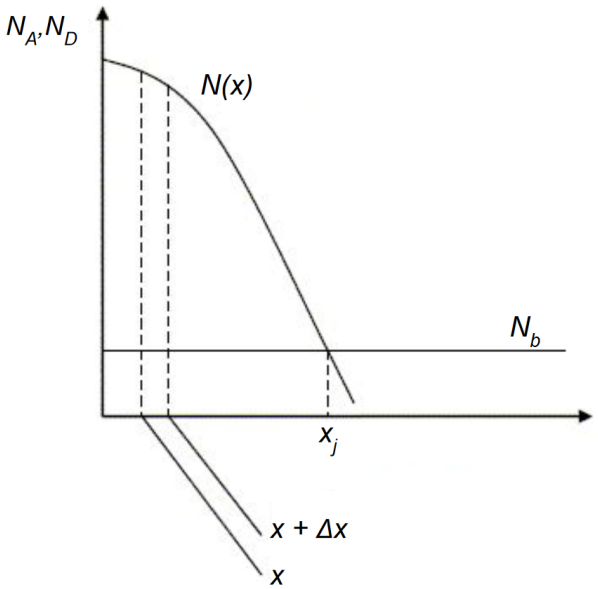

Figure 3.28: Due to the dopant profile, the carrier concentration $N(x)$ varies over the depth x. The profile can be subdivided into thin layers with width Δx up to the junction depth x_j to determine the sheet resistance R_S.

The R_S of a nonuniform profile follows through the summation of the layers Δx. When $\Delta x \to 0$, the summation becomes an integral. The summation and integral are indicated in equation 3.7.13.

$$\frac{1}{R_S} = \sum_{i=0}^{x_j} q\mu(x_i)N(x_i)\Delta x \overset{\Delta x \to 0}{=} q\int_0^{x_j} \mu(x)N(x)dx \tag{3.7.13}$$

Based on the above equation, the mobility varies with the dopant concentration. Analytical expressions for the electron mobility μ_e and hole mobility μ_h have been derived from experimental data. Based on the model of Arora et al. [141], the following expressions for the mobilities have been derived for the μ_e and μ_p respectively:

$$\mu_e(x) = 88\left(\frac{T}{300}\right)^{-0.57} + \frac{7.4\times10^8 T^{-2.33}}{1+0.88\left[\frac{N_D(x)}{1.26\times10^{17}\left(\frac{T}{300}\right)^{2.4}}\right]\left(\frac{T}{300}\right)^{-0.146}} \tag{3.7.14}$$

$$\mu_h(x) = 54.3\left(\frac{T}{300}\right)^{-0.57} + \frac{1.36\times10^8 T^{-2.23}}{1+0.88\left[\frac{N_A(x)}{2.35\times10^{17}\left(\frac{T}{300}\right)^{2.4}}\right]\left(\frac{T}{300}\right)^{-0.146}} \tag{3.7.15}$$

The sheet resistance R_S will be experimentally determined on the nonuniformly doped samples. When Si is consumed, part of the surface is etched away. This step height can be determined by using the Dektak profilometer. Different step heights will be considered for each type of sample. Using the four-point probe, the sheet resistance can be determined. The thickness of the sample up to the junction depth decreases through the etching process and this has to be taken into account for the eventual resistivity profile. Equation 3.7.13 can be rewritten to take into account this reducing thickness:

$$R_S = \frac{1}{q\int_x^{x_j} \mu(x)N(x)dx} = \frac{1}{\sigma(x)} \tag{3.7.16}$$

The position x is the distance from the original surface into the sample. The above equation takes into account the averaged value over the thickness $(x_j - x)$ and is equivalent to $1/\sigma(x)$. The resistivity as a function of the depth $\rho(x)$ can be determined through a number of steps and by using Leibniz's theorem, indicated in equation 3.7.17 [135].

$$\frac{d}{dc}\int_a^b f(x,c)dx = \int_a^b \frac{\partial}{\partial c}[f(x,c)]dx + f(b,c)\frac{\partial b}{\partial c} - f(a,c)\frac{\partial a}{\partial c} \tag{3.7.17}$$

Using and applying this theorem to the sheet resistance and using that $\rho(x) = 1/\sigma(x)$, results in the expression for the resistivity as a function of position in equation 3.7.18. This method assumes that the sheet resistance increases with increasing depth.

$$\rho(x) = -\frac{1}{d\left[1/R_S(x)\right]/dx} = \frac{R_S^2(x)}{dR_S(x)/dx} \tag{3.7.18}$$

The sheet resistance $R_S(x)$ and the step height are determined in the etching process. First, $R_S(x)$ will simulated based on equation 3.7.16. The experimentally determined sheet resistances will be compared to the simulated sheet resistance profile. The Advanced Instruments Technology CMT-series four-point probe is used to measure the R_S on the samples. This four-point probe is capable of measuring a sheet resistance between 1 m$\Omega/\square$ - 2 M$\Omega/\square$ [142].

Chapter 4

Improving galvanostatic measurement setup

This chapter presents the initial discharge results of the Si-air battery setup that follow from the defined methods in chapter 3. First, the start-up procedure is determined in section 4.1. In section 4.2, based on the start-up procedure a long discharge is performed to see the behavior of the battery. Based on the findings, the initial setup limitations are shown in section 4.3. The improved setup is discussed in section 4.4. Based on the improved setup, discharge profiles are analyzed for different discharge current densities. In section 4.5, the effect of changing the electrolyte concentration is studied.

The first experimental efforts of this work are aimed at achieving stable battery discharges, such that the results of Prins [64] can be reproduced and the measurements can be expanded. Prins has shown results regarding discharge times of up to 70 hours with an applied current density of 150 μA/cm^2 by optimizing the pre-wetting time of the air cathode [64].

In the first subsection, the start-up procedure for experiments is determined by studying the discharge profiles. In a discharge profile, the battery's potential is plotted as a function of time. This is done for open circuit potential (OCP) and current densities ranging from 10 to 50 μA/cm^2 using p-type wafers. The next subsection shows, based on the chosen start-up procedure, a long uninterrupted measurement of 70 hours. Based on the findings, the next subsection shows the shortcomings of the initial setup after which the improved setup will be discussed by directly comparing the discharge results.

4.1 Start-up procedure

Ideally, a battery should maintain a very constant potential during OCP conditions and as it discharges to keep powering the load. Besides, the time the battery can discharge before the potential drops below a certain threshold potential should be as long as possible. To create the optimal conditions for the Si-air battery, Prins used to pre-wet the air cathode in the potassium hydroxide (KOH) electrolyte before discharging. He optimized the pre-wet time at 8 hours to achieve the longest discharge time of 70 hours at a potential of 1.05 V and an applied current density of 150 μA/cm^2.

The optimal pre-wetting time, but also 4 and 6 hour periods, were used in this work before discharging the battery. However, this led to mixed outcomes and not the results that were to be expected. Using the pre-wet periods for OCP conditions yielded an expected initial potential of 1.4 V, but this potential quickly dropped to lower values and eventually started to oscillate. This can be observed in figure 4.1. The same procedure was followed on discharging of the battery, but only resulted in a discharge time of 4.5 hours at a very low potential of 0.2-0.3 V for a current density of 50 μA/cm^2 instead of 150 μA/cm^2, as illustrated in figure 4.2.

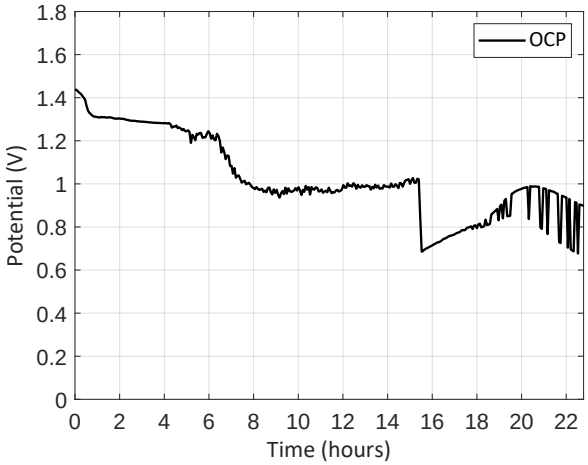

Figure 4.1: The OCP after 8 hour pre-wetting in KOH. The potential does not remain very constant and starts oscillating.

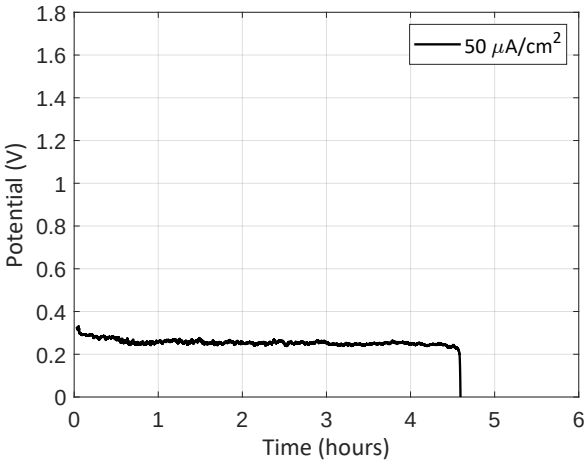

Figure 4.2: Discharging the battery after 8 hour pre-wetting results in a discharge period of only 4.5 hours.

Discharging with current densities higher than 50 μA/cm^2 was not possible as they resulted in the stop-condition of the galvanostat to be fulfilled immediately, i.e. a potential smaller than 0 V. This is likely due to passivation, as the generation rate of $Si(OH)_4$ is increased for increasing current densities and the reaction product cannot dissolve fast enough in the solution. This leads to the formation of a passivation layer. A discharge current density of at most 50 μA/cm^2 was chosen, in line with findings of Durmus et al. [43] and Zhong et al. [41] for flat surfaces. Increasing the surface area increases the dissolution rate of $Si(OH)_4$ and postpones passivation, but this also increases the corrosion rate and is therefore not taken into account in this work.

While pre-wetting the air cathode may not have resulted in the expected outcomes, some form of pre-wetting of the anode is needed before the battery can be discharged. Si forms a native oxide layer, SiO_2, on exposure to the outside air [114]. The thickness of this layer converges to roughly 2.1 nm [115]. SiO_2 increases the impedance and acts as an insulator [116]. KOH also etches, besides Si, SiO_2, albeit at a much slower rate. It was found that at room temperature and the 30% concentration level of the KOH solution, the SiO_2 is etched at a rate of 3.4 nm/hour [100]. This means that it will roughly take 40 minutes to etch the SiO_2 layer away and make the Si surface active again, assuming it has a uniform thickness. This increase in potential within a one hour period can be observed in figure 4.3.

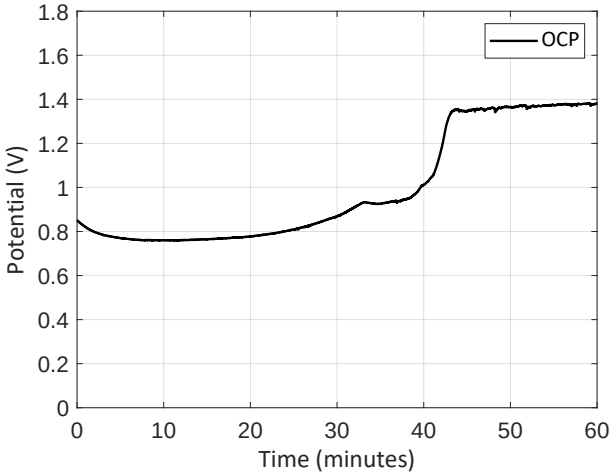

Figure 4.3: After a one hour period at OCP conditions, the native oxide on the Si is removed and the OCP reaches the expected value of 1.4 V.

The expected OCP of ca. 1.4 V [44] is reached within a one hour period and the Si surface is now active. This means the reaction product $Si(OH)_4$ can better dissolve into the electrolyte and the discharge can continue. Comparing this behavior to directly discharging once the setup is installed, the surface is quickly passivated on direct discharging. This is shown in figure 4.4.

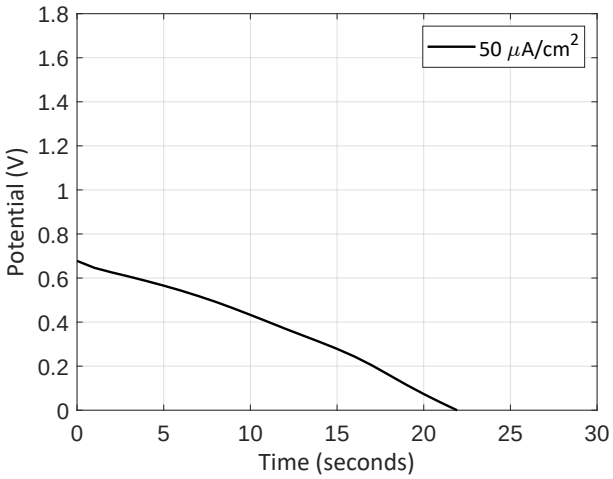

Figure 4.4: If the battery is directly discharged after assembly, the native oxide has not yet been removed and the battery can only discharge for 20 seconds. Therefore, a one hour OCP period should be taken into account after assembly.

The battery stops discharging after 22 seconds, ascribed to surface passivation. Therefore, the initial one hour OCP period should be taken into account after the assembly of the battery parts. With a clear start-up procedure, the following subsection studies the performance of the battery in a long consecutive discharge.

4.2 Long consecutive discharge

The ability of the battery setup to achieve long, stable discharges will be analyzed in this subsection. The same setup has been used in discharge periods of up to 70 hours before in the work of Prins. This is repeated for the start-up procedure as defined in the previous subsection. A single discharge of 70 hours is shown in figure 4.5. The discharge potential is fairly constant with a slight increase in the beginning. The discharge current density was set at 50 μA/cm^2 resulting in a potential of on average 0.55 V, which is lower compared to the 1.0 V in the work of Prins. The surface of the Si anode after discharge clearly shows an etched structure in a circular area, as can be seen in figure 4.6. The origin of the lowered discharge potentials appeared to be coming from the setup and is discussed in the next subsection.

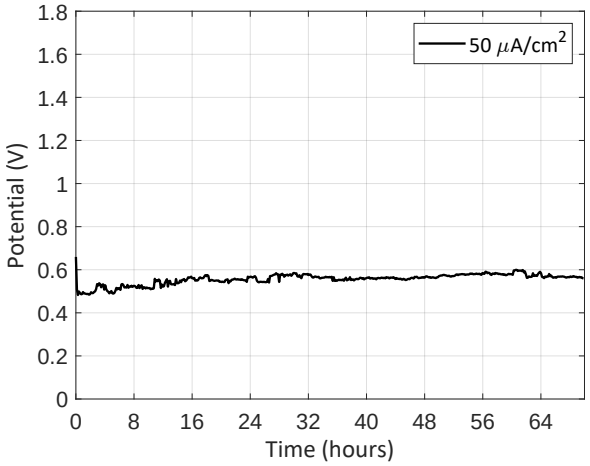

Figure 4.5: The discharge profile of a 70 hour measurement with an applied current density of 50 μA/cm^2.

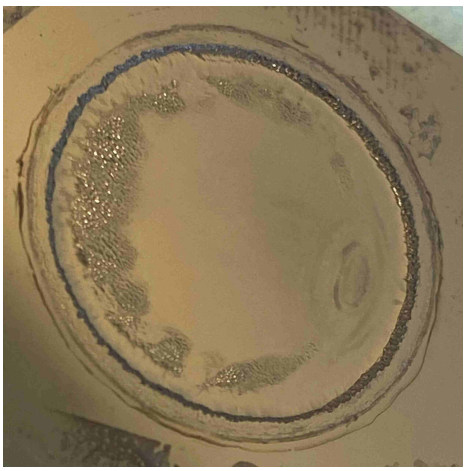

Figure 4.6: The etched surface of the Si sample after the long discharge period is clearly visible.

4.3 Initial setup

When comparing the achieved discharge potentials to the values achieved by other students and to values of alkaline Si-air batteries in literature of Durmus et al. [43][44] and Zhong et al. [41], the discharge potentials in the results presented in the previous subsections are lower than expected. These papers used n-type Si wafers, whereas in the first results of this work, p-type Si wafers are used. The paper by Park et al. used p-type Si and achieved lower discharge voltages than n-type Si at around 0.8 V for 10 μA/cm^2 [46]. As can be seen in figure 4.7, the discharge potential for 50 μA/cm^2 is only 0.4 V. Using a multimeter, the contact resistance in both cables was measured. It appeared that in one cable a series resistance of ca. 10 kΩ was measured. At an applied current density of 50 μA/cm^2, this results in an Ohmic loss of 0.5 V. When looking at the contact in figure 4.8, a clear crystallized residue of KOH is visible at the backside. It is likely that this has affected the contact after being soaked for numerous hours in KOH and left to dry and crystallize. Efforts and several designs have been made to improve the contacts of the setup. The outcome of this will be discussed in the next subsection.

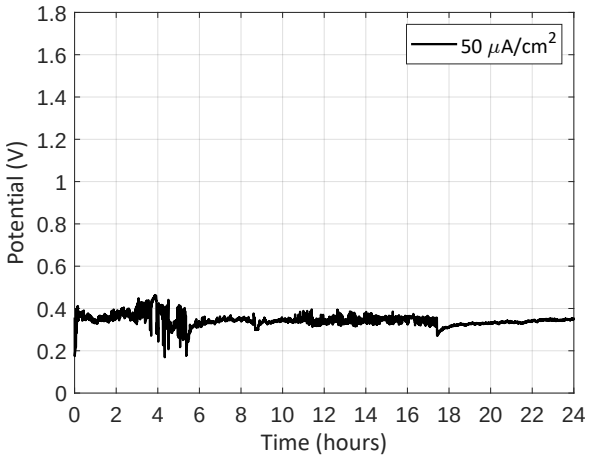

Figure 4.7: The discharge potential is too low at around 0.4 V for 50 μA/cm^2. Based on literature findings, a 0.8 V, or higher, potential is expected [46].

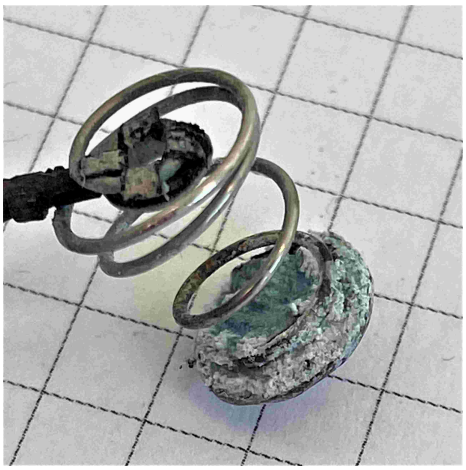

Figure 4.8: Severely affected electrical contact covered with crystallized KOH. This increased the contact resistance to around 10 kΩ.

4.4 Improved setup

A 1.55 mm thick gold plated printed circuit board (PCB) with perforations that allow oxygen to diffuse at the air cathode was designed and fixed inside the PTFE holders. Figure 4.9 shows the integration of the PCB into the holder.

Figure 4.9: The redesigned electrical contact consists of a gold-plated PCB. The gold is not affected by KOH and can survive longer discharge times without affecting the discharge potential of the battery.

With the PCB, the OCP remains more constant at a higher voltage and applying a current density of 50 μA/cm^2 now yields a more stable and higher discharge potential of 0.8 V. This can be seen in figures 4.10 and 4.11.

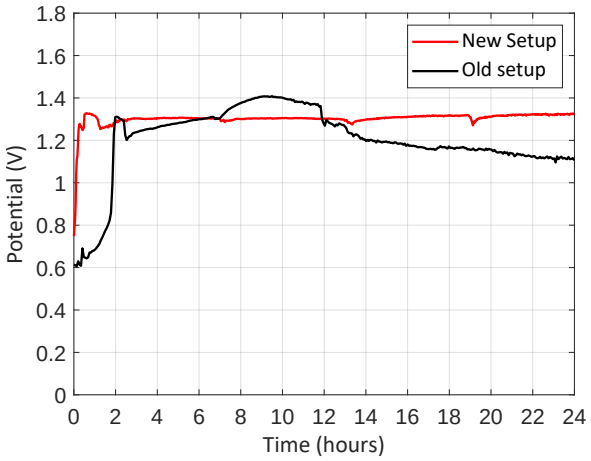

Figure 4.10: Comparing OCP plots before and after the improved setup. The new electrical contacts resulted in a more continuous OCP-profile.

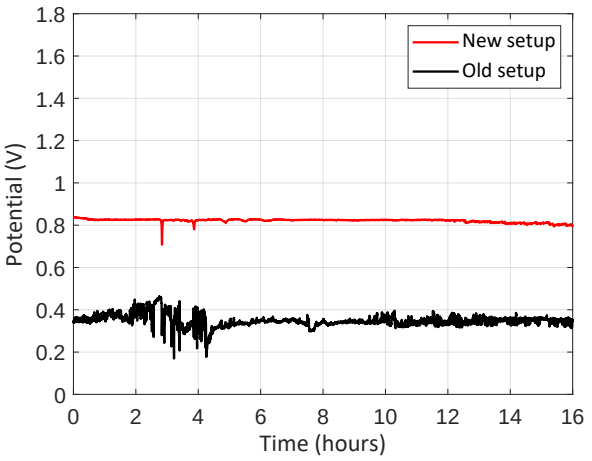

Figure 4.11: Comparing active discharging plots before and after the improved setup at the same current density of 50 μA/cm^2.

Based on the improved setup, the discharge profiles for different current densities are determined for both p-type and n-type Si wafers. No direct comparison between these types in KOH was made before in literature. The applied current densities are, 10, 25 and 50 μA/cm^2. These profiles include the 1 hour OCP period after which the discharge starts. Figure 4.12 shows the discharge profiles for p-type and figure 4.13 for n-type Si.

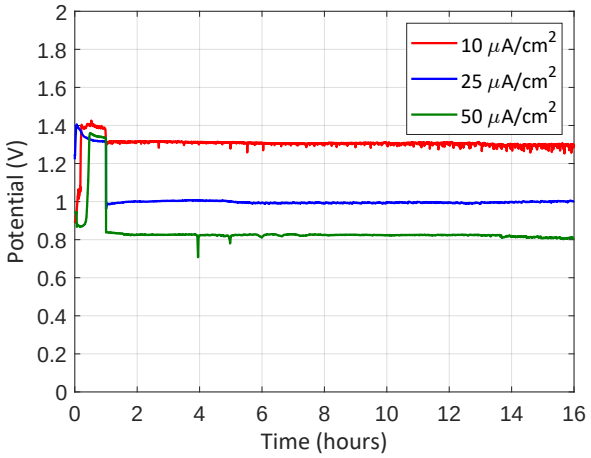

Figure 4.12: The discharge curves for p-type Si with varying current densities. A one hour OCP period is included in the beginning.

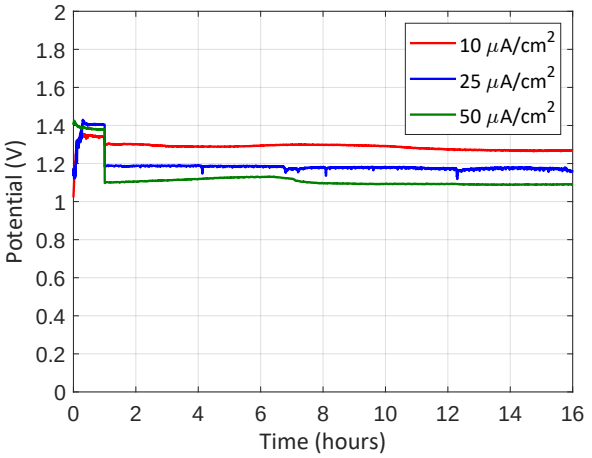

Figure 4.13: The discharge curves for n-type Si with varying current densities. A one hour OCP period is included in the beginning.

As can be seen in the figures above, for OCP and a low discharge current density of 10 μA/cm^2, the potentials for n-type and p-type are very similar. This indicates a similar internal resistance. For higher applied current densities of 25 and 50 μA/cm^2, the internal resistance increases through increased ohmic losses. As can be seen in the figures above, the internal resistances in p-type Si appear larger than in n-type Si as the distances between the lines is larger and the potentials lower. The change in potential between discharging with 10, 25 and 50 μA/cm^2 does not scale linearly for p-type Si. This indicates, besides ohmic, other losses contributing to the overpotentials.

4.5 Diluted electrolyte

In literature it was shown that changing the electrolyte concentration has an effect on the discharge behavior [41][43][44]. Dilution requires the addition of a measured amount of water to a known amount of KOH. The initial concentration of the used KOH is 6.6M (30 m%). One has to add 50 ml of DI-water to 10 ml of KOH to lower the concentration to 1.1M. The effect of lowering the concentration on the discharge behavior at a current density of 10 μA/cm^2 is illustrated in figure 4.14. The effect that decreasing the electrolyte concentration has on the conductivity of the electrolyte is portrayed in figure 4.15.

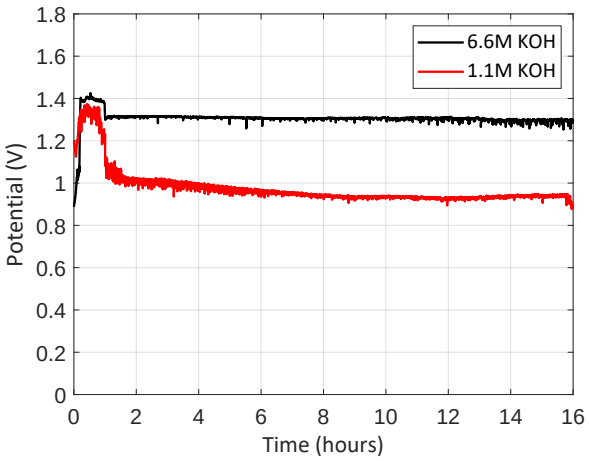

Figure 4.14: Discharge curves for different electrolyte concentrations at a current density of 10 μA/cm^2. The discharge potential is lowered by more than 0.3 V, while OCP-value is similar.

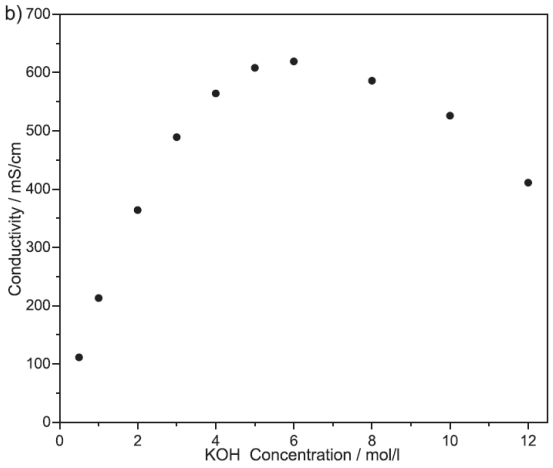

Figure 4.15: The conductivity of the electrolyte as function of KOH concentrations. The conductivity significantly lowers for lower concentrations. Figure taken from [44].

Decreasing the electrolyte concentration lowered the discharge potential with over 0.3V for the relatively low discharge current density of 10 μA/cm^2, while the OCP remained roughly the same. A lower electrolyte concentration decreases the conductivity and consequently the reaction kinetics. This increases the overpotentials in the battery, according to equation 3.6.1. Increasing the discharge current density to 50 μA/cm^2 resulted in a quick passivation of the Si as can be seen in figure 4.17. The initial OCP graph in figure 4.16 shows the expected value of around 1.3 V after one hour. Once discharging starts, the potential drops to 0 V after 40 seconds.

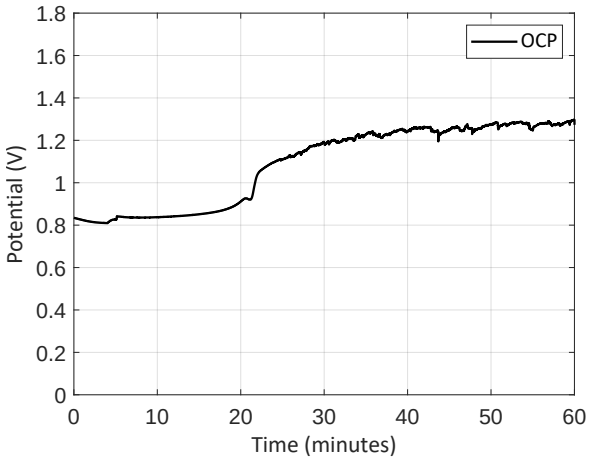

Figure 4.16: The OCP as a function of time for the first hour in 1.1M KOH. It increases to the same potential as with the 6.6M KOH.

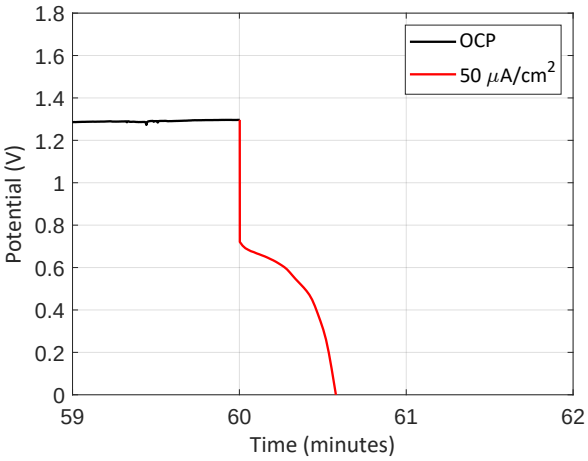

Figure 4.17: When a discharge current density of 50 μA/cm^2 is applied, the Si surface is quickly passivated and the discharge stops.

Due to the earlier passivation with a diluted electrolyte, the original 6.6M KOH concentration is used in further experiments in this work.

Chapter 5

Dopant profiles

In this chapter the properties of the dopant profiles are determined, based on the steps described in chapter 3. This is first done by simulating the profiles, as described in section 5.1. Based on the simulations, the diffusion process is carried out by using the same parameters and the thermal oxide layer is inspected in section 5.2. To verify if the simulated dopant profiles have been experimentally achieved in the used samples, further analysis is carried out in this chapter to determine the dopant profile. First, the sheet resistance will be simulated for the nonuniformly doped samples in section 5.3. These simulations are compared to the experimentally determined sheet resistances in section 5.4. The spreading resistance is determined by an external company through spreading resistance profiling (SRP). This is shown in section 5.5. The results of the sheet resistance and the spreading resistance are compared with each other in section 5.6.

5.1 Simulated dopant profiles

Implementing a dopant profile to direct the electrons towards the current collector, assumes that the electrons have a significant contribution in the corrosion reaction. Based on recent results of Durmus et al. in the field of alkaline Si-air batteries [44], the role of electrons is expected to be of measurable influence. On discharging, the flow of OH^- ions onto the Si surface increases. This increases the corrosion rates of 1.5 μm/h at OCP to 2.2 μm/h with discharging [44]. In accordance with this, it was found that the measured corroded mass increases on applying a discharge current with respect to OCP [43][143]. Based on the Arrhenius plot created for an alkaline Si-air battery in figure 2.38, the activation energy was determined at 0.57 eV [44]. This value of activation energy indicates a surface-reaction limited process originating from, for instance, electron transfer.

To experimentally observe if nonuniform doping will have the desired effect, two scenarios are tested that are based on diffusion of charge carriers. The first scenario uses p-type Si. In p-type Si, holes are the majority carriers. Nonuniformly doping a p-type wafer with additional acceptors at the side of the Si-electrolyte interface means that positively charged holes will diffuse to the side with a lower acceptor concentration. This gives the high acceptor doped region a net negative charge. Equivalently, electrons diffuse to the higher doped acceptor side. This is shown schematically in figure 5.1a. As the resistivity level of the used p-type wafers is high, the electron concentration is relatively high as well. The idea here is that corrosion might increase due to electrons diffusing from the bulk to the silicon-electrolyte interface. More electrons will react with H_2O to form OH^- and H_2, increasing corrosion, as described in the reaction given in equation 2.10.2.

The second scenario will focus on n-type Si, where electrons are majority carriers. A donor concentration gradient is directed to the right into the bulk Si, shown in figure 5.1b. This means that negatively charged electrons will be removed from the interface into the bulk as a consequence of electron diffusion and the internal electric field directed into the bulk Si. Based on the proposed corrosion model of Durmus et al., the idea is that corrosion decreases due to fewer electrons available at the cathodic sites of the anode to react with H_2O. More electrons

then contribute to the external circuit current and corrosion should decrease.

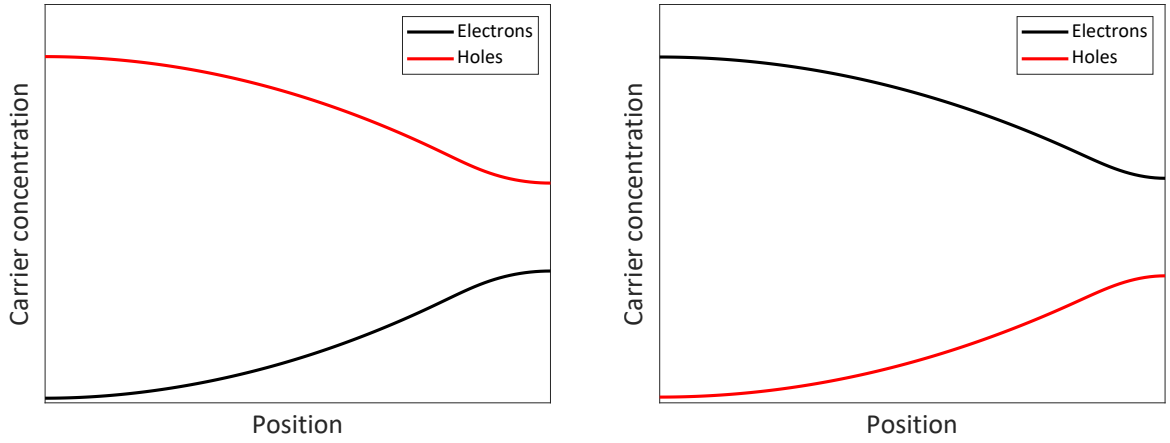

Figure 5.1: Schematic logarithmic plot with the carrier concentrations in thermal equilibrium as function of position in nonuniformly doped Si: (a) p-type on p-type and (b) n-type on n-type. The Si-electrolyte interface is situated at the left. The corrosion is expected to increase for p-type Si due to electrons diffusing to the surface instead of being removed from it. Corrosion is expected to decrease for n-type Si, as the internal electric field is directed into the bulk of the Si, removing the electrons.

As Si is very reactive in alkaline electrolytes, the corrosion reaction starts directly at OCP and continues during discharge. To observe the effect of nonuniform doping for as long as possible, the dopant profile should ideally reach deep into the bulk of the c-Si. Before nonuniformly doped wafers are fabricated, simulations are performed in Excel and Matlab to determine the shape of the dopant profiles. This will be explained in the next subsection.

Before the wafers are put inside a furnace to start the diffusion process, simulations will be performed to determine the required parameters for the diffusion process, including the temperature and diffusion time. This is done in several iterations with varying temperatures above 1100 °C and diffusion times longer than 6 hours. These iterations are illustrated for B-doped wafers with a deposited p-type a-Si:H layer on top in figure 5.2 for temperature and in figure 5.3 for time. Coefficients from table 2.2 have been used and N_b is the base concentration of the wafer. The dose of the deposited impurity layers was determined in section 3.3.1 for PECVD and in section 3.3.2 for epitaxial growth. For the p-type a-Si:H diffused layer, the dose was estimated at $5{\times}10^{15}$ B atoms/cm^2. The base concentration originates from the resistivity of the wafer. The resistivity is 1000 Ωcm, i.e. $1.3{\times}10^{13}$ B atoms/cm^3.

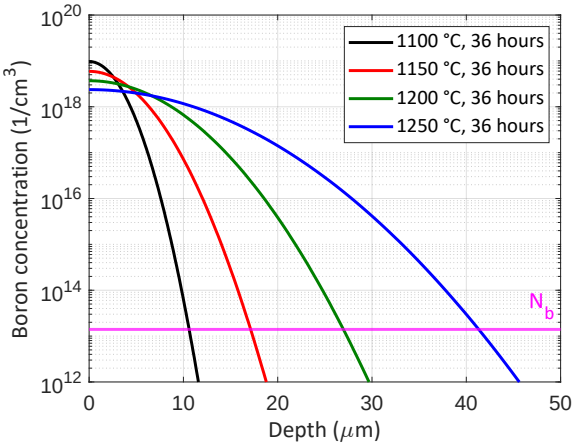

Figure 5.2: Logarithmic dopant profile for different temperatures after 36 hours. N_b is the base dopant concentration in the bulk Si.

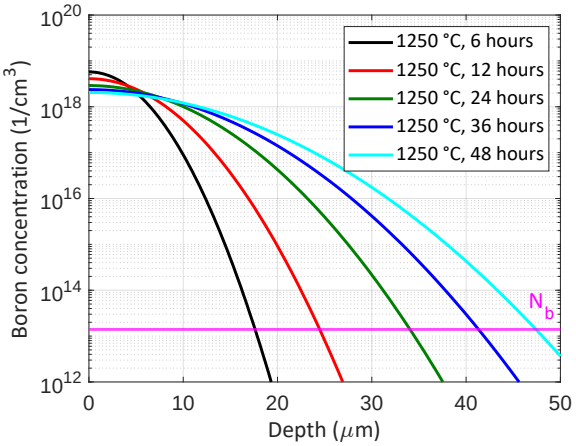

Figure 5.3: Logarithmic dopant profile for different time periods at 1250 °C. N_b is the base dopant concentration in the bulk Si.

After a couple of iterations, a temperature of 1250 °C and a drive-in period of 36 hours were

chosen. This yields a large junction depth of ca. 42 μm for p-type a-Si:H deposited on p-type Si, as can be seen in the blue line in figures 5.2 and 5.3. This process is repeated for deposited n-type a-Si:H on an n-type wafer and this yields a junction depth of 32 μm. The epitaxially B-deposited wafers have a simulated junction depth of 38 μm. The simulated profile for p-type a-Si:H is depicted in figure 5.4. This is repeated for n-type a-Si:H in figure 5.6. The simulated dopant profile for the epitaxially diffused B on p-type Si is depicted in figure 5.5.

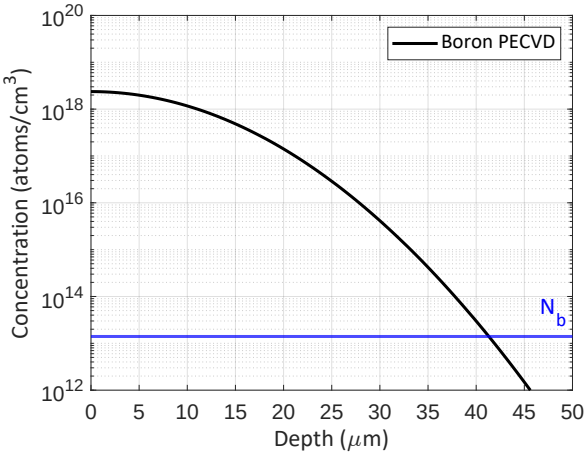

Figure 5.4: Logarithmic profile of PECVD diffused B after 36 hour drive-in at 1250 °C. The junction depth is 42 μm. N_b is the base dopant concentration in the bulk Si.

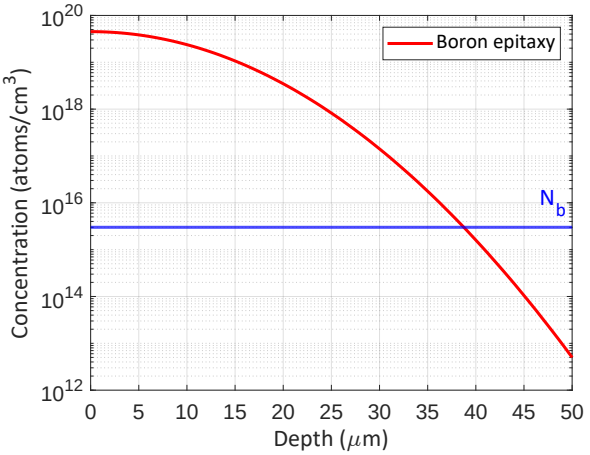

Figure 5.5: Logarithmic profile by epitaxially diffused B after 36 hour drive-in at 1250 °C. The junction depth is 38 μm. N_b is the base dopant concentration in the bulk Si.

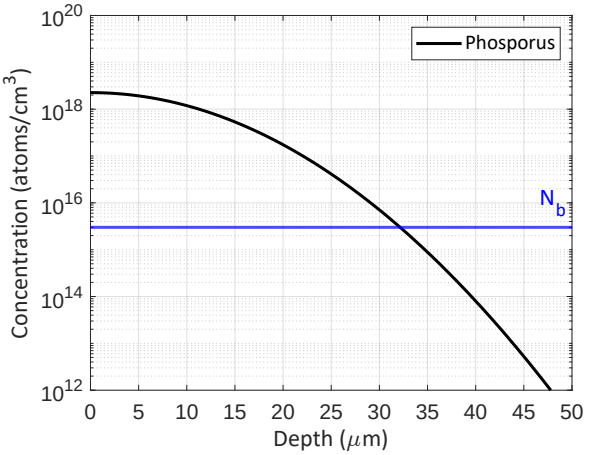

Figure 5.6: Logarithmic profile of P by PECVD diffusion after 36 hour drive-in at 1250 °C. The junction depth is 32 μm. N_b is the base dopant concentration in the bulk Si.

The junction depth x_j can be clearly seen at the point where the profile crosses the horizontal line, at which the dopant concentration is equal to N_b. Even though the p-type wafer used in the epitaxial growth has a lower resistivity than the wafer used in the PECVD process, a comparable drive-in depth of the B atoms is achieved due to the significantly higher surface concentration of 4.8×10^{19} atoms/cm^3 after diffusion. This surface concentration would be sufficient to achieve a reduction in the corrosion rate in KOH electrolytes as was documented by Seidel et al. [100]. In this way, corrosion in p-type Si should decrease with respect to uniform p-type Si. The corrosion results of the nonuniformly doped wafers will be discussed in chapter 6.2.

5.2 Thermal oxide inspection

With the parameters extracted from the simulations in the previous section, the thin layer depositions and subsequently the diffusion process are carried out. After the diffusion process, the wafers were taken out of the furnace and the surface was inspected. On inspection, a clear

thermal oxide layer, i.e. SiO_x, had formed on the wafer surfaces, as can be seen in figure 5.7. Based on the graph in figure 3.7, the thickness is estimated to be around 300 nm.

As indicated in section 3.3.4, this thermal oxide layer can be removed using buffered hydrofluoric acid (BHF) with a ratio of 1 part BHF and 7 parts H_2O. When the wafers are immersed in the solution for 4 min, the oxide layer is clearly removed. This can be observed in figure 5.8 for a n-type wafer. BHF etches the thermal oxide layer with rougly 80 nm/min, while not etching Si [130].

Figure 5.7: A thermal oxide layer is clearly visible on this n-type wafer after diffusion.

Figure 5.8: After 4 min oxide etch in 1:7 BHF, the thermal oxide layer on the n-type wafer is removed.

Beside the thermal oxide layer, inhomogeneously spread black areas can be spotted on the front side of the wafer that were not removed with BHF. These black areas were only visible on the n-type a-Si:H deposited wafer. The thermal oxide was visible on all wafers after the diffusion process. After cleaning the back side of the wafer, the Al-Cr back-contact was applied with EBPVD.

5.3 Simulated sheet resistances

In section 3.7.4, an approach to determine the sheet resistance in the nonuniformly doped wafers is outlined. Based on this theory, simulations are first performed to determine the sheet resistance as a function of depth by using the simulated dopant profiles, that were determined in section 5.1.

The temperature T is assumed to be 300 K and the electron and hole concentration are equal to donor concentration N_D and acceptor concentration N_A, respectively. The lower limit of the integral in equation 3.7.13 increases with increasing depth. Combining all the information yields figure 5.9 for the p-type PECVD grown wafer, figure 5.10 for p-type epitaxially grown wafer and on the next page figure 5.11 for the n-type PECVD grown wafer.

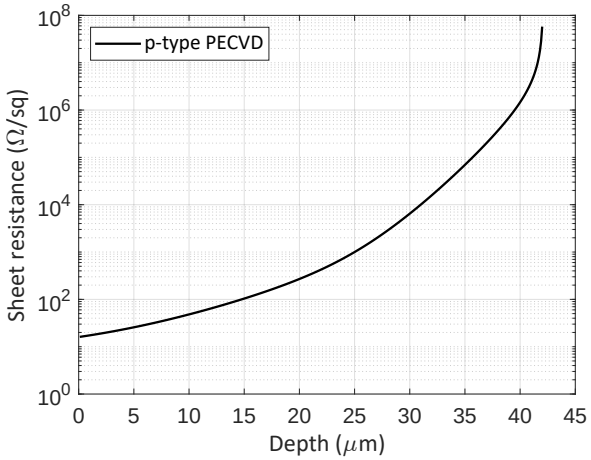

Figure 5.9: Simulated sheet resistance for p-type PECVD grown wafer with $x_j = 42$ μm.

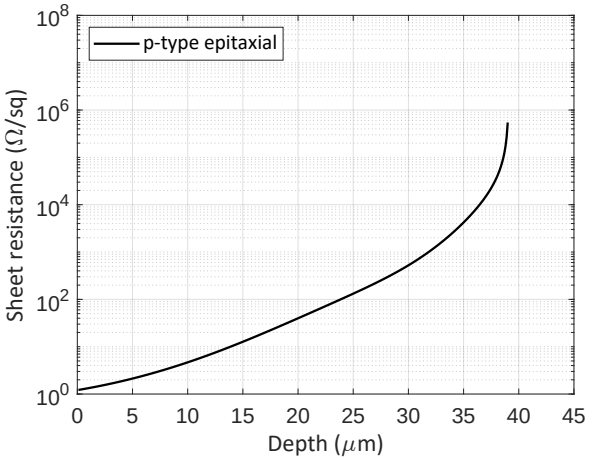

Figure 5.10: Simulated sheet resistance for p-type epitaxially grown wafer with $x_j = 38$ μm.

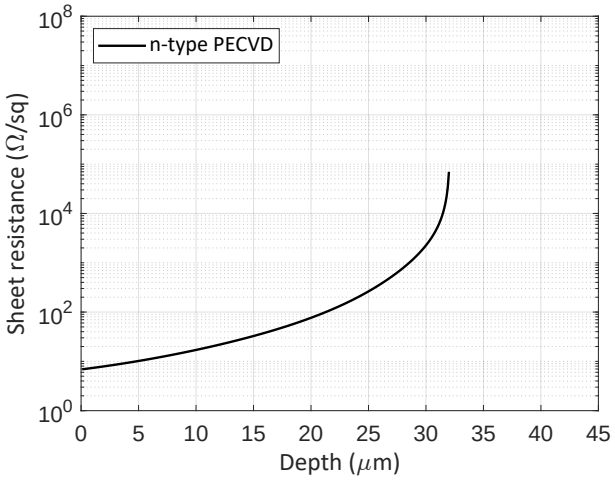

Figure 5.11: Simulated sheet resistance for n-type PECVD grown wafer with $x_j = 32$ μm.

The sheet resistance will be experimentally determined in the next section on the 16 mm x 16 mm samples by using the four-point probe setup. The measured sheet resistance as a function of depth is compared to the above simulated sheet resistance. As the Si is consumed in the reaction, part of the surface is etched away. This step height is determined with the Dektak profilometer. The sheet resistance will be determined at different, increasing step heights.

5.4 Experimental sheet resistances

The sheet resistance will be determined with the four-point probe for the p-type PECVD and epitaxial grown Si samples and for the n-type PECVD grown Si samples. As the Si is consumed in the reaction, part of the surface is etched away. This step height is determined with the Dektak profilometer. The sheet resistance will be determined at different, increasing step heights. This measured sheet resistance is compared to the simulated sheet resistance from the previous section.

5.4.1 P-type: PECVD

The sheet resistance R_S is determined for multiple samples of the p-type wafer with the PECVD grown B impurity layer. For each step height a squared sample is used. The results of the R_S are compared to the simulation in figure 5.12.

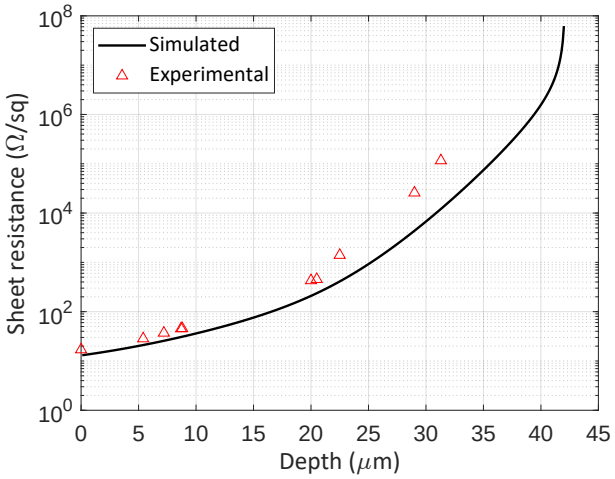

Figure 5.12: Comparison between the simulated and measured sheet resistance for p-type PECVD grown wafer with $x_j = 42$ μm. The simulated profile uses a diffusion temperature of 1250 °C.

As can be seen from figure 5.12, for small step height the measured R_S is very close to the simulated R_S, especially for the smaller step heights. For step heights above 22 μm, the R_S increases at a faster rate than simulated. This can be due to a smaller junction depth x_j, which causes the R_S to increase for smaller depths at a faster rate.

When the measured R_S points are converted to dopant concentrations, the effect of the smaller junction depth should also be visible. All dopant atoms are assumed to be ionized, such that it holds that $p \approx N_A$. In figure 5.13, the simulated dopant concentration is compared to the four-point probe measurements. The simulation uses a diffusion temperature of 1250 °C. In figure 5.14, the effect on the dopant profile of lowering the diffusion temperature by 20 °C is illustrated. This variation may originate from the furnace's accuracy and not from the settings.

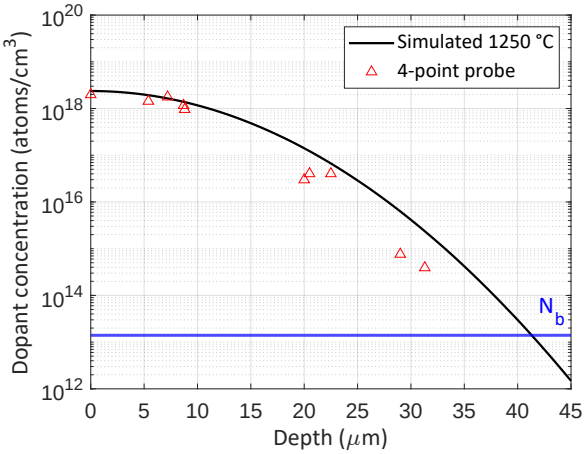

Figure 5.13: The four-point probe measurements are compared to the simulated dopant profile. The results align with a diffusion profile, but differ at depth larger than 22 μm. N_b is the base concentration in the wafer.

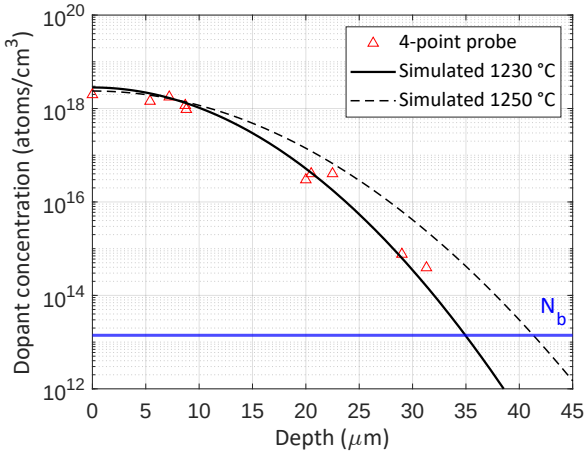

Figure 5.14: The four-point probe measurements are compared to the simulated dopant profile. Lowering the diffusion temperature to 1230 °C fits better to the achieved four-point probe results. N_b is the base concentration in the wafer.

Using a lower diffusion temperature results in a smaller junction depth. Based on the comparison in figure 5.14, a lower diffusion temperature seems to fit better to the measurements point of the four-point probe at depths above 22 μm. The findings of the four-point probe align very well to the simulated dopant profile.

5.4.2 P-type: epitaxy

The sheet resistance R_S is also determined for multiple samples of the p-type wafer with the epitaxially grown impurity layer. For each step height a squared sample is used. The results of

the R_S are compared to the simulated R_S in figure 5.15.

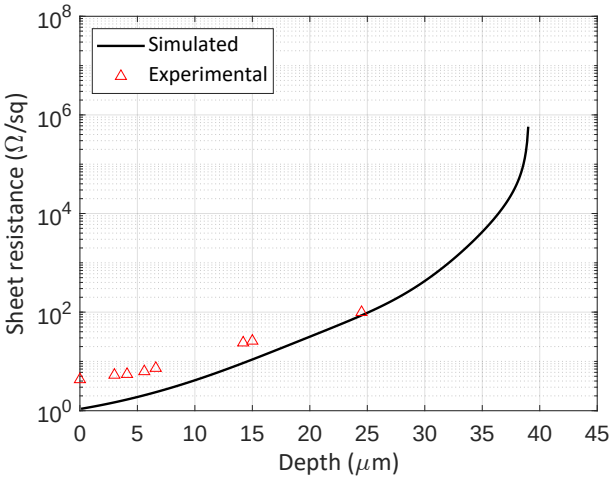

Figure 5.15: Comparison between the simulated and measured sheet resistance for p-type epitaxially grown wafer with $x_j = 38$ μm. The simulated profile uses a diffusion temperature of 1250 °C.

As can be seen from figure 5.15, for small step heights the measured R_S is larger than the simulated R_S and has a different slope. For step heights above 22 μm, the measured R_S is closer to the simulated values. The measured R_S has not been determined for depths larger than 24.5 μm. The measured R_S points are converted to dopant concentrations and are compared to the simulated dopant concentrations. This is illustrated in figure 5.16. The effect on the dopant profile of lowering the diffusion temperature by 20 °C, which yielded a better fit for the p-type PECVD wafer, is also included in figure 5.16.

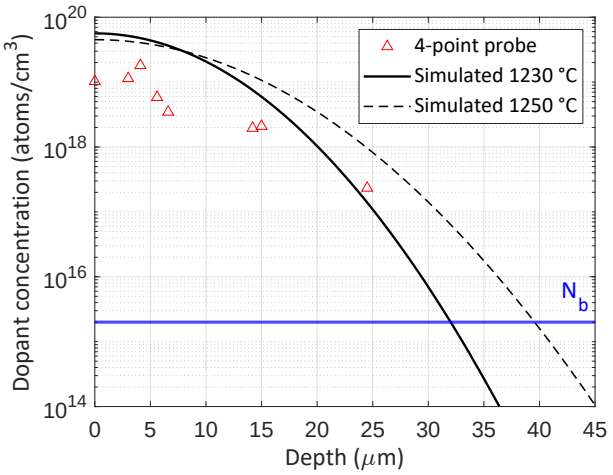

Figure 5.16: The four-point probe measurements are compared to the simulated dopant profile. Lowering the diffusion temperature to 1230 °C, as was used for p-type PECVD, yields no significant improvement in the fitting as the measured concentrations are significantly lower than the simulated concentrations. N_b is the base concentration in the wafer.

Dopant concentrations determined with the four-point probe are not as close to the simulated dopant profile as was the case for the p-type PECVD wafer. The effect of including a lower diffusion temperature is limited and only causes the deepest measured point to align with the dopant profile, similar to the measured and simulated R_S. Moreover, the dopant concentration increases at the third measurement point instead of decreasing. Overall, dopant concentrations are higher than observed for the p-type PECVD wafer, as expected based on the simulations.

5.4.3 N-type: PECVD

Lastly, the sheet resistance R_S is also determined for multiple squared samples of the n-type wafer with the PECVD grown impurity layer. The results of the R_S are compared to the simulated R_S in figure 5.17.

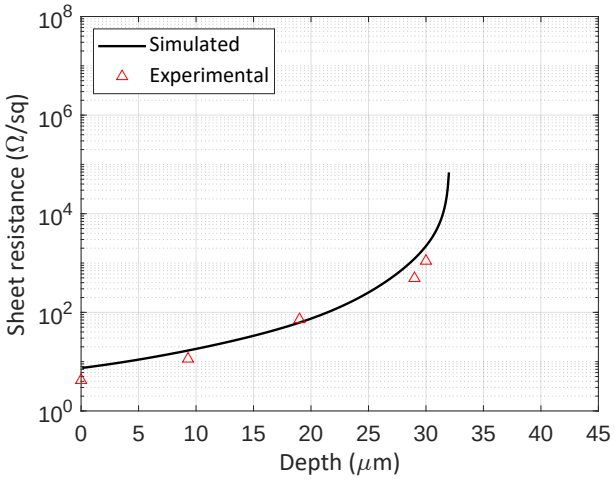

Figure 5.17: Comparison between the simulated and measured sheet resistance for n-type PECVD grown wafer with $x_j = 32$ μm. The simulated profile uses a diffusion temperature of 1250 °C.

Measuring the R_S for the n-type samples proved to be more difficult with the four-point probe frequently giving an error reading. After readjusting the sample, the four-point probe still encountered errors. This means that the number of successful measurements is reduced to only five data points. However, the limited number of data points for the R_S measurements seem to align closely with the simulated R_S, as can be seen in figure 5.17. The R_S-values are converted to dopant concentrations and are compared to the simulated dopant concentrations. This is illustrated in figure 5.18. The effect on the dopant profile of lowering the diffusion temperature by 20 °C, which yielded a better fit for the p-type PECVD wafer, is also included in figure 5.19.

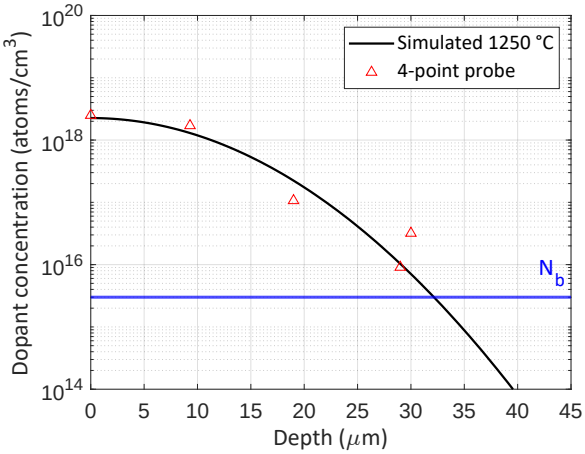

Figure 5.18: The four-point probe measurements are compared to the simulated dopant profile. The results align with the diffusion profile, but still show some variations. N_b is the base concentration in the wafer.

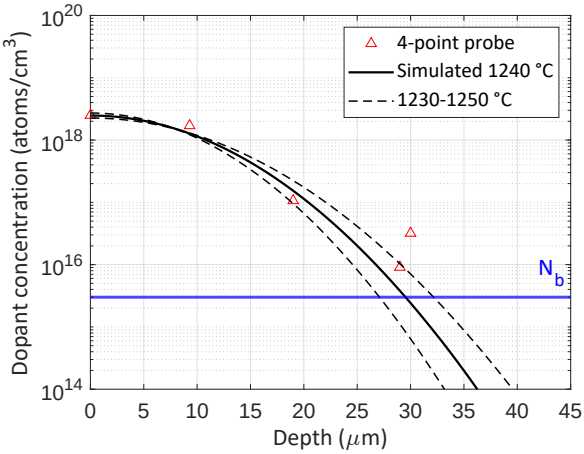

Figure 5.19: The graph includes the effect of a lower diffusion temperature. The dopant profile falls in between the measurement points from the four-point probe for a temperature of 1240 °C. N_b is the base concentration in the wafer.

Despite the limited number of data points, the experimentally determined dopant profile through the use of the four-point probe seems to agree with the simulated profile. However, the measurement point at $x = 30$ μm is far off from the simulated profile. Overall, it seems that a dopant profile has been implemented into the wafer up to a depth of at least 30 μm as the R_S still increased for this depth.

5.5 Spreading resistance profiling (SRP)

The company of SGS Fresenius GmbH performed SRP analysis on two of the nonuniformly doped p-type samples, the PECVD and epitaxially grown samples. The results include the measured depth, resistance, resistivity and consequently the carrier concentration. In this case the carrier concentration is equal to the B concentration, as all dopant atoms are ionized, i.e. $p \approx N_A$. The parameters of the used SRP system are indicated in table 5.1. The scan depth is smaller for the epitaxially grown wafer as the base concentration was measured at an smaller depth compared to the PECVD grown wafer. The step size in the measurement ranges is equal to 0.5 μm.

Table 5.1: The parameters of the SRP system used by SGS Fresenius GmbH for the analysis of the samples.

Parameter [unit]	**Value**
Bias voltage [mV]	5
X-step size [μm]	5
Probe load [g]	10
Probe spacing [μm]	37
Bevel angle [°]	5.739
Depth [μm]	59.4762 - 73.944

5.5.1 P-type: PECVD

For the PECVD grown wafer, the results of the spreading resistance $R_{SP}(x)$, and consequently the resistivity $\rho(x)$, are illustrated in figure 5.20. The left y-axis indicates the measured resistance, while the right (red) y-axis indicates the resistivity. In figure 5.21, the dopant concentrations determined through the SRP analysis are compared to the simulated profiles within a temperature range of 1230 °C to 1250 °C. The base concentration N_b is included in the profiles.

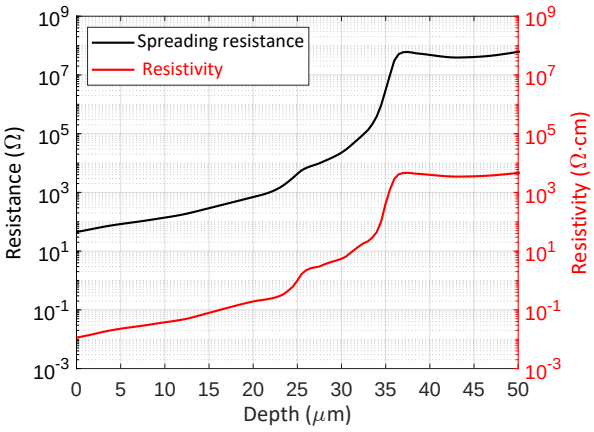

Figure 5.20: The measured R_{SP} (black) and consequently the ρ (red) are plotted as function of depth for the PECVD sample. A junction depth of 36 μm is achieved, instead of the simulated 42 μm.

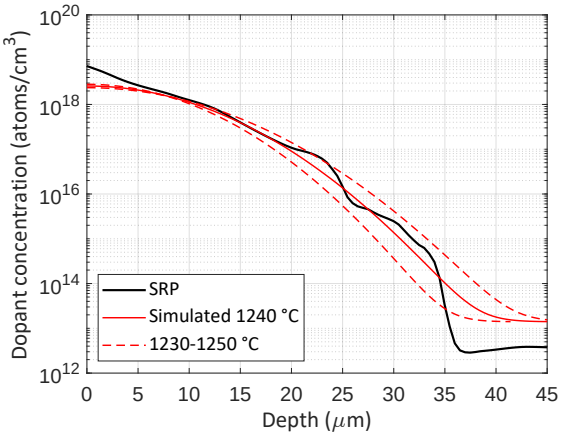

Figure 5.21: The dopant profile through SRP (black) is compared to the simulated profiles for 1230-1250 °C (red-dotted). The simulated profile of 1240 °C (red-solid) seems to match the SRP the best.

Based on the R_{SP}-profile, the junction depth x_j is estimated at 36 μm. In the simulation, x_j was 42 μm. This means that the B impurities did not diffuse as far as was simulated. This reduction in x_j can also be observed in figure 5.21. The black line becomes horizontal after around 36 μm, indicating that the concentration is equal to the base concentration N_b of the wafer. A set diffusion temperature of 1240 °C causes the simulated and measured profile to overlap for a significant part of the profile. The measured dopant profile is not as fluent and continuous in slope as the simulated profile. Besides, the measured surface concentration is higher than the simulated concentration. Overall, the experimental achieved profile seems to match the simulated profile of 1240 °C quite well.

5.5.2 P-type: epitaxy

For the epitaxially grown wafer, the results of the spreading resistance R_{SP} and consequently the resistivity ρ are illustrated in figure 5.22. On the left y-axis the measured resistance is indicated, while the right (red) y-axis indicates the resistivity. In figure 5.23, the dopant concentrations determined through the SRP analysis are compared to the simulated profiles within a temperature range of 1230 °C to 1250 °C.

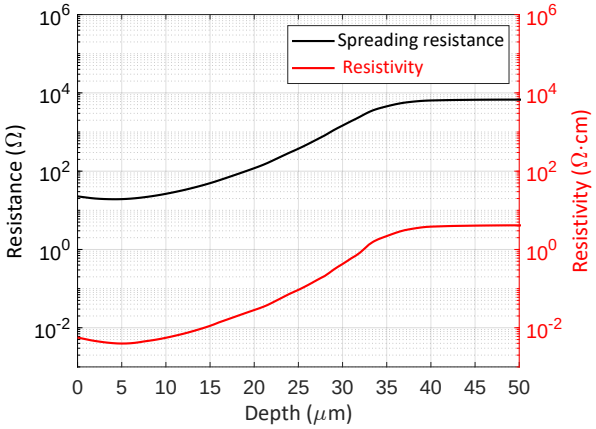

Figure 5.22: The measured R_{SP} (black) and consequently the ρ (red) are plotted as function of depth for the epitaxial sample. A junction depth of roughly 37 μm is achieved instead of the simulated 38 μm.

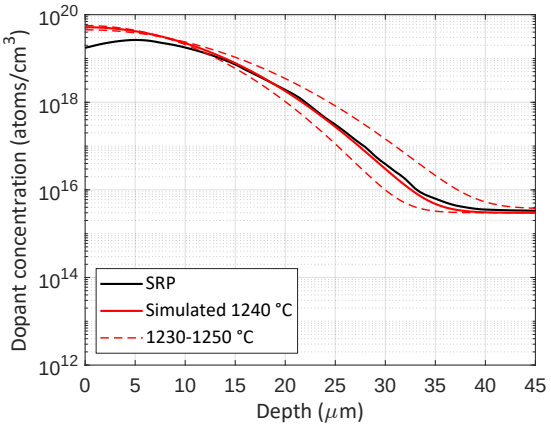

Figure 5.23: The dopant profile through SRP (black) is compared to the simulated profiles for 1230-1250 °C (red-dotted). The simulated profile of 1240 °C (red-solid) seems to match the best.

Based on the R_{SP}-profile, the junction depth x_j is estimated at 37 μm. In the simulation, x_j was 38 μm, which means that the experimental results are very close to the simulated profiles. The reduction in x_j can also be observed in figure 5.23. The black line becomes horizontal after around 36 μm.

When the diffusion temperature is lowered from 1250 °C to 1240 °C, a close overlap between the simulated and measured profile can be observed for a significant part of the profile. The measured surface dopant concentration is lower than the simulated concentration, but increases in the first 5 μm of the dopant profile. After this increase, the dopant concentration decreases according to a Gaussian profile. Overall, the experimental achieved profile seems to match the simulated dopant profile of 1240 °C very well.

5.6 Comparison SRP and sheet resistance

In the previous subsections, the sheet resistance and SRP have been used to determine the dopant profile of the produced samples. In this subsection, the results of both methods are directly compared to each other. In figure 5.24, the dopant profile of the PECVD grown wafer is shown over a dynamic range of 8 orders of magnitude in concentration, i.e. from 10^{12} to 10^{20} atoms/cm^3. The dopant profile of the epitaxially grown wafer is shown in figure 5.25. The data points of the four-point probe and the simulated profiles have been added to the SRP profiles to allow for a direct comparison.

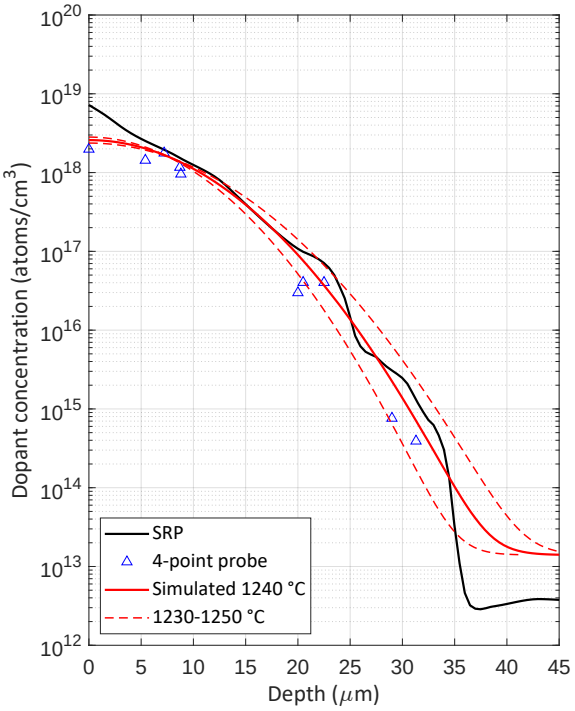

Figure 5.24: Comparing the SRP (black) with the four-point probe and simulated (red) dopant profiles for the PECVD grown wafer.

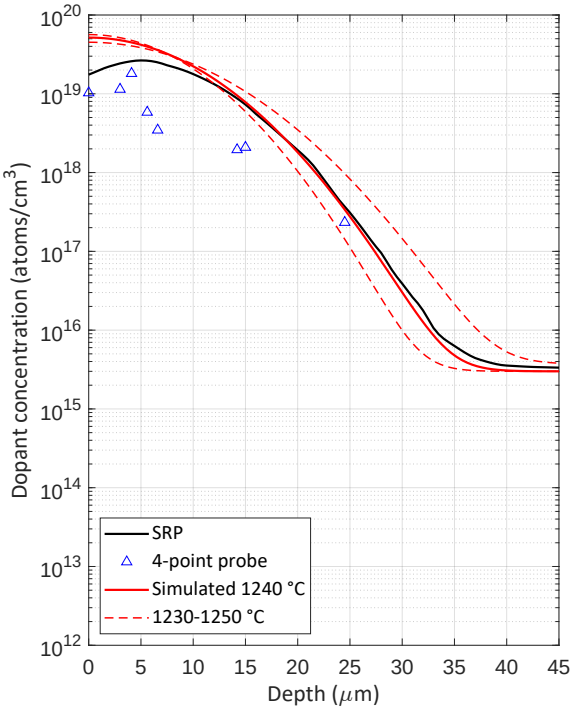

Figure 5.25: Comparing the SRP (black) with the four-point probe and simulated (red) dopant profiles for the epitaxially grown wafer.

As can be observed from figure 5.24, the dopant profile for the p-type PECVD grown wafer spreads over nearly 7 orders of magnitude, i.e. 10^{12} - 10^{19} atoms/cm^3. The base concentration of 4×10^{12} atoms/cm^3 is lower than the expected 1×10^{13} atoms/cm^3. This slightly increased the junction depth. When comparing the profile to the epitaxially grown wafer in figure 5.25, it can be clearly seen that the base concentration is higher in the epitaxial wafer. The surface concentration is also higher in the epitaxial wafer and further increases for the first 5 μm, as a highly B-doped Si is placed on top of the pure B layer. This increase in the beginning has extended the junction depth as the concentration gradient of both profiles is similar.

For the PECVD grown n-type wafer it can be observed that the dopant concentrations determined by the four-point probe measurements closely approximate the simulated dopant profile, despite the limited number of available data points. For all levels of concentration, ranging from low to high, the data points are near the simulated profile. The SRP profile contains more data points and closer approximates the real experimental dopant concentrations in the samples. The SRP profile compares best to the simulated dopant profile with a diffusion temperature of 1240 °C.

The results observed in the epitaxially grown wafer are somewhat different compared to the PECVD grown wafer. The dopant concentrations determined with the four-point probe for low depths are not very consistent with the simulated and SRP dopant profile. For larger depths this is more in line with the simulations and SRP, but is still off to some extent. The larger the depth, the lower the dopant concentration and thus the higher the measured sheet resistance. For higher dopant concentrations the four-point probe measurements differ more from the simulated concentrations. The SRP dopant profile is very close to the simulated profile with a lowered diffusion temperature of 1240 °C.

Chapter 6

Corrosion results

In this chapter the corrosion in the used setup is quantified by studying the mass consumption, conversion efficiencies and step heights. In section 6.1, the corrosion in uniformly doped Si is quantified. These results are also compared to literature. Section 6.2 presents the results from the nonuniformly doped wafers to see to what extent corrosion has been mitigated.

6.1 Uniformly doped silicon

With the setup being more stable due to the improvements discussed in chapter 4, the corrosion of the Si anode in this setup can now be studied. Before the proposed solution to mitigate the corrosion in alkaline Si-air batteries can be tested, the corrosion first needs to be quantified to function as a reference. The corrosion will be quantified by looking at the mass consumption of the Si anode as well as the step height. The methodology to determine these parameters follows from the steps described in section 3.7. These steps are followed for both p-type and n-type Si. The results are compared to values achieved in literature.

6.1.1 P-type

The first experimental efforts are focused on characterizing the corrosion in p-type Si. For the non-aqueous RTIL electrolytes, it was found by Durmus et al.[42], based on mass consumption data, p-type Si corroded at a considerably lower rates than n-type Si. B-doped Si samples had corrosion rates of 66 nm/h, while antimony doped Si samples had corrosion rates of 175 nm/h. For aqueous electrolytes, the corrosion rates for n-type Si have been determined, whereas they have not yet been characterized for p-type Si.

The mass consumption is determined using the approach described in section 3.7.2. At time intervals of 8, 16, 24 and 48 hours the mass before and after discharge is determined. These steps are repeated for OCP and increasing current densities of 10, 25 and 50 μA/cm^2. Through initial experiments it turned out that discharge periods of at least several hours were needed to observe a measurable mass consumption. Moreover, these periods are chosen such that they can be started and finished at convenient times during the day. The mass consumption data is plotted as a function of time in figure 6.1.

Based on the mass consumption, the mass conversion efficiency can be calculated using the total consumed mass m_t and the electrochemical discharged mass m_d as was given in equation 3.7.4. The electrochemcial reaction assumes that the reaction is a four electron process. The mass conversion efficiency is averaged for each current density over the four time intervals. The standard deviation in these averaged measurements is also taken into account in the errorbars. The results are presented in figure 6.2. In the work of Durmus et al. [44], the conversion efficiencies were determined in a similar manner but then for n-type Si. These results are included as a reference in figure 6.2.

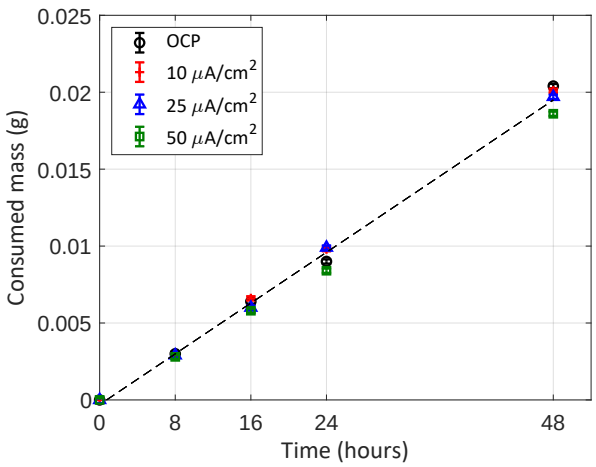

Figure 6.1: The mass consumption of p-type Si before and after discharge for time intervals of 8 hours up to 48 hours and different current densities and OCP. A linear fit through all points is added.

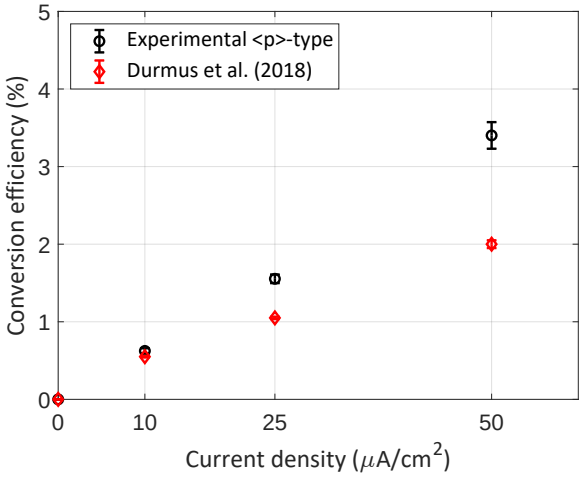

Figure 6.2: The average conversion efficiency is determined for each current density, based on the results in the plot on the left. The experimental results are compared to literature [44].

As can be seen in figure 6.1, the mass consumption increases linearly with respect to time. This means that the consumption of Si takes places at a constant rate. Moreover, the mass consumption at OCP conditions is very similar to the mass consumption at applied current densities, with only small changes close to the accuracy limit of the used scale. Based on these mass consumption results, a maximum specific capacity of 135 mAh/g is achieved for p-type Si.

The achieved mass conversion efficiencies show in figure 6.2 are very low when compared to the nearly 100% efficient Li-ion batteries, but they are higher than values currently achieved in literature through similar experiments conducted by Durmus et al. for n-type Si [44]. This indicates that the corrosion rates of p-type are indeed lower.

Another method of quantifying the corrosion is by determining the step height between the active and inactive surface of the samples. The O-ring covers the surface of the Si sample to expose only a 1 cm^2 area to the electrolyte. This means that the rest of the surface remains unaffected and flat. During OCP and discharge, the Si is actively being consumed. The step height thus increases in absolute values over time. The corrosion rate in μm/h can be determined by dividing the total step height by the total discharge time in hours.

A step height profile for a discharged Si sample at a current density of 50 $\mu A/cm^2$ is given in figure 6.3. This sample has first been discharged for a period of 24 hours, taken out of the setup, rinsed and dried, put back into the same setup and discharged for another 24 hours. The step height after 24 hours was 30 μm and after 48 hours this has increased to 60 μm. This corresponds to an average corrosion rate of 1.25 μm/h. The horizontal plateau in between the two vertical etch lines indicates that the sample was misaligned by roughly 500 μm, or 0.5 mm, when it was reinstalled in the setup. When the step heights of different samples for 8, 16, 24 and 48 hour discharge periods at a current density of 50 $\mu A/cm^2$ are included in one graph, as illustrated in figure 6.4, it can be clearly seen that this results in similar profiles with similar corrosion rates of ca. 1.25 μm/h. Only for the 48 hour discharge period, the corrosion has slightly increased to 1.27 μm/h, as the step height increased to 61 μm. This means that the corrosion rates remain fairly constant throughout the discharge process.

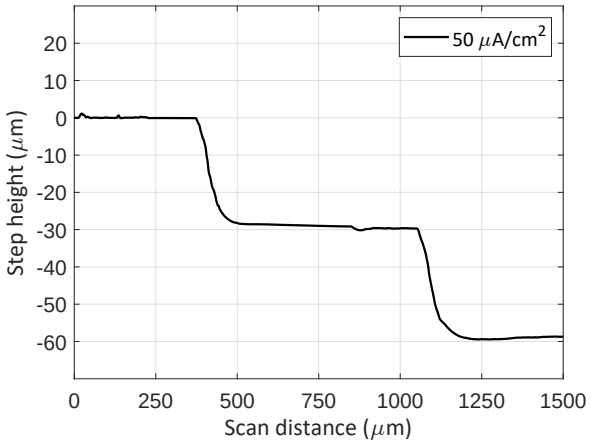

Figure 6.3: Step height profile for a single sample that has been discharged for 24 hours, disconnected and discharged for an additional 24 hours.

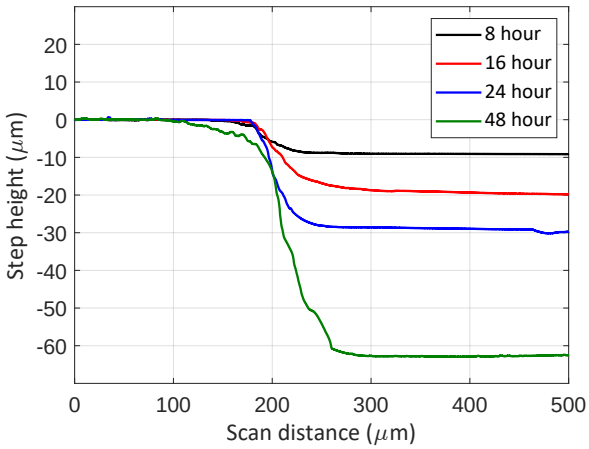

Figure 6.4: Step height profiles of p-type Si for different samples that have been discharged at 50 μA/cm^2 for periods of 8, 16, 24 and 48 hours.

To observe whether the consumed mass is proportional to the step height, is to look at the mass consumption as a function of the step height. The mass consumption at an applied current density of 50 μA/cm^2 shown in figure 6.1 is combined with the step height shown in figure 6.4 at the same current density. The result is shown in figure 6.5, with the addition of a linear fit.

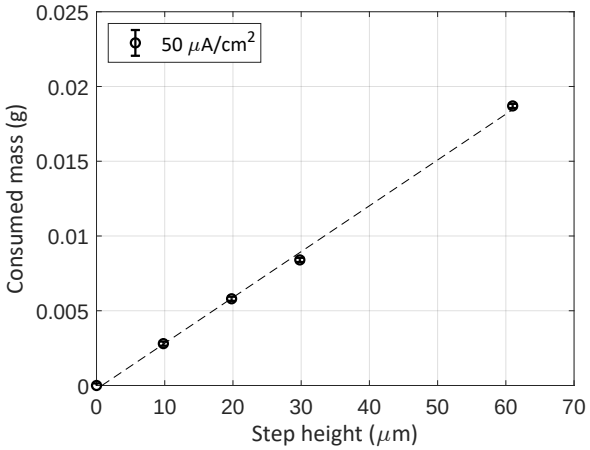

Figure 6.5: The mass consumption is plotted as a function of the step height for the samples discharged at 50 μA/cm^2.

From figure 6.5 it becomes clear that the consumed mass scales linearly with the step height, since a straight line, starting at the origin, can be fitted through the data points with only small deviations. The points lie either on the line or are very close to it. The same steps are repeated for n-type Si in the next subsection.

6.1.2 N-type

The same quantification steps are repeated for n-type Si. The mass consumption is determined at time intervals of 8, 16, 24 and 48 hour for 10, 25 and 50 μA/cm^2 current densities. Figure 6.6 depicts the mass consumption. The mass conversion efficiency is calculated using the total consumed mass and the electrochemical discharged mass, which is based on a four electron process. The conversion efficiencies are compared to the results of Durmus et al. [44], where similar experiments are conducted, also for n-type Si samples.

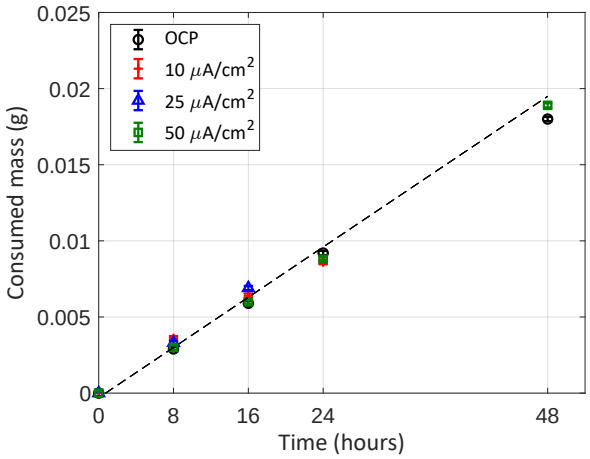

Figure 6.6: The mass consumption of n-type Si before and after discharge for time intervals of 8 hours up to 48 hours and different current densities and OCP.

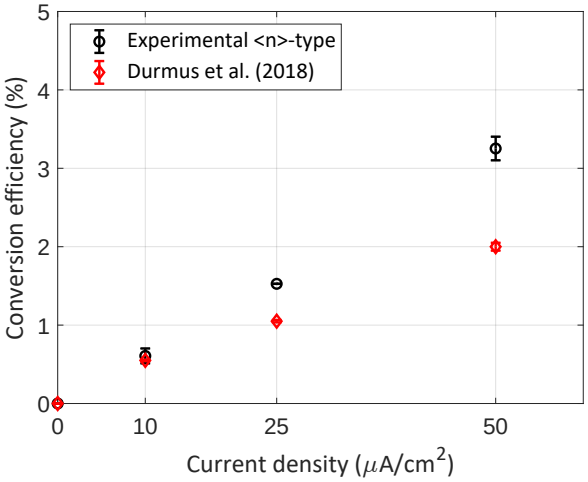

Figure 6.7: The average conversion efficiency is determined for each current density, based on the results in the plot on the left. The experimental results are compared to literature [44].

Similar to p-type Si, the mass consumption increases linearly with respect to time, indicating a constant consumption of Si at the anode. The absolute mass consumption is also similar in size compared to p-type Si. Based on the differences between the consumption at OCP and at an applied current density, the consumption of Si appears also chemical in nature as the effect of applying a current density is very small. Based on these mass consumption results, a maximum specific capacity of 130 mAh/g is achieved for n-type Si. The step heights of different samples for 8, 16, 24 and 48 hour discharge periods at a current density of 50 μA/cm^2 are included in one graph in figure 6.8.

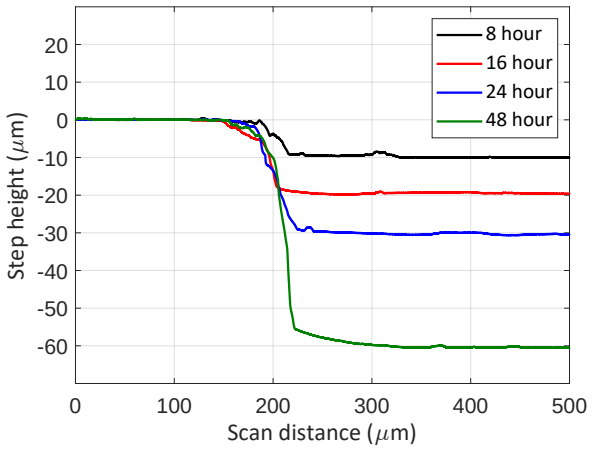

Figure 6.8: Step height profiles of n-type Si for different samples that have been discharged at 50 μA/cm^2 for periods of 8, 16, 24 and 48 hours.

It can be clearly seen from the step heights that n-type Si has similar etch profiles with similar constant corrosion rates of around 1.25 μm/h, compared to p-type Si.

The mass consumption at an applied current density of 50 μA/cm^2 shown in figure 6.6 is combined with the step height shown in figure 6.8 at the same current density. The result is shown in figure 6.9, with the addition of a linear fit.

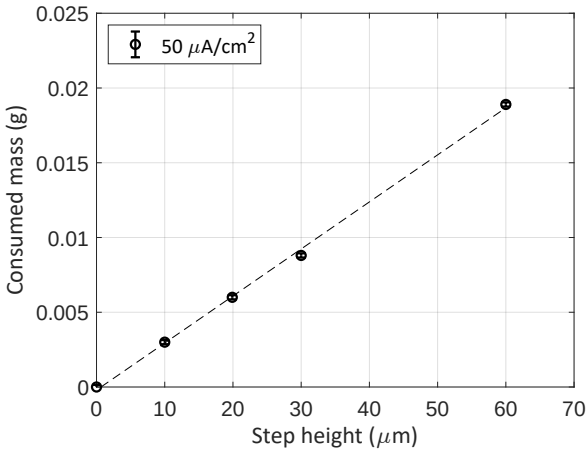

Figure 6.9: The mass consumption for 8-48 hour discharging is plotted as a function of the step height for the same samples discharged at 50 μA/cm^2.

Based on the graph in 6.9, the consumed mass scales linearly with the step height.

6.1.3 Comparison

The results of both p-type and n-type Si will be compared with each other and with values found in literature [44]. The comparison is based on a number of parameters that are listed in table 6.1. This includes the wafer type, surface structure, wafer resistivity, crystal orientation, electrolyte volume and concentration, applied current density, achieved corrosion rates and the efficiency.

Table 6.1: Direct comparison between the results of Durmus et al. [44] and the results presented in this section. Both experimental setups use KOH as an electrolyte.

Parameter [unit]	**Durmus et al. [44]**	**This work**	
Type of wafer	<n>	<n>	<p>
Wafer surface	Flat	Flat	Flat
Wafer resistivity [Ωcm]	0.001 - 0.007	1 - 5	> 1000
Crystal orientation	<100>	<100>	<100>
Electrolyte volume [ml]	0.5	4.0	4.0
KOH concentration [mol/l]	5	6.6	6.6
Current density [μA/cm^2]	50	50	50
Corrosion rate [μm/h]	2.2	1.25	1.25-1.27
Efficiency [%]	2.00±0.05	3.25±0.15	3.40±0.17

The corrosion rates in the results of these work are lower when compared to the results of Durmus et al. [44], despite the higher electrolyte concentration. This means that corrosion is more suppressed in this setup. The main difference between the work of Durmus et al. and this work lies in the lower resistivity in the used wafers and smaller electrolyte volume by Durmus et al.

While in the results of Cohn et al. [42], a clear reduced mass consumption, and thus corrosion, was observed for p-type Si with respect to n-type Si, the results in this work show very similar mass consumption and consequently step height for p-type and n-type Si. This is illustrated in figure 6.10, where the consumed mass is plotted as a function of step height for both p-type and n-type Si.

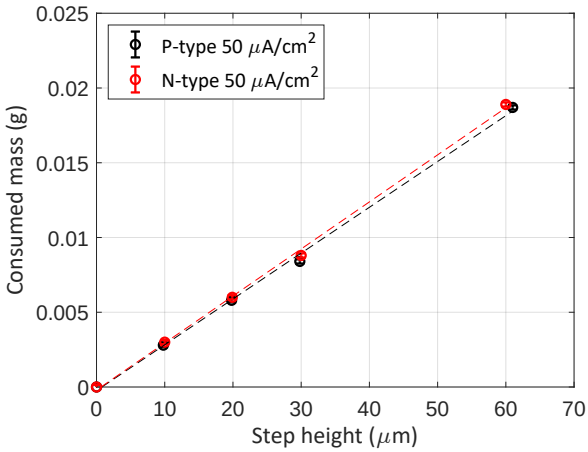

Figure 6.10: For p-type and n-type Si, the mass consumption for 8-48 hour discharging is plotted as a function of the step height for the same samples discharged at 50 μA/cm^2.

Cohn et al. used a non-aqueous electrolyte, while an (aqueous) alkaline electrolyte is used in this work. The small difference in conversion efficiency between p-type and n-type Si in this work is due to the lower average mass consumption of p-type Si for the current density of 50 μA/cm^2, as can be observed in figure 6.10. The mass consumption for 24 and 48 hours is slightly lower in p-type Si, while the step height is slightly larger for 48 hours in p-type Si. This contradicts each other.

The conversion efficiencies in this work are higher than the efficiencies in the work of Durmus et al. [44], but they are still low in the range of only 3%. This means that the parasitic consumption of Si, i.e. corrosion, is significant. The results in the next section present efforts in the mitigation of this corrosion in alkaline Si-air batteries.

6.2 Nonuniformly doped silicon

Based on the results of the previous section, the corrosion of the Si anode on discharging should be reduced in order to increase the efficiency of the battery. A proposed method to mitigate this corrosion is the implementation of a dopant profile in the Si anode through the diffusion of impurity atoms. The exact steps were described in the experimental method in section 3.3.

6.2.1 P-type: PECVD

The results of the p-type wafer with a deposited p-type a-Si:H layer by PECVD are presented here. First, the discharge behavior is analyzed and compared to the discharge behavior of uniformly doped Si, as determined in section 4.4. In the battery setup, the anode material is changed from a uniformly doped sample to a nonuniformly doped sample. All other parts in the setup are kept the same.

In one of the galvanostatic discharges at 50 μA/cm^2, the battery's potential gradually increased from 0.65 V to 0.90 V during discharge, but after 12 hours gradually decreased again to the initial value of 0.65 V. This behavior is portrayed in figure 6.11. To verify these results, the measurement is repeated under the same conditions, but with a different sample from the same wafer. This is illustrated in figure 6.12. In this second attempt, the potential remained constant and in line with the uniform doped Si.

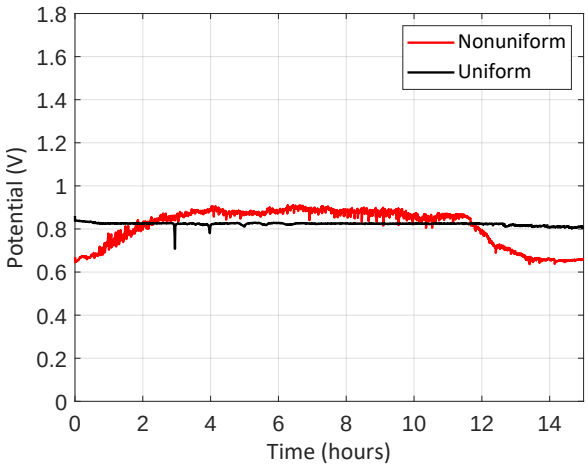

Figure 6.11: Galvanostatic discharge at 50 μA/cm^2. The potential of the nonuniformly doped p-type Si anode increased in the first 12 hours, while the uniform p-type anode's potential remained constant. The potential decreased again after 12 hours.

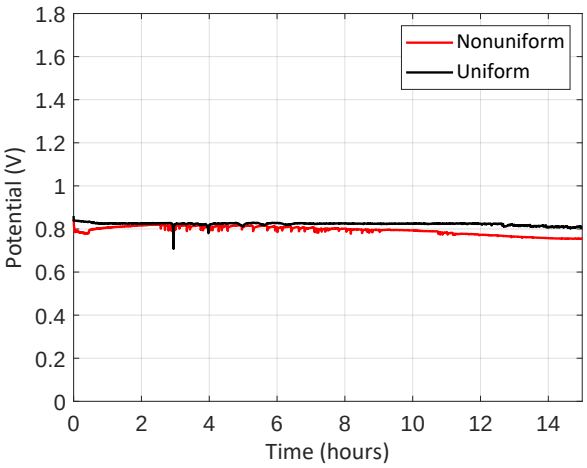

Figure 6.12: Galvanostatic discharge at 50 μA/cm^2. When the measurement was repeated under the same conditions, but with a new sample, the increase in potential was not observed. In fact, the potential is aligned with the uniform potential behavior.

The mass consumption in OCP and discharge conditions is determined for the time periods of 5, 8, 16 and 24 hours. To see whether the mass consumption accelerates or decelerates over time due to the dopant profile, the time step of 5 hours is added. Based on the simulated dopant profiles, the concentration gradient, and thus the diffusion of charge carriers, reaches its maximum at $x = \sqrt{2Dt} = 8.5\mu$m. Taking into account the corrosion rate of 1.25 μm/h for uniform doped Si, it will roughly take 6.8 hours before this steepest point is reached. The 5 hour period enables to observe any change in corrosion rate before and after this steep point.

The OCP mass consumption for the nonuniform doped Si is given in figure 6.13 and is compared to the uniform Si mass consumption. A current density of 50 μA/cm^2 is applied as this provides the largest possible electron injection with respect to OCP conditions. The effect of applying a current density on the mass consumption is shown in figure 6.14.

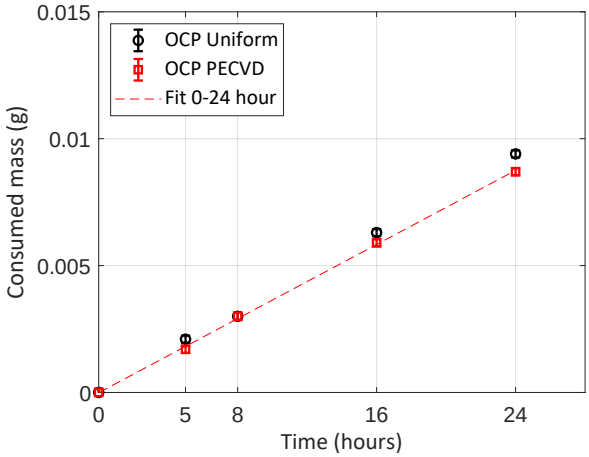

Figure 6.13: The mass consumption of p-type Si before and after discharge for time periods of 5 hours up to 24 hours for OCP. A linear fit is added for the nonuniformly doped Si data points.

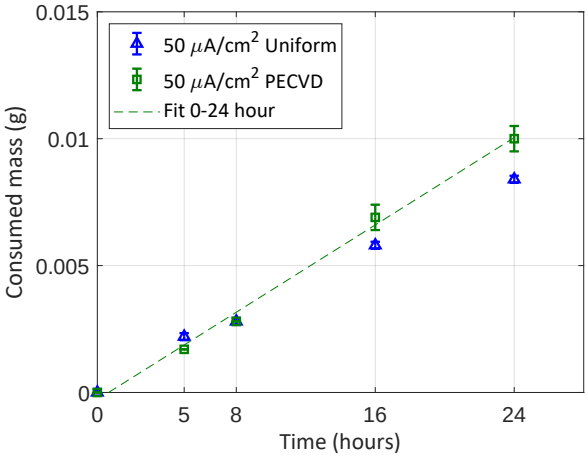

Figure 6.14: The mass consumption of p-type Si before and after discharge for time periods of 5 hours up to 24 hours for 50 μA/cm^2. A linear fit is added for the nonuniformly doped Si data points.

From figure 6.13 it can be seen that the mass consumption with the PECVD diffused impurity layer during OCP conditions is very similar with respect to the uniform Si. After 8 hours, the mass consumption of the PECVD diffused Si decreases a bit. These steps are very small, only in the order of a 0.3±0.14 mg.

With an applied current density, the mass consumption is again very similar for time periods

up to 8 hours, but starts to increase for longer time periods. After 16 hours, the consumed mass has increased by 0.95±0.14 mg, or 15%. For the 24 hour period, the mass consumption increased by roughly 10%. The efficiency was lowered on average from 3.40% to 3.0%. Overall, with the implementation of a dopant profile in actively discharging p-type Si, the corroded mass has increased slightly with respect to OCP.

Besides the mass consumption, the step height is studied for the nonuniform doped Si samples. Again, the time steps of 5, 8, 16 and 24 hours are considered on discharging. These step heights are illustrated in figure 6.16.

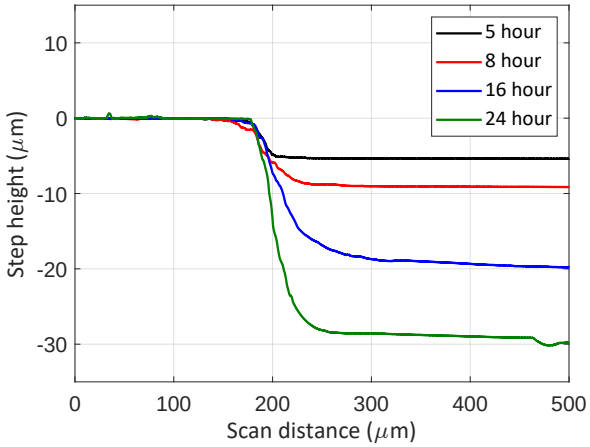

Figure 6.15: Step height profiles of uniform p-type Si after periods of 5, 8, 16 and 24 hours of discharging. A smooth Si surface is visible in both the etched and non-etched part.

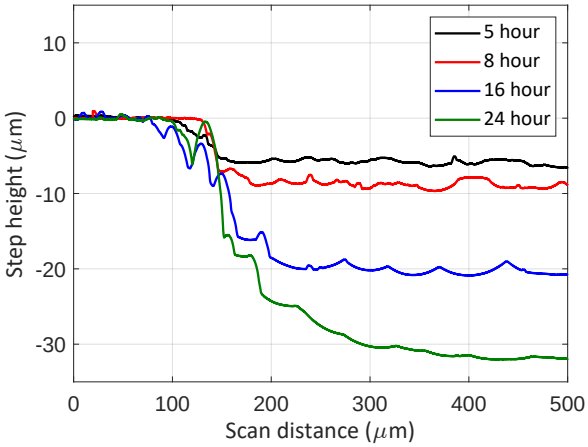

Figure 6.16: Step height profiles of nonuniformly doped p-type Si discharged at 50 μA/cm^2 for periods of 5, 8, 16 and 24 hours. The corrosion rate is nearly constant over time, with a rough surface.

When looking at figure 6.16 above, it can be noticed is that the graphs are wobbly and the surface is rougher for nonuniformly doped Si when compared to the uniformly doped Si in figure 6.15. The exact step heights are therefore difficult to determine and have a lower accuracy. On average, the step height has not increased by the same amount that the mass consumption increased for the 16 and 24 hour period. The results suggest that the active surface area increases with increasing roughness.

In figure 6.17, the mass consumption at an applied current density of 50 μA/cm^2 is combined with the step heights of figure 6.8 at the same current density. A linear fit is added.

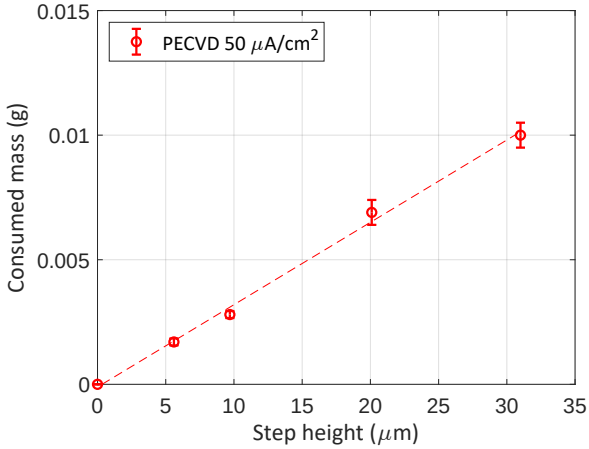

Figure 6.17: The mass consumption is plotted as a function of the step height for nonuniformly doped p-type samples made with PECVD and discharged at 50 μA/cm^2.

From figure 6.17 it can be seen that the mass does not increase linearly with the step height for all discharges. The mass consumption is too high for 20 μm, while being closer for the 31 μm step height. The uncertainty in mass consumption is also larger for these measurements.

6.2.2 P-type: epitaxy

The results of the p-type wafer with an epitaxially grown B layer are presented here. The same steps are repeated as was done for the PECVD grown wafer. First, the discharge behavior is compared to uniform doped p-type Si. As can be observed in figure 6.18, when a discharge current density of 50 μA/cm^2 is applied, the surface is quickly passivated within a little more than one minute. Repeating this for a new sample resulted in the exact same behavior, with a passivated surface after a little more than one minute of discharge.

Lowering the discharge current density to 25 μA/cm^2 resulted in a successful discharge with similar potentials of 1.0-1.1 V as the uniform p-type wafers, while the surface remains oxide free. This is illustrated in figure 6.12. In further experiments, the discharge current density for the epitaxial wafer is limited to 25 μA/cm^2.

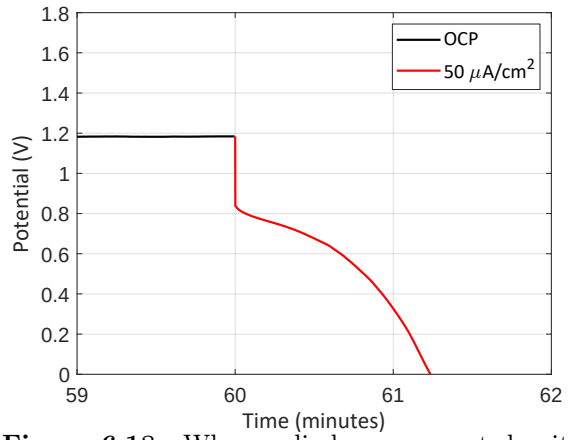

Figure 6.18: When a discharge current density of 50 μA/cm^2 is applied, the Si surface is quickly passivated and the discharge stops.

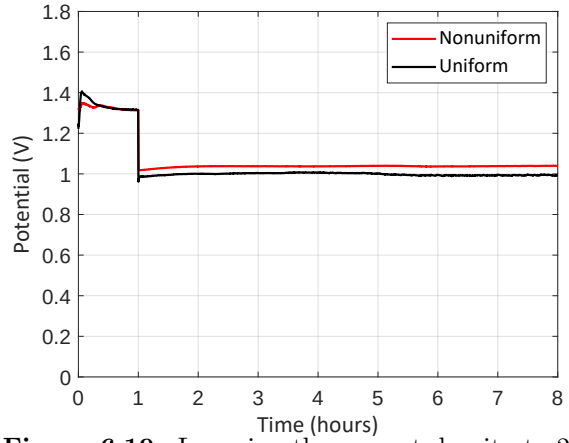

Figure 6.19: Lowering the current density to 25 μA/cm^2 yields a potential curve that is aligned with the uniform potential behavior.

The simulated surface concentration of 4.8×10^{19} atoms/cm^3 in the epitaxial wafer is higher than in the PECVD grown wafer. The influence of this high concentration on the mass consumption of the Si anode in the Si-air battery is studied. Based on the simulated dopant profiles determined in section 5.1, the first 10 μm with a concentration above 2×10^{19} atoms/cm^3 are likely to etch slower. The 5 hour period enables to observe any change in corrosion rate in these first μm. The OCP mass consumption for the nonuniformly doped Si is given in figure 6.20 and is compared to the uniformly doped Si mass consumption. A current density of 25 μA/cm^2 is applied. The effect of a current on the mass consumption is shown in figure 6.21.

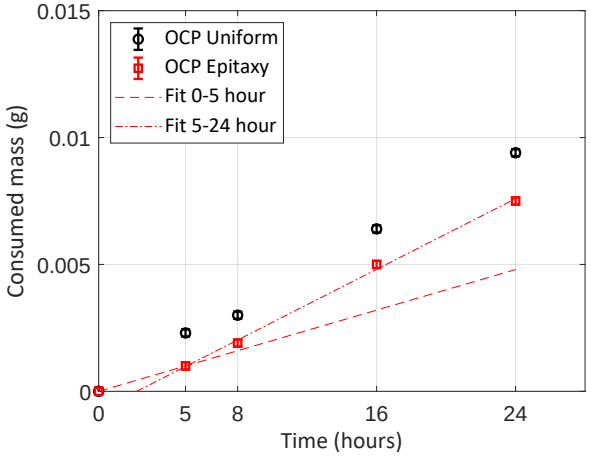

Figure 6.20: The mass consumption of p-type Si before and after discharge for time periods of 5 hours up to 24 hours for OCP. Separate fitted slopes are included for the epitaxy data points in the time period [0,5] and [5,24] hours.

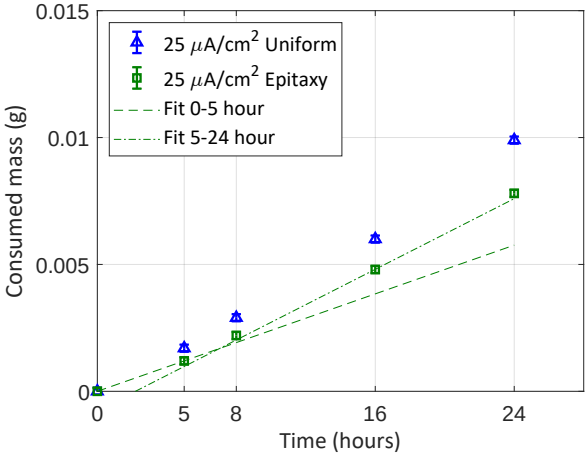

Figure 6.21: The mass consumption of p-type Si before and after discharge for time periods of 5 hours up to 24 hours for 25 μA/cm^2. Separate fitted slopes are included for the epitaxy data points in the time period [0,5] and [5,24] hours.

The mass consumption with the epitaxially grown layer is lower for OCP, when compared to the uniform wafer. In the first 5 hours of OCP, the consumed mass decreased to 1.0±0.14 mg instead of 1.9±0.14 mg for the uniformly doped wafer. This trend continues for longer OCP periods, with the mass consumption increasing from 1.0 to 2.0±0.14 mg for 8 hours and to 4.4±0.14 mg for 16 hours. At 24 hours the mass consumption has increased to 7.5±0.14 mg. When inspecting these numbers, the mass consumption seems to increase at a faster rate after the first 5 hours, which is also visible in the slope between the measurement points in figure 6.20. The slope from 5 to 24 hours is steeper than from 0 to 5 hours.

The mass consumption with an applied current density shows a similar trend as was observed with OCP conditions. In the first 5 hours the consumed mass was 1.2±0.14 mg instead of 1.7±0.14 mg for the uniformly doped wafer. For longer discharge periods the mass consumption increased from 1.2 to 2.2±0.14 mg for 8 hours and to 4.8±0.14 mg for 16 hours. After 24 hours of discharging, the mass consumption had increased to 7.8±0.14 mg. As shown in figure 6.21, the difference in slope between the first 5 hours and the following hours is less pronounced. With the lower mass consumption, the efficiency has increased, on average, from 1.5% to 2.0%. The lower discharge current density of 25 μA/cm^2 limits the efficiency to reach the maximum of 3.4 % that was achieved with the uniform doped Si.

To observe whether the decrease in corroded mass can also be observed in the step heights, the Dektak profilometer is used to inspect this. Time steps of 5, 8, 16 and 24 hours are considered here when the battery is discharged at a current density of 25 μA/cm^2. These step heights are compared to the uniform doped p-type Si, illustrated in figure 6.22. The nonuniformly doped samples are illustrated in figure 6.23.

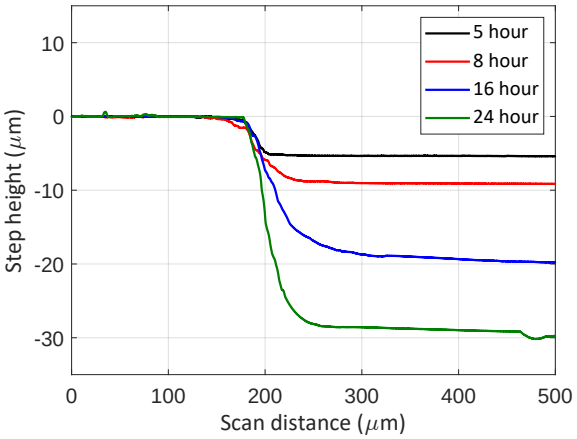

Figure 6.22: Step height profiles of uniformly doped p-type Si after discharging for periods of 5, 8, 16 and 24 hours. A smooth Si surface is visible in both the etched and non-etched part.

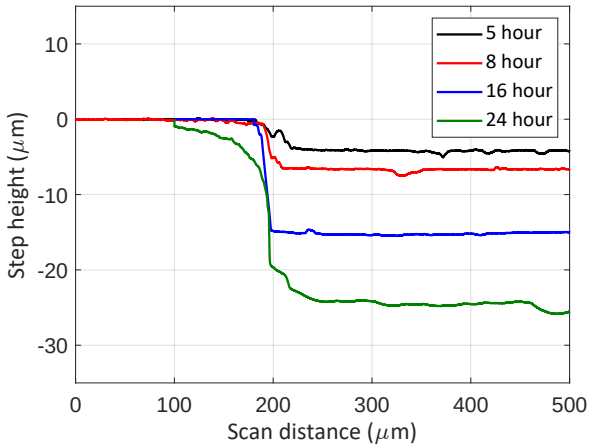

Figure 6.23: Step height profiles of nonuniformly doped p-type Si after discharging at 25 μA/cm^2 for periods of 5, 8, 16 and 24 hours. The surface is rougher compared to uniform doped p-type Si.

The step heights of the nonuniformly doped Si after discharging align with the mass consumption. The step heights are thus lower when compared to the uniformly doped Si. For the 5 hour period, the step height is 4.1 μm. This increased to 6.6 μm for 8 hours and to 15.2 μm for 16 hours. After 24 hours, a step height of 24.6 μm was reached. This means that the etch rate increases from, on average, 0.83 μm/h in the first 8 hours to 1.12 μm/h in the next 16 hours.

In figure 6.24, the mass consumption at an applied current density of 50 μA/cm^2 is combined with the step height shown in figure 6.8 at the same current density. A linear fit is added.

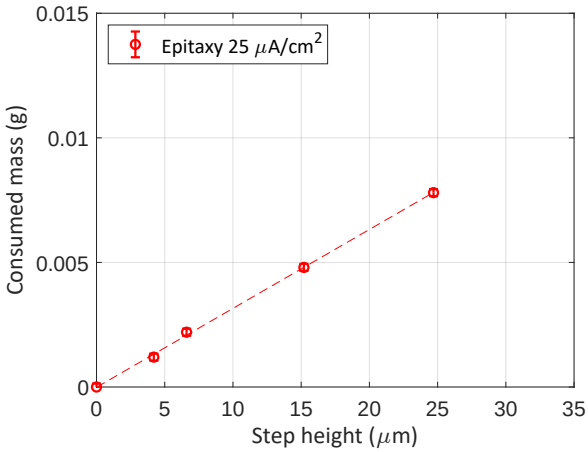

Figure 6.24: The mass consumption is plotted as a function of the step height for nonuniformly doped p-type samples made with epitaxial growth and discharged at 25 μA/cm^2.

From figure 6.24 above, it can be seen that the consumed mass scales linearly with the step height, since a straight line, starting at the origin, can be fitted through the data points with only small deviations for the smalles step height. The points lie either on the line or are very close to it. The same steps are repeated for n-type Si in the next subsection.

6.2.3 N-type: PECVD

The results of the n-type wafer with a diffused n-type a-Si:H layer by PECVD are presented here. First, the discharge behavior is analyzed. A discharge with a sample from the black area, indicated in figure 5.8, is depicted in figure 6.25. When the discharge current density of 50 μA/cm^2 was applied after one hour of OCP, the battery's potential initially showed a constant 1.1 V, a bit higher than the uniform potential of 1.05 V at this current density. After around 3 hours discharging, the potential started to decrease and after 6 hours the potential decreased to 0.1 V. After 9.5 hours of discharging the potential increased to 0.35 V, after which it started to oscillate and eventually drop to 0 V. To see whether these results are consistent in discharging, the measurement is repeated under the same conditions, but with a different sample from a clearer part of the wafer. This is illustrated in figure 6.26. The discharge potential starts at a slightly higher potential of 1.15 V, but drops gradually to 1.05 V, in line with the uniform doped Si. Samples from the clear part on the wafer were taken in the following experiments. This reduced the number of samples that could be used from the wafer.

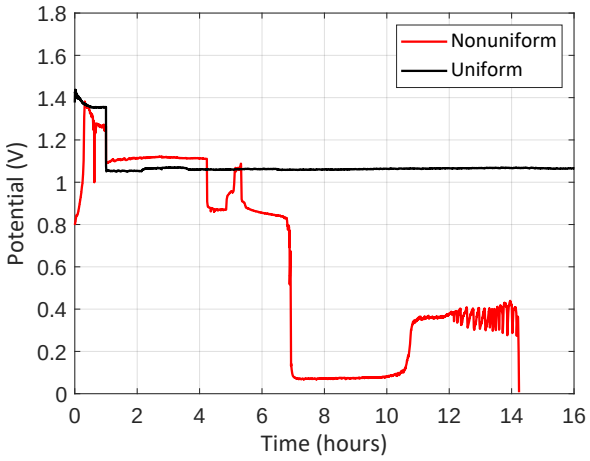

Figure 6.25: A discharge current density of 50 μA/cm^2 is applied, and the potential shows multiple "plateaus" with different - decreasing - potentials.

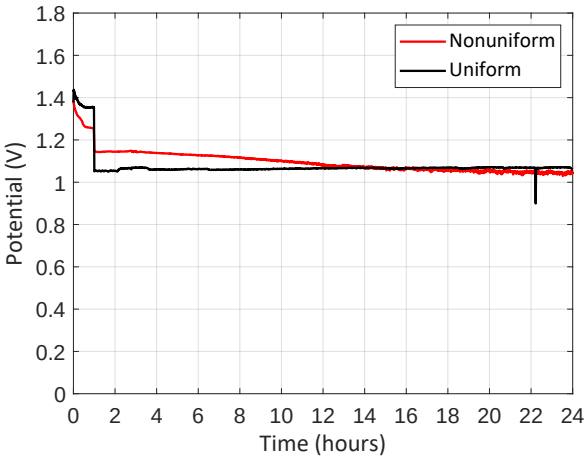

Figure 6.26: A repeated measurement under the same conditions, showed a initially higher potential that gradually decreased to the uniform doped Si potential.

The mass consumption during OCP conditions for the nonuniformly doped Si is given in figure

6.27 and is compared to the uniform Si mass consumption for time periods of 8, 16 and 24 hour. A current density of 50 μA/cm^2 is applied. The effect of applying a current density on the mass consumption is shown in figure 6.28.

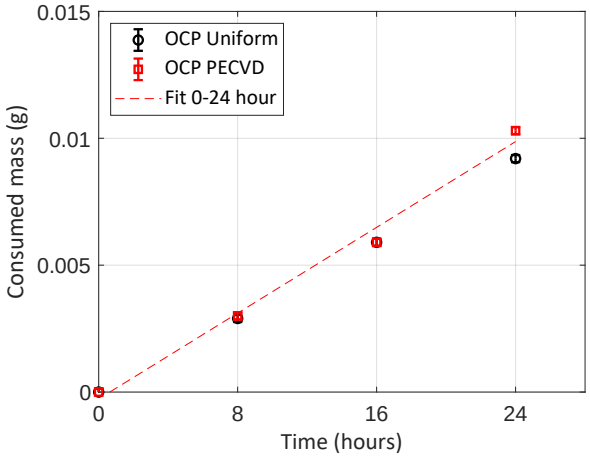

Figure 6.27: The mass consumption of n-type Si before and after discharge for time intervals of 8 hours up to 24 hours for OCP. A linear fit is added for the nonuniformly doped Si data points.

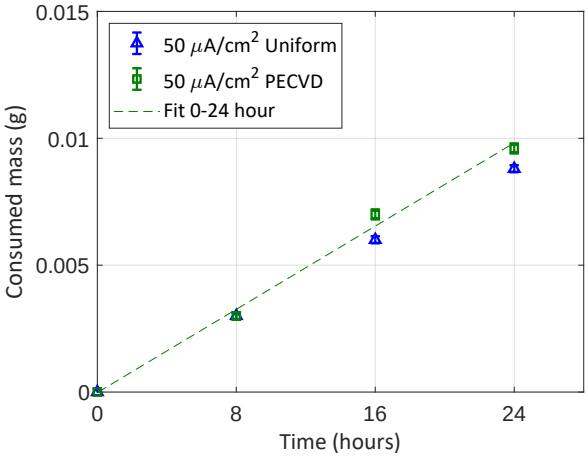

Figure 6.28: The mass consumption of n-type Si before and after discharge for time intervals of 5 hours up to 24 hours for 50 μA/cm^2. A linear fit is added for the nonuniformly doped Si data points.

The mass consumption with the nonuniformly doped n-type Si at OCP is very similar with respect to the uniformly doped Si, for time periods up to 16 hours. After 24 hours, the mass consumption of the nonuniformly doped Si has increased a bit to 10.2±0.14 mg.

The mass consumption of nonuniformly doped Si with an applied current density starts to increase for time periods longer than 16 hours. After 16 hours, the consumed mass has increased by 1.0±0.14 mg with respect to uniformly doped Si, as can be seen in figure 6.28. For the 24 hour period, the mass increased as well, but to a relatively smaller extent with 0.8±0.14 mg compared to uniformly doped Si. The efficiency was lowered on average from 3.25% to 2.9%. Overall, with the implementation of a dopant profile in actively discharging p-type Si, the corroded mass has slightly increased.

The step height is studied for the n-type nonuniformly doped Si samples. Time periods of 8, 16 and 24 hours are considered while discharging. The step heights are illustrated in figure 6.30.

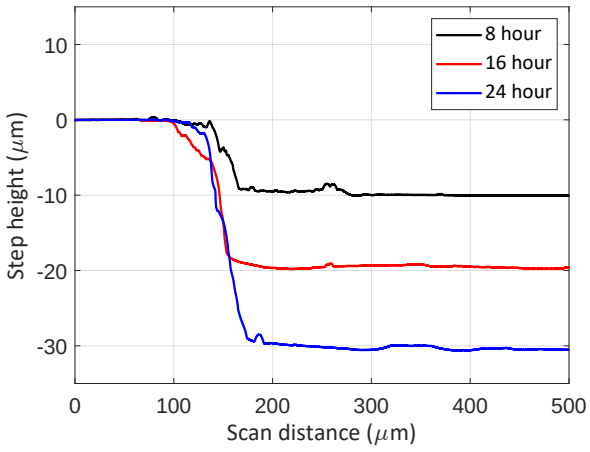

Figure 6.29: Step height profiles of uniform n-type Si that has been discharged at 50 μA/cm^2 for periods of 8, 16 and 24 hours. The corrosion rate is constant.

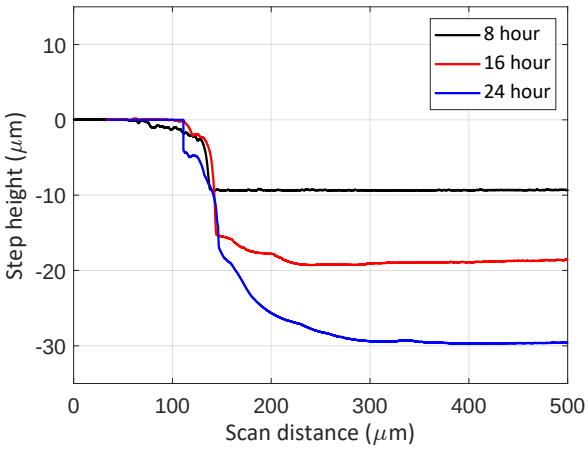

Figure 6.30: Step height profiles of nonuniformly doped n-type Si for different samples that have been discharged at 50 μA/cm^2 for periods of 8, 16 and 24 hours. The corrosion rate is constant.

The step heights are similar in size and the etch rate is constant over time. The step height after 16 hours is 18.6 μm, which is doule the step height of 9.3 μm after 8 hours. The step heights

are determined for different samples from the same wafer. Compared to the results of p-type PECVD grown wafers in subsection 6.2.1, the surface is much smoother and comparable to the uniform n-type Si. However, the increase in mass consumption is not translated into an increase in step height as well.

In figure 6.31, the mass consumption at an applied current density of 50 μA/cm^2 is combined with the step height that was shown in figure 6.8 at the same current density. A linear fit is added.

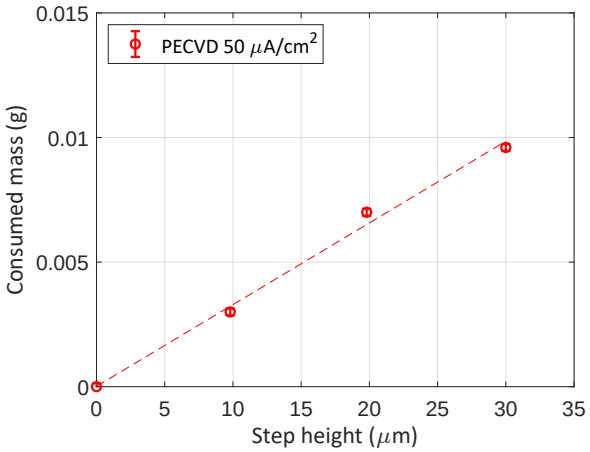

Figure 6.31: The mass consumption is plotted as a function of the step height for nonuniformly doped n-type samples made with PECVD and discharged at 50 μA/cm^2.

The mass does not increase linearly with the step height for all discharges, as shown in figure 6.31. The mass consumption is too high around 20 μm, while being closer to the straight line for a 30 μm step height.

Chapter 7

Discussion

The results presented in chapters 4, 5 and 6 are discussed in this chapter. First, the general setup and the improvements made to the setup are discussed in 7.1. The results of the dopant profile analysis are discussed in section 7.2. The corrosion results for both uniformly and nonuniformly doped Si are discussed in section 7.3, which includes separate subsections for the uniformly and nonuniformly doped Si.

7.1 Setup adaptations

The first presented results in this work were aimed at achieving long and stable discharges. These results will be discussed in this section. The start-up procedure for the discharge experiments is discussed in subsection 7.1.1. After this, the setup improvement is discussed in subsection 7.1.2. In subsection 7.1.3, the discharge behavior of uniform p-type and n-type Si samples is discussed. Finally, the results of the diluted electrolyte experiments are discussed in subsection 7.1.4.

7.1.1 Start-up procedure

Prins used systematic pre-wetting of the air cathode to improve the discharge behavior [64]. The same pre-wet times were used in this work, but resulted in mixed outcomes. The OCP gradually dropped from the initial 1.4 V to 1.0 V in a matter of hours and the maximum discharge time that could be achieved was just over 4 hours after the optimal 8 hours of pre-wetting. Pre-wetting was performed by submerging the entire air cathode in the used electrolyte, i.e. 30 m% KOH. Having the entire air cathode saturated with KOH could result in the oxygen reduction stopping earlier at discharging of the battery due to blockage of all pores. Another solution could have been to only pre-wet the active area of the air cathode, such that the oxygen can diffuse through from the unsaturated sides in the inactive area of the cathode as well. This has not been tested.

By all means, a form of pre-wetting was used to improve the discharge behavior of the battery. This pre-wetting was aimed at the Si anode through the removal of the insulating native oxide (SiO_2) layer by the KOH electrolyte. The OCP increased within one hour from 0.70-0.8 V to the expected value of 1.35-1.4 V. 30 m% KOH etches SiO_2 at a much slower rate than Si. At room temperature, the etch rate of SiO_2 is only 3.4 nm/hour [100]. It thus requires roughly 40 minutes to remove the native oxide layer of 2.1 nm thick. This time period could be observed in the discharge plots, albeit with some variations in how fast the OCP recovered. This is caused by the thickness of the SiO_2 layer that can vary over the active surface area and the kinetics of the dissolution reaction of SiO_2 into the electrolyte. The thickness of the SiO_2 has not been determined. As the native oxide layer of SiO_2 is in general very thin, the effect on the overall electrolyte composition and its conductivity is small when it is removed from the surface, especially since the electrolyte volume of 4 ml is much larger than used in setups in literature. This larger volume allows a slower build-up of reaction product and consequently a saturation of the electrolyte. This extends the discharge time before the electrolyte needs to be refreshed. A

faster approach to remove the native oxide layer would have been to use HF, but considering the toxicity issues regarding HF and the large number of discharge experiments that were conducted in this research, it was safer to use as little HF as possible. A visual inspection to see whether the SiO_2 layer has been removed, is the formation of hydrogen bubbles at the surface. As the used cell setup was fully enclosed, this approach could not be tested.

7.1.2 Initial versus improved setup

The initial used setup suffered from high ohmic losses due to a high contact resistance in one of the electrical contacts. A redesigned electrical contact used a gold-plated PCB contact that is more resilient against KOH. The discharge potentials increased by almost 0.5 V using the new PCB contacts. A cable is soldered to the back-side of the PCB that connects to the galvanostatic setup. The connection of the cable to the PCB was not as resilient to KOH as the PCB itself. This still required resoldering of the cables to the PCB after a month of intensive use. The measured contact resistances with the PCB-contact remained very low at less than 0.1 Ω throughout its lifetime, which is still considerably better than the intitial used contacts with measured resistances of up to 10 kΩ.

7.1.3 Discharge behavior p-type and n-type

Once the setup was more stable, the discharge behavior of p-type and n-type Si wafers was compared by studying the discharge plots. Based on the discharge plots, the OCP values for p-type and n-type Si are very similar after the one hour period and reach values of 1.35-1.4 V, comparable to literature [41][43][44]. The theoretical cell voltage of an alkaline Si-air battery is 2.09 V, but because of overpotentials the actual cell voltage is lower. Besides, for the low current densities used in the experiments, the potential of the air electrode is lowered by roughly 0.4 V [132]. This is likely the main reason for the lowered battery cell potential.

On discharging, the potential of p-type Si agreed to the potential of n-type Si for 10 $\mu A/cm^2$. However, for higher current densities the potentials of p-type Si decreased at a faster rate than n-type Si, as could be observed in figure 4.12. Overpotentials might be the source of this. There are several sources of overpotentials. Ohmic overpotentials scale linearly with the applied current density, i.e. $\eta = iR$, and this can be observed for n-type Si in figure 4.13. This indicates that ohmic losses are the dominant source of overpotential n-type Si. In p-type Si, additional overpotentials are likely to be present. An activation overpotential results in an energy barrier and accumulates the electrons at the surface, obstructing the electrons to contribute to the external circuit. This mainly happens for low current densities to begin the redox reactions. This discharge potential of 1.3 V for p-type Si is similar to that of the 1.3 V of n-type Si for 10 $\mu A/cm^2$, so the lowered potential for p-type Si does not take place immediately. Therefore the lowered potential of p-type Si for higher current densities is unlikely to be caused by activation overpotentials. Concentration overpotentials increase when reaction products cannot dissolve fast enough. This occurs at higher current densities, as reaction rates increase and the mass transport can become a limiting step. As the used current densities are very low at only tens of $\mu A/cm^2$, the concentration overpotential is not likely to be the dominant factor. Moreover, this overpotential would then also have to be visible for n-type Si, since it has the same chemical reactions and uses the same current densities. This is, however, not the case. Therefore, the decreasing potential for p-type Si is likely to be caused by another mechanism. The lower potential for p-type Si might be due to the fact that p-type Si has a lower electron concentration compared to n-type Si. Therefore, the reduced number of free electrons in p-type Si might limit the electron transfer for higher current densities, as the reaction rate increases for higher current densities. This increases the overpotential and, consequently, decreases the observed discharge potential.

7.1.4 Electrolyte dilution p-type

The effect of the KOH concentration on the discharge potential for p-type Si was also studied by diluting the KOH electrolyte from 6.6M to 1.1M. This resulted in a decrease in discharge potential of 0.3 V with respect to the 6.6M concentration for a current density of 10 $\mu A/cm^2$, while the OCP only slightly decreased compared to its original value with 6.6M KOH. Besides, the Si surface was passivated within one minute of discharging at 50 $\mu A/cm^2$.

It was expected that, based on the Nernst-equation and the electrolyte conductivity, a lower electrolyte concentration would increase the overpotentials and consequently reduce the discharge potential of the battery. However, the observed 0.3 V difference is larger than expected. In literature, a larger than expected drop in potential is attributed to increased overpotentials at the surface of the Si anode and a reduced ionic conduction in the electrolyte [43]. Both effects reduce the reaction kinetics and thus result in a lower discharge potential. Due to less available OH^- ions in the diluted electrolyte, the dissolution rate of $Si(OH)_4$ is lowered. In literature it was found that the dissolution of $Si(OH)_4$ at low concentrations can be increased by increasing the surface area of the Si anode [41]. As this also increases the corrosion rates, this approach was not further worked out due to the scope of this work. The effect of lowering the electrolyte concentration was not further studied for n-type Si.

7.2 Dopant profiles

Based on the defined experimental method to fabricate the nonuniformly doped Si samples, Matlab and Excel simulations have been performed to determine the dopant profile. These simulations will be discussed in subsection 7.2.1. Based on the parameters obtained from the simulations, the diffusion process was carried out. These steps are discussed in subsection 7.2.2. To verify whether the results of the simulations have been experimentally achieved in the used samples, further analysis was carried out by spreading resistance profiling (SRP) and the four-point probe to determine the dopant profile. The results from these dopant profile characterizations will be discussed in subsection 7.2.3.

7.2.1 Dopant profile simulations

Before the fabrication of the nonuniformly doped Si samples, simulations were performed to determine the dopant profiles. These simulations are based on the drive-in process explained in section 2.10.2. The drive-in process first deposits one thin impurity layer with a high concentration on a c-Si wafer. The impurity atoms in the impurity layer subsequently diffuse into the c-Si when the wafer is heated to high temperatures. This results in a Gaussian dopant profile, as the impurity are not continuously supplied at the surface. Simplifications have been made in the simulations.

The dose of the impurity layer in atoms/cm^2 is based on the impurity layer thickness and impurity concentration. In the deposition process of the thin impurity layer, it is assumed that the layer has a uniform thickness and uniform concentration over the deposited surface. The thickness and achieved impurity concentration were based on previous recipes made by Dr. Z. Yao, obtained in private communication.

For PECVD, a single impurity layer is deposited. However, with epitaxial growth, three thin layers were deposited on a c-Si wafer, where the outer layers function as encapsulation. In the simulations, the concentration and thickness of one layer was taken into account to determine the dose. It was assumed that the layer with the highest impurity concentration would achieve the most significant drive-in of impurity atoms. In case of the samples to be made with epitaxial growth, this is the 10 nm thick B layer grown on top of c-Si. Therefore, the effect of the other layers on the drive-in depth and surface concentration is not taken into account. However, these layers will have an effect on the experimental diffusion profile.

7.2.2 Fabrication steps

Through deposition by PECVD and epitaxial growth, thin impurity layers of B and P with a very high concentration have been deposited on the c-Si wafers. The impurity atoms in these layers were diffused into the bulk Si through a drive-in process at high temperatures. To achieve a Gaussian dopant profile that extends up to 42 μm in the bulk Si, a diffusion temperature of 1250 °C was set at the furnace for a period of 36 hours. A furnace outside the cleanroom environment was used to conduct this diffusion process. This furnace was generally used to heat salts and is therefore not as clean as the furnaces available in the cleanrooms of EKL. After the diffusion process some traces of reaction products that deposited on the wafers were visible that would not rinse of in a cleaning process. Especially after the diffusion of the n-type wafer, clear contamination was visible on the wafer surface. The same pre-processing cleaning process was followed for the diffused wafers as was done for the uniform wafers, as described in Appendix A.2. The contamination therefore is likely to originate from the furnace. The exact material composition of the contamination has not been determined.

Before the diffusion process was started, the furnace was first pumped to a vacuum by a turbo-pump and flushed with N_2 gas. The reached level of vacuum was not documented. This was repeated several times to remove all the oxygen. During the diffusion, the furnace was flushed continuously with N_2 to prevent the formation of a thermal oxide layer on the Si surface. The growth of the thermal oxide layer should especially be prevented at the beginning of the diffusion process as the concentration of impurity atoms is then the highest. Based on the visual appearance of the wafers after the diffusion process, as was shown in figure 5.7, a thermal oxide layer was visible, meaning oxygen was inside the furnace during the diffusion process. After 4 min of etching in BHF, the oxide layer was removed, indicating a thickness of roughly 320 nm [130]. For the scope of this thesis, the exact thickness of oxide was not of interest. It only has to be removed before further processing. It is likely that the oxide layer will have consumed some of the B impurity atoms in the diffusion process, but it is unknown when the oxygen started entering the furnace. The purity of the used N_2 gas was not stated and therefore it is possible that some oxygen was already present in the - assumed to be pure - N_2 gas. As the thermal oxide layer was visible on all samples that have been diffused using this furnace, it is likely that some oxygen was present in the N_2 gas.

7.2.3 Four-point probe and spreading resistance profiling (SRP)

P-type PECVD

The four-point probe measurements of the p-type PECVD grown wafer, presented in subsection 5.4.1, showed that the sheet resistance increased with increasing step height. Besides, all data points followed a similar profile as was simulated for the sheet resistance. When comparing the results of the four-point probe to the SRP, presented in section 5.6, the data points measured with the four-point probe seem to match the SRP the best from around 10 μm. The following bulletpoints give explanations for the observed differences:

- As was shown in figure 5.21, the achieved surface concentration was higher than simulated. This implies that the dose in atoms/cm^2 of the deposited a-Si:H layer was higher than the value used in the simulations. A higher impurity concentration or thicker than 50 nm layer could be an explanation for this. The thickness of the deposited a-Si:H layer has not been determined through, for instance, spectroscopic ellipsometry. The deposition time of a recipe that deposited 10 nm of p-type a-Si:H was increased by a factor five to end up with 50 nm.
- In figure 5.21 it was shown that the expected junction depth was slightly lower than the simulated junction depth and could be explained by a lowered diffusion temperature. Decreasing the diffusion temperature by 10 °C approximated the SRP profile the best. This means that the actual temperature achieved in the furnace is 1240 °C, a decrease of 0.65% from 1250 °C. The position of the temperature probe inside the furnace with respect to

the position of the samples seems a logical explanation, as the wafers could not be placed close enough to the probe for an accurate temperature reading at the wafer position. A 10 °C variation is therefore not unlikely.
- The profile in figure 5.21 is not a perfect Gaussian profile, but has some variations. Inhomogeneity in the deposited p-type a-Si:H layer might have caused this. The deposited layer has not been analyzed through scanning electron microscopy (SEM) or atomic force microscopy (AFM).
- The resistivity of the used c-Si wafer was higher than used in the simulations. In the simulations a resistivity of 1000 Ωcm was assumed, while the resistivity obtained from the SRP analysis was over 3000 Ωcm. On the wafer box a resistivity of "$>$ 1000 Ωcm" was indicated. It was not expected to be so far off in reality, but it is not uncommon for such low dopant concentrations. Despite the low base dopant concentration, the used p-type Si wafers still showed a continuous discharge result in figure 6.12.

P-type epitaxy

For the epitaxially grown wafer, the four-point probe measurements did not agree as well with the simulated sheet resistance and dopant profile, as was shown in section 5.4.2. The sheet resistances were higher, resulting in lower dopant concentrations than simulated and obtained through SRP. As was shown in figure 5.15, the measured sheet resistances were very close to each other, although the step heights differed by several μm. The following bulletpoints give explanations for the observed differences:

- In the SRP concentration profile in figure 5.23, a small hill was visible. This small increase in dopant concentration is likely to be caused by the B-doped Si encapsulation layer that had a lower B concentration than the deposited pure B layer. The method to determine the sheet resistance, given in subsection 3.7.4, assumes an monotonic increasing sheet resistance as function of position. With an increasing resistance, most current will flow through the top layer with the lowest resistance. Since the actual resistance in the epitaxial wafer decreases with increasing depth for the first few μm, the current will not flow predominantly through the top layer but through a layer deeper into the bulk. This distorts the measurements of the sheet resistance. This may explain why the measured sheet resistances were so close to each other in the first μm.
- Moreover, the used method in determining the incremental sheet resistance is less accurate for n-type on n-type or p-type on p-type diffused layers. Ideally, an insulating layer should separate the diffused layer from the rest of the wafer. This insulating layer confines the current to the top (diffused) layer. Therefore, pn-junctions are more suitable for this method. PN-junctions have a space-charge region that functions as the needed insulating layer. A narrower probe spacing, combined with thinner probes, reduces the depth at which the current travels, meaning that the current will flow nearer to the surface. This could result in more accurate incremental sheet resistance measurements in nonuniformly doped wafers.
- The difference between the simulated and SRP dopant profile for the epitaxially grown wafer, as was shown in figure 5.23, can partly be explained by the lower diffusion temperature inside the furnace and partly by the simplifications made in the simulation. It is likely that the additional B layer and B-doped Si layer affected the first μm of the profile. Redistribution of the higher impurity concentration pure B layer into the lower impurity concentration B-doped Si might be the effect underlying this increase in concentration, as redistribution of impurity atoms is not limited to the Si-SiO_2 interface [127]. Overall, as was shown in figure 5.23 the simulation at 1240 °C approximated the experimentally achieved profile closely.
- Compared to PECVD, epitaxial growth has resulted in a more homogeneous concentration distribution in the deposited B layer as the dopant profile, shown in figure 5.23, is much smoother. This is due to a highly controlled and accurate growth of the B atoms on

top of the c-Si during epitaxial growth. The deposited B layer has, therefore, likely a more homogeneous concentration than the layer grown with PECVD. This is, however, not verified or analyzed.

N-type PECVD

The dopant profile in the n-type PECVD grown wafer was only analyzed by the four-point probe method and not with SRP. Only a limited number of samples could be analyzed with the four-point probe, as some samples resulted in errors. On the surface of some discharged samples, black dots were visible that are likely to have distorted the measurement. The successful measurements aligned with the simulated sheet resistance profile. The measurement points were spread out over the simulated dopant profile. Therefore, a lower diffusion temperature did not necessarily result in a better fit to the results. Based on the sheet resistance measurement points, a dopant profile appears to be implemented into the n-type wafer. However, the dopant profile has not been verified with the more accurate method of SRP.

7.3 Corrosion results

The corrosion is quantified for both uniformly and nonuniformly doped p-type and n-type Si in section 6.1 and 6.2, respectively. The corroded mass is determined by inspecting the mass consumption during OCP and during active discharging. The corrosion rate (μm/h) is quantified by inspecting the step-height. First, uniformly doped Si will be discussed in subsection 7.3.1. Next, uniformly doped Si will be discussed in subsection 7.3.2.

7.3.1 Uniformly doped silicon

For p-type and n-type Si the mass consumption and step height are comparable and take place at a constant rate over time. The number of time steps at which the mass and step height were measured is limited to four, but the overall constant behavior of the mass consumption is clearly visible.

Based on the results, corrosion is more suppressed in this battery setup compared to the paper of Durmus et al. [44], as the corrosion rate is on average 1.25 μm/h instead of 2.2 μm/h. Durmus et al. also used flat <100>-oriented c-Si wafers in their experiments, but their electrolyte volume was much smaller at 0.5 ml compared to the 4 ml used in this work's setup and the electrolyte concentration was slightly lower at 5M. The larger electrolyte volume in this work's setup was chosen to ensure the discharging to continue for long periods without passivation and saturation to gel-like solutions. The conductivity of the 5M KOH is comparable to the 6.6M KOH concentration used in this work. The effect of a larger electrolyte volume on the internal resistance was calculated and resulted in a very small potential drop of 0.17 mV at 50 μA/cm^2. This possible downside of the larger electrolyte volume is therefore of no significant influence on the discharge results.

The decrease in corrosion rates resulted in a higher conversion efficiency compared to the findings of Durmus et al. On average, for n-type Si the efficiency was 3.25%, while for p-type the efficiency was a bit higher at 3.40%. This was due to the slightly lower average mass consumption at 50 μA/cm^2 for p-type Si, despite the increase in step height of 1.0 μm after 48 hours. An explanation for this could be an error in the mass determination before or after the discharge, as the difference is very small and close to the accuracy limit of the scale. A more accurate scale could be used to resolve this issue.

In the efficiency calculations, only the electrochemically discharged mass and the total mass consumption are taken into account. Besides, it is assumed that the reaction is a four-electron process and thus purely electrochemical. However, it is uncertain whether all electrons participate in the reaction and whether there are other reactions involved at the discharge of the alkaline Si-air battery besides the redox and corrosion reaction.

What was noticed from the mass consumption in figures 6.1 and 6.6, was that the effect of applying a current density on the mass consumption with respect to OCP conditions is not as significant as was stated in the work of Durmus et al. [43]. In their work it was found that the consumed mass increased by 50% on discharging, while in the results of this work no consistent and significant increase was visible. The used setups can, however, not directly be compared due to the difference in electrolyte volume. Therefore, it is likely that the used setup in this work has had an influence on the corrosion rate.

The results of this work indicate that the corrosion of Si is mainly chemical in nature, as the electrochemical component is virtually zero at OCP conditions and the measured corrosion at OCP was similar to the corrosion with an applied current density. These results were further validated by the implementation of a dopant profile and will be discussed in the next section.

7.3.2 Nonuniformly doped silicon

The effect of implementing a dopant profile in the Si anode was studied as a mitigation solution for the corrosion reaction. The results of the different types of samples are discussed below.

P-type PECVD

The p-type PECVD grown wafer showed similar discharge behavior compared to the uniformly doped wafers in figure 6.12, with similar discharge voltages. Similar discharge current densities of 50 μA/cm^2 could be achieved without suffering from passivation. The mass consumption at OCP was also very similar to the uniformly doped wafer, as was shown in figure 6.13. However, with applying a current density the mass consumption increased by 15% after 16 hours, with respect to uniformly doped Si. This was illustrated in figure 6.14. It was stated that due to the high concentration of electrons in the p-type Si wafers, caused by the high resistivity, the effect of diffusion of electrons from the bulk to the Si-electrolyte interface might be larger than the induced internal electric field that removes the electrons from the interface. This would in fact increase corrosion in nonuniformly doped p-type Si with respect to uniformly doped p-type Si.

When comparing the mass consumption between OCP and discharging, for the nonuniformly doped Si, the mass consumption has increased, but only slightly on discharging. It indicates that the electrochemical reaction, where H_2O reacts with four electrons produced in the oxidation reaction, might play a (minor) role in the corrosion.

The step heights after 5, 8, 16 and 24 hours were inspected in figure 6.16 and were similar to the uniformly doped samples in figure 6.22. The step heights only increased for the 16 and 24 hour period, in line with an increase in mass consumption. However, the step height for the 16 hour period has not increased by the same amount as was expected based on the mass consumption, i.e. a 15% increase. This was also visible in figure 6.17, where the mass consumption was plotted as a function of step height. As only a small area is inspected within a scan of the profilometer, it is uncertain whether the step height has increased on the rest of the active surface. For other areas on the wafer that were not inspected, the step height should have increased in order to explain the additional mass consumption. Starting from the 5 hour period, the surface of the nonuniformly doped wafer showed a more rough structure instead of a very flat surface observed on the uniform wafer. This makes it more difficult to determine the step height. The rough surface has likely an increased surface area compared to the flat surface, but this has not been measured. In the PECVD process, an a-Si:H layer has been deposited. This a-Si:H quickly crystallizes at high temperatures to poly-Si [120]. The rougher surface that is visible could be caused by corrosion along the grain boundaries of poly-Si. Durmus et al. stated that an increased surface area, increases the corrosion as well [38][43]. However, the surface area also increased during OCP, without additional mass consumption. Therefore, it is not likely that the larger surface area increased the corrosion during discharging. Overall, the absolute increase in mass consumption with discharging is small. This indicates that if there is any additional consumption of Si due to more electrons being available as a result of diffusion from the bulk to the interface, the effect is still limited.

P-type epitaxy

The p-type epitaxially grown wafers showed similar discharge behavior compared to the uniformly doped p-type wafers in figure 6.19, but only at low discharge current densities up to 25 μA/cm^2. A current density of 50 μA/cm^2 resulted in almost immediate passivation and stopped the discharge, as was shown in figure 6.18. Based on the dopant profile simulations in section 5.1 and through the SRP analysis discussed in subsection 5.5.2, the maximum B concentration was at some point above 2×10^{19} atoms/cm^3. Above this concentration, the corrosion-rate, i.e. etch-rate, of Si in KOH decreases by an inverse fourth power with increasing B concentration [100]. The four stems from the four OH^- ions needed to dissolve one Si atom, as shown in the oxidation reaction in subsection 2.4.5. Therefore, the dissolution rate of $Si(OH)_4$-atoms into the electrolyte appears to decrease by a reduction in corrosion. This passivates the surface at 50 μA/cm^2, while the uniformly doped p-type wafer, which had a lower surface concentration, could still be discharged at 50 μA/cm^2. This would mean that if the B concentration is increased further to, for instance 10^{20} atoms/cm^3, the etch rate would drop further and passivation is likely to also occur sooner. This would imply that at some point discharging becomes impossible. However, this has not been verified in this work.

The reduction in corrosion was also observed in the mass consumption and consequently the step height in figure 6.21 and figure 6.23, respectively. The mass consumption scaled linearly with the step height, similar to the uniformly doped Si samples. The average corrosion rate over 24 hours had decreased from 1.25 μm/h to 1 μm/h. However, after 8 hours the mass consumption and step height increased at a faster rate than in the first 8 hours. Based on the high concentration visible in the simulated dopant profile in figure 5.5, it was expected that in the first 10 μm the corrosion rate would be lower and that it would increase once the dopant concentration dropped below the threshold of 2×10^{19} atoms/cm^3. This effect has been experimentally shown. Corrosion appears to have decreased by using a very high boron concentration and not necessarily by the implementation of a dopant profile.

N-type PECVD

After the diffusion process, black areas were visible on the surface of the n-type PECVD grown wafer, as was shown in figure 5.8. When a sample from this area was used to perform a discharge, an inconsistent discharge curve was observed, shown in figure 6.25. Switching to a cleaner part of the wafer resolved the issue. The exact material composition of the dark areas has not been investigated. Therefore, it is unknown what the origin might be. Between the PECVD and diffusion process it was not visible on the wafer surface. Hence, it is likely that it has happened during the diffusion process. The n-type wafer was diffused in a different run than the p-type PECVD and p-type epitaxially grown wafers.

The n-type PECVD grown wafer showed similar discharge behavior compared to the uniformly doped n-type wafer at 50 μA/cm^2, illustrated in figure 6.26. The mass consumption was shown in figure 6.27 and figure 6.28 for OCP and discharging, respectively. The mass consumption up to 16 hours was similar for OCP, but increased slightly for discharging. After 24 hours, both the mass consumption for OCP and discharging increased. In fact, the mass consumption during OCP increased above the mass consumption for discharging.

However, the increase in mass is not translated to an increase in step height. It is unclear whether the increase in mass is systematic or that it is due to an error in the measurement. The surface observed in the step height profiles in figure 6.30 is smooth, unlike the rough surface of the p-type a-Si:H diffused layer. The rough surface in p-type Si was likely caused by poly-Si grain boundaries, but this rough surface could also be expected on n-type Si made with a diffused a-Si:H impurity layer. This is, however, not the case.

Despite the flat surface, the surface was not passivated on applying 50 μA/cm^2. Based on the results, no clear trend or behavior is visible in the mass consumption. By all means, the corrosion did not decrease as a result of the nonuniform doping, while this was expected to occur for nonuniformly doped n-type wafers based on diffusion of electrons away from the interface and

the electric field directed towards the bulk of the Si.

Based on the reaction included in the corrosion model presented by Durmus et al. [44], it was expected that corrosion could be decreased, resulting in an increased conversion efficiency, by removing the electrons from the silicon-electrolyte interface. This has not been experimentally shown in the wafers that were nonuniformly doped. This can be due to several reasons. One reason could be that the measurement techniques used to characterize the corrosion in this work are not accurate enough to measure the effect. It could also be that the role of the electrons is too limited in the corrosion reaction to be able to reduce the corrosion, indicating that it mainly a chemical process. As the theory is based on a model for the corrosion reaction, the model itself could also be incorrect or incomplete. The model assumes that electrons consumed at the cathodic sites are limiting the conversion efficiency of the battery, while this may not necessarily be true, since removing the electrons from the cathodic sites with a dopant profile did not result in an increased conversion efficiency.

Chapter 8

Conclusions and recommendations

The research objective of this work is the mitigation of the corrosion reaction in alkaline silicon-air (Si-air) batteries through the implementation of a dopant profile. Many experiments have been performed throughout this work to study the alkaline Si-air battery. First, main conclusions of this work are summarized. Second, recommendations for further improvement of the research into Si-air batteries are outlined.

Conclusions

The corrosion in the Si-air battery setup is first quantified for uniformly P-doped (n-type) and uniformly B-doped (p-type) flat c-Si wafers by studying the mass consumption and step height after open-circuit potential (OCP) and galvanostatic discharge with current densities up to 50 μA/cm^2. The results of the experiments conducted with both types of dopants are directly compared to each other and to results measured in previous research. The results of the experiments with the uniformly doped wafers function as reference results to later compare to the results obtained by conducting experiments with nonuniformly doped wafers.

The results of the uniformly doped wafers in this work do not match the results documented in literature, as the overall corrosion rate of 1.25 μm/h is lower than the 2.2 μm/h measured in previous research. Furthermore, applying a current density, and thus increasing the electron injection, does not change the mass consumption compared to OCP. In this work, the reduction in corrosion increases the conversion efficiency from 2.0% to 3.4%, corresponding to a specific capacity of 130 mAh/g. Also, there is no noticeable difference in the magnitude of corrosion between n-type and p-type Si. The differences between this work's results and the results obtained in previous research appear to originate from the difference in the used setup electrolyte volumes, as the used steps to determine the corrosion are similar.

Nonuniformly doped wafers are made by depositing thin impurity layers on c-Si through plasma-enhanced chemical vapor deposition (PECVD) and epitaxial growth. Subsequently, a drive-in diffusion process is used to move the impurity atoms into the Si wafer and to create a profile in the dopant concentration. The dopant profiles are first simulated to determine the required diffusion temperature of 1250 °C and diffusion time of 36 hours to achieve a large junction depth. This junction depth is needed to observe changes in the mass consumption and step height over the same time periods used in the uniformly doped wafers. To validate whether the experimental profiles correspond to the simulated dopant profiles, both the sheet resistance and spreading resistance profiling (SRP) are used to obtain the dopant profiles of the samples. The measured results verify that a doping profile is present. The junctions depths reached a maximum of 36 μm.

In the nonuniformly doped Si samples made with PECVD, the corrosion increases slightly on discharging with respect to uniformly doped Si for both p-type and n-type Si. This means that the corrosion rate is not clearly affected by nonuniform doping of the Si anode, while this was expected to occur based on the used model for the corrosion reaction.

For nonuniformly doped p-type Si samples made with epitaxial growth, corrosion significantly decreases to 0.82 μm/h compared to 1.25 μm/h with uniformly doped Si. However, after 8 hours of discharging, the B concentration is smaller than 2×10^{19} atoms/cm^3, as a consequence of the dopant profile, and the corrosion rate increases again to 1.12 μm/h. Corrosion thus decreases by using a very high B concentration and not through the implementation of a dopant profile.

It is concluded that nonuniform doping does not influence the corrosion in alkaline Si-air batteries and, therefore, does not mitigate the corrosion reaction.

Recommendations

The progress made in this work still leaves room for further improvement. Possible solutions for the further enhancement of the efficiency of the Si-air battery are outlined in this section and can provide insights for future research into this topic.

- The effect of changing the setup's electrolyte volume on the discharge results and the corrosion should be further inspected, as significant differences were observed in this work and the work of previous research. A suggestion would be to decrease the electrolyte volume in the setup and redo galvanostatic discharges with the same uniformly doped Si wafers used in this work to observe any changes.

- In this work, the corrosion in alkaline Si-air batteries decreased by using a high B concentration above 2×10^{19} B atoms/cm^3. This high concentration was only achieved in nonuniformly doped wafers. Uniformly doped wafers with this high B concentration were not available at the EKL or PVMD facilities during writing of this work, but are available for purchase at external companies. The effect on the corrosion of having a uniformly doped wafer with such a high B concentration could be further studied as a possible corrosion mitigation.

- Despite the measured reduction in corrosion rate in alkaline KOH Si-air batteries with the high B concentration Si anode, corrosion has not been resolved and still significantly limits the efficiency of the Si-air battery. Therefore, several research papers have instead focused on the more efficient, but also more dangerous, non-aqueous RTIL electrolytes that contain HF and also form HF in the reactions. Fortunately, there are other RTIL's available that are less harmful than EMIm$(HF)_{2.3}$F. Further research should focus on these RTIL's instead.

- Flat c-Si wafers were used in this work. As passivation was observed for lower current densities compared to prior research, texturing the surface from flat to more porous increases the dissolution rate and might delay the passivation. This increases the current densities that can be applied to discharge the battery. In future experiments, surface texturing can be implemented on a high B concentration wafer to delay the passivation but also obtain lower corrosion rates.

- As in this work only a p-type impurity layer was deposited on a p-type Si wafer and a n-type impurity layer on a n-type Si wafer, it would be interesting to see the effect of depositing p-type on n-type Si and vice versa. This will create a pn-junction with a space charge region. The use of pn-junctions as anode material in Si-air batteries has not yet been documented in literature.

- Based on the step height figures of the p-type PECVD grown wafer, a rougher surface was observed. A useful addition to this work would have been to include surface inspections made with scanning electron microscopy (SEM). This can also provide more insight in the difference in surface between uniformly and nonuniformly doped wafers.

- Due to contamination issues, sputtering an Al:Si back-contact was not possible for the nonuniformly doped wafers. Therefore, the back-contact was changed to pure Al and Cr

deposited by EBPVD at room temperature. Al is in principle a p-type dopant for Si, but the metal-semiconductor barrier height is large at 0.85 eV. Choosing a metal with a larger work function than Al, such as gold, lowers the contact resistance between the metal and semiconductor.

- Besides the use of the four-point probe and SRP to determine the dopant profile, neutron depth profiling (NDP) can be performed to determine the dopant profile. Such a device is available at Delft University of Technology. Unfortunately during this work, this device was unavailable for analysis. It was mentioned that it would become available again at the end of 2022. NDP can only be used to accurately detect B concentrations in Si and not P, as the number of neutrons in P and Si are too similar to distinguish with the used technique.

Bibliography

[1] J. Hansen, M. Sato, R. Ruedy, K. Lo, D. W. Lea, and M. Medina-Elizade. Global temperature change. 2006.

[2] NASA. Global temperature: Latest annual average anomaly. 2020.

[3] M. Venkataramanan and Smitha. Causes and effects of global warming. *Indian Journal of Science and Technology*, 4(3), 2011.

[4] World Meteorological Organization. 2020 was one of three warmest years on record, 2021.

[5] Berkeley Earth. Global temperature report for 2020, 2021.

[6] M. Lynas, B. Z. Houlton, and S. Perry. Greater than 99% consensus on human caused climate change in the peer-reviewed scientific literature. *Environmental Research Letters*, 16(11):114005, oct 2021.

[7] Energy Information Administration. EIA projects nearly 50% increase in world energy usage by 2050, led by growth in Asia, 2019.

[8] Yahoo Finance. Dutch TTF Natural Gas Calendar, 2021.

[9] T.F. Stocker, D. Qin, and G.-K. Plattner. Climate Change 2013: The Physical Science Basis. Contribution of Working Group I to the Fifth Assessment Report of the Intergovernmental Panel on Climate Change. page 33–115, 2013.

[10] H. Ritchie and M. Roser. Energy. *Our World in Data*, 2020.

[11] D. Gielen. Perspectives for the energy transition investment needs for a low-carbon energy system. 2017.

[12] Lazard. Lazard's levelized cost of energy analysis - version 14.0. 2020.

[13] Z. Yang, J. Zhang, M. C. W. Kintner-Meyer, X. Lu, D. Choi, J. P. Lemmon, and J. Liu. Electrochemical energy storage for green grid. *Chemical Reviews*, 111(5):3577–3613, 2011.

[14] F. M. Mulder. Implications of diurnal and seasonal variations in renewable energy generation for large scale energy storage. *Journal of Renewable and Sustainable Energy*, 6(3):033105, 2014.

[15] A. Evans, V. Strezov, and T. J. Evans. Assessment of utility energy storage options for increased renewable energy penetration. *Renewable and Sustainable Energy Reviews*, 16(6):4141–4147, 2012.

[16] M. Steilen and L. Jörissen. Chapter 10 - hydrogen conversion into electricity and thermal energy by fuel cells: Use of h2-systems and batteries. In *Electrochemical Energy Storage for Renewable Sources and Grid Balancing*, pages 143–158. Elsevier, Amsterdam, 2015.

[17] B. Nykvist and M. Nilsson. Rapidly falling costs of battery packs for electric vehicles. *Nature Climate Change*, 5:329–332, 03 2015.

[18] O. Schmidt, A. Hawkes, A. Gambhir, and Iain Staffell. The future cost of electrical energy storage based on experience rates. *Nature Energy*, 6:17110, 07 2017.

[19] M. Bos. Storage of renewable electricity in methanol: Technology development for co2 air capture and conversion to methanol. 2019.

[20] F. Schüth. 1.2 energy storage strategies. In *Chemical energy storage*, pages 35–48. De Gruyter, 2012.

[21] IEA. World Energy Model, 2021.

[22] R. Huggins. *Advanced Batteries*. Springer, 2009.

[23] D. C. Meyer, T. Leisegang, M. Zschornak, and H. Stöcker, editors. *Electrochemical Storage Materials: From Crystallography to Manufacturing Technology*. De Gruyter, 2018.

[24] E. M. Stuve. *Overpotentials in Electrochemical Cells*, pages 1445–1453. Springer New York, New York, NY, 2014.

[25] D.O. Akinyele and R.K. Rayudu. Review of energy storage technologies for sustainable power networks. *Sustainable Energy Technologies and Assessments*, 8:74–91, 2014.

[26] R. Israel, A. Daniels, K. Whitehead, and M. Zwi. Technology disruptions affecting infrastructure (part 1). 2016.

[27] J. B. Quinn, T. Waldmann, K. Richter, M. Kasper, and M. Wohlfahrt-Mehrens. Energy density of cylindrical li-ion cells: A comparison of commercial 18650 to the 21700 cells. *Journal of The Electrochemical Society*, 165(14):A3284–A3291, 2018.

[28] N. Niarchos. The dark side of congo's cobalt rush. 2021.

[29] C. W. Kamienski, D. P. McDonald, M. W. Stark, and J. R. Papcun. *Lithium and Lithium Compounds*. John Wiley & Sons, Ltd, 2004.

[30] Millennium Ecosystem Assessment. Ecosystems and human well-being: Biodiversity synthesis. *World Resources Institute*, page 41, 2005.

[31] Trading Economics. Lithium prices 2021. 2021.

[32] L. Maighe. French patent no.243.454, zinc-air battery. 1878.

[33] A. G. Olabi, E. T. Sayed, T. Wilberforce, A. Jamal, A. H. Alami, K. Elsaid, S. M. A. Rahman, S. K. Shah, and M. A. Abdelkareem. Metal-air batteries—a review. *Energies*, 14(21), 2021.

[34] Y. Li and J. Lu. Metal–air batteries: Will they be the future electrochemical energy storage device of choice? *ACS Energy Letters*, 2(6):1370–1377, 2017.

[35] Y.E. Durmus. Modeling of silicon-air batteries. 12 2013.

[36] M. Wu, Z. Wen, Y. Liu, X. Wang, and L. Huang. Electrochemical behaviors of a li3n modified li metal electrode in secondary lithium batteries. *Journal of Power Sources*, 196(19):8091–8097, 2011.

[37] G. Girishkumar, B. McCloskey, A. C. Luntz, S. Swanson, and W. Wilcke. Lithiumair battery: Promise and challenges. *The Journal of Physical Chemistry Letters*, 1(14):2193–2203, 2010.

[38] H. Weinrich, Y. E. Durmus, H. Tempel, H. Kungl, and R.A. Eichel. Silicon and iron as resource-efficient anode materials for ambient-temperature metal-air batteries: A review. *Materials*, 12:2134, 07 2019.

[39] B. Lung-Hao Hu, F. Wu, C. Lin, A. N. Khlobystov, and L. Li. Graphene-modified lifepo4 cathode for lithium ion battery beyond theoretical capacity. *Nature communications*, 4(1):1–7, 2013.

[40] Gil Cohn, David Starosvetsky, Rika Hagiwara, Digby Macdonald, and Yair Ein-Eli. Silicon–air batteries. *Electrochemistry Communications*, 11:1916–1918, 10 2009.

[41] X. Zhong, H. Zhang, Y. Liu, J. Bai, L. Liao, Y. Huang, and X. Duan. High-capacity silicon-air battery in alkaline solution. *ChemSusChem*, 5:177–80, 01 2012.

[42] Y. E. Durmus, S. Jakobi, T. Beuse, Ö. Aslanbas, H. Tempel, F. Hausen, L. Haart, Y. Ein-Eli, R.-A. Eichel, and H. Kungl. Influence of dopant type and orientation of silicon anodes on performance, efficiency and corrosion of silicon–air cells with emim(hf) 2.3 f electrolyte. *Journal of The Electrochemical Society*, 164:A2310–A2320, 01 2017.

[43] Y. E. Durmus, Ö. Aslanbas, S. Kayser, H. Tempel, F. Hausen, L.G.J. de Haart, J. Granwehr, Y. Ein-Eli, R.-A. Eichel, and H. Kungl. Long run discharge, performance and efficiency of primary silicon–air cells with alkaline electrolyte. *Electrochimica Acta*, 225:215–224, 2017.

[44] Y. E. Durmus, S. S. Montiel Guerrero, Ö. Aslanbas, H. Tempel, F. Hausen, L.G.J. Haart, Y. Ein-Eli, R.-A. Eichel, and H. Kungl. Investigation of the corrosion behavior of highly as-doped crystalline si in alkaline si–air batteries. *Electrochimica Acta*, 265:292–302, 03 2018.

[45] Y. E. Durmus, C. Roitzheim, H. Tempel, F. Hausen, Y. Ein-Eli, H. Kungl, and R.-A. Eichel. Analysis on discharge behavior and performance of as- and b-doped silicon anodes in non-aqueous si–air batteries under pulsed discharge operation. *Journal of Applied Electrochemistry*, 50:93–109, 2019.

[46] D. Park, S. Kim, J. Ocon, G. H. Abrenica, J. Lee, and J. Lee. Controlled electrochemical etching of nanoporous si anodes and its discharge behavior in alkaline si – air batteries. *ACS applied materials & interfaces*, 7, 01 2015.

[47] Ahmed Garamoun, Markus B. Schubert, and Jürgen H. Werner. Thin-film silicon for flexible metal-air batteries. *ChemSusChem*, 7 12:3272–4, 2014.

[48] G.T.A. Kovacs, N.I. Maluf, and K.E. Petersen. Bulk micromachining of silicon. *Proceedings of the IEEE*, 86(8):1536–1551, 1998.

[49] Peter C. K. Vesborg and Thomas F. Jaramillo. Addressing the terawatt challenge: scalability in the supply of chemical elements for renewable energy. *RSC Adv.*, 2:7933–7947, 2012.

[50] Michael. Fleischer. Recent estimates of the abundances of the elements in the earth's crust. 1953.

[51] National Minerals Information Center. Mineral commodity summaries 2022. 2022.

[52] G. Cohn and Y. Ein-Eli. Study and development of non-aqueous silicon-air battery. *Journal of Power Sources*, 195(15):4963–4970, 2010.

[53] A. Manthiram, X. Yu, and S. Wang. Lithium battery chemistries enabled by solid-state electrolytes. *Nature Reviews Materials*, 2:16103, 02 2017.

[54] G. Cohn, A. Altberg, D. D. Macdonald, and Y. Ein-Eli. A silicon–air battery utilizing a composite polymer electrolyte. *Electrochimica Acta*, 58:161–164, 2011.

[55] T. Tsuda, T. Nohira, Y. Nakamori, K. Matsumoto, R. Hagiwara, and Y. Ito. A highly conductive composite electrolyte consisting of polymer and room temperature molten fluorohydrogenates. *Solid State Ionics*, 149(3):295–298, 2002.

[56] A. Inoishi, T. Sakai, Y. Ju, S. Ida, and T. Ishihara. A rechargeable si–air solid state oxygen shuttle battery incorporating an oxide ion conductor. *J. Mater. Chem. A*, 1:15212–15215, 2013.

[57] X. G. Zhang. Electrochemistry of silicon and its oxides. *Journal of Solid State Electrochemistry*, 7, 2001.

[58] P. Jakes, G. Cohn, Y. Ein-Eli, F. Scheiba, H. Ehrenberg, and R.-A. Eichel. Limitation of discharge capacity and mechanisms of air-electrode deactivation in silicon–air batteries. *ChemSusChem*, 5(11):2278–2285, 2012.

[59] G. Cohn, D. Macdonald, and Y. Ein-Eli. Remarkable impact of water on the discharge performance of a silicon-air battery. *ChemSusChem*, 4:1124–9, 08 2011.

[60] H. Seidel, L. Csepregi, A. Heuberger, and H. Baumgärtel. Anisotropic etching of crystalline silicon in alkaline solutions: I . orientation dependence and behavior of passivation layers. *Journal of The Electrochemical Society*, 137(11):3612–3626, nov 1990.

[61] O. J. Glembocki, E. D. Palik, G. R. Guel, and D. L. Kendall. Hydration model for the molarity dependence of the etch rate of si in aqueous alkali hydroxides. *Journal of The Electrochemical Society*, 138:1055–1063, 1991.

[62] R. Hagiwara, T. Hirashige, T. Tsuda, and Y. Ito. A highly conductive room temperature molten fluoride: EMIF·2.3hf. *Journal of The Electrochemical Society*, 149(1):D1, 2002.

[63] M. Lin, H. Chen, and H. Dai. Ionic liquids based electrolytes for rechargeable batteries. *Material Matters*, 13(1), 2018.

[64] J. Prins. Alkaline pre-treatment of the air electrode in a si-air battery. 8 2020.

[65] *Electrochemical Systems*, chapter 3, pages 46–60. John Wiley & Sons, Ltd, 2000.

[66] K. Schmidt-Rohr. How batteries store and release energy: Explaining basic electrochemistry. *Journal of Chemical Education*, 95(10):1801–1810, 2018.

[67] G. In Cutler J. Cleveland and Christopher Morris, editors, *Dictionary of Energy (Second Edition)*, pages 247–273. Elsevier, Boston, second edition edition, 2015.

[68] W. Wang, X. Wei, D. Choi, X. Lu, G. Yang, and C. Sun. Chapter 1 - electrochemical cells for medium- and large-scale energy storage: fundamentals. In Chris Menictas, Maria Skyllas-Kazacos, and Tuti Mariana Lim, editors, *Advances in Batteries for Medium and Large-Scale Energy Storage*, Woodhead Publishing Series in Energy, pages 3–28. Woodhead Publishing, 2015.

[69] D. Neamen. *Semiconductor Physics And Devices.* McGraw-Hill, Inc., USA, 4th edition, 2012.

[70] A. Smets, K. Jäger, O. Isabella, R. van Swaaij, and M. Zeman. *Solar Energy: The Physics and Engineering of PV Conversion Technologies and Systems.* UIT Cambrigde, 2016.

[71] H. F. Sterling and R. C. G. Swann. Chemical vapour deposition promoted by r.f. discharge. *Solid State Electronics*, 8(8):653–654, August 1965.

[72] H. Zhang, X. Zhong, J. Shaw, L. Liu, Y. Huang, and X. Duan. Very high energy density silicide–air primary batteries. *Energy & Environmental Science*, 6:2621, 09 2013.

[73] R. Teki, M. K. Datta, R. Krishnan, T. C. Parker, T. Lu, P. N. Kumta, and N. Koratkar. Nanostructured silicon anodes for lithium ion rechargeable batteries. *Small*, 5(20):2236–2242.

[74] Je. R. Szczech and S. Jin. Nanostructured silicon for high capacity lithium battery anodes. *Energy Environ. Sci.*, 4:56–72, 2011.

[75] Y. Bing, H. Liu, L. Zhang, D. Ghosh, and J. Zhang. Nanostructured pt-alloy electrocatalysts for pem fuel cell oxygen reduction reaction. *Chem. Soc. Rev.*, 39:2184–2202, 2010.

[76] B. Sljukic Paunkovic, C. Banks, and R. Compton. The search for stable and efficient sonoelectrocatalysts for oxygen reduction and hydrogen peroxide formation: azobenzene and derivativeselectronic supplementary information (esi) available: Plot of peak current versus square root of scan rate. see http://www.rsc.org/suppdata/cp/b4/b405025h/. *Physical Chemistry Chemical Physics (Incorporating Faraday Transactions)*, 6:4034–, 07 2004.

[77] F. Jaouen, E. Proietti, M. lefèvre, R. Chenitz, J. Dodelet, G. Wu, H. Chung, C. Johnston, and P. Zelenay. Recent advances in non-precious metal catalysis for oxygen-reduction reaction in polymer electrolyte fuel cells. *Energy & Environmental Science*, 4, 12 2010.

[78] K. Gong, F. Du, Z. Xia, M. Durstock, and L. Dai. Nitrogen-doped carbon nanotube arrays with high electrocatalytic activity for oxygen reduction. *Science (New York, N.Y.)*, 323:760–4, 03 2009.

[79] R. Bansal, P. Menon, and R. Sharma. Silicon–air batteries: progress, applications and challenges. *SN Applied Sciences*, 2, 06 2020.

[80] G. Zhang, J. Zheng, R. Liang, C. Zhang, B. Wang, M. Hendrickson, and E. Plichta. Lithium-air batteries using swnt/cnf buckypapers as air electrodes. *Journal of The Electrochemical Society - J ELECTROCHEM SOC*, 157, 01 2010.

[81] S. Beattie, D. Manolescu, and S. Blair. High-capacity lithium–air cathodes. *Journal of The Electrochemical Society - J ELECTROCHEM SOC*, 156, 01 2009.

[82] X. Yang and Y. Xia. The effect of oxygen pressures on the electrochemical profile of lithium/oxygen battery. *Journal of Solid State Electrochemistry*, 14:109–114, 01 2010.

[83] Fa. Cheng and J. Chen. Metal–air batteries: from oxygen reduction electrochemistry to cathode catalysts. *Chem. Soc. Rev.*, 41:2172–2192, 2012.

[84] K. Matsumoto, R. Hagiwara, R. Yoshida, Y. Ito, Z. Mazej, P. Benkič, B. Žemva, O. Tamada, H. Yoshino, and S. Matsubara. Syntheses, structures and properties of 1-ethyl-3-methylimidazolium salts of fluorocomplex anions. *Dalton Trans.*, pages 144–149, 2004.

[85] R. Hagiwara, Y. Nakamori, K. Matsumoto, and Y. Ito. The effect of the anion fraction on the physicochemical properties of emim(hf)nf (n = 1.02.6). *The Journal of Physical Chemistry B*, 109(12):5445–5449, 2005. PMID: 16851579.

[86] R. Gilliam, J. Graydon, Don Kirk, and S. Thorpe. A review of specific conductivities of potassium hydroxide solutions for various concentrations and temperatures. *International Journal of Hydrogen Energy - INT J HYDROGEN ENERG*, 32:359–364, 03 2007.

[87] P. Czuprynski and O. Joubert. X-ray photoelectron spectroscopy analyses of silicon dioxide contact holes etched in a magnetically enhanced reactive ion etching reactor. *Journal of Vacuum Science & Technology B: Microelectronics and Nanometer Structures Processing, Measurement, and Phenomena*, 16(3):1051–1058, 1998.

[88] S. Franssila. *Introduction to Microfabrication.* John Wiley & Sons, Ltd, 2010.

[89] D L Kendall. Vertical etching of silicon at very high aspect ratios. *Annual Review of Materials Science*, 9(1):373–403, 1979.

[90] K.E. Bean. Anisotropic etching of silicon. *IEEE Transactions on Electron Devices*, 25(10):1185–1193, 1978.

[91] C. A. Koval and J. N. Howard. Electron transfer at semiconductor electrode-liquid electrolyte interfaces. *Chemical Reviews*, 92(3):411–433, 1992.

[92] A.J. Bard and L.R. Falkner. *Electrochemical Methods - Fundamentals and Applications*. Wiley and Sons, 2nd edition, 2001.

[93] A. Nikolaychuk. The revised pourbaix diagram for silicon. *Silicon*, 6:109 – 116, 11 2014.

[94] J. A. V. Butler. Studies in heterogeneous equilibria. part iii. a kinetic theory of reversible oxidation potentials at inert electrodes. *Trans. Faraday Soc.*, 19:734–739, 1924.

[95] E. J.F. Dickinson and A. J. Wain. The butler-volmer equation in electrochemical theory: Origins, value, and practical application. *Journal of Electroanalytical Chemistry*, 872:114145, 2020. Dr. Richard Compton 65th birthday Special issue.

[96] E. D. Palik, O. J. Glembocki, I. Heard, P. S. Burno, and L. Tenerz. Etching roughness for (100) silicon surfaces in aqueous koh. *Journal of Applied Physics*, 70(6):3291–3300, 1991.

[97] E. D. Palik, V. M. Bermudez, and O. J. Glembocki. Ellipsometric study of orientation-dependent etching of silicon in aqueous KOH. *Journal of The Electrochemical Society*, 132(4):871–884, apr 1985.

[98] P. Allongue, V. Costa-Kieling, and H. Gerischer. Etching of silicon in NaOH solutions: II . electrochemical studies of n-si(111) and (100) and mechanism of the dissolution. *Journal of The Electrochemical Society*, 140(4):1018–1026, apr 1993.

[99] C. A. Desmond, C. E. Hunt, and S. N Farrens. The effects of process-induced defects on the chemical selectivity of highly doped boron etch stops in silicon. *Journal of the Electrochemical Society*, 141(1):178, 1994.

[100] H. Seidel, L. Csepregi, A. Heuberger, and H. Baumgärtel. Anisotropic etching of crystalline silicon in alkaline solutions: II . influence of dopants. *Journal of The Electrochemical Society*, 137(11):3626–3632, nov 1990.

[101] Y.E. Durmus, M. A. Liauw, and Rü.-A. Eichel. Investigation and Development of a Resource Efficient Metal–Air Battery – Silicon–Air. 2018.

[102] M.W. Chan, Chris McCoy, Sara Wodin-Schwartz, Clinton Warren, and Athulan Vijayaraghavan. Mems kinematic clamp for repeatable precision alignment. 07 2009.

[103] X. Zhong, Y. Qu, Y. Lin, L. Liao, and X. Duan. Unveiling the formation pathway of single crystalline porous silicon nanowires. *ACS Applied Materials & Interfaces*, 3(2):261–270, 2011. PMID: 21244020.

[104] S. Arrhenius. Über die dissociationswärme und den einfluss der temperatur auf den dissociationsgrad der elektrolyte. *Zeitschrift für physikalische Chemie*, 4(1):96–116, 1889.

[105] X. Wang, N. Gao, Q. Zhou, H. Dong, H. Yu, and Y. Feng. Acidic and alkaline pretreatments of activated carbon and their effects on the performance of air-cathodes in microbial fuel cells. *Bioresource technology*, 144, 07 2013.

[106] G. Cohn, R.-A. Eichel, and Y. Ein-Eli. New insight into the discharge mechanism of silicon-air batteries using electrochemical impedance spectroscopy. *Physical chemistry chemical physics : PCCP*, 15, 01 2013.

[107] E. Koren, Y. Rosenwaks, J. E. Allen, E. R. Hemesath, and L. J. Lauhon. Nonuniform doping distribution along silicon nanowires measured by kelvin probe force microscopy and scanning photocurrent microscopy. *Applied Physics Letters*, 95(9):092105, 2009.

[108] A. A. Betekbaev, B. N. Mukashev, L. Pelissier, P. Lay, G. Fortin, L. Bounaas, D. M. Skakov, and A.A. Pavlov. Doping optimization of solar grade (sog) silicon ingots for increasing ingot yield and cell efficiency. *Modern Electronic Materials*, 2(3):61–65, 2016.

[109] J. Pelleg. *Mechanism of Diffusion*, pages 31–39. Springer International Publishing, Cham, 2016.

[110] S. Mirabella, D. De Salvador, E. Napolitani, E. Bruno, and F. Priolo. Mechanisms of boron diffusion in silicon and germanium. *Journal of Applied Physics*, 113(3):031101, 2013.

[111] B. W. Williams. *Basic Semiconductor Physics and Technology*, pages 3–7. Macmillan Education UK, London, 1987.

[112] American Cleanroom Systems. US FED STD 209E Cleanroom Standard.

[113] H. Föll. Wafer flats.

[114] C. Bohling and W. Sigmund. Self-limitation of native oxides explained. *Silicon*, 8, 07 2016.

[115] S. I. Raider, R. Flitsch, and M. J. Palmer. Oxide growth on etched silicon in air at room temperature. *Journal of The Electrochemical Society*, 122(3):413–418, mar 1975.

[116] S. Xun, X. Song, L. Wang, M. Grass, Z. Liu, V. Battaglia, and G. Liu. The effects of native oxide surface layer on the electrochemical performance of si nanoparticle-based electrodes. *Journal of the Electrochemical Society*, 158:A1260–A1266, 01 2011.

[117] A. Sherman. In situ removal of native oxide from silicon wafers. *Journal of Vacuum Science & Technology B: Microelectronics Processing and Phenomena*, 8(4):656–657, 1990.

[118] Krawczak, E. and Gulkowski, S. Electrical properties of aluminum contacts deposited by dc sputtering method for photovoltaic applications. *E3S Web Conf.*, 19:03011, 2017.

[119] H. B. Michaelson. The work function of the elements and its periodicity. *Journal of Applied Physics*, 48(11):4729–4733, 1977.

[120] R. Kakkad, J. Smith, W. S. Lau, S. J. Fonash, and R. Kerns. Crystallized si films by low-temperature rapid thermal annealing of amorphous silicon. *Journal of Applied Physics*, 65(5):2069–2072, 1989.

[121] IBS - Innovative Ion Implant. Ion implantation service.

[122] P. Sberna and T. Scholtes. Pure boron chemical vapour deposition in epitaxial growth reactor.

[123] K. Pangal, J. C. Sturm, S. Wagner, and T. H. Büyüklimanli. Hydrogen plasma enhanced crystallization of hydrogenated amorphous silicon films. *Journal of Applied Physics*, 85(3):1900–1906, 1999.

[124] H. Kakiuchi, H. Ohmi, M. Harada, H. Watanabe, and K. Yasutake. Highly efficient oxidation of silicon at low temperatures using atmospheric pressure plasma. *Applied Physics Letters*, 90(9):091909, 2007.

[125] J. X.J. Zhang and K. Hoshino. Chapter 2 - fundamentals of nano/microfabrication and scale effect. In John X.J. Zhang and Kazunori Hoshino, editors, *Molecular Sensors and Nanodevices (Second Edition)*, Micro and Nano Technologies, pages 43–111. Academic Press, second edition edition, 2019.

[126] A. S. Grove, O. Leistiko, and C. T. Sah. Redistribution of acceptor and donor impurities during thermal oxidation of silicon. *Journal of Applied Physics*, 35(9):2695–2701, 1964.

[127] E Stewart, Malcolm Carroll, and J Sturm. Boron segregation and electrical properties in polycrystalline sigec. *MRS Proceedings*, 669, 01 2011.

[128] B. E. Deal and A. S. Grove. General relationship for the thermal oxidation of silicon. *Journal of Applied Physics*, 36(12):3770–3778, 1965.

[129] J. Henrie, S. Kellis, S. M. Schultz, and A. Hawkins. Electronic color charts for dielectric films on silicon. *Opt. Express*, 12(7):1464–1469, Apr 2004.

[130] Electronic Chemicals Group. Technical data: Buffered oxide etchants.

[131] K.R. W., K. Gupta, and M. Wasilik. Etch rates for micromachining processing-part ii. *Journal of Microelectromechanical Systems*, 12(6):761–778, 2003.

[132] Electric Fuel. Air electrode.

[133] LabChem. Msds potassium hydroxide, 30% w/v, 2018.

[134] G.L. Squires. *Fysisch experimenteren.* Aula : het wetenschappelijke boek. Uitgeverij Het Spectrum N.V., 1972.

[135] D. K. Schroder. *Resistivity*, pages 1–59. 2006.

[136] R. Holm. *Constriction resistances when conditions deviate from those in section 4, but with ρ still a constant*, pages 19–26. Springer Berlin Heidelberg, Berlin, Heidelberg, 1967.

[137] T. Clarysse, M. Caymax, P. De Wolf, T. Trenkler, W. Vandervorst, J. S. McMurray, J. Kim, C. C. Williams, J. G. Clark, and G. Neubauer. Epitaxial staircase structure for the calibration of electrical characterization techniques. *Journal of Vacuum Science & Technology B: Microelectronics and Nanometer Structures Processing, Measurement, and Phenomena*, 16(1):394–400, 1998.

[138] W. R. Thurber. *The relationship between resistivity and dopant density for phosphorus- and boron-doped silicon*, volume 400. US Department of Commerce, National Bureau of Standards, 1981.

[139] D. S. Perloff. Four-point sheet resistance correction factors for thin rectangular samples. *Solid-State Electronics*, 20(8):681–687, 1977.

[140] H. Topsoe. *Geometric factors in four point resistivity measurement*, volume 472. 1968.

[141] N.D. Arora, J.R. Hauser, and D.J. Roulston. Electron and hole mobilities in silicon as a function of concentration and temperature. *IEEE Transactions on Electron Devices*, 29(2):292–295, 1982.

[142] Advanced Instrument Technology. CMT-SR2000N / CMT-SR2000N-PV.

[143] E. D. Palik, O. J. Glembocki, and I. Heard. Study of bias-dependent etching of si in aqueous KOH. *Journal of The Electrochemical Society*, 134(2):404–409, feb 1987.

[144] Siegert Wafer. Silicon wafers stock list, 2022.

[145] Metrohm Autolab. Autolab PGSTAT204.

[146] Metrohm Autolab. Basic overview of the working principle of a potentiostat/galvanostat (PGSTAT) – Electrochemical cell setup, 2018.

[147] Veeco. Dektak 150 surface profiler, 2006.

Appendix A

Experimental equipment

The process steps and parameters of the equipment used to perform the experiments on the battery setup will be discussed in this chapter. First, the standard 100 mm silicon wafer properties are mentioned. The cleaning steps and (native/thermal) oxide layer removal will be discussed hereafter. For uniform doped wafers an electrical back-contact is applied through sputtering, but electron beam physical vapour deposition (EBPVD) will also be used. Dopant profiles are created by using pressure enhanced chemical vapour deposition (PECVD). The impurity atoms are diffused into the bulk by a tube furnace. After the diffusion process, the wafer is then cut into smaller samples that fit inside the battery setup. After this, the battery can be discharged. The surface of the silicon wafer material is inspected after discharging with a profilometer.

A.1 Wafer starting material

The silicon-air battery consists of a silicon wafer as anode material. This anode material will undergo some transformations before it can be used in the experiments. It all starts with a commercially produced four inch wafer (100 mm) with certain properties. These properties are listed in table A.1 and A.2.

Table A.1: Starting material properties of double side polished (DSP) silicon wafer. Brand is Siegert Wafer [144].

Type:	process wafer
Dopant material:	B (p-type)
Growth method:	Floatzone
Polish:	DSP
Orientation:	1-0-0, 0 $\pm$ 1.0 degree off orientation
Resistivity:	$>$ 1000 Ωcm
Thickness:	500 $\pm$ 10 μm
Diameter:	100 $\pm$ 0.5 mm

Table A.2: Starting material properties of single side polished (SSP) silicon wafer. Brand is Siegert Wafer [144].

Type:	process wafer	process wafer
Dopant material:	P (n-type)	B (p-type)
Growth method:	Czochralski	Czochralski
Polish:	SSP	SSP
Orientation:	1-0-0, 0 $\pm$ 1.0 degree off orientation	1-0-0, 0 $\pm$ 1.0 degree off orientation
Resistivity:	1 - 5 Ωcm	1 - 5 Ωcm
Thickness:	525 $\pm$ 15 μm	525 $\pm$ 15 μm
Diameter:	100 $\pm$ 0.5 mm	100 $\pm$ 0.5 mm

A.2 Cleaning and removing oxide

Before processing a new silicon wafer with additional layers, the wafer has to be cleaned using nitric acid (HNO_3) in several steps in the cleaning bench in the CR100. Besides, silicon is a material of which the surface oxidizes to silicon dioxide (SiO_2) at exposure to air at room temperature and normal pressure [114]. SiO_2 increases the impedance and acts as an insulator and has to be removed [116]. A common way to do this is by performing an hydrofluoric-acid (HF) dip with the Marangoni setup in the CR100 [117]. The description of the used steps in this thesis are given in the next subsection. The steps described to remove a thermal oxide layer with buffered HF (BHF) are also outlined in separate steps.

Flowchart

- Standard cleaning (45 min)
  - **Cleaning bench** - HNO_3 99% Si (RT) and HNO_3 69.5% Si (110 °C)
  - Ahead of cleaning, check if heating of HNO_3 69.5% is on as it is used at elevated temperature.
  - Clean 10 minutes in fuming HNO_3 99% at RT.
  - Rinse in DI water for 5 minutes.
  - Clean 10 minutes in concentrated HNO_3 69.5% with neoprene gloves.
  - Rinse in DI water for 5 minutes.
  - Dry with Spin Rinse Dryer (SRD) with standard program.
- Native oxide removal (15 min)
  - **Etching line** - HF 0.55% Si Marangoni (RT)
  - Ahead of cleaning, check if HF switch in technical room is switched on and volume in tank exceeds 10 liters.
  - Dump bath content and load wafers with primary flat down.
  - Fill bath with HF solution and lower wafers.
  - Etch for 4 minutes and start timer when 50% of wafers are covered.
  - Start DI water flow after 4 minutes for a duration of 5 minutes.
  - Start IPA flow in the final minute of the DI water flow for a duration of 2 minutes.
  - Wafers can be lifted up from bath.
  - **Single batch - wet bench** - HF 0.5% Si (RT)
  - A Teflon container has to be used, as glass is attacked by HF.
  - Wear an apron, neoprene gloves, a face shield and glasses when working with HF.
  - Use a 40% HF bottle and DI-water. The HF has to be diluted 80 times in order to achieve 0.5% HF.
  - Depending on the size of the container, determine the amount of DI-water and fill the container.
  - Pour a measured amount of 40% HF inside the Teflon container.
  - Etch for 2 minutes and start timer when 50% of wafers are covered.
  - Check whether Si surface is hydrophobic. If this is the case, rinse in DI-water.
- Thermal oxide removal (15 min)
  - **Single batch - wet bench** - BHF 1:7 (RT)
  - A Teflon container has to be used, as glass is attacked by BHF.
  - Wear an apron, neoprene gloves, a face shield and glasses when working with BHF.
  - Use the pre-made BHF 1:7 bottle and a container filled DI-water to rinse.
  - Etch for 4 minutes and start timer when 50% of wafers are covered.
  - Check whether Si surface is hydrophobic and greyish. If this is the case, rinse in DI-water. Otherwise, etch longer.

A.3 PVD (Trikon Sigma 204 Dealer)

With the silicon surface is cleaned and free from SiO_2, the next step is to immediately apply a metal back-contact that functions as a current collector of the electrode. It is key to handle fast as the native oxide starts to grow once the wafer is exposed to air again. An Al:Si layer is deposited on the clean silicon wafer using the principle of sputtering, a form of Physical Vapor Deposition (PVD), with the Trikon Sigma 204 dealer inside the CR100. The 99% Al/1% Si is a standard target in the EKL CR100 and is therefore always available, while other targets might fluctuate in availability. The wafers are loaded in a cassette and can each undergo a different metallization process. The use of a dummy wafer prior to the clean wafers is advised to clean the target as there might be debris left in the sputtering chamber when it has been inactive for more than two hours. The Trikon Sigma is shown in figure A.1. The chosen flowchart using the Trikon Sigma is discussed in the next subsection.

Figure A.1: Trikon Sigma 204 Dealer

Flowchart

- Metallization of Al:Si back contact (30 min)
  - **Trikon Sigma 204** - HSE and Dev A (350 °C)
  - Choose the target chamber with 99% Al and 1% Si: Dev A.
  - Insert wafers in cassette with a dummy wafer on the first position.
  - Select two recipes: one for the dummy wafer, one for the clean Si wafers. A 675 nm thick layer of Al:Si will be deposited on the clean wafers. This enables a good electrical contact.
    - Dummy: *_TrgtClean_350C*
    - Clean: *AlSi_675nm_350C*
  - After the deposition check the wafers, they should look shiny
  - Put system in IDLE after you are done.

A.4 EBPVD (Provac Pro500S)

Besides the metallization of the back contact with the Trikon Sigma inside the CR100, an Electron Beam Physical Vapor Deposition (EBPVD) tool in the CR10000, the Provac Pro500s, can be used. The Wafers that are placed inside the chambers of the Trikon Sigma need to be as clean as possible to prevent contamination, whereas with the Provac contamination is less of an issue. To obtain a good conducting electrical contact, the native oxide should ideally be removed just before applying the metal back contact. Another benefit of the Provac is that it operates at room temperature, meaning that no time is needed to heat up the chamber and the wafers.

The Provac operates in vacuum at room temperature. This reduces heating time, but since the deposition chamber is considerably larger than in the Trikon Sigma, as can be seen in figure A.2, pumping it to the required level of vacuum takes more than an hour after venting. Inside the chamber, four wafers can be mounted to a carousel, but they will all receive the same deposition material recipe. Such a recipe can be custom made and includes settings such as the material, layer thickness and deposition speeds. Available materials are, among others, aluminum, chromium, silver and titanium. A quartz crystal measures the evaporation rate and shows the thickness on the control screen as can be seen in figure A.3. The wafer is deposited from the bottom side only. If both sides need a metal contact, the wafer has to be flipped and the process repeated.

Figure A.2: The Provac Pro500S setup in the CR10000.

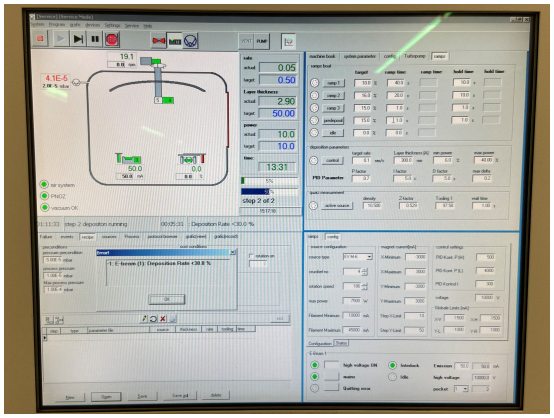

Figure A.3: The control display of the Provac Pro500s.

Flowchart

- Metallization of back contact (2 hours)
  - **Provac Pro500S** - (RT)
  - Ideally remove the native oxide before depositioin with 0.55% HF. Wafers that are deposited later can be mounted at the top inside the chamber to remain in vacuum.
  - Mount the wafers on a square holder with the to be deposited side downwards.
  - Load the wafers on the caroussel. The caroussel can be turned counterclockwise.
  - Once the wafers are mounted, close the chamber and engage the vacuum pump. Wafers that are deposited with a different recipe can be mounted at the top inside the chamber, such that they remain in vacuum. Achieving the required vacuum of $2{\times}10^{-}5$ mbar takes roughly 45 min till one hour.
  - Enter the recipe:
    - Aluminum layer : *Al_ 500nm*, 1 nm/s growth rate, pocket 4
    - Chromium layer : *Cr_ 50nm*, 0.5 nm/s growth rate, pocket 3
  - The chamber is vented automatically 300 seconds after the deposition is done.
  - After the deposition check the wafers. The layer should look uniform.
  - Put system back in vacuum after you remove the deposited wafers.

A.5 PECVD (AMOR)

A thin impurity layer is deposited on top of the c-Si wafer to function as a source layer for the drive-in process. Plasma Enhanced Chemical Vapor Deposition (PECVD) is a widely applied technique for depositing very uniform thin layers on solar cells at low temperatures around 200 degree Celsius by using a plasma that provides the required energy [88]. Once the plasma is on, a purple glow can be observed in the reaction chamber, as is illustrated in figure A.5.

The AMOR, built by the company Elettrorava, is used to deposit hydrogenated amorphous Silicon (a-Si:H) on top of c-Si. Boron and Phosphorus are used as dopant atoms to deposit p-type and n-type a-Si:H respectively. These deposited layers act as a source layer for the drive-in process that follows after this deposition. Through experimental analysis of other researchers it was found that the deposited layers in the AMOR can reach dopant concentrations of 10^{21} atoms/cm^3.

Only reaction chambers MPZ1 (p-type) and MPZ2 (n-type) are used. The available gases are limited per chamber as, for instance, diborane (B_2H_6) can only be used in chamber MPZ1 and phoshpine (PH_3) only in chamber MPZ2.

Wafers have to be mounted on grounded holders. Each holder can only hold one wafer. The wafers are fed one by one into the AMOR through a load lock located at the front. After the load lock the holder is moved through a transport chamber into the deposition chamber. The setup is shown in figure A.4.

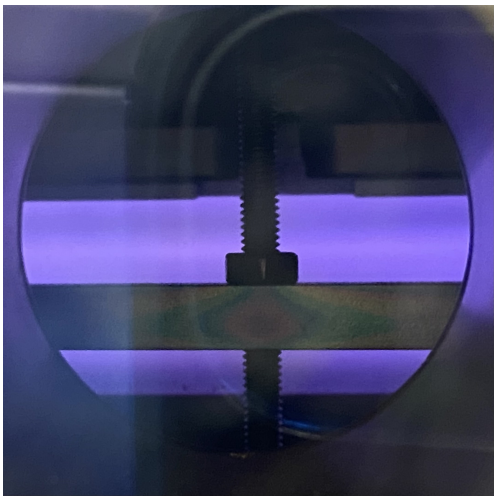

Figure A.4: When the plasma of the PECVD process is on, the layer is being deposited and a clear purple colored glow is visible inside the reaction chamber.

Figure A.5: The AMOR setup. The load lock is the round tube at the front and is used to enter the wafer holders. The wafers are put in one by one.

Flowchart & recipes

- PECVD (2-4 hours)
  - **AMOR** - MPZ1 and MPZ2 (298 °C)
  - Load wafer on holder and put in load lock with the to be deposited side pointing downwards. Align the holder slightly to the right.
  - Label the loaded wafer with a run-number such that it can be tracked throughout the system.
  - Pump down load lock and transfer wafer through the transport chamber into the deposition chamber.
  - Wait 45 min after the wafer is put into chamber to let it heat up.
  - Open *gas-in* and open *purge* for 2 min. Enter flow values for process gases, deposition pressure and power from recipe.
  - Open process gas flows and set the throttle valve from *open* to *throttle*. Set *tune* and *load* of matchbox to automatic.
  - Click on *RF on* and inspect the reflected power. This should ideally be as low as possible to transfer the power as effectively as possible. Otherwise tune manually from a high to low value.
  - Inspect if the plasma is on by looking into chamber. Start timer once the plasma is on.

– Once the deposition time is over swith of the plasma by pressing *RF off*. Switch the throttle valve from *throttle* to *open* and close the process gas flow switches.
– Purge again for 2 min and close the *purge* and *gas-in* afterwards.
– Transfer the wafer from the deposition chamber to the load lock to let it cool down for at least 45 min.

Table A.3: Recipe parameters for growing a 50 nm thick a-Si:H layer for both n-type and p-type. The gas flows are indicated in standard cubic centimeters per minute (sccm). The recipes are based on work of Dr. Zhirong Yao, Postdoc researcher at PVMD group of Delft University of Technology.

p-type a-Si:H

Parameter [unit]	**Value**
SiH_4 [sccm]	8
B_2H_6 (2% in H_2) [sccm]	5
H_2 [sccm]	100
P_{RF} [W]	5
p_{depo} [mbar]	2.0
T_{heater} [°C]	298
Duration [min]	6

n-type a-Si:H

Parameter [unit]	**Value**
SiH_4 [sccm]	4
PH_3 (2% in H_2) [sccm]	4.8
H2 [sccm]	35
P_{RF} [W]	5
p_{depo} [mbar]	1.0
T_{heater} [°C]	298
Duration [min]	12

A.6 Tube furnace (TNW-RID)

The drive-in process is performed by using a tube furnace located at the Reactor Institute Delft. This furnace is capable of reaching temperatures of 1600 degree Celsius for long time periods. In this research it is operated at 1250 degree Celsius for a period of 36 hours. The wafers are loaded on a ceramic holder that slides into the tube, as can be seen in figure A.6. The settings are programmed on the controller in figure A.7.

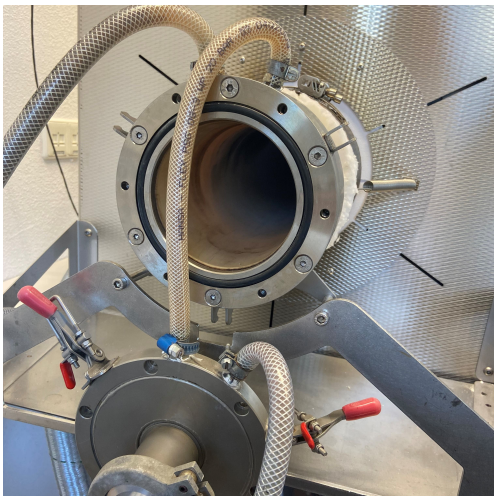

Figure A.6: The loading side of the tube furnace that seals to allow for a vacuum to be reached. The hoses are used for water cooling at the edges.

Figure A.7: The control panel of the tube furnace, with three time periods with corresponding temperatures to be set: ramp up, continuous and ramp down temperature.

Flowchart

- Diffusion of a-Si:H and epitaxial grown layers (50 hours)
  – **Nabertherm** (1250 °C)
  – Load the dummy wafer and the deposited wafer on top of each other on the ceramic block. The ceramic block has to be pushed to the middle of the furnace, near the temperature probe. Close the load lock once the block is in place.

- Pump down the tube with the vacuum turbo-pump. Keep the vacuum pump running, but close the in-between switch.
- Fill the tube with N_2 by opening the valve. Wait till the expansion valve starts venting because of overpressure (1 atm + 10 mbar). Then close the N_2 flow switch.
- Pump down chamber again and repeat process two times.
- Set the N_2 flow knob to *flush* to keep flushing throughout the drive-in process.
- Fill in the temperatures and durations (h:min):
  * 01: T_a = 0 °C, T_b = 1250 °C, t = 6:40
  * 02: T_a = 1250 °C, T_b = 1250 °C, t = 36:00
  * 03: T_a = 1250 °C, T_b = 0 °C, t = 6:40
- Press start and observe if current levels on gauge are increasing.
- When the thermal annealing process is done and the furnace is cooled down to room temperature, close the N_2 flush and coolant flow. The load lock can be opened.

A.7 Laser Cutter

Once the Al:Si, or any other back contact, layer is deposited on the back side of the silicon wafer, the wafer can be cut into the desired shapes that fit inside the battery setup. A fast and easy way is to cut the wafer using a powerful laser cutter (20 W, λ = 1064 nm). The Electrical Sustainable Power (ESP) laboratory has such a laser cutter. The wafer can be placed inside a designated chamber that has a camera mounted at the top to have a view on the wafer as can be seen in figure A.8. Once the wafer is in place, the pattern design can be customized. An example of a design is given in figure A.9. As the wafer is placed on top of a perforated surface it is possible to clamp it down to prevent it from moving.

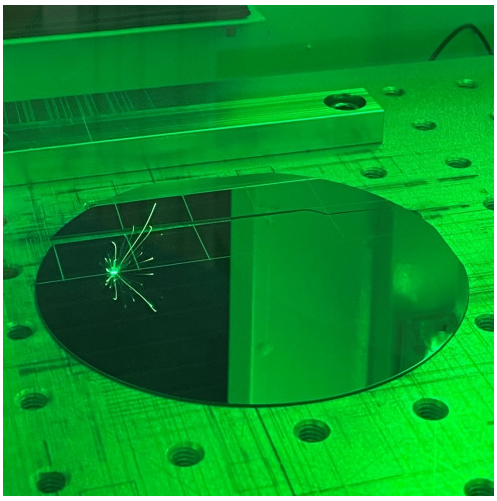

Figure A.8: The laser cutter in action. A too large number of sequential laser scribes caused this wafer to break by itself.

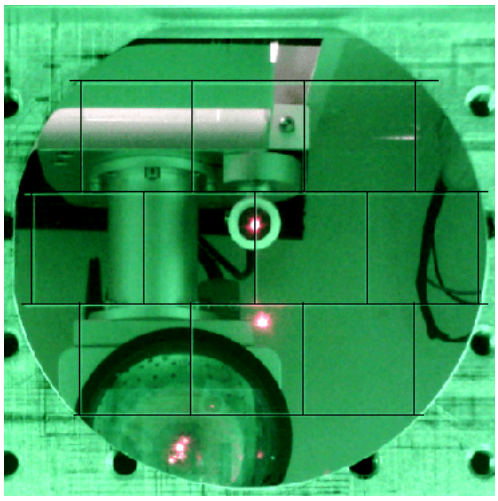

Figure A.9: The designed patterns, in this case 23 by 23 mm squares. Horizontal lines across the entire wafer ease the breaking.

The samples are retrieved from the wafer by using the principle of bend-and-break as silicon is a very brittle material. Once the laser has finished the designed pattern, the wafer can be broken alongside the crystal orientation in the desired shapes. For a 1-0-0 wafer orientation, this is parallel or perpendicular to the primary flat. To make sure that the wafer breaks in a straight line, it is advised to draw lines across the entire wafer. The exact steps and used parameters are described in the next subsection.

Flowchart

- Laser cutting into samples (30 min)
  - **Laser cutter** (RT)
  - Place wafer inside chamber with the back-contact directed upwards to the camera.
  - In the design the required pattern use lines instead of square boxes. This prevents the laser to go over the same area twice on overlapping points and reduces time.
  - Selected parameters for a 500 μm thick wafer:
    - Loop count: 50
    - Speed (MM/second): 150
    - Power (%): 100
    - Frequency (kHz): 100
  - When the process is done (maximum 10 min), let wafer cool down for a minute before picking it up wearing gloves.
  - Wear safety goggles and nitrile gloves when you break the wafer into samples.

A.8 Galvanostat (Metrohm Autolab PGSTAT)

The assembled battery can be discharged with a constant discharge current using a galvanostat. The setup used in this thesis is the Metrohm Autolab PGSTAT. This device is equipped with the NOVA 2.1 software that allows for a user-friendly interface. In the CR10000, the Autolab is integrated in the Meco Copperplating setup of the PVMD-group. Only the cables connecting the battery and the Autolab will be used. This is placed inside the white box in figure A.10.

Figure A.10: The Autolab setup sits inside the white box, creating a safe work environment to place the cell setup filled with chemicals.

The Autolab is capable of measuring currents and voltages with very high precision. The limits in the current and voltage measurement data is listed in table A.4. The current range should be limited to the closest value with respect to the set current.

Table A.4: Specifications of the Autolab's voltage and current output accuracy and resolution. Data taken from [145].

Parameter	Value	Unit
Potential range	± 10	V
Potential resolution	150	μV
Potential accuracy	± 0.2%	V
Measured potential resolution	300	nV
Current range	10 - 1	nA - A, in decades
Current resolution	0.015%	of current range
Current accuracy	± 0.2%	of current range
Measured current resolution	0.00003%	of current range
Input impedance	> 1	TΩ

Connections

The Autolab is used in a two-electrode setup. This means that the whole cell setup behavior is investigated. Such a two-electrode setup is common to use for batteries, fuel cells and solar cells. Four of the five available electrodes are used. The counter electrode (CE) and reference electrode (RE) are short-circuited on the side of the anode, while the working electrode (WE) and sense (S) are short-circuited at the cathode. The connections are shown in figure A.11. In a galvanostatic discharge, the current level between the WE and the CE is maintained constant, while the potential difference is measured between the RE and WE.

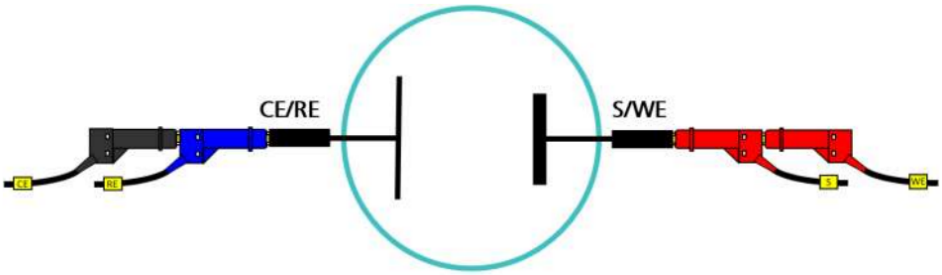

Figure A.11: The two-electrode setup as used in the Autolab cell setup. The CE and RE connect to the Si anode, while the WE and S connect to the air cathode. Figure taken from [146].

A.9 Profilometer (Veeco Dektak 150)

After the samples have been discharged, the part of the sample's surface within the O-ring is corroded by the KOH electrolyte. This is an area of 1 cm^2. The area outside of the O-ring is not affected by the KOH and remains flat. This creates a so-called step height that can be measured with a profilometer.

The Veeco Dektak 150 is used to measure the step height between the active and inactive part of the sample's surface. A thin needle with a radius of 12.5 μm scans over the surface and the resulting profile is stored in the computer. Step heights as small as 1 Åcan be measured with the Dektak at a vertical range of 6.55 μm. The needle can either scan uphill or downhill over the surfaces, i.e. from the etched active area to the flat inactive area or vice versa. The scan distance and speed can be set. The used parameters for the measurements used in this thesis are listed in table A.5. The Dektak setup is shown in figure A.12.

Table A.5: Table with Dektak parameters used in the measurements of this research. Data taken from [147].

Parameter [unit]	Value
Scan length [μm]	1,000
Scan duration [s]	60
Scan resolution [μm/sample]	0.056
Vertical range [μm]	65.5 - 524
Stylus force [mg]	3.00
Profile	Valleys

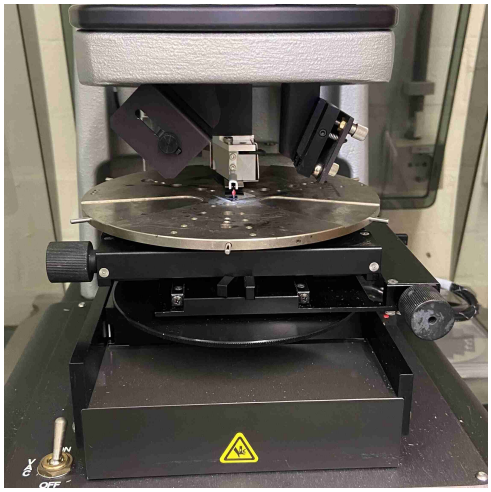

Figure A.12: The Dektak 150 setup availabe in the MEMS-lab. The needle moves in backwards direction observed from this angle.